Graded photonics crystals on SOI platform for near-infrared applications

Quan Yue

université
PARIS-SACLAY

Graded photonics crystals on SOI platform for near-infrared applications

Cristaux photoniques à gradient sur plate-forme SOI pour des applications dans le proche infrarouge

Thèse de doctorat de l'université Paris-Saclay

École doctorale n°575 : electrical, optical, bio-physics and engineering (EOBE)
Spécialité de doctorat : Electronique et Optoélectronique, Nano- et Microtechnologies
Graduate School : Sciences de l'ingénierie et des systèmes. Référent : Faculté des sciences d'Orsay

Thèse préparée dans l'unité de recherche **Centre de Nanosciences et de Nanotechnologies** (Université Paris-Saclay, CNRS), sous la direction d'**Éric AKMANSOY**, Maître de conferences (HDR)

Thèse soutenue à Paris-Saclay, le 7 Décembre 2022, par

Quan YUE

Composition du Jury

Membres du jury avec voix délibérative

Eric LHEURETTE Professeur des Universités, Université de Lille	Président
Ségolène CALLARD Professeure des Universités, École Centrale de Lyon	Rapporteur & Examinatrice
Emmanuel CENTENO Professeur des Universités, Université Clermont-Auvergne	Rapporteur & Examinateur
Olivier GAUTHIER LAFAYE Professeur des Universités, Université Toulouse 3	Examinateur

THESE DE DOCTORAT

NNT : 2022UPAST138

université PARIS-SACLAY

DOCTORAL SCHOOL
Electrical, Optical, Bio: Physics and Engineering (EOBE)

Titre : Cristaux photoniques à gradient sur plate-forme SOI pour des applications dans le proche infrarouge

Mots clés : Cristal Photonique à Gradient, Photonique du Silicium, Proche Infrarouge, Nanotechnologie

Résumé : Les cristaux photoniques gradient (GPC) permettent de contrôler efficacement le flux de lumière grâce à la forme de leurs bandes photoniques. L'optique GRaded INdex (GRIN) connaît un renouveau car elle permet de réduire la taille des systèmes optiques, ouvrant ainsi une nouvelle voie à la conception optique. La nanotechnologie permet de fabriquer efficacement des cristaux photoniques, que nous mettons en œuvre pour fabriquer des GPC pour l'optique GRIN. L'objectif principal de ce sujet de doctorat est d'explorer les cristaux photoniques gradient et les optiques à gradient d'indice connexes dans le domaine du proche infrarouge pour des applications sur des plates-formes Silicon On Insulator (SOI). Une partie importante de ce travail est le processus de fabrication et de caractérisation des cristaux photoniques à gradient dans le domaine du NIR. Nous nous concentrons sur la technologie de nanofabrication ainsi que sur la caractérisation des SNOM. Le SOI a été choisi comme plateforme de traitement pour ce travail, compte tenu de la bonne compatibilité de la plateforme à base de silicium avec les dispositifs photoniques et de sa capacité à bien s'intégrer aux techniques de nanofabrication. En outre, un autre aspect important de ce travail est d'explorer l'effet de la variation des paramètres du cristal photonique sur son indice de réfraction effectif. Nous tentons de manipuler l'indice de réfraction effectif des cristaux photoniques en modifiant leurs paramètres. La démonstration expérimentale d'une lentille en cristal photonique à gradient d'indice de réfraction négatif et de dispositifs en cristal photonique à gradient connexes est mise en évidence.

Title : Graded photonics crystals on SOI platform for near-infrared applications

Keywords : Graded Photonic Crystal, Silicon Photonics, Near-Infrared, Nanotechnology

Abstract : Graded Photonic Crystals (GPC) allow to efficiently control the flow of light thanks to the shape of their photonic bands. GRaded INdex (GRIN) optics is undergoing a renewal because it allows downsizing optical systems, opening a new way to optical design. Nanotechnology enables to efficiently fabricate photonic crystals, which we implement to fabricate GPC for GRIN optics. The main purpose of this Ph.D. topic is to explore graded photonic crystals and related gradient index optics in the near-infrared domain for applications on Silicon On Insulator (SOI) platforms. A significant part of this work is the fabrication and characterization process of gradient photonic crystals in the NIR field. We focus on nano-fabrication technology as well as SNOM characterization. SOI was chosen as the processing platform for this work, considering the good compatibility of the silicon-based platform with photonic devices and its ability to integrate well with nanofabrication techniques. In addition, another emphasized aspect of this work is to explore the effect of the variation of the photonic crystal parameters on its effective refractive index. We attempt to manipulate the effective refractive index of photonic crystals by changing their parameters. Experimental demonstration of negative refractive index gradient photonic crystal lens and related gradient photonic crystal devices is highlighted.

One's destiny, of course, depends on personal struggle, but it also needs to take the historical itinerary into consideration.

-An elder

Acknowledgements

The period of my PhD life have passed by in a flash, and I feel grateful in my heart when I look back on the years I have spent. On this moment of completing my thesis, I would like to express my sincere gratitude to all those who helped and cared for me.

First of all, I would like to express my sincere thanks to my supervisor, Eric Akmansoy. Without him I would not have been able to work on this exciting Ph.D. subject. I would like to thank him for providing me with a comfortable working environment and adequate computing equipment, and for his time in guiding my research during my Ph.D. study. I have benefited greatly from his rigor in revising my thesis and his enthusiasm for scientific work.

I am also very thankful to Segolene Callard and Emmanuel Centeno for accepting to be my thesis reviewer, and to the other members of my jury, Olivier Gauthier Lafaye, Eric Lheurette and Anatole Lupu. Thank you very much for taking your precious time to attend my defense.

In addition, I would like to thank all the faculty members in our research team CRIME. I am grateful for their support during my PhD studies in France, both in life and in my studies. A special thanks goes to Anatole Lupu, our team leader. I am impressed by his profound academic knowledge and broad academic vision. I am also very appreciative of his valuable advice and fruitful discussions on my PhD project.

In addition, I would like to express my gratitude to Xavier Le Roux, our clean room engineer. To this day I can still remember the first meeting with him. Without him my sample fabrication could not have been realized. His rich experience in clean room processing and his sharp scientific opinion helped me a lot in my research. I would like to express the same gratitude to the other engineers in the clean room including Jean-Rene COUDEVYLLE, Samson EDMOND, Frederic MAHUT, Fabien BAYLE, David BOUVILLE. Likewise, I would like to thank Benoît Cluzel who helped me with the SNOM characterization. I sincerely thank him for making time to help me with characterization in his busy research work. I learned a lot from the discussions with him. I would also like to thank the administrative staff I met, including Sylvie LAMOUR, Melissa LEGENDRE, Lydia ANDALON, Laurie VINCENT, Vanessa DELAISSE, Alexia COURTOIS, Hinde NEKKAZ. They helped me a lot in registration and adapting to the new lab environment.

Also, I would like to express my enthusiastic appreciation to my friends and colleagues.

Thanks to Yaoyao Liang, Rui Feng, Menglan Lin, Xin Zheng, Jihye Baik, Amina Djemmah, Zhengrui Tu, Yulong Fan, Yao Pei, Haiteng Sun, Rui Dai, Yuxuan Zhao, Shaochen Wang, Fulie Chen, Yi Peng, Guanda Wang, Yuan Hao. They have enriched my life in a foreign country. Thank them for their help and encouragement in my life.

Last but not least, I would like to express my deepest gratitude to my family and parents, my mother Huiyuan Yu, my father Zhongxing Yue. I thank them for their care, encouragement, understanding and trust along the way. In addition, I sincerely thank my wife Mengxi Zhou for her love and companionship.

YUE Quan
December 2022

Résumé en français

L'objectif principal de cette thèse est d'appliquer les dispositifs de cristaux photoniques à gradient aux plateformes SOI. Grâce aux techniques avancées de nanofabrication à base de silicium, l'optique à gradient d'indice de réfraction, dominée par les cristaux photoniques à gradient, sera étendue au domaine du proche infrarouge. Selon la théorie de l'électromagnétisme sub-longueur d'onde, la taille du dispositif doit être d'un ordre de grandeur par rapport à la longueur d'onde de fonctionnement. Ainsi, contrairement au domaine des micro-ondes, un grand défi dans le domaine du proche infrarouge est la fabrication et la caractérisation des dispositifs correspondants. Une partie importante de ce travail se concentre sur le processus de fabrication et de caractérisation des cristaux photoniques à gradient dans le domaine du proche infrarouge. Le SOI a été choisi comme plateforme de traitement pour ce travail, compte tenu de la bonne compatibilité de la plateforme à base de silicium avec les dispositifs photoniques et de sa capacité à bien s'intégrer aux techniques de nanofabrication.

Le déroulement de cette thèse commence par une introduction aux connaissances de base pertinentes dans le **Chapitre 1**. Nous commençons par une brève démonstration des bases des cristaux photoniques et des concepts associés tels que les diagrammes de bande et les courbes iso-fréquence. Cela contribue de manière importante à la conception ultérieure des lentilles pour les cristaux photoniques. Nous présentons ensuite les différents phénomènes de dispersion dans les cristaux photoniques. Dans cette thèse, nous nous intéressons davantage au phénomène de l'indice de réfraction négatif. Nous présentons ensuite le concept des cristaux photoniques à gradient ainsi que l'histoire et l'état actuel de leur développement. Les méthodes FDTD et d'expansion des ondes planes utilisées dans la thèse sont également présentées à la fin du **Chapitre 1**.

Le chapitre suivant, le **Chapitre 2**, s'attache à montrer la partie de la photonique sur silicium qui est concernée par cette thèse. Plus précisément, ce chapitre présente les concepts liés à la plateforme de traitement SOI utilisée dans la thèse dans le domaine du proche infrarouge. Certaines des méthodes de préparation du SOI et de son couplage aux fibres hors puce sont d'abord présentées. Dans cette thèse, le couplage de bord est choisi comme méthode d'introduction de la lumière dans la couche de silicium SOI. Nous présentons ensuite la méthode de l'indice de réfraction effectif utilisée dans cette thèse comme une approximation pour calculer le diagramme de bande d'une plaque de cristal photonique. Enfin, nous présentons plusieurs guides d'ondes optiques différents. Dans cette thèse, le guide d'ondes à fil est

choisi comme support pour la propagation de la lumière sur la puce.

Le **Chapitre 3** se concentre sur la présentation des résultats de conception et de simulation des dispositifs à cristaux photoniques à gradient dans cette thèse. Pour la lentille à cristaux photoniques à gradient, nous nous concentrons sur le cas où les fréquences normalisées se trouvent dans les première et deuxième bandes de son diagramme de bande. Pour la forme du lattice du cristal photonique, nous présentons deux cas principaux, à savoir le lattice hexagonal et le lattice carré. Les possibilités de conception de lentilles à cristaux photoniques à gradient sont discutées pour ces cas et des simulations sont effectuées pour des lentilles à gradient dans lesquelles un milieu homogène peut être formé. Les diagrammes de bande des cristaux photoniques et les courbes d'iso-fréquence sont calculés à l'aide du logiciel libre MPB du MIT[1]. Les simulations ultérieures de la structure ont été effectuées en utilisant l'environnement de simulation 3D de Lumerical FDTD. Finalement, la thèse a choisi le cas où la fréquence normalisée se trouvait dans la deuxième bande du cristal photonique à réseau hexagonal pour le traitement suivant (voir Figure R1). Nous présentons également la conception et la simulation d'une lentille Half Maxwell fisheye basée sur cristal photonique à gradient. Ce chapitre présente également les idées de conception et les résultats de simulation d'une source ponctuelle sur SOI. Les résultats de la simulation sont également présentés pour différents emplacements sur la surface de la lentille, en conjonction avec la technique de caractérisation SNOM utilisée suivante.

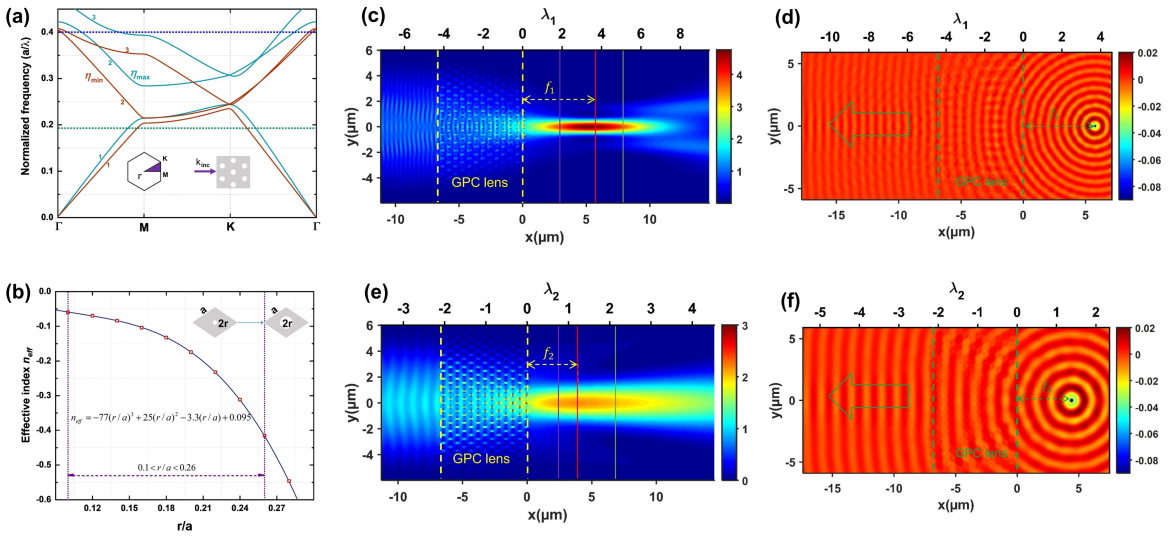

Figure R1: Résultats de la modélisation et de la simulation partielle des fréquences normalisées de la deuxième bande d'un cristal photonique à réseau hexagonal. (a) Diagramme de bande correspondant. (b) Courbe déduite. (c) et (d) Résultats de la simulation pour l'incidence d'une onde plane et d'une source ponctuelle à une longueur d'onde de 1.55 μm. (e) et (f) Résultats de la simulation pour une longueur d'onde de 3.2 μm.

La mise en place des techniques de nanofabrication et des plateformes de caractérisation impliquées dans cette thèse sont présentées dans le **Chapitre 4**. Deux des principales

techniques de traitement intermédiaire salle blanche sont la nanolithographie et la gravure sèche. La machine de nanolithographie utilisée dans cette thèse est la Nanobeam 4. Son courant de calibration a été réglé à 0.5nA pour obtenir une taille de pas de 2 nm. En fait, le courant de calibration sera entre 0.48nA et 0.51nA à chaque fois. Les erreurs de traitement sont donc inévitables. La tension a été réglée à 80 kV pour obtenir une taille de faisceau d'électrons de 5 nm. Pour la gravure sèche, nous avons utilisé l'ICP-DRIE de *SPTS technologies*. Un processus standard de gravure du silicium à 220nm de profondeur a été appliqué au SOI. Le reste des opérations de la salle blanche tournera autour de ces deux étapes principales. La plupart des traitements sont effectués dans la salle blanche du C2N. Le travail à l'extérieur de la salle blanche se concentre sur le masque du faisceau d'électrons et la préparation des fichiers pour NB4. Les échantillons finaux sont traités sur des feuilles SOI de 2cmx2cm. Après découpe, un échantillon testable parfait est un long morceau rectangulaire d'environ 2cmx0.8cm. Aussi, deux méthodes principales de caractérisation sont utilisées dans cette thèse (voir Figure R2). L'une d'entre elles consiste à recueillir l'intensité du champ à l'extrémité émettrice de la lentille sous la forme d'un ensemble de guides d'ondes de sortie. De cette façon, l'intensité du guide de lumière est collectée dans la couche supérieure de silicium du SOI. Cette méthode de caractérisation est réalisée en C2N. L'autre consiste à utiliser la technique plus avancée du SNOM. La méthode de caractérisation SNOM est réalisée dans ICB laboratoire à Dijon.

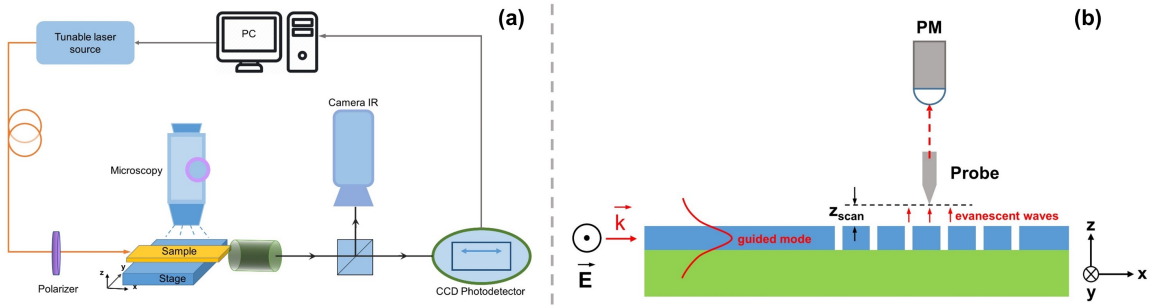

Figure R2: (a) Configuration pour la caractérisation en utilisant des ensembles de guides d'ondes de sortie. (b) Mise en place de la caractérisation à l'aide du SNOM.

La présentation SEM de l'échantillon final et les résultats obtenus par les deux méthodes de caractérisation sont présentés au **Chapitre 5**. De plus, les résultats préliminaires concernant le traitement des lentilles Half Maxwell fisheye sont mentionnés dans ce chapitre. Les images SEM de certains des échantillons sont présentées dans la Figure R3. Tout d'abord, pour la structure cellulaire de l'une ou l'autre méthode de caractérisation, une section de filtre monomode de 200µm de long et 450nm de large est présente à l'extrémité d'entrée pour s'assurer que le mode fondamental TE est obtenu. Des guides d'ondes coniques de différentes tailles relient le filtre au guide d'ondes droit. Pour les structures cellulaires utilisant les guides d'ondes de sortie, le côté entrée de la lentille est un guide d'ondes de 10 µm de large pour simuler une onde plane approximative. A la sortie de la lentille se trouvent 13

guides d'ondes de 700nm de large et espacés de 300nm. La distance entre eux est progressivement augmentée en forme d'éventail pour éviter le couplage entre les guides d'ondes. En faisant varier la distance entre ce groupe de guides d'ondes et le côté sortie de la lentille, nous pouvons obtenir des informations sur l'intensité du champ de sortie. Un total de 60 distances différentes, de 0.5 µm à 30 µm, ont été traitées sur une seule feuille SOI. Et pour la caractérisation de la structure de la cellule échantillon à l'aide de la technique SNOM, nous devons utiliser la structure MMI. Un bras auxiliaire est utilisé pour l'alignement de la fibre d'entrée pour la caractérisation SNOM. L'autre bras est connecté à notre lentille et la sonde SNOM va scanner dans la zone de l'objectif et derrière lui. Pour cette structure cellulaire, nous traitons plusieurs sur une feuilles SOI afin de garantir la tolérance du traitement. Enfin, nous avons conçu la source ponctuelle sur puce qui est également usinée sur le SOI. Encore une fois, en faisant varier la distance entre la source ponctuelle et la lentille, nous avons essayé de trouver une situation où elle pourrait être collimatée.

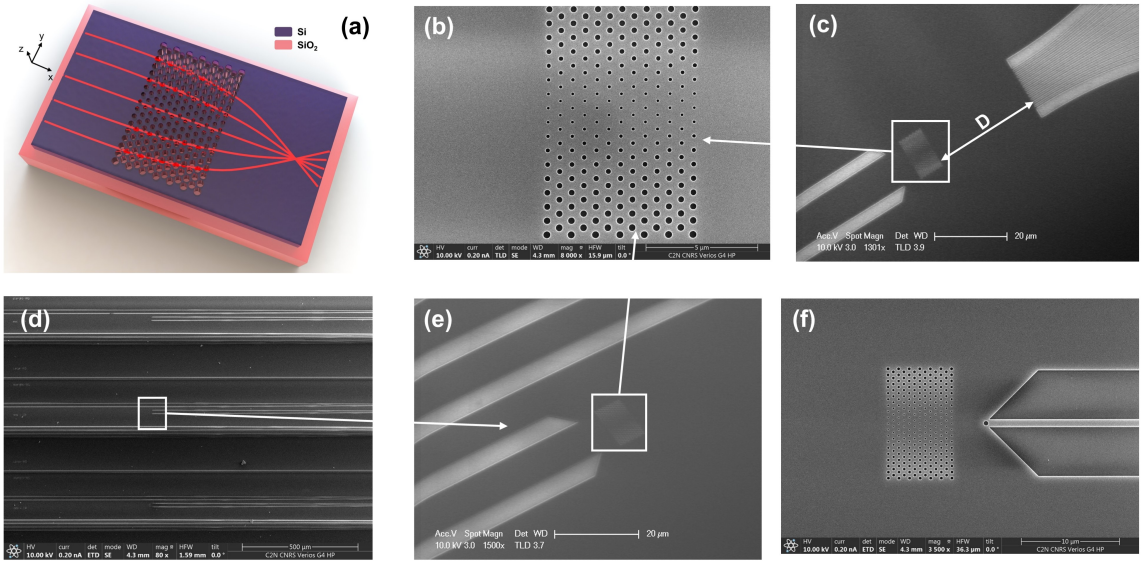

Figure R3: (a) Schéma de la lentille plate. (b) SEM image de la lentille. (c) Lentille avec guide d'ondes d'entrée et guide d'ondes de sortie. (d) Plusieurs structures unitaires sont disposées en parallèle. (e) Affichage partiel de la structure de l'unité pour la caractérisation du SNOM. (f) Une possible pour source ponctuelle sur la puce.

Lors de l'utilisation du groupe de guides d'ondes de sortie pour la caractérisation, nous avons effectué des tests de balayage en utilisant différentes longueurs d'onde de lumière (1.5 µm à 1.64 µm, espacées de 1 nm) pour chaque distance D. Nous avons donc obtenu des distributions d'intensité spectrale à différentes positions D (voir Figure R4). Nous avons ensuite extrait les données de manière analytique pour obtenir la distribution de l'intensité du champ à différentes distances de la sortie de la lentille à des longueurs d'onde spécifiques. Grâce à notre analyse, nous avons constaté que les lentilles font converger la lumière à des longueurs d'onde de 1.6µm à 1.64µm. Dans ce cas, l'intensité du champ de sortie est presque

toujours concentrée dans le guide d'ondes central. Le point focal est situé à 5 µm de la surface de sortie de la lentille. Une autre analyse non normalisée montre que l'objectif a la plus grande transmission à 1.64 µm. L'intensité du champ au point focal à cette longueur d'onde est plus grande qu'aux autres longueurs d'onde. L'analyse du décalage de la longueur d'onde est également présentée au **Chapitre 5**.

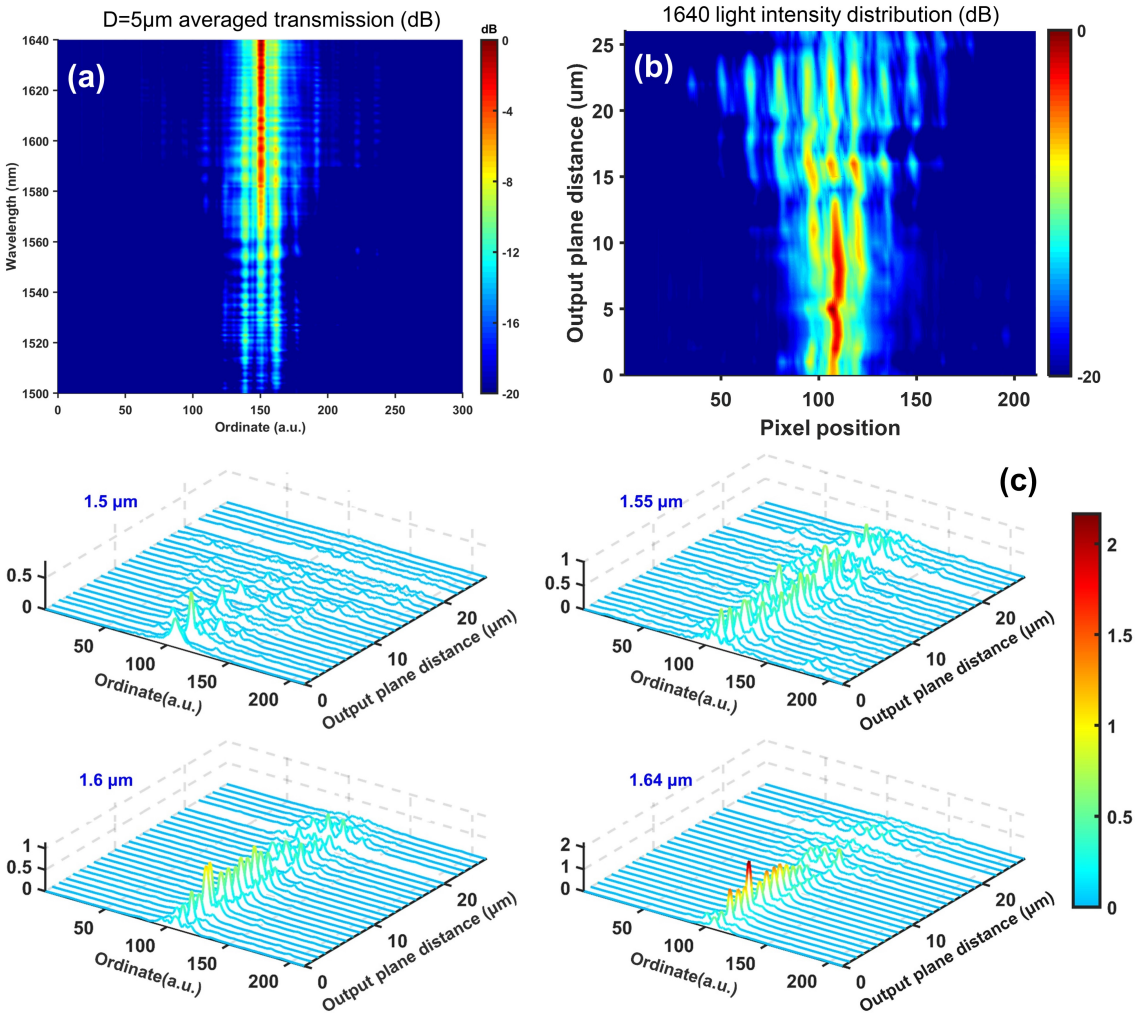

Figure R4: (a) Distribution de l'intensité du champ à différentes longueurs d'onde à 5 µm de la lentille. (b) Distribution normalisée de l'intensité du champ à une longueur d'onde de 1.64 µm. (c) Comparaison de la distribution non normalisée de l'intensité du champ à quatre longueurs d'onde. On peut voir que la lentille convergent à 1.64 µm et que l'intensité du champ est maximale au point focal.

De même, les résultats de caractérisation obtenus à l'aide de SNOM sont présentés au chapitre 5. Lors du balayage avec SNOM, différentes sondes ont été essayées et répétées pour obtenir les meilleurs résultats. En même temps, la distance entre la sonde et la surface de la couche de silicium a été ajustée(en mode champ proche était de 4 nm, en mode champ lointain était de 100nm ou 250nm). Sur la base des résultats déjà obtenus en utilisant le guide d'onde

de sortie, les longueurs d'onde balayées par le SNOM étaient principalement concentrées à 1,63 µm. La zone balayée par la sonde était une zone rectangulaire de 30µmx15µm incluant la lentille. Après avoir obtenu les données brutes, les données ont été analysées et traitées à l'aide du logiciel open source WSXM. Dans le même temps, nous utilisons la méthode du champ proche moins le champ lointain pour minimiser l'effet du champ diffusé généré par les trous d'air (voir la figure R5). Les résultats montrent une convergence des ondes résonnantes à haute fréquence générées par la lumière guidée dans le guide d'ondes. Ce résultat est cohérent avec les résultats des simulations précédentes. Les résultats de l'analyse SNOM ont ensuite été quantifiés. En ajustant la position de départ de la sonde de balayage, nous avons obtenu deux ensembles de résultats de balayage. Nous pouvons observer que les résultats obtenus expérimentalement dans les directions verticale et horizontale du champ derrière la lentille sont cohérents avec les résultats théoriques des simulations précédentes.

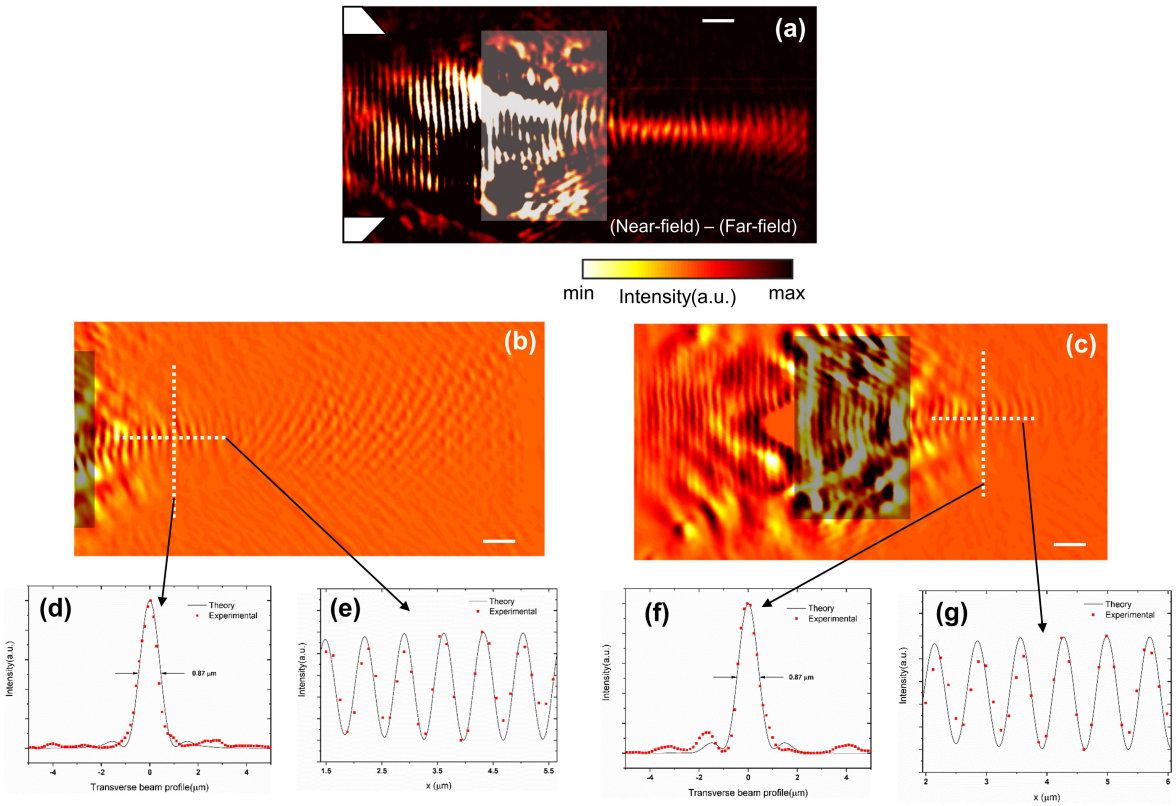

Figure R5: (a) Image SNOM de la lentille après soustraction de l'image du champ proche par celle du champ lointain. (b) et (c) image après filtre dérivatif pour réduire l'impact du champ diffusé. (d) (e) et (f) (g) Comparaison des données expérimentales et données théoriques à la ligne verticale et à la ligne horizontale en pointillés blancs montrées dans (b) et (c) correspondant. La zone de couleur grise correspond à la portée de la lentille. Barre d'échelle de 2 µm.

Dans l'ensemble, les travaux de cette thèse portent sur le développement et l'application de dispositifs à cristaux photoniques à gradient dans la bande du proche infrarouge. Nous

avons analysé la faisabilité de la conception de lentilles pour différents cristaux photoniques à réseau avec différentes bandes et avons conçu, traité et caractérisé des lentilles à indice de réfraction négatif. Les travaux de cette thèse offrent des perspectives et des possibilités pour le développement de systèmes intégrés sur puce basés sur le SOI.

Contents

Abbreviations and units

Used Abbreviations

2D	two dimension
3D	three dimension
CAD	computer aided design
DRIE	deep reactive ion etching
EBL	electron beam lithography
EFC	equal frequency curve
EIM	effective index method
FWHM	full width at half maximum
GDS	graphic design system
GRIN	graded index
GPC	graded photonic crystal
IPA	isopropyl alcohol
IR	infrared
ICP	inductively coupled plasma
IFC	iso-frequency curve
MMI	multi mode interferometer
NIR	near infrared
PhC	photonic crystal
PMMA	polymethyl methacrylate
Si	silicon

SEM	scanning electron microscopy
SOI	silicon on insulator
SNOM	scanning near field optical microscopy
TE	transverse electric
TM	transverse magnetic

Used indications

ε	dielectric permittivity
$\vec{E}$	electric field
η	filling factor
$\vec{H}$	magnetic field
f	focus distance
n	refractive index
$\vec{k}$	wave vector

Used units of measurements

dB	decibel
kV	kilovolt
µm	micrometer/micron
nA	nanoampere
nm	nanometer
mm	millimeter
sec	second
THz	terahertz

Chapter 1

Introduction

Contents

With the continuous development of science and technology, photon as a carrier of information is gradually entering people's vision. Compared with electrons, photons have the advantages of fast transmission of information, large transmission bandwidth and very weak interactions between photons. Therefore, using photons as the carrier of information can greatly improve the speed of information transmission, reduce energy loss, enhance anti-interference performance and confidentiality. And photonic crystal is such a new type of medium. It uses photons as information carriers. The movement of photons in a photonic crystal is like the movement of electrons in a semiconductor material. Photonic crystals can control the motion behavior of photons just as semiconductor materials control electrons. Photonic crystals, a low-loss periodic medium, can be used as a way to control and manipulate light. In particular, photonic crystals with photonic band gaps can be designed and manufactured to block the propagation of light of a particular frequency in a particular direction. In addition, photonic crystals can also manipulate light so that it propagates in an anomalous but more useful and efficient manner.

This chapter is devoted to presentation of some basic concepts related to photonic crystals and fundamental computational analysis methods used in this thesis. Firstly, photonic crystals in nature and the concept of photonic crystals in different dimensions will be introduced. Then we will learn about two important concepts in photonic crystals, namely band diagrams and equal frequency curves. They have an important role in this thesis. After that we will introduce the dispersion properties in photonic crystals and learn about several typical dispersion phenomena. Then we will focus our attention on the concept of graded photonic crystals and their research development history. Finally, we will briefly introduce several numerical modeling methods used in this thesis.

1.1 Photonic crystal

The concept of photonic crystals was independently proposed by Eli Yablonovitch and Sajeev John in 1987 [2, 3], respectively. The traditional concept of crystal is a solid substance made of molecules or atoms repeatedly arranged in space in a certain regular cycle. Photonic crystals, on the other hand, are artificial media structures with a periodic distribution of nodal constants. Photonic crystals have the characteristic of periodicity, i.e., their structure is periodic. In addition, the period size of a photonic crystal matches about half of the corresponding wave length. For example, the period of photonic crystals in the optical communication band is usually on the order of microns and nanometers. Photonic crystals in the microwave band are usually in the millimeter range. The most important feature of photonic crystals is that they have a photonic band gap similar to the energy band of a semiconductor, so that photons with frequencies in the forbidden band will not be able to propagate. This section will start with a brief introduction to photonic crystals in the natural environment. Subsequently, the concept of photonic crystals in different dimensions will be introduced. Finally, the concept

of photonic crystal slabs, which is involved in this thesis, will be introduced.

1.1.1 Photonic crystal in nature environment

Long before artificial photonic crystals were synthesized, researchers have discovered that many complex, elaborate biological photonic crystal structures, such as opals and butterfly wings, existed in nature [4–8]. Electron microscopy has shown that they are also composed of periodic structures, and using different frequencies of light scattered and projected on them in different directions, they exhibit beautiful colors. Several studies have shown that nat-

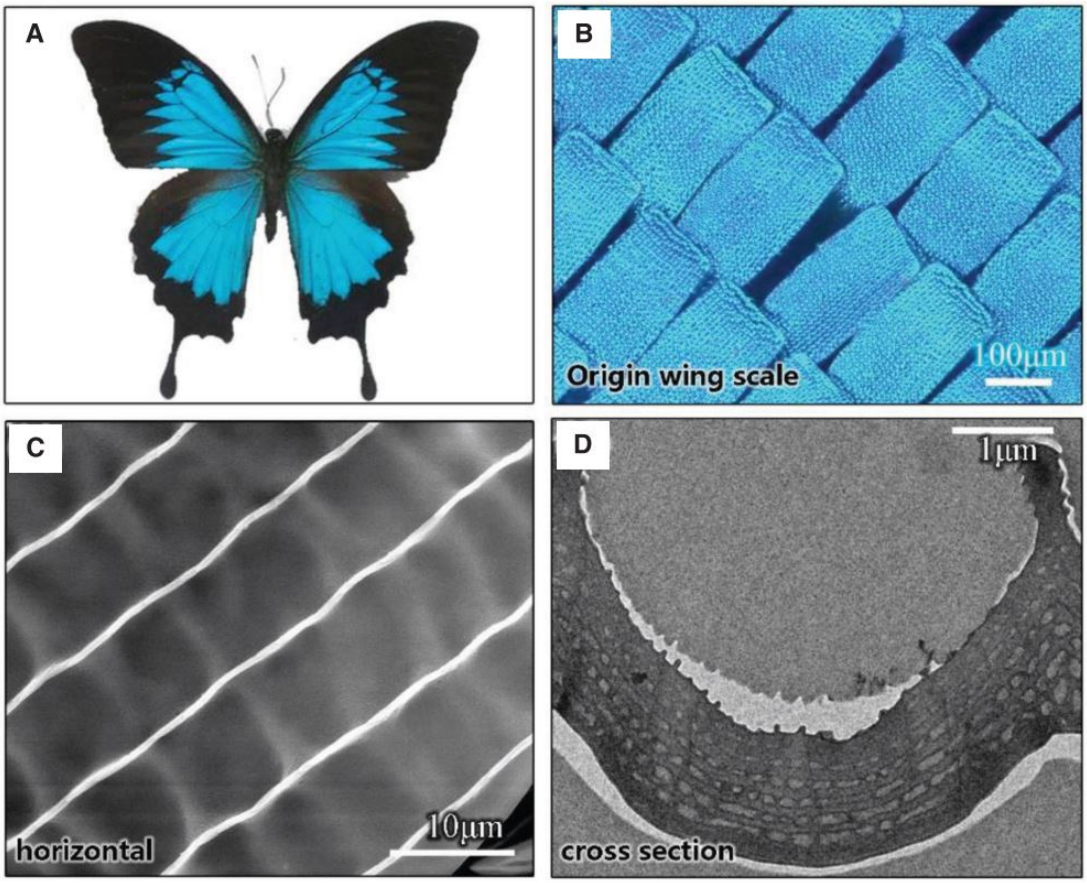

Figure 1.1: Sparkling color and periodic concave multilayer of the Papilio ulysses wing with PC structure. (A) Digital photo of natural Papilio ulysses butterfly. (B) Optical microscopy image of Papilio ulysses wing scale. (C) SEM micrograph of Papilio ulysses from a horizontal view. (D) TEM micrograph of Papilio ulysses from a cross-section view [9].

ural photonic crystals are widely found in marine organisms (See Figure 1.1). Brink et al. applied field emission scanning electron microscopy to observe the abalone shell microstructure and studied the reflection spectrum of the abalone shell with a spectrometer and found that the interference effect of the abalone shell plays an important role in producing colorful reflections [10, 11]. They humanized that this multilayer structure is a one-dimensional

biophotonic bandgap structure. There are also many interesting photonic crystal structures in hairy annelids, such as worm bristles, for example. In these animals, the cross-section of each bristle consists of two-dimensional porous hexagonal photonic crystals, whose entire length can be seen as a natural pseudo-photonic crystal fiber [12]. Other photonic crystal structures in some insects are also well known [13]. The colors of winged insect structures like butterflies and moths are also associated with various physical mechanisms, including multilayer interference, diffraction, Bragg scattering, Rayleigh scattering, etc. Transmission electron microscopy analysis shows that the colored wings of butterflies are closely related to coherent scattering caused by their nanostructures.

Photonic crystal structures also exist in plants, and researchers have found that leaves of the Pinaceae have periodically arranged structures [14]. In addition, certain ferns also have photonic crystal structures and exhibit partial photonic band gap properties, and such plants generally exhibit structural coloration. Its trip laminar periodic structures in plant leaves, fruits and stem veins produce iridescent colors.

1.1.2 1D, 2D and 3D Photonic crystal

Based on the spatial topology, photonic crystals can be divided into three major categories: one-dimensional photonic crystals, two-dimensional photonic crystals, and three-dimensional photonic crystals, as shown in Figure 1.2. One-dimensional photonic crystals are formed by overlapping two or more media with different dielectric constants. This structure has actually been studied for many years and is widely used in various optical systems. As early as 1887, Lord Rayleigh published the first analytical theory of the optical properties of multilayer films. The Bragg reflector, for example, is a one-dimensional photonic crystal with a film thickness of a quarter of a wavelength. For a particular frequency of light, this photonic crystal is a mirror when the angle of incidence is out of a certain range. Also, if it has a defect within its structure, then it can localize the light at this defect.

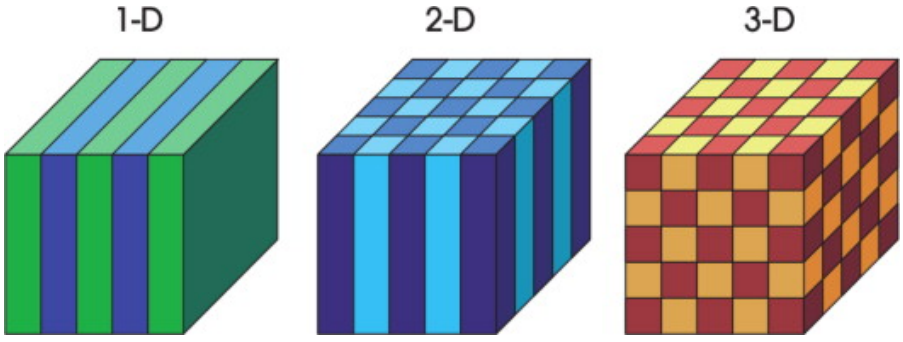

Figure 1.2: Simple examples of 1D, 2D, and 3D photonic crystal structures [15].

Two-dimensional photonic crystals are structures in which the dielectric constants are arranged periodically in two dimensions. A typical two-dimensional photonic crystal structure

consists of a number of round or square dielectric columns arranged periodically in an air background; or of air holes arranged regularly in a dielectric background with a dielectric constant that is a function of spatial period in the direction perpendicular to the dielectric columns, but does not vary with spatial position in the direction parallel to the dielectric. Thus, the two-dimensional photonic crystal is periodic in the $X-Y$ plane and continuous in the Z direction.

A three-dimensional photonic crystal is a spatially periodic structure made of two different media. It is periodic in all XYZ planes, i.e., it has frequency cutoff bands in all three directions, rather than having photonic band gaps in one or two directions. Thus it is called a complete photonic band gap. The structure of a three-dimensional photonic crystal is usually made of spherical or hexahedral-shaped cells arranged in a face-centered cubic, body-centered cubic. Eli Yablonovitch first successfully prepared a three-dimensional photonic crystal in 1991 [16]. It is a masked version consisting of a triangular array of holes overlaid on a dielectric medium. It is then formed by drilling along each hole as illustrated in Figure 1.3. This three-dimensional photonic crystal has a complete band gap and it works at the centimeter scale.

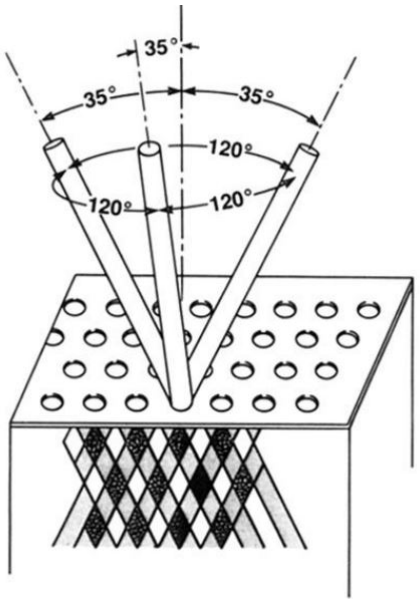

Figure 1.3: The method for constructing Yablonovite: a medium of dielectric is covered by a mask consisting of a triangular array of holes [16].

1.2 Band diagram and Equi-frequency curve

In order to study the properties of photonic crystals, we need to first understand two important concepts in crystal theory, namely, reciprocal space and Brillouin zone (See Figure 1.4). From there we can further understand the band structure diagrams and Equi-frequency curve (EFC)

of photonic crystals that are used in many places this thesis. This subsection will focus on these basic concepts.

1.2.1 The reciprocal lattice and the Brillouin zone

The reciprocal lattice is usually the Fourier transform of the Bravais lattice. And the space that exists by the reciprocal lattice and the reciprocal lattice vector we call the reciprocal space or vector space. The reciprocal lattices bring a lot of convenience to the study of solid physics. In this thesis, only a brief introduction is given for subsequent applications. Mathematically speaking, if a_1, a_2, a_3 is the initial basis vector of the lattice, then we define

$$b_1 = 2\pi \frac{a_2 \times a_3}{a_1 \cdot a_2 \times a_3}; b_2 = 2\pi \frac{a_3 \times a_1}{a_1 \cdot a_2 \times a_3}; b_3 = 2\pi \frac{a_1 \times a_2}{a_1 \cdot a_2 \times a_3}, \tag{1.1}$$

which represent the initial basis vector of the reciprocal lattice. Each vector defined by Equation 1.1 is orthogonal to the two axis vectors of the lattice. As a result, b_1, b_2, b_3 has the following properties:

$$b_i \cdot a_j = 2\pi\delta_{\text{ij}}, \tag{1.2}$$

where when $i = j$, we have $\delta_{\text{ij}} = 1$; and when $i \neq j$, $\delta_{\text{ij}} = 0$. In the reciprocal lattice, each lattice point is given by the following set of vectors:

$$G = v_1 b_1 + v_2 b_2 + v_3 b_3 \tag{1.3}$$

where v_1, v_2, v_3 is taken as an integer. A vector with this situation is called an reciprocal lattice vector.

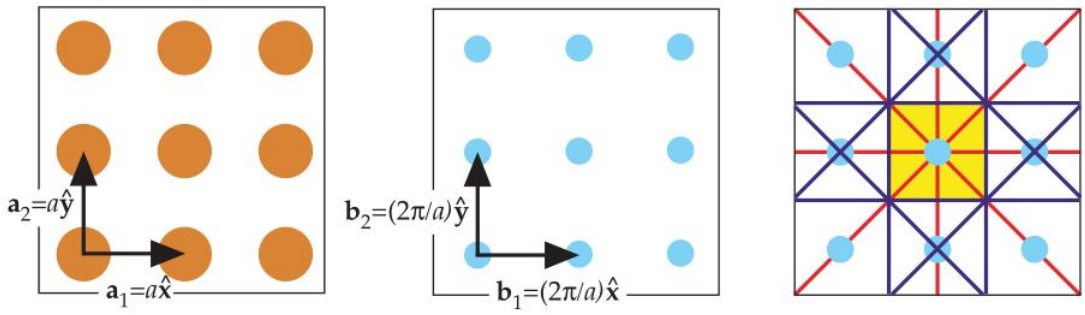

Figure 1.4: The square lattice. On the left is the network of lattice points in real space. In the middle is the corresponding reciprocal lattice. On the right is the construction of the first Brillouin zone [15]. Here, $\hat{x}$ and $\hat{y}$ are the primitive lattice vectors in x and y directions.

An intuitive description of the Brillouin zone is that around any lattice point in reciprocal lattice space, the Brillouin zone highlights the region closer to that lattice point. The smallest

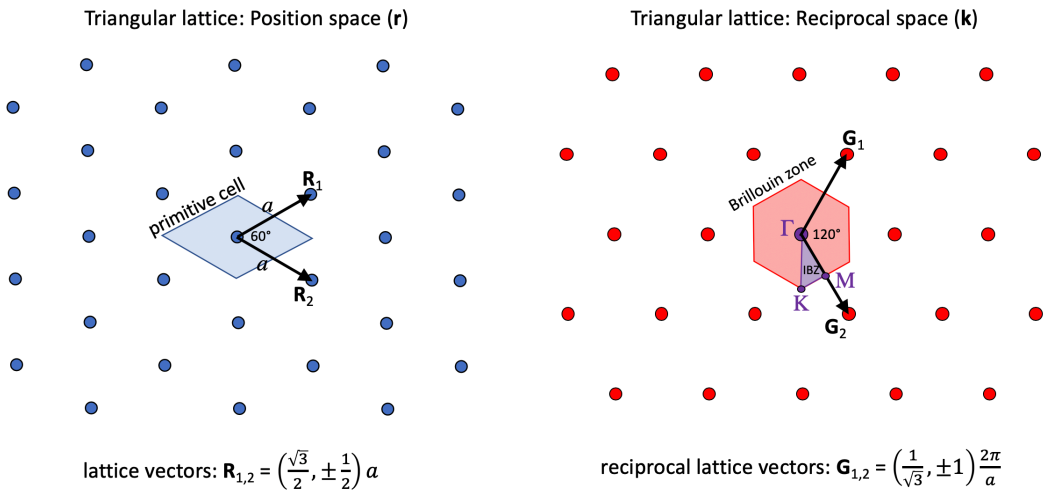

Figure 1.5: The triangular lattice. On the left is the network of lattice points in real space. On the right is the corresponding reciprocal lattice and Briliion zone [15].

part of the Brillouin zone that cannot be obtained by symmetry operations is called the irreducible Brillouin zone. The information contained in the remaining regions of the Brillouin zone is contained in the irreducible Brillouin zone. The reciprocal space and Brillouin zone of a two-dimensional square lattice and a triangular lattice are shown in Figure 1.5.

1.2.2 Band diagram

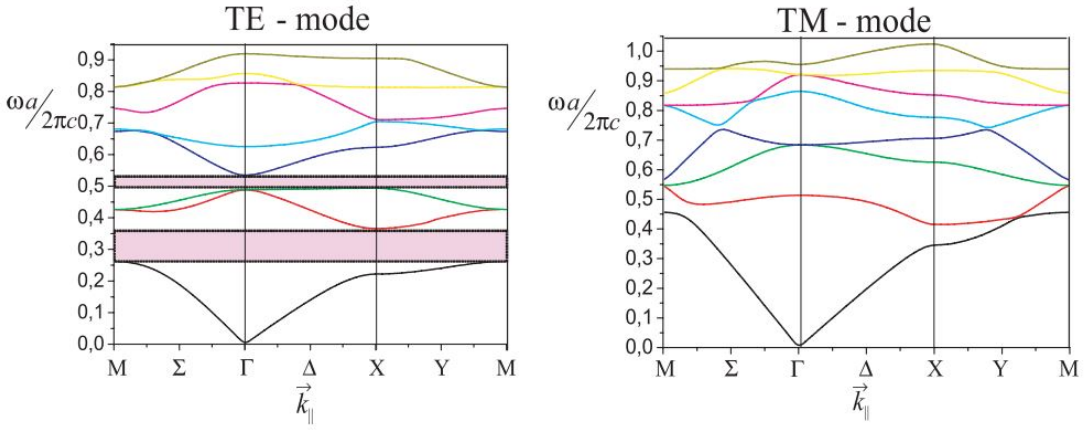

Figure 1.6: Photonic band structure of TE and TM-modes in 2D PhC made of air rods in Si-material. The pink area is the bandgap [17].

The band diagram of a photonic crystal is a diagram that contains information about the electromagnetic field states within the photonic crystal (See Figure 1.6). It is also the diagram of the dispersion relation between frequency and wave vector. Some optical properties of the

photonic crystal can be predicted by analyzing and studying the band diagram of the photonic crystal. From the Bloch theory and the symmetry of the photonic crystal, it is clear that the relationship between the wave vector and the electromagnetic field modes contains the full symmetry. Thus, we only need to calculate the band diagram in the irreducible Brillouin zone. In short, it is a calculation to find possible electromagnetic field modes along the boundary of the irreducible Brillouin zone. And on the boundary of the irreducible Brillouin zone is the wave vector $\vec{k}$.

And for different lattices there are different irreducible Brillouin zones. The irreducible Brillouin zone of a square lattice is an isosceles right triangle. The sequence of the wave vector $\vec{k}$ is $\Gamma - X - M$ when calculating the band diagram. While the irreducible Brillouin zone of a triangular lattice is a right triangle with sharp angles of 30 degrees and 60 degrees. The sequence of the wave vector $\vec{k}$ when calculating the band diagram is $\Gamma - M - K$. In the

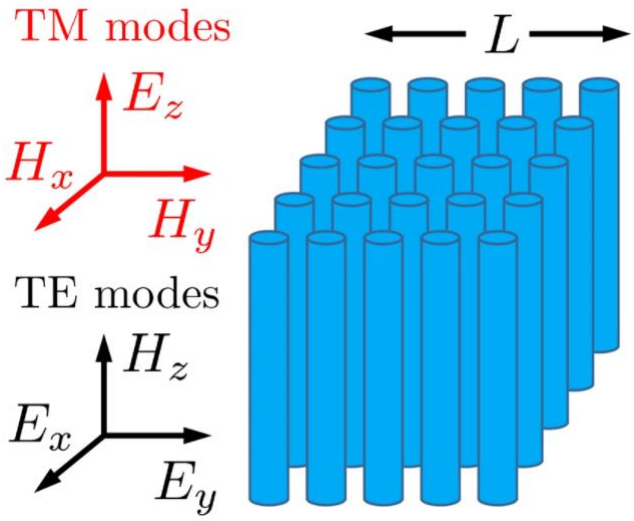

Figure 1.7: 2D square array of dielectric cylinders aligned along the z. The TM (TE) modes of the electromagnetic field have the electric (magnetic) field parallel to z [18].

two-dimensional photonic crystal that will be used mainly in this thesis, an electromagnetic field can be divided into two independent polarization states: TE mode and TM mode, as shown in Figure 1.7. For the former TE mode, the magnetic field is parallel to *z* direction. For the latter TM mode, on the contrary, the electric field is parallel to *z* direction. We must note that the calculation of the two-dimensional photonic crystal band diagram must indicate in advance which mode it is. In general, the band diagram is different for a given photonic crystal TE mode and TM mode.

1.2.3 Equi-frequency curve

As introduced in the previous subsection, the band diagram is composed of states on the boundary of the Brillouin zone. It is natural to think that if we are given a normalized fre-

quency ω, we can then plot the wave vector $\omega(k_x, k_y)$ in the Brillouin zone. This kind of diagram we call it Equi-frequency curve (EFC). From the EFC we can infer the propagation direction of the refracted and reflected waves. And the group velocity V_g is perpendicular to $\omega(k_x, k_y)$ countour and points in the direction of increasing ω, according to the vector calculus theorem [19]

$$V_g = \nabla_k \omega(K). \tag{1.4}$$

Also, by the ratio of the radius of the EFC to the radius of the light cone, we can calculate the effective refractive index of an isotropic medium.

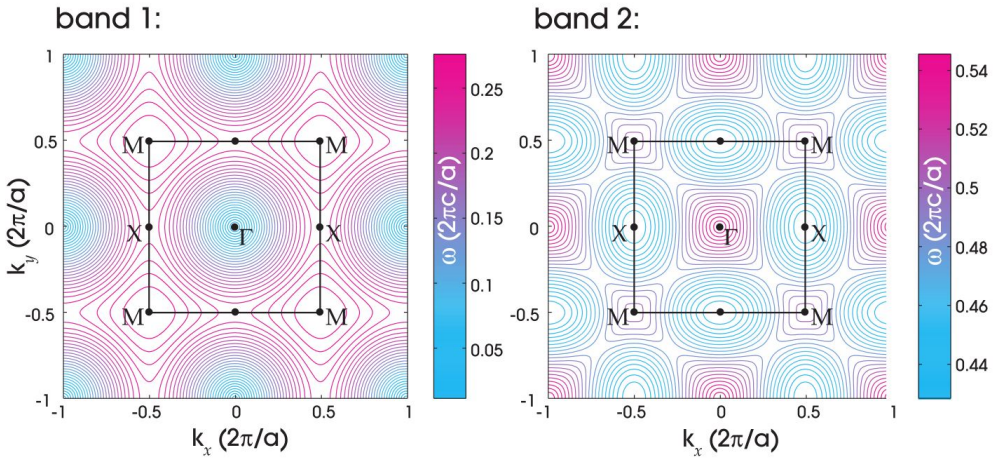

Figure 1.8: EFC diagrams: contour plots of $\omega(k_x, k_y)$ for the first two TM bands of a square lattice of radius 0.2a dielectric rods in air. The first Brillouin zone is shown as black squares [15].

The equal frequency curves in Figure 1.8 are formed for different normalized frequencies in a given photonic crystal. We can initially obtain that in the first band, for different normalized frequencies, the EFCs centered on Γ are essentially circular. While for the second band, the equi-frequency curve centered at Γ is closer to the shape of the lattice. There will be more applications of the EFCs in this thesis, which we will discuss in later chapters.

1.3 Dispersion property in photonic crystal

When the concept of photonic crystals first appeared, much of the research focused on the band gap of photonic crystals. By analyzing the properties of photonic crystals, people tried to find photonic crystals with a complete band gap [20–22], which means that the gap can extend to cover all possible directions [15]. It can also introduce defects and cavities in complete photonic crystals to achieve the purpose of slowing down the speed of light [23, 24]. This thesis, however, will focus on the part of the photonic crystal band diagram that is outside the band gap. That is, the nature of the free propagation of light in photonic crystals. To this aim,

this subsection will first introduce the two basic concepts of group velocity and phase velocity. This is followed by the presentation of several examples of light propagating dispersion in photonic crystals like negative refraction, superprism effect and supercollimation effect.

1.3.1 Phase velocity and group velocity

We are familiar with phase velocity v_p, which indicates the rate at which light travels in any medium. Usually, the rate of propagation of any phase of a wave including its crest and trough can be expressed in terms of phase velocity. It is defined as

$$v_p = \frac{\lambda}{T} = \frac{\omega}{k}, \tag{1.5}$$

where λ is the wavelength and T is the time period, ω is the frequency and k is the wave number. Because of the periodicity of photonic crystals, the phase velocity in them is difficult to be defined. Also, the phase velocities of light at different wavelengths in dispersive media are not the same. The group velocity, on the other hand, can solve these problems well. Only a simple derivation process is given here, and the detailed solution is given in Ref [25]. In a dispersive medium, we can consider the wave packet $u(x,t)$ as a function of the general position x and time t. Here, a wave packet is a short burst of localized wave action that travels as a unit. A wave packet can be analyzed into, or can be synthesized from, an infinite set of component sinusoidal waves of different wavenumbers, with phases and amplitudes such that they interfere constructively only over a small region of space, and destructively elsewhere [26].

$$u(x,t) = \frac{1}{\sqrt{2\pi}} \int_{-\infty}^{\infty} A(k) e^{\mathrm{ikx-i\omega(k)t}}\, dk \tag{1.6}$$

where $A(k)$ is the amplitude function which can be given by

$$A(k) = \frac{1}{\sqrt{2\pi}} \int_{-\infty}^{\infty} u(x,0) e^{-\mathrm{ikx}}\, dk \tag{1.7}$$

We assume that the wave packet is monochromatic. So that $A(k)$ is sharply peaked around a central wavenumber k_0. Then the frequency $\omega(k)$ can be expanded by the first order Taylor series as

$$\omega(k) = \omega_0 + \left.\frac{\mathrm{d}\omega}{\mathrm{dk}}\right|_0 (k - k_0) + ... \tag{1.8}$$

Thus, we have

$$u(x,t) \approx \frac{e^{\,i[k_0(\mathrm{d}\omega/\mathrm{dk})|_0 - \omega_0]t}}{\sqrt{2\pi}} \int_{-\infty}^{\infty} A(k) e^{e^{\,i[x-(\mathrm{d}\omega/\mathrm{dk})|_0 t]k}}\, dk \tag{1.9}$$

Here, $A(k) = u\,(x', 0)$, where $x' = x - (d\omega/dk)|_0 t$. Bringing this term into Equation 1.9 we get

$$u(x,t) \approx u(x - t\frac{\mathrm{d}\omega}{\mathrm{dk}}\Big|_0, 0)e^{\,i[k_0(\mathrm{d}\omega/\mathrm{dk})|_0 - \omega_0]t} \tag{1.10}$$

From Equation 1.10 we see that, excluding a global phase factor, the wave packet propagates at a velocity known as the group velocity

$$v_g = \frac{\mathrm{d}\omega}{\mathrm{dk}}\Big|_0 . \tag{1.11}$$

The group velocity is usually considered as the direction of propagation of the wave energy [27]. If the wave propagates in an anisotropic medium, the direction of the group velocity and the phase velocity may be different. Also, the group velocity can be positive or negative, determined by the direction of its vector. It can also be expressed as a function of the band index n and the wave vector k as follows [15]

$$v_n(k) \triangleq \nabla_k \omega_n \triangleq \frac{\partial \omega_n}{\partial k_x}\hat{x} + \frac{\partial \omega_n}{\partial k_y}\hat{y} + \frac{\partial \omega_n}{\partial k_z}\hat{z}, \tag{1.12}$$

where ∇_k is the graded with respect to k. This formula gives us an important message that the group velocity is perpendicular to the EFC at a given ω and points in the direction of increasing ω.

1.3.2 Negative refraction

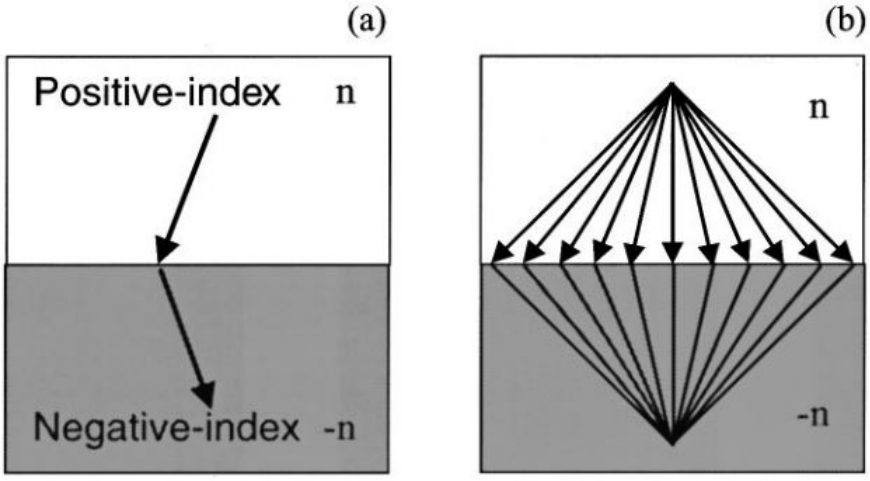

Figure 1.9: Schematic diagrams of light propagation in negatively refractive photonic crystals: (a) negative refraction, (b) mirror inverted imaging effect [19].

The phenomenon of negative refraction in a homogeneous medium was proposed by Veselago in 1968 [28]. Although no natural material can have a negative refractive index, as a photonic crystal, a negative effective refractive index can be obtained by equivalent

approximation under certain conditions as shown in Figure 1.9. With a reasonable design, photonic crystals can exhibit negative refractive index within a certain range of ω, where the incident and refracted light are on the same side of the normal [19]. In this thesis, a photonic crystal-based negative refractive index lens operating in the near-infrared band will be designed, processed, and characterized.

Studies on negative refractive indices have focused on the corresponding phenomena in metamaterials or crystalline materials. Pendry theoretically described the principle of subwavelength imaging of negative refractive index materials in 2000 [29]. In the same year, Smith proposed artificial materials with both negative permittivity and magnetic permeability for microwave applications [30]. Anomalous reflection and refraction phenomena were observed in optically thin arrays of metallic antennas on silicon with a linear phase variation along the interface by Yu et al. [31]. This opens the door to the study of meta-surfaces. For crystalline materials, especially photonic crystals, Luo et al. analyzed the role of surface states in imaging of fully dielectric two-dimensional photonic crystals [32]. Subsequently, Foteinopoulou et al. systematically investigated the phenomenon of anomalous refraction at the interface of two-dimensional photonic crystals and discusses several different cases leading to negative refraction [33]. Decoopman et al. demonstrated that photonic crystal can mimic homogeneous dielectric materials with negative permittivity and permeability when they are properly designed [34]. In the near-infrared field (wavelength 1.26–1.42μm), Matsumoto et al. experimentally proved the light focusing by negative refraction in a photonic crystal slab superlens [35]. Xu et al. experimentally demonstrated a bulk metamaterial with an all-angle negative index of refraction, and used it to achieve Veselago flat lensing and all-optical modulation in the ultraviolet [36].

1.3.3 Superprism effect

The EFCs in Figure 1.8 are not all circle shape. We can find some of these EFCs have sharp corners. When the refracted wave approaches these corners, small changes in frequency or angle of incidence may cause the group velocity of the refracted wave to switch rapidly from one side of the corner to the other (See Figure 1.10). And the superprism phenomenon describes this situation.

The concept of superprism began at the end of the 20th century. A considerable amount of research has consequently been carried out on the basis of this concept. In 1998, Kosaka et al. proposed superprism phenomenon and demonstrated this extraordinary angle-sensitive light propagation at optical wavelength in photonic crystals with three-dimensional-periodic structure fabricated on Si substrate [37]. Lupu et al. experimentally demonstrated a planar superprism in silicon micro-photonics technology using silicon on insulator (SOI) substrates [38]. Luo et al. proposed the possibility of realizing agile beam steering based on purely phase-velocity effects [39]. Dellinger et al. provided a direct experimental observation of

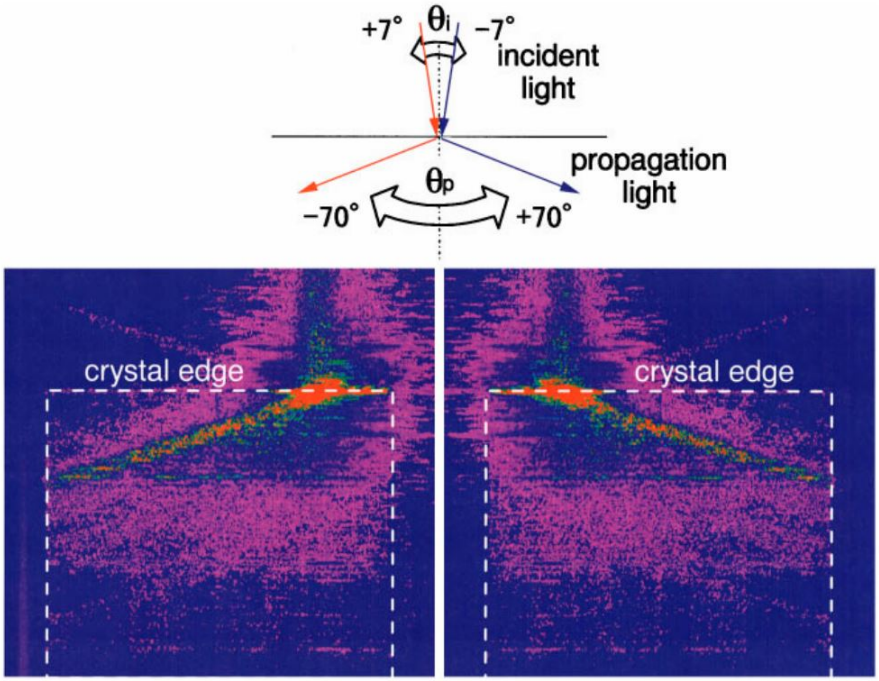

Figure 1.10: In superprismatic phenomena, a small change in the incident angle causes a large change in the refracted wave angle [37].

the refracted beam propagation inside a photonic crystal structure displaying a superprism effect by using near-field microscopy [40].

1.3.4 Supercollimation effect

Literally speaking supercollimation is well understood. It means that the light beam diverges very slowly as it propagates. In photonic crystals, the implementation of supercollimation depends on the application of equal frequency curves as shown in Figure 1.11. We know that the shape of the light cone in air is always circular. The equi-frequency curve of a photonic crystal, on the other hand, has a flat, straight shape under certain circumstances. When the beam has multiple components in the direction perpendicular to the EFC, the flat EFC causes the dispersion angle of these wave vectors to become small. It also means that the direction of the group velocity is almost parallel everywhere. This allows the light to propagate in one direction with as little diffraction as possible.

In practice, a large number of studies have confirmed the existence of super collimation phenomena in photonic crystals. Kosaka et al. first proposed the concept 'supercollimation' and demonstrated self-collimated light propagation in PCs [41]. Wu et al. proved a self-collimating phenomena within a 20° incident angular range over 25-nm bandwidth in planar PhCs [42]. Shin et al. introduced the theoretical criterion for achieving three-dimensional self-collimation of light in a photonic crystal. Based on this criterion, they numerically

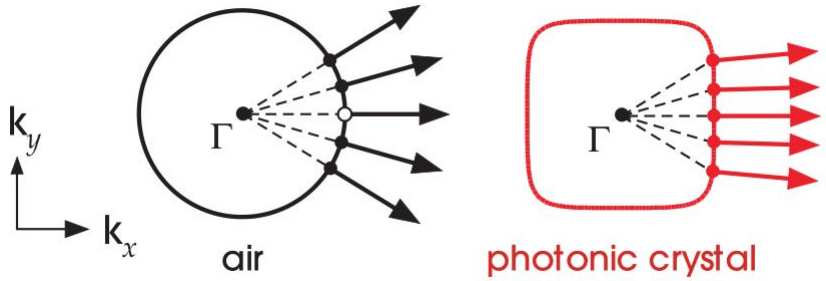

Figure 1.11: Schematic diagram of the principle of supercollimation phenomenon in photonic crystals [15].

demonstrated a body-center-cubic structure that supported wide-angle self-collimation [43]. E. Hamam et al. proposed a two dimensional photonic crystal structure that supported supercollimation over a large frequency range [44]. Rakich et al. experimentally achieved centimetre-scale supercollimation with almost no spreading [45]. In their study, a photonic-crystal slab (a square lattice of about 10^9 air holes in silicon) designed to operate at λ=1.5μm was used. Purlys et al. proposed and experimentally demonstrated the mechanism of beam supercollimation by axisymmetric photonic crystals [46].

1.4 Introduction to graded photonic crystal

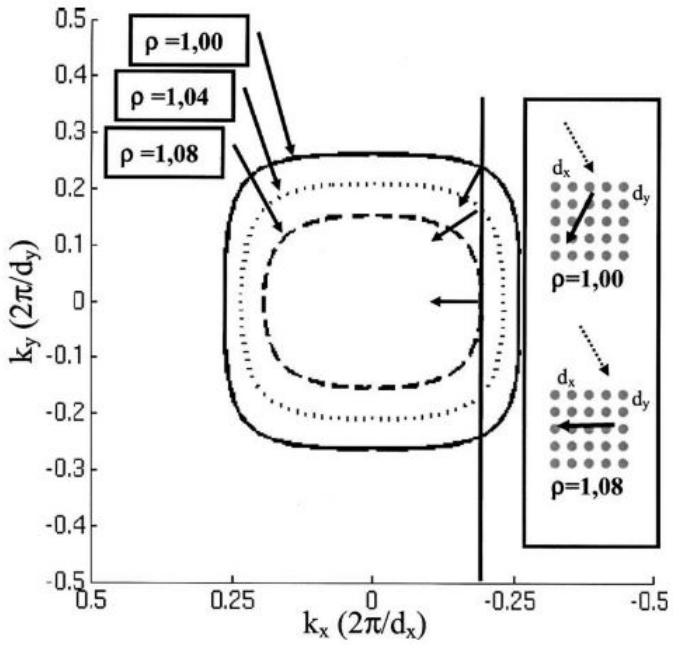

Figure 1.12: Equi-frequency curve for the wavelength 1550nm and for three aspect ratios. The arrows indicate the light propagation directions [47].

The concept of graded photonic crystals was proposed by Centeno et al. in 2005 [47]. Its core principle is to change the shape of the equi-frequency curve by varying parameters such as the filling factor or lattice constant in the photonic crystal, which in turn gradually changes the direction of the group velocity of the waves in the photonic crystal [48]. Thus, the purpose of changing the propagation direction of light is achieved. Figure 1.12 illustrates a method to change the equi-frequency curve by changing the lattice constant of a photonic crystal.

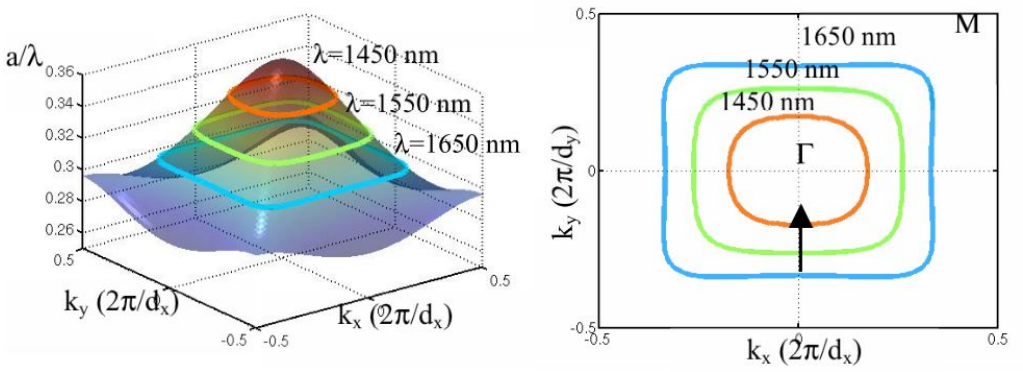

Figure 1.13: Dispersion surface of the second band for the TE mode (left). Three EFCs are plotted (right) [49].

In Centeno's paper [47], they designed three different photonic crystal regions by changing the lattice constants. Simulations were carried out by the multiple scattering method [50, 51]. The results showed that the designed graded photonic crystal exhibited negative refractive index for waves of wavelengths 1550nm and 1530nm and was able to change the direction of light propagation in the photonic crystal.

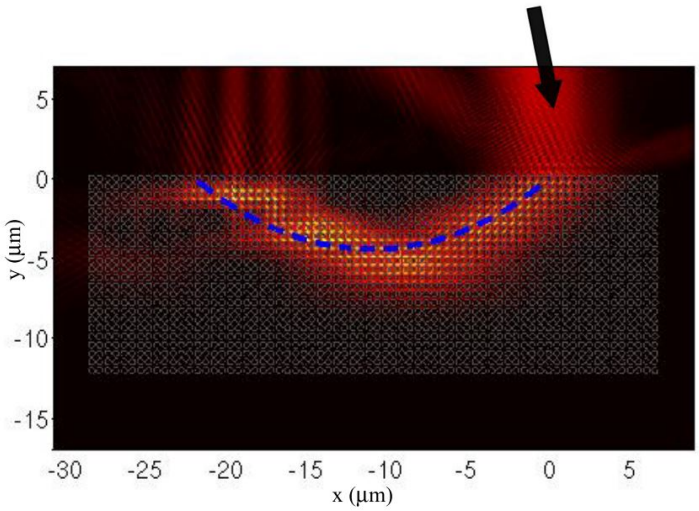

Figure 1.14: Simulation result of magnitude of the Poynting vector inside a GPC enlightened by a Gaussian beam [49].

Then, Centeno et al. investigated the mirage effect of the graded photonic crystal on light [49, 52, 53]. By changing the lattice constant of a rectangular in one direction, they gradually changed the shape of the EFC (See Figure 1.13 and 1.14). The simulation results demonstrate that a light beam with an incident angle of 5° undergoes a bending effect by changing the propagation path in the photonic crystal. By comparing with the mirage in the atmosphere, they concluded that both photonics and atmospheric mirages are caused by the change of light propagation path through the change of refractive index in space.

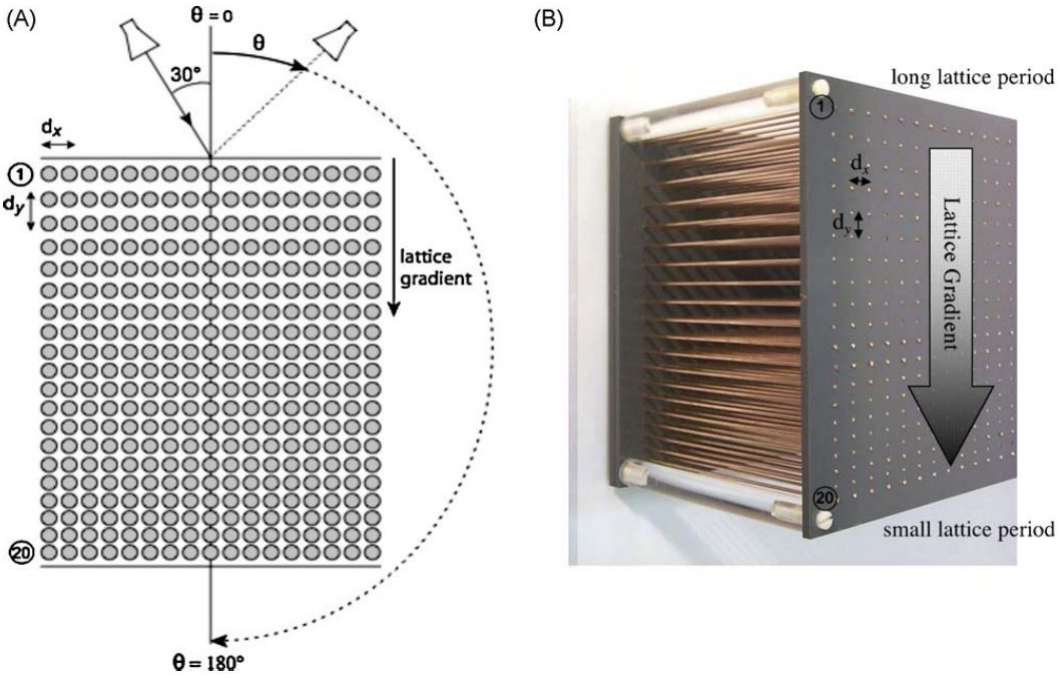

Figure 1.15: (A) Schematics of the measurement setup. (B) Fabricated GPhC structure, which consists of 20 rows of copper rods [54].

The experimental validation was done by Akmansoy et al. in 2008 [54, 55]. In their work, the photonic crystals are composed of copper columns as shown in Figure 1.15. The rectangular lattice constant is gradually modified along one direction. The experimental results in the microwave band 10GHz are consistent with the simulation results. Light waves in photonic crystals undergo a change in propagation path and a bending effect. This verifies experimentally the mirage effect in photonic crystals.

Additional graded refractive index photonic crystals can be seen in Kurt et al.'s article. By changing the filling factor (radius of the air hole or material column) or lattice constant in the photonic crystal, they applied the graded photonic crystal to different scenarios, like flat lens [56–58], Luneburg lens [59], etc. More applications of graded photonic crystals in the near-infrared band have been investigated in Hadi Badri et al.'s article. In their work, most of the graded photonic crystal devices are set to be processed on SOI. The same purpose of changing the spatial refractive index is achieved by varying the thickness of the silicon

waveguide and changing the filling factor in PhCs. They have designed and simulated many examples of graded photonic crystal applications, like Maxwell fisheye [60], Luneburg lens [61] and Eaton lens [62–64], etc.

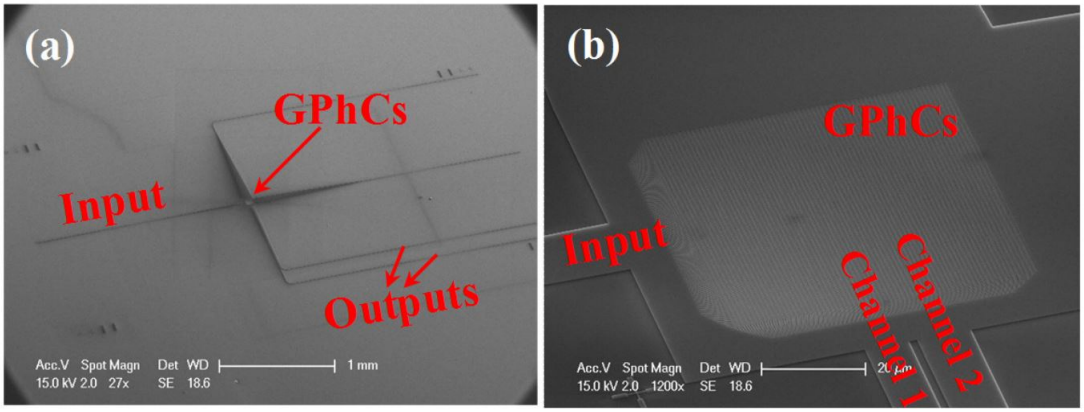

Figure 1.16: Scanning electron microscope images of (a) a two-channel wavelength demultiplexer and (b) its zoom at larger magnification [65].

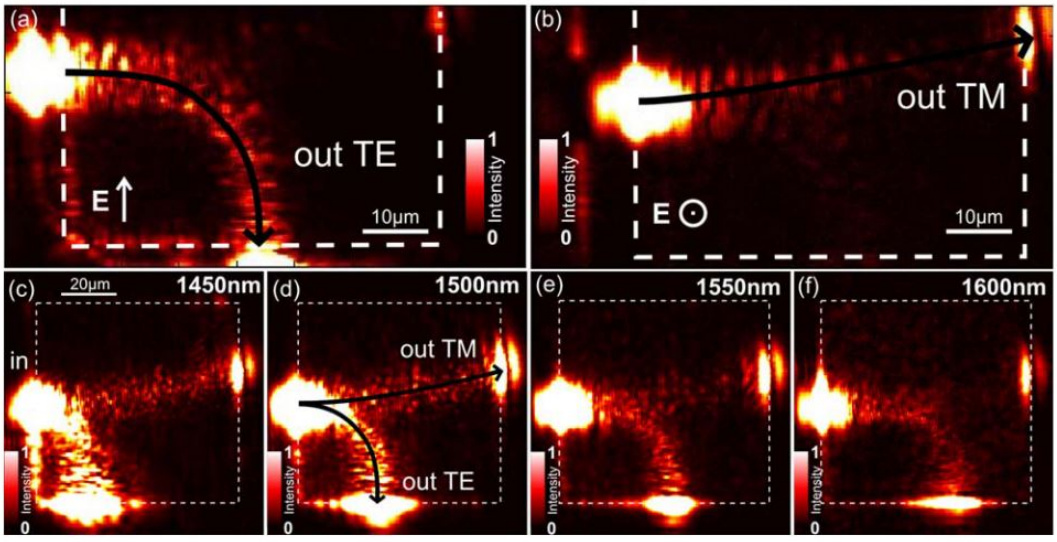

Figure 1.17: (a) SNOM image obtained at λ=1550nm for a TE polarization of the input light. (b) SNOM image obtained at λ=1550nm for a TM polarization of the input light. (c) –(f) Hyp-SNOM images obtained at λ=1450, 1500, 1550, and 1600nm with a nonpolarized laser [66].

The MiNAPHOT group in the C2N lab has been focusing on silicon-based photonic research. Van Do et al. has designed and simulated and fabricated a wavelength multiplexer based on a two-dimensional graded photonic crystal [65, 67, 68]. Based on this sample, Dellinger et al. then used the scanning near-field optical microscopy (SNOM) technique to observe the light propagation in the graded photonic crystal [69]. After processing by the

SNOM technique, they obtained a spectral propagation map with colors. In their work, the effective refractive index of a square graded photonic crystal decreases in all directions with a scattering shape centered on the lower left corner. The samples were processed using electron beam lithography. The purpose of bending light at optical frequencies was achieved by changing the distribution of the effective refractive index in space. Figure 1.16 shows the sample under the electron microscope. The light is coupled by the edges into the on-chip system. Upon entering the graded photonic crystal, light at different frequencies will be bent and redirected into different output channels because the photonic crystal exhibits different equivalent refractive index for different wavelengths of light.

Subsequently, using the same design approach, Cassan et al. designed, simulated and fabricated a polarization beam splitter based on a two-dimensional on-chip graded photonic crystal in 2013 [66]. With the help of SNOM technique, they visualized the propagation of light in the sample. For TE and TM modes, as shown in Figure 1.17, the graded photonic crystal exhibited different birefringence properties. This is due to the different scattering characteristics of the EFCs of the photonic crystal for TE and TM modes.

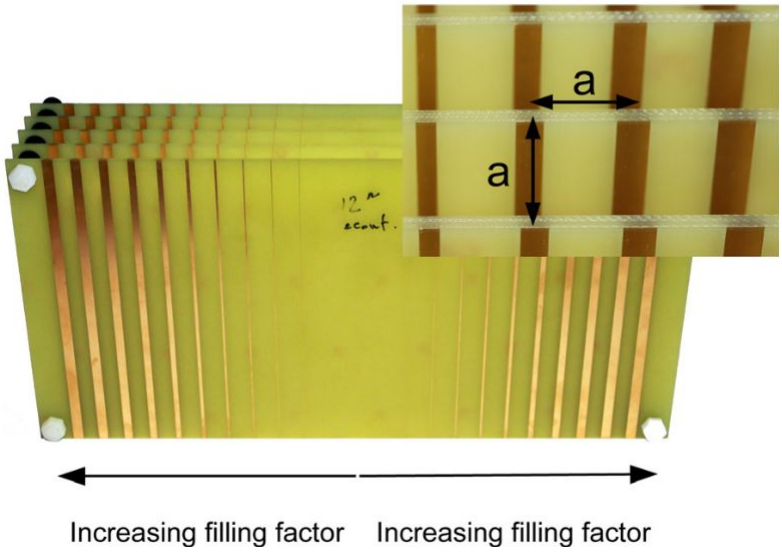

Figure 1.18: Fabricated GRIN metallic Photonic Crystal Lens which consists of five layers of printed circuit boards (PCB) [70].

Also, F. Gaufillet, a former PhD student in CRIME group, has done a lot of work in the field of graded photonic crystals. His work was mainly focused on the microwave domain. It is well known that a photonic crystal can be considered as an isotropic homogeneous medium when the equi-frequency curve is circular. He changed the equi-frequency curve by changing the filling factor in the photonic crystal. In turn, the change of the equivalent refractive index in space is achieved and it satisfies the variation law of a flat lens [70–72], a Luneburg lens [73] or a Maxwell fisheye lens [74]. Devices for microwave domain applications were processed on printed circuit boards (PCB) as illustrated in Figure 1.18. Different widths of

copper strips were printed on the board to simulate different filling factors in the photonic crystal. Characterization results show that the gradient photonic crystal lens are capable of converging microwave plane waves and collimating point sources.

The main focus of this thesis is on graded photonic crystal devices in the near infrared domain. The platform on which the experiments are based is mainly a silicon-based optical waveguide. The specific design, simulation and experimental processing with SOI technology will be described in detail later in Chapter 4.

Gradient-index optics

Closely related to the gradient photonic crystals in this thesis is gradient index (GRIN) optics. This is an ancient branch of optics [75]. For a conventional converging lens, light is refracted from air into a medium of uniform refractive index material. The light then travels through the lens in a straight line. At the time of exit, it undergoes a sudden change from the refractive index of the material to the refractive index of the air, resulting in a secondary refraction. From this we can see that it is the curved surface of the lens, a physical structure, that makes the light converge or image. In the case of gradient index optics, the refractive index inside the lens is not uniform (See Figure 1.19). The path of light through the lens media is not straight. This gradient refractive index lens can have a flat surface. Compared to conventional lens, the surface of these lens does not need to have a high precision curved shape, but can achieve the same convergence of light. At the same time, the thickness of the gradient refractive index lens can be made very thin. This provides greater flexibility in the use of product space.

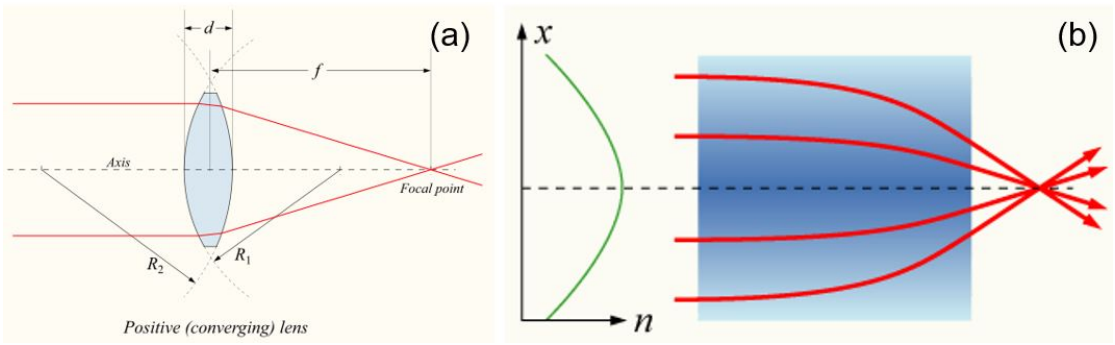

Figure 1.19: (a)Diagram of the imaging principle of a conventional convex lens. (b)Schematic of a gradient refractive index lens [76].

The most common example of gradient refractive index optics in nature is the human eye. The refractive index of the lens in the eye decreases gradually from the central to the marginal layers. This allows us to see both near and distant objects. Another common example is the atmosphere. As mentioned above, gradient index lens can improve space utilization. Therefore it can be used in precision optics as well as in small size imaging systems [77]. In

addition, gradient refractive index optics also plays an important role in fiber optic communication [78]. The refractive index at the fiber axis is higher than the refractive index near the cladding. This property reduces modal dispersion and improves communication efficiency. In the field of micro and nano processing, gradient refractive index optics also has important developments. Scientists at the University of Illinois at Urbana-Champaign have used 3D printing to create sub-micron Luneburg lens [79]. The spherical lens has a unique optical property with an increasing refractive index gradient toward the center.

1.5 Numerical calculation method

This subsection will focus on the main numerical calculation methods and tools used in this thesis. For the calculation of the band diagrams and the equi-frequency curves in photonic crystals, I used the free software package MPB developed by MIT [1], which calculates electromagnetic fields in the frequency domain using the plane wave expansion (PWE) method. For the electromagnetic simulations of the designed structures in the near-infrared band, the FDTD commercial software of Lumerical was used during this thesis. As the name suggests, it uses the FDTD algorithm to perform theoretical EM field calculations in the time domain.

First we will briefly review the set of fundamental Maxwell equations in classical electromagnetism. We will then present the two main algorithms for computing the electromagnetic fields covered in this thesis, namely the plane wave expansion (PWE) method and the Finite-difference time-domain (FDTD) algorithm.

1.5.1 Maxwell equation

The system of Maxwell's equations in vacuum consists of four differential equations:

$$\nabla \cdot \mathbf{E} = \frac{\rho}{\varepsilon_0} \tag{1.13}$$

$$\nabla \cdot \mathbf{B} = 0 \tag{1.14}$$

$$\nabla \times \mathbf{E} = -\frac{\partial \mathbf{B}}{\partial t} \tag{1.15}$$

$$\nabla \times \mathbf{B} = u_0 \mathbf{J} + u_0 \varepsilon_0 \frac{\partial \mathbf{E}}{\partial t} \tag{1.16}$$

For the physical meaning of the symbols represented in the equations system and their units are as follows:

- **E** it the electric field (volt/meter).
- **B** is the magnetic field (tesla).
- $\varepsilon_0 = 8.85418781 \times 10^{-12}$ is the vacuum permittivity (farads/meter).

- $u_0 = 1.256637062{\times}10^{-6}$ is the Vacuum permeability (henry/metre).
- **J** is the total current density (ampere/meter^2).

Equation 1.13 is also known as Gauss's law. Its physical meaning is that the electric flux through any closed surface is proportional to the amount of charge enclosed by that closed surface, indicating that the electric field is a source field. It can also describe how the electric charge produces the electric field.

Equation 1.14 is known as Gauss's law for magnetism. Its physical meaning is that the magnetic flux through any closed surface is equal to zero, indicating that the magnetic field is a source-free field. It shows that magnetic monopoles do not exist.

Equation 1.15 is known as Faraday's law of electromagnetic induction. Its physical meaning is that a time-varying magnetic field produces an electric field, which generates an induced current in the conductor. It can also be said that a time-varying magnetic field produces an induced electric potential.

At last, equation 1.16 is called Ampère-Maxwell circuital law. Its physical meaning is that time-varying electric fields and electric currents can produce magnetic fields. Where $\varepsilon_0 \frac{\partial \mathbf{E}}{\partial t}$ stands for Maxwell Displacement current density.

And in practical use, electromagnetic waves propagate in the medium most of the time. In macroscopic electromagnetism, the law of electromagnetic wave propagation in a medium (e.g., photonic crystal) can also be expressed by the corresponding set of Maxwell equations

$$\nabla \cdot \mathbf{D} = \rho_f \tag{1.17}$$

$$\nabla \cdot \mathbf{B} = 0 \tag{1.18}$$

$$\nabla \times \mathbf{E} = -\frac{\partial \mathbf{B}}{\partial t} \tag{1.19}$$

$$\nabla \times \mathbf{H} = \mathbf{J}_f + \frac{\partial \mathbf{D}}{\partial t}. \tag{1.20}$$

Most of the symbols in the equation contain the same physical meaning as in Maxwell's equations in a vacuum. But Maxwell's equations in the dielectric introduce **D**, which represents the potential shift flux. And ρ_f and $\mathbf{J}_f$ stand for free charge density and free current density.

Electromagnetism is a problem of solving the eigenvalues of Maxwell's equations. Around this problem, many solutions have been proposed like plane wave expansion method [80, 81], finite element method [82], transmission matrix method [83], finite difference time domain method [84], etc. In the following, the application of the plane wave expansion method to calculate the band diagram of a photonic crystal and the basic principle of the finite difference time domain method will be introduced.

1.5.2 Plane wave expansion method

The plane wave expansion method refers to a computational technique which 1) expand the electromagnetic wave in the form of a plane wave, 2) transform Maxwell's equations into an eigenvalue problem, 3) solve for the eigenvalue to obtain the photon energy band. Assuming that the electromagnetic wave propagates in an uniform, source-free periodic dielectric with no free charge or free current, we have $\rho_f = \mathbf{J}_f = 0$, then we have $\mathbf{D}(\mathbf{r}) = \varepsilon(\mathbf{r})\mathbf{E}(\mathbf{r})$, where $\mathbf{r}$ is the position in cartesian coordinates. For most dielectric materials, the permeability is close to 1, and we approximate $\mathbf{B} = \mathbf{H}$. Assuming a low loss dielectric medium, and neglecting the dependence of the dielectric constant on frequency, after a simple derivation, we can change Maxwell's equations to the following form

$$\begin{cases} \nabla \cdot \mathbf{H} = 0 \\ \nabla \times \mathbf{E} + \dfrac{1}{c}\dfrac{\partial \mathbf{H}}{\partial t} = 0 \\ \nabla \cdot \varepsilon(\mathbf{r})\mathbf{E}(\mathbf{r}, t) = 0 \\ \nabla \times \mathbf{H}(\mathbf{r}, t) - \dfrac{\varepsilon(\mathbf{r})}{c}\dfrac{\partial \mathbf{E}(\mathbf{r}, t)}{\partial t} = 0. \end{cases} \tag{1.21}$$

For computational convenience, the electric and magnetic fields of an electromagnetic wave propagating through a medium in some time-domain space generally take the exponential form

$$\begin{cases} \mathbf{H}(\mathbf{r}, t) = \mathbf{H}(\mathbf{r})e^{-i\omega t} \\ \mathbf{E}(\mathbf{r}, t) = \mathbf{E}(\mathbf{r})e^{-i\omega t}. \end{cases} \tag{1.22}$$

Bring equation 1.22 into equation 1.21. If there is no potential shift and no source of magnetic field in the magnetic field, for a certain frequency it is obtained that

$$\nabla \cdot \mathbf{H}(\mathbf{r}) = \nabla \cdot \mathbf{E}(\mathbf{r}) = 0. \tag{1.23}$$

In addition, the propagation of electric and magnetic fields in space are transverse waves, then the equations of $\mathbf{E}(\mathbf{r})$ and $\mathbf{H}(\mathbf{r})$ can be simplified as

$$\nabla \times \mathbf{E}(\mathbf{r}) - i\omega\mu_0\mathbf{H}(\mathbf{r}) = 0 \tag{1.24}$$

$$\nabla \times \mathbf{H}(\mathbf{r}) + i\omega\varepsilon_0\varepsilon(\mathbf{r})\mathbf{E}(\mathbf{r}) = 0. \tag{1.25}$$

Further simplifying the equation, where ε_0 and μ_0 can be replaced by the speed of light: $c = 1/\sqrt{\varepsilon_0\mu_0}$, we can obtain an equation describing the electric field as follows

$$\frac{1}{\varepsilon(\mathbf{r})}\nabla \times \nabla \times \mathbf{E}(\mathbf{r}) = \left(\frac{\omega}{c}\right)^2 \mathbf{E}(\mathbf{r}). \tag{1.26}$$

and a propagation equation describing the strength of the magnetic field

$$\nabla \times (\frac{1}{\varepsilon(\mathbf{r})} \nabla \times \mathbf{H}(\mathbf{r})) = \left(\frac{\omega}{c}\right)^2 \mathbf{H}(\mathbf{r}) \tag{1.27}$$

In a photonic crystal, $\varepsilon(\mathbf{r})$ is a periodic function. For a given frequency, solving the above equation yields the mode of magnetic field strength **H(r)**, which is then brought into the equation to give

$$\mathbf{E}(\mathbf{r}) = \frac{i}{\omega \varepsilon_0 \varepsilon(\mathbf{r})} \nabla \times \mathbf{H}(\mathbf{r}). \tag{1.28}$$

Expanding **E(r)** into a series of plane waves, converting its differential equation 1.26 into a series of linear equations, and then solving it by computer will give the allowed frequency modes associated with the wave vector k.

Most of the band structure calculations for photonic crystals in this thesis are in two dimensions. Therefore, the band structure calculation of two-dimensional photonic crystals using the plane wave expansion method will be described below [1].

The permittivity $\varepsilon(\mathbf{r})$ of a photonic crystal varies periodically in space, which makes both **E(r)** and **H(r)** a function of the periodic function of $\mathbf{r}$. Here we expand $\varepsilon(\mathbf{r})$, **E(r)** and **H(r)** into a Fourier power series as follows

$$\frac{1}{\varepsilon(\mathbf{r})} = \sum_G \mathbf{K}(G) e^{iG \cdot \mathbf{r}} \tag{1.29}$$

$$\mathbf{E}(\mathbf{r}) = \sum_G \mathbf{B}(k+G) e^{iG \cdot \mathbf{r}} \tag{1.30}$$

$$\mathbf{H}(\mathbf{r}) = \sum_G \mathbf{A}(k+G) e^{iG \cdot \mathbf{r}}. \tag{1.31}$$

Here G is reciprocal lattice vectors. In a two-dimensional structure, taking into account the TE mode or TM mode polarizability of electromagnetic waves, the electric and magnetic fields can be written as

$$\mathbf{H}(\mathbf{r}, t) = \mathbf{H}_0(\mathbf{r}) e^{-i\omega t} = [0, 0, \mathbf{H}_3(\mathbf{r})] e^{-i\omega t} \tag{1.32}$$

$$\mathbf{E}(\mathbf{r}, t) = \mathbf{E}_0(\mathbf{r}) e^{-i\omega t} = [E_x(\mathbf{r}), E_y(\mathbf{r}), 0] e^{-i\omega t}. \tag{1.33}$$

where **r** is a vector in the x and y directions. We expand the previous equation 1.24 and 1.25 and bring it into the Fourier power series equation to obtain the expression for $\mathbf{H}_3$ as

$$\frac{\partial}{\partial x}(\frac{1}{\varepsilon(\mathbf{r})} \frac{\partial \mathbf{H}}{\partial x}) + \frac{\partial}{\partial y}(\frac{1}{\varepsilon(\mathbf{r})} \frac{\partial \mathbf{H}}{\partial y}) + \left(\frac{\omega}{c}\right)^2 \mathbf{H} = 0. \tag{1.34}$$

Bringing equation 1.31 into equation 1.34, we get

$$\sum_{G'} \mathbf{K}(G - G') \mathbf{A}(k + G')(k + G) = (\frac{\omega}{c}) \mathbf{A}(k + G). \tag{1.35}$$

The above equation is the equation for the propagation of an electromagnetic wave TE polarized in a photonic crystal. In this way, we only need to solve for the eigenvalues and eigenfunctions of a symmetric matrix. For TM polarization, a similar equation can be obtained as follows

$$\sum_{G'} \mathbf{K}(G-G')\mathbf{B}(k+G')|k+G|^2 = (\frac{\omega}{C})\mathbf{B}(k+G). \tag{1.36}$$

Each of these two equations 1.35 and 1.36 becomes an eigenvalue equation with NxN matrix elements, which can be solved by numerical computation.

1.5.3 Finite Difference Time Domain method

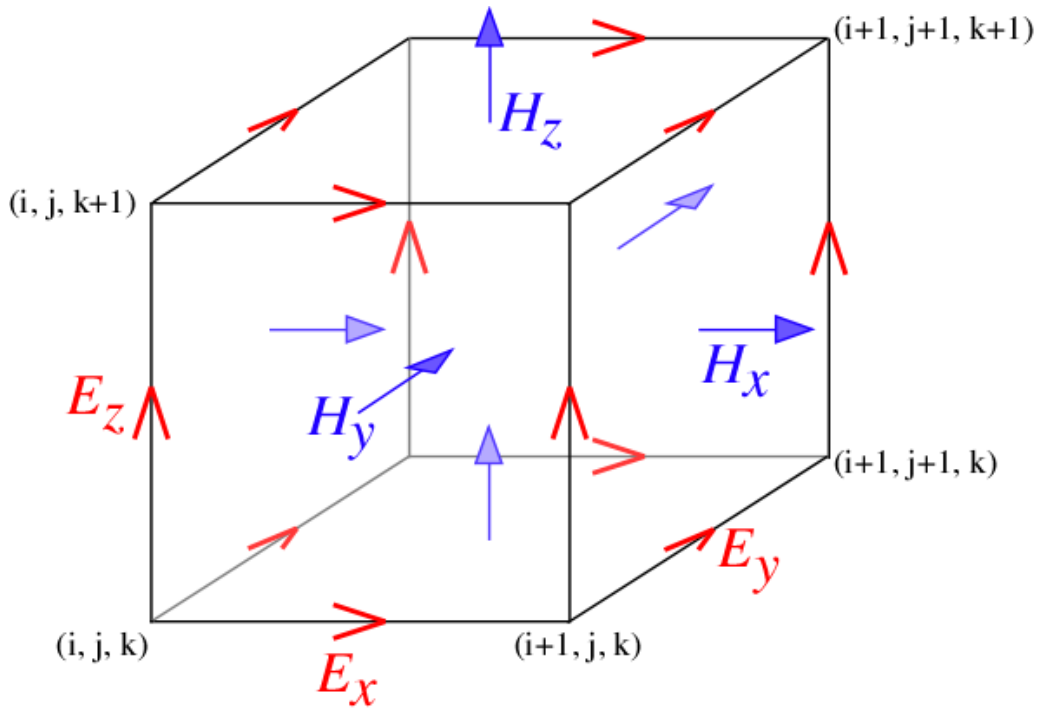

Figure 1.20: Schematic diagram of Yee cell [85].

FDTD is one of the most commonly used methods for the numerical calculation of electromagnetic fields, and it is widely used in the calculation of electromagnetic wave problems, such as wave propagation [86–88], scattering [89, 90] and antenna analysis [91–93]. Its algorithm was first proposed by Yee in 1966 [94] and is therefore known as Yee's algorithm. Then in 1975, Taflove and Brodwin reported the first sinusoidal steady-state FDTD solutions of 2D and 3D electromagnetic wave interactions with material structures [95]. Subsequently in 1980, Taflove coined the acronym FDTD and released the first validated FDTD model [96]. This method directly performs a finite difference between the two curl equations 1.15 and 1.16 of Maxwell's equations, and then adds appropriate boundary conditions (periodic or

absorption boundaries) based on the actual solution model to obtain the discrete electromagnetic field matrix equations. The resulting finite-difference equations are solved in software in a leapfrog manner: the electric field vector components in a volume of space are solved at a given instant in time; then the magnetic field vector components in the same spatial volume are solved at the next instant in time; and the process is repeated over and over again until the desired transient or steady-state electromagnetic field behavior is fully evolved [97].

The discretization of Maxwell's equations by the time-domain finite difference method does not lead to excessive computational errors and can handle photonic crystals of arbitrary geometry. In addition, the Fourier transform allows a single calculation to include results for a wide range of frequencies, giving an intuitive picture of the light transport behavior in photonic crystals. The time-domain finite-difference method can calculate not only the transmission and reflection properties of finite structures, independent of the solid-liquid structure form and other factors, but also the band structure in periodic structures.

This thesis focuses on the simulation of photonic crystal models using the FDTD Solutions software developed by Lumerical, Inc. This commercial software has an embedded optimization engine and parallel computing capabilities. It is capable of analyzing the interaction of complex structures at wavelength scales with UV, visible and IR electromagnetic waves. The basic principles of the FDTD algorithm are described below.

Applying the method proposed by Yee, it is possible to discretize Maxwell's equations in space and time domain. Figure 1.20 represents a time-domain finite-difference three-dimensional grid diagram of a Yee progenitor cell. The difference equation of the time-domain finite-difference method in the three-dimensional coordinate system can be expressed as six component equations

$$H_x\Big|_{i,j,k}^{n+1/2} = H_x\Big|_{i,j,k}^{n-1/2} - \frac{\Delta t}{\mu_{i,j,k}}\left(\frac{E_z\Big|_{i,j+1,k}^{n} - E_z\Big|_{i,j,k}^{n}}{\Delta y} - \frac{E_y\Big|_{i,j,k+1}^{n} - E_y\Big|_{i,j,k}^{n}}{\Delta z}\right) \tag{1.37}$$

$$H_y\Big|_{i,j,k}^{n+1/2} = H_y\Big|_{i,j,k}^{n-1/2} - \frac{\Delta t}{\mu_{i,j,k}}\left(\frac{E_x\Big|_{i,j,k+1}^{n} - E_x\Big|_{i,j,k}^{n}}{\Delta z} - \frac{E_z\Big|_{i+1,j,k}^{n} - E_z\Big|_{i,j,k}^{n}}{\Delta x}\right) \tag{1.38}$$

$$H_z\Big|_{i,j,k}^{n+1/2} = H_z\Big|_{i,j,k}^{n-1/2} - \frac{\Delta t}{\mu_{i,j,k}}\left(\frac{-E_y\Big|_{i+1,j,k}^{n} + E_y\Big|_{i,j,k}^{n}}{\Delta x} - \frac{E_x\Big|_{i,j+1,k}^{n} - E_x\Big|_{i,j,k}^{n}}{\Delta y}\right) \tag{1.39}$$

$$E_x\Big|_{i,j,k}^{n+1} = \frac{\varepsilon_{i,j,k} - \sigma_{i,j,k}\Delta t/2}{\varepsilon_{i,j,k} + \sigma_{i,j,k}\Delta t/2} E_x\Big|_{i,j,k}^{n} - \frac{\Delta t}{\varepsilon_{i,j,k} + \sigma_{i,j,k}\Delta t/2} \left(\frac{H_z\Big|_{i,j,k}^{n+1/2} - H_z\Big|_{i,j-1,k}^{n+1/2}}{\Delta y} - \frac{H_y\Big|_{i,j,k}^{n+1/2} - H_y\Big|_{i,j,k-1}^{n+1/2}}{\Delta z} \right) \tag{1.40}$$

$$E_y\Big|_{i,j,k}^{n+1} = \frac{\varepsilon_{i,j,k} - \sigma_{i,j,k}\Delta t/2}{\varepsilon_{i,j,k} + \sigma_{i,j,k}\Delta t/2} E_y\Big|_{i,j,k}^{n} - \frac{\Delta t}{\varepsilon_{i,j,k} + \sigma_{i,j,k}\Delta t/2} \left(\frac{H_x\Big|_{i,j,k}^{n+1/2} - H_x\Big|_{i,j,k-1}^{n+1/2}}{\Delta z} - \frac{H_z\Big|_{i,j,k}^{n+1/2} - H_z\Big|_{i-1,j,k}^{n+1/2}}{\Delta x} \right) \tag{1.41}$$

$$E_z\Big|_{i,j,k}^{n+1} = \frac{\varepsilon_{i,j,k} - \sigma_{i,j,k}\Delta t/2}{\varepsilon_{i,j,k} + \sigma_{i,j,k}\Delta t/2} E_z\Big|_{i,j,k}^{n} - \frac{\Delta t}{\varepsilon_{i,j,k} + \sigma_{i,j,k}\Delta t/2} \left(\frac{H_y\Big|_{i,j,k}^{n+1/2} - H_y\Big|_{i-1,j,k}^{n+1/2}}{\Delta x} - \frac{H_x\Big|_{i,j,k}^{n+1/2} - H_x\Big|_{i,j-1,k}^{n+1/2}}{\Delta y} \right), \tag{1.42}$$

where, the superscript n is the number of time steps and the subscript i, j, k is the location of the grid points in each of the three directions of x, y, z. Δt is the time evolution step and $\Delta x, \Delta y, \Delta z$ is the distance between two adjacent grid points in each of the three directions.

The equations derived from Maxwell's rotational equations by the Yee grid have an explicit differential format that can be used to calculate the propagation variation law of electromagnetic waves in the computational space by advancing step by step in time steps. These differential equations have a stability problem, i.e., certain conditions must be satisfied between the time variable step and the space variable step, otherwise numerical instability will occur. The stability of Yee's difference format was discussed by Taflove et al. in 1975 [95], and the constraint on the time step was derived as follows

$$\Delta t \leq \frac{1}{c\sqrt{(\Delta x)^{-2} + (\Delta y)^{-2} + (\Delta z)^{-2}}}, \tag{1.43}$$

where c is the speed of light in vacuum, Δt is the time step, and $\Delta x, \Delta y, \Delta z$ is the space step in x, y, z direction, respectively.

If the characteristics of the medium in which the electromagnetic wave is propagating are related to frequency, the propagation speed of the electromagnetic wave will also be a function of frequency, a phenomenon known as dispersion. The medium in which dispersion occurs is called a dispersive medium. It is obvious that in a non-dispersive medium, the propagation speed of electromagnetic waves should be independent of frequency. Therefore, the

phase velocity of a plane wave modeled using the time-domain finite-difference equation is independent of frequency. However, since the time-domain finite-difference equation is only an approximation of the original Maxwell's rotational equation, when the propagation of electromagnetic waves is simulated in the computer's storage space, the dispersion phenomenon also occurs in the non-dispersive medium space, and the phase velocity v_g of electromagnetic waves varies with wavelength, propagation direction, and the dispersion of variables. This non-physical dispersion phenomenon can be called numerical dispersion. Numerical dispersion can lead to the destruction of the pulse waveform, the appearance of artificial anisotropy and false refraction and other phenomena. Therefore, numerical dispersion is an important problem of the time-domain finite-difference method, and it is an important limitation to improve the accuracy of this algorithm.

The basic method for analyzing numerical dispersion problems is to substitute the general form of a monochromatic plane wave into the difference equation. After a simple derivation the equation between frequency and time and space steps, i.e. the numerical dispersion relation, can be derived as follows [98]

$$\begin{aligned}\left(\frac{1}{\upsilon\Delta t}\right)^2 \sin\left(\frac{\omega\Delta t}{2}\right) =& \frac{1}{\Delta r^2}\sin^2\left(\frac{k_r\Delta r}{2}\right) + \\ & \frac{1}{r^2\Delta\varphi^2}\sin^2\left(\frac{k_\varphi\Delta\varphi}{2}\right) + \frac{1}{\Delta z^2}\sin^2\left(\frac{k_z\Delta z}{2}\right).\end{aligned} \tag{1.44}$$

In the electromagnetic field, the dispersion relation can be analytically obtained for a plane electromagnetic wave in the space of a uniform non-consuming isotropic medium by

$$\frac{\omega^2}{\upsilon^2} = k_r^2 + k_\varphi^2 + k_z^2. \tag{1.45}$$

It can be seen that when $\Delta t, \Delta r, \Delta z, \Delta\varphi$ all tend to zero, the limit of Eq. 1.44 is Eq. 1.45. This indicates that the numerical dispersion is caused by the approximate difference quotient calculation instead of the continuous microquotient. Therefore shortening the values of the time step and space step in the discrete process can reduce the effect of numerical dispersion. Of course, this reduction is limited by the actual computational resources. The reduction of the time and space steps implies an increase in the total number of cells in the computational mesh space. Therefore, the storage space and computation time requirements of the computer increase accordingly. Thus, the time and space steps are always chosen appropriately according to the nature of the problem and the actual conditions in order to minimize the effect of numerical dispersion on the results.

When the spatial step is chosen to satisfy:

$$\Delta x = \Delta y = \Delta z \leq \frac{\lambda}{15} \tag{1.46}$$

and the time step Δt is guaranteed to satisfy the numerical stability condition equation 1.43,

the numerical dispersion can be controlled within an acceptable error range.

An important feature of the time-domain finite-difference algorithm is the need to resume the Yee grid computational space over the entire region of the computed electromagnetic field. Therefore the grid must be cut off at the appropriate places. This algorithm for grid cutoff is called the setting of boundary conditions. A novel perfectly matched layer (PML) consisting of an absorbing medium proposed by Berenger in 1994 [99] is used in most cases in this thesis. This artificially designed perfect match layer consists of a dissipative conductive and permeable medium that can absorb incident electromagnetic waves at any incident angle, any frequency, and any polarization state.

In addition, there is another very important boundary condition, namely periodic boundary condition, in the calculation of electromagnetic fields of periodic subwavelength structures such as photonic crystals. Since the photonic crystal structure is a periodic structure, the electromagnetic field is characterized by a distinct periodic distribution. Therefore, the electromagnetic field distribution of the entire space can be deduced by accurately calculating the electromagnetic field distribution of a single cell. In view of this, the use of periodic boundary conditions will greatly reduce the simulation time and help improve the simulation accuracy.

1.6 Thesis motivation and manuscript organizations

The main purpose of this PhD topic is to explore graded photonic crystals and related gradient index optics in the near infrared domain for applications on Silicon On Insulator (SOI) platforms. Gradient photonic crystals in the microwave band have been investigated by previous PhD students Fabian Gaufillet in our group. This work then attempts to extend the application to the near-infrared field. According to the theory of subwavelength electromagnetism, the size of the device should be of the same order of magnitude as the operating wavelength. Thus, unlike the previous microwave field, a big challenge in the NIR field is the fabrication and characterization of the corresponding devices. A significant part of this work is focused on the fabrication and characterization process of gradient photonic crystals in the NIR field. SOI was chosen as the processing platform for this work, considering the good compatibility of the silicon-based platform with photonic devices and its ability to integrate well with nanofabrication techniques. In addition, another emphasized aspect of this work is to explore the effect of the variation of the photonic crystal parameters on its effective refractive index. Thus, the case of normalized frequencies in different photonic crystal energy bands is also a direction of investigation. We attempt to manipulate the effective refractive index (even negative refractive index) of photonic crystals by changing their parameters. Experimental demonstration of negative refractive index gradient photonic crystal lens and related gradient photonic crystal devices will be highlighted.

1.6. Thesis motivation and manuscript organizations

This manuscript is organized as follows. The first chapter will be used to present the research background of this work and the introduction of the basic concepts which have important role in this thesis.

The second chapter will further present photonic crystal devices on a silicon-on-insulator (SOI) platform in particular. The effective refractive index method used in the modeling of photonic crystal slabs in this work will be presented. The silicon-based coupling method used in the thesis work and the related concepts of silicon-based waveguides will also be introduced.

Chapter 3 will present theoretical modeling methods and simulation results for gradient photonic crystals in the NIR domain. For flat lens, the case of different bands in square lattice and hexagonal lattice photonic crystals will be analyzed and discussed. In addition, Half Maxwell-Fisheye lens will also be designed and simulated.

Chapter 4 will focus on nano-fabrication techniques in the near-infrared. Among the most important Electron-beam lithography (EBL) and deep etching techniques will be highlighted. Subsequently, two characterization methods in the NIR field used in this thesis will also be shown.

Samples obtained by nano-fabrication will be shown in Chapter 5 by means of electron microscopy. Subsequently, the characterization results of the samples processed in this thesis will also be presented.

Chapter 2

Silicon photonics for infrared applications

Contents

Research in silicon photonics enables a full range of light generation, transmission, modulation, interconnection and detection in silicon and silicon-based materials. Thus the function and role of silicon as a photonic material has become particularly important. Silicon is known to be the best material for large-scale integrated circuits. It will also be the most suitable material for optoelectronic integration, and now it is becoming a new type of inexpensive photonic material. Using silicon or silicon-based materials we can fabricate a wide variety of photonic devices. For instance, by integrating electronic devices ($Si_{1-x}Ge_x$quantum devices, heterojunction bipolar transistors, CMOS, RF devices, tunneling diodes, etc.), photonic devices (lasers [100], detectors [101], optical switches [102], optical modulators [103], etc.) and optical waveguide loops on the same silicon wafer or SOI, we can obtain optoelectronic integrated circuits with many special optoelectronic properties. These special optoelectronic properties can not only be widely used in systems such as optical communication [104], biosensing [105], military field [106], optical instruments and space vehicles, but also enable optical interconnection [107], photonic computing [108] and artificial intelligence [109] in the near future.

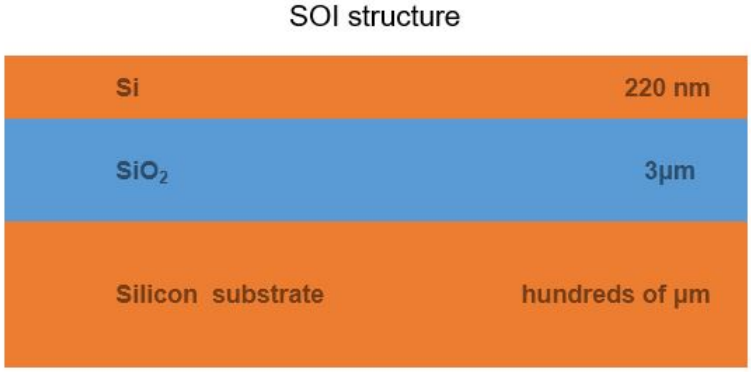

Figure 2.1: SOI structure used in this thesis.

This chapter will first introduce the SOI platform used in the thesis. It mainly includes the preparation method of SOI and the optical coupling method on the SOI platform. We will then introduce the effective refractive index method used in this thesis. Finally we will introduce the different optical waveguides in silicon photonics and their single-mode conditions. The losses in optical waveguides will also be briefly introduced.

2.1 Silicon on Insulator

Silicon on insulator (SOI) material is a silicon-based integrated circuit and optoelectronic integration material. It is a thin layer of silicon (Si) set on an insulating substrate (SiO_2). This thin layer of silicon is called the device layer, and various transistor devices or photonic devices are prepared on this thin layer of silicon. By introducing a buried oxide layer between

the top layer of silicon and the back substrate silicon, SOI technology forms a thin semiconductor layer on an insulator, a special structure that gives SOI some unparalleled advantages. The structure of SOI used in this thesis is given in Figure 2.1.

Among the many waveguide materials used in the telecommunication wavelength, SOI materials offer many advantages. In the infrared band used in this thesis, SOI materials have extremely low absorption loss for light, making them ideal for optical communication and on-chip optical interconnection. Furthermore, the refractive index difference between the Si (n_{Si}=3.47) and SiO_2 layers (n_{SiO_2}=1.44) in SOI greatly enhances the light limiting effect of the waveguide layer. This allows the size of the waveguide to be reduced under the micron scale. And the preparation process of the device on SOI is compatible with the conventional integrated circuit process, which is conducive to reducing the fabrication cost of photonic devices. Several photonic devices fabricated on SOI are given in Figure 2.2.

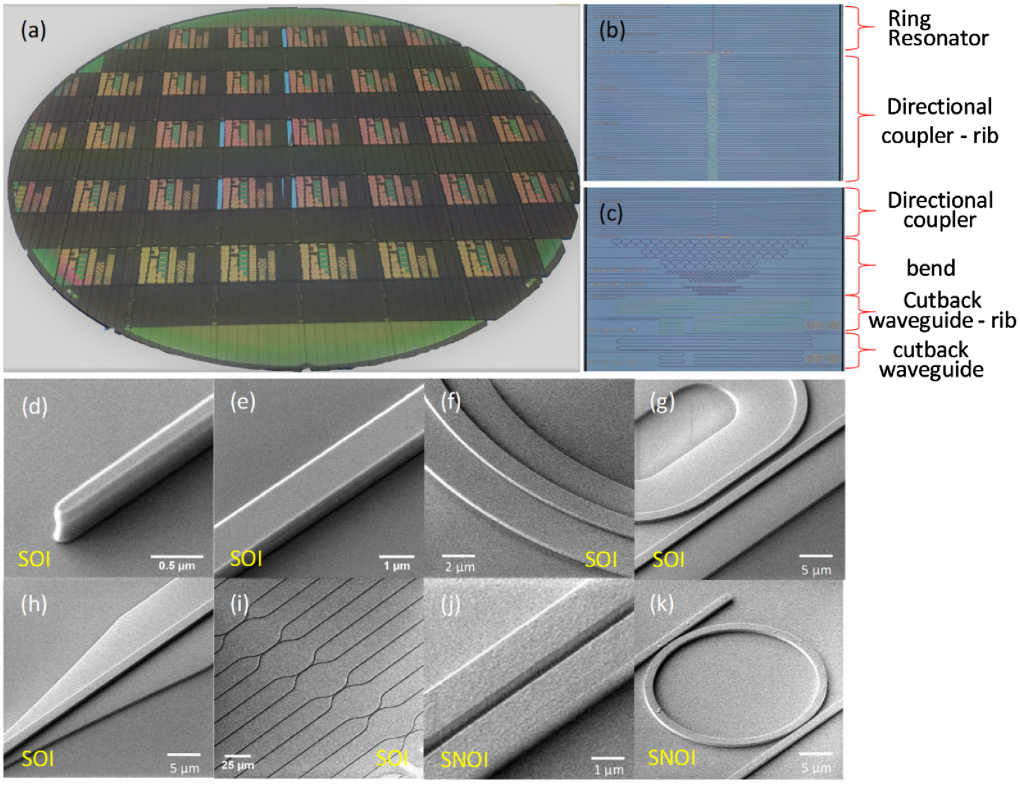

Figure 2.2: (a) Fabricated 8-in. silicon wafer with MIR devices after wafer dicing for characterization. (b) SOI strip ring resonators and rib DCs. (c) SOI strip DCs, bends, waveguides, and rib waveguides. (d)–(k) SEM images ofthe fabricated devices. (d) SOI waveguide taper tip. (e) SOI wire waveguide. (f) SOI rib waveguide. (g) SOI rib DC. (h) SOI strip to rib converter. (i) SOI strip DC array. (j) SNOI DC. (k) SNOI add–drop ring resonator [110].

2.1.1 Fabrication technology for SOI

Since the invention of SOI materials, a variety of preparation methods have emerged, including bond and etch-back SOI (BESOI), separation by implantation oxygen (SIMOX), smart-cut process, zone melting re-crystallization (ZMR). Some of these methods have gradually faded from people's view, while some other preparation methods have gradually become the mainstream preparation technology for SOI due to their low-cost process and reliable quality. The properties of SOI materials obtained by different preparation methods are different and are thus suitable for the preparation of different electronic and photonic devices.

The smart-cut technology [111, 112] will be mainly introduced here (See Figure 2.3). This is also the most dominant SOI preparation method nowadays. The hydrogen injection

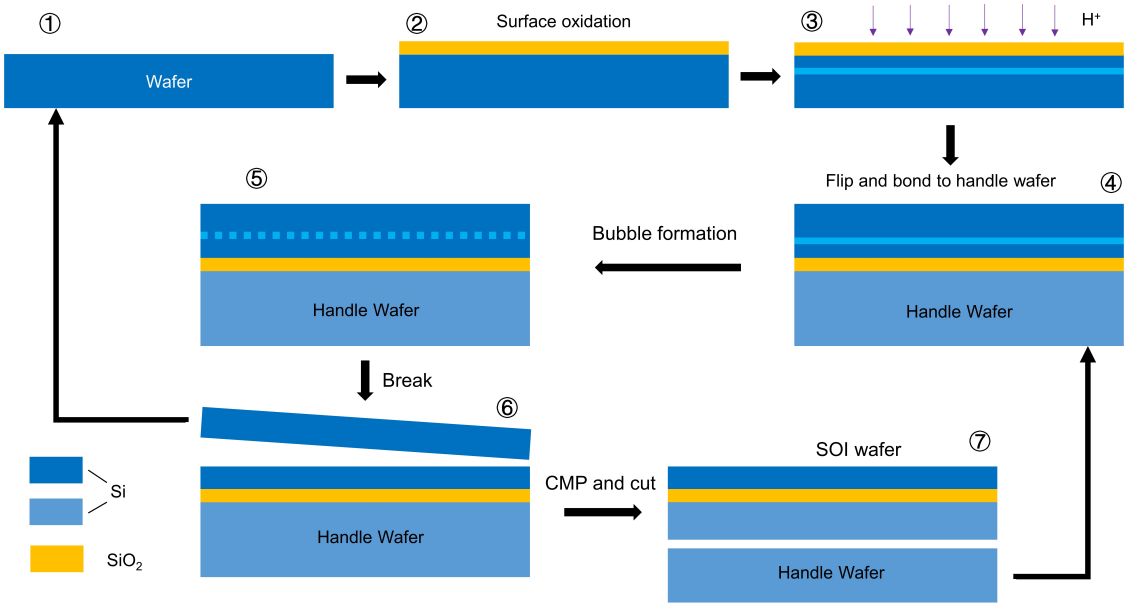

Figure 2.3: Steps of smart-cut technology in SOI fabrication. CMP stands for chemical mechanical polishing.

smart stripping technique combining hydrogen ion injection and bonding was first proposed by Mr.Bruel [113], one of the founders of SOITEC in France. The SOI materials prepared by Smart-cut technology are also known as UNIBOND materials. This technique combines ion injection technology with wafer bonding technology to transfer a superficial silicon layer from one wafer to another wafer or other insulating substrate. Its basic process steps include:

1) Hydrogen ions are injected into the silicon wafer with oxidized surface. The injected dose is of $5 \times 10^{16}/cm^2$ magnitude. Microcavities and microbubbles are formed at this stage in the area of the wafer at a depth of R_p injection distance. The wafer is prepared with a SiO_2 cover layer by oxidation prior to injection. This SiO_2 cover layer will become a hidden SiO_2 layer in the SOI structure at the end of the smart-cut process. During the

hydrogen ion injection process, the oxide surface loses hydrophilicity due to some carbon contamination on the surface. Therefore, the wafer must be carefully cleaned to restore the hydrophilicity of the surface prior to wafer bonding.

2) Hydrophilic bonding of the wafer and the support sheet is performed. The support wafer can be either a bare silicon wafer or an oxidized silicon wafer. This depends on the desired thickness of the buried oxygen layer in the final SOI.

3) This is followed by a two-stage heat treatment of the bonded wafer. In the first stage the temperature is kept at 500°C. The hydrogen ion injected wafer splits into two parts: one is the thin layer of single crystal silicon still bonded to the support wafer and the other is the remaining part of the wafer. The remaining part can be reused as another support wafer. The basic mechanism of silicon wafer splitting due to hydrogen ion injection and heat treatment is similar to the process of blistering and flaking of the surface of the material after bombardment with helium ions or protons. During the annealing process, the average size of the microcavities within the silicon wafer increases. This increase in the size of the microcavities is carried out in a direction parallel to the wafer surface. And the microcavities interact with each other, eventually leading to the expansion of the cleavage throughout the silicon wafer. The direction of crack expansion is strictly parallel to the wafer surface. The second stage of heat treatment is carried out at a higher temperature (1100°C) to strengthen the bonding between the SOI silicon layer and the support wafer.

4) Finally, the SOI sheet is mechanically and chemically polished to obtain the desired mirror-like surface. After the splitting of the wafer in the previous step, the top silicon layer of the SOI structure shows a significant micro-roughness. This must therefore be contact polished. The polishing process can reduce the surface roughness of the SOI wafer to 0.15 nm.

The typical silicon layer thickness of SOI materials prepared by Smart-cut technology is about 200 nm. Since the introduction of this technology, a large number of related technologies have been researched and developed, mainly by SOITEC in France. SOITEC has also become the world's leading supplier of thin-layer SOI with Smart-cut technology.

2.1.2 Light coupling method

Although SOI submicron waveguides are capable of achieving many compact structures and excellent features, the loss problem of fiber-waveguide coupling must first be solved in order to be used in real-world communication systems for SOI submicron waveguides on a large scale. The coupling methods of the fiber to the waveguide can be broadly classified into edge coupling and grating coupling. As the name implies, edge coupling uses optical fibers aligned to the end face of an integrated waveguide to guide the light into the chip. And grating coupling uses optical fibers to illuminate the grating waveguide for optical coupling.

In this thesis, edge coupling was chosen as the coupling method to channel light into the SOI platform (See Figure 2.4). The loss between the fiber and the waveguide is composed of the

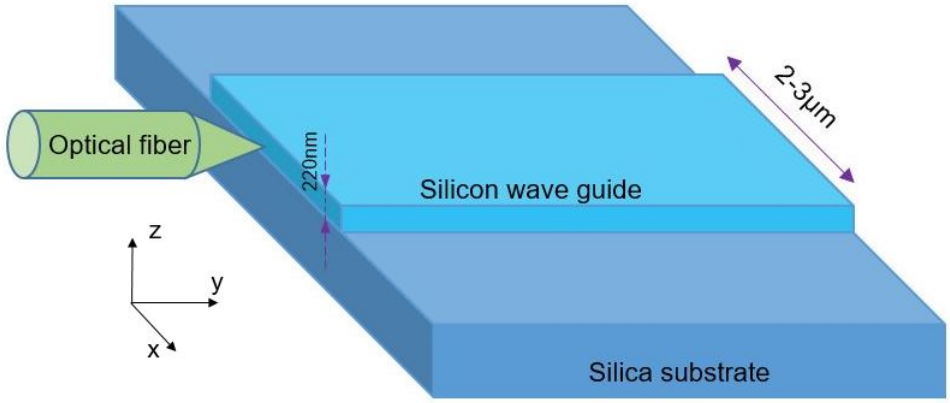

Figure 2.4: Coupling an optical beam from a fiber into an optical waveguide using edge coupling method.

following components:

- Transverse dislocation loss between the fiber and the waveguide.
- Longitudinal spacing loss between fiber and waveguide.
- Fiber and waveguide axial angle tilt loss.
- Mode-field matching loss.
- Numerical aperture difference loss.

The magnitude of the first three losses depends on the alignment of the fiber and the waveguide. We can use a precision optical stage to adjust the position of the fiber in three *x*-*y*-*z* directions to make it precisely aligned. The last two losses depend on the size structure of the fiber and the waveguide itself. In general, the mode spot size in the fiber is 8-10µm, and the cross-sectional size of the input waveguide we use in this thesis is 220nm x 2µm. The matching of the mode spot size between the two in this way will bring a large loss. In order to minimize the loss, we use the lensed fiber to improve it. A typical single-mode fiber SMF28 and several different polishing methods are shown in Figure 2.5. The (b)(d)(e) structure in Figure 2.5 is mainly used for edge coupling, while the (c) structure can be used for grating coupling. In our case, for lensed fiber, its end face is polished to a semi-ellipsoidal or conical tip. This way the 10um fiber mode field core is reduced to 2-4um, which enables better mode field matching with SOI waveguides [115]. This approach significantly improves the efficiency of fiber-to-chip edge coupling, although the smaller spot size leads to proportionally tighter alignment tolerances. In addition, care must be taken when adjusting the fiber position

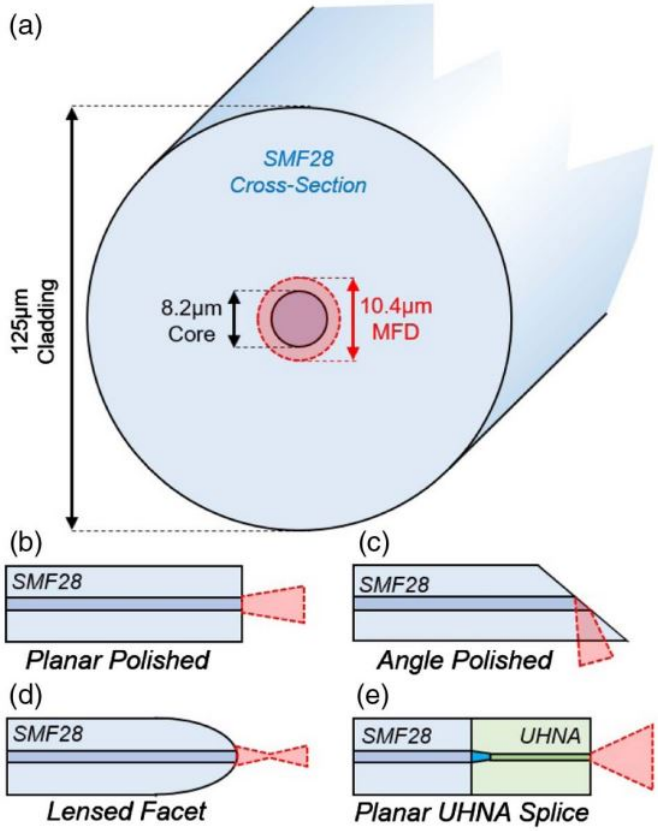

Figure 2.5: (a) Cross-section schematic of an SMF28 fiber, showing the 8.2µm fiber core centered in the cladding layer, wave-guiding the 10.4µm MFD 1.55 µm mode. Side view schematics of (b) planar polished, (c) angle polished, and (d) lensed SMF28. (e) Schematic of UHNA-to-SMF28 splicing, showing the thermally expanded adiabatic taper [114].

to avoid direct contact between the end of the fiber and the sample input, which could result in fiber damage. The end face created when cleaving the sample can also affect the coupling efficiency. Thus, we should try to keep the fiber input side of the sample as flat as possible, both vertically and horizontally.

2.2 Effective index method

The final fabrication platform we realized is SOI, a planar shaped structure. The most important difference between the SOI and the 2D structure is that the SOI is limited in the vertical direction, that is, the light will be localized in the vertical direction. The method used in this thesis to calculate the dispersion relation diagram for this three-dimensional planar photonic crystal is the effective refractive index method as shown in Figure 2.6. In this subsection, the basic principles and application of the effective refractive index method will be described. The effective refractive index method has been applied in photonic crystals at a very early stage [117–120]. It is based on the principle of using the effective refractive index of the

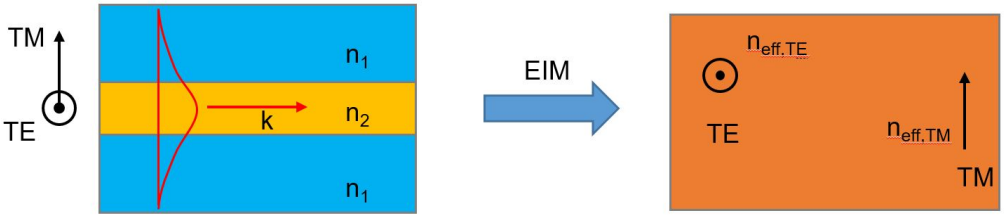

Figure 2.6: Schematic representation of the Effective Index Method (EIM). 3D structures are approached by 2D calculations with the effective index in vertical direction. [116]

fundamental guided mode in a three-dimensional heterostructure instead of the refractive index in a dielectric material. This allows us to use simple two-dimensional calculations to approach complex three-dimensional calculations. The obvious advantage of this method is that it is simple, efficient and not high computationally consuming. It is relatively limited in accuracy. Also, it is clear that the effective refractive index of the fundamental guided mode varies with the wavelength.

For the application of the effective refractive index in the band diagram calculation of flat photonic crystals, Qiu compared this method with the 3D vector FDTD calculation in his papers [116, 121]. He concluded that the accuracy of the effective refractive index method is in good agreement with the three-dimensional calculation for the calculation of the band diagram of a flat planar photonic crystal. Subsequently, Berrier et al. applied the effective refractive index method for modeling and calculations, and demonstrated experimentally for the first time negative refraction in a two-dimensional photonic crystal in the near-infrared region [122]. Many studies have since been conducted to improve the accuracy of the effective refractive index or to address the frequency dependence of the effective refractive index [123–126].

The first step in the effective refractive index method is to find the effective refractive index of each mode (the polarization fraction, TE and TM) in the one-dimensional slab waveguide. Figure 2.7 gives the variation of the effective refractive index of each mode in the 1D silicon waveguide at a wavelength of 1550 nm. The black dotted line in the figure is the refractive index of the silica substrate. Modes with an effective refractive index below this value cannot be guided. From the figure, we can see that at a wavelength of 1550 nm, a single TE mode or a single TM mode exists in the slab only when the slab thickness is below 240 nm (black vertical line). For our case, the thickness of the slab is 220 nm (red vertical line). Then the slab is single mode. Further, the effective refractive index of the single TE mode in the slab is greater than that of the single TM mode. Roughly, $n_{eff,TE} = 2.845$ and $n_{eff,TM} = 2.051$. This means that the single TE mode is better confined to the waveguide than the single TM mode. Therefore, the design modeling in this thesis will mainly focus on TE mode, in which case the $n_{eff} = 2.845$ [128]. Also, the effect of the SiO_2 cladding coverage on the effective refractive index of the silicon waveguide is negligible [128]. Our

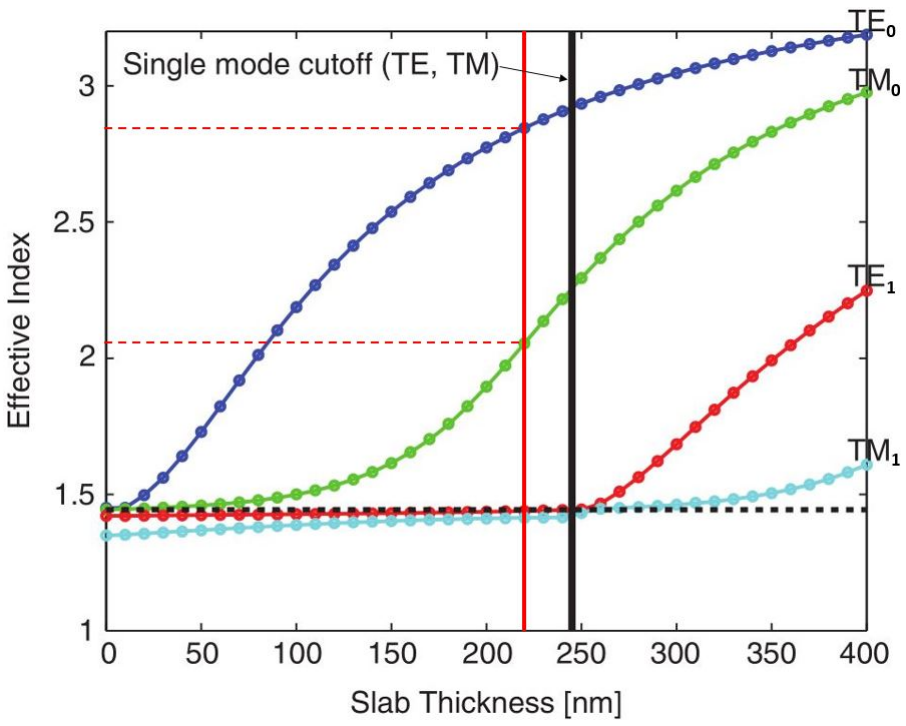

Figure 2.7: Simulation of the effective index n_{eff} of the Si slab waveguide modes versus the thickness of the slab at 1.55µm [127]. Waveguide is cladded with silicon dioxide. The black vertical line represents the single mode condition of 240nm thickness in the slab. The red vertical line represents the slab thickness of 220nm in our case. The black dotted line is the refractive index of the SiO_2 substrate.

samples have an air cladding surface.

Knowing the effective refractive index of the single TE mode in a 1D slab waveguide, we can use this value instead of the refractive index of the dielectric material used in the 2D calculation. As we can see from the previous discussion, the band diagram of the photonic crystal slab so calculated is in good agreement with the results obtained from the three-dimensional calculation. In fact, the combination of the effective refractive index method and 2D calculations has been applied in the design of many photonic crystals, MIR devices [129], including gradient photonic crystals [130].

To summarize, the effective refractive index method combined with the 2D calculation proceeds as follows:

1) Identification and obtaining of the TE fundamental mode in the slab waveguide in the targeted wavelength range.

2) The effective refractive indices of the specific modes (TE or TM) in the slab waveguide at the targeted wavelength are obtained by meshing of the structure and taking into consideration of the vertical slab mode profile.

3) Using the effective refractive index to replace the index of the dielectric material and perform the band diagram calculation. In our case, the Eigenmode calculation method of MPB package from MIT was used [1].

In this thesis, the effective index method is used to model the lens of photonic crystals or photonic crystals devices. Specifically, it is used to calculate the band structure of photonic crystals. By using the EIM, we applied the effective index of Si, that is used in the 2D modelization, accounts for the third dimension of the top Si layer. Thus, the light cone is not necessarily presented in the band diagram. Similar approach can be observed in reference [122, 131]. Finally, we could obtain information on the diameter of air holes at different locations in the photonic crystal. After the modeling is completed, the model is simulated in Lumerical software using 3D FDTD method. This is a 3D model with air holes fabricated on a silicon slab using an deep etching method. We have described the finite difference time domain algorithm in Chapter 1 and will not repeat it here. The simulation results obtained using the 3D FDTD algorithm we will show in Chapter 3.

2.3 Optical wave guides in silicon photonics

As we all know, waveguide optics is based on the electromagnetic theory of the propagation, scattering and polarization of light waves in optical waveguides. It is the theoretical basis to design various optical waveguide devices and fiber optic technology [132, 133]. Specifically in silicon-based materials such as SOI, we need to study the transmission, coupling and interaction of light with external fields. For this purpose, we need to study, in particular, the single-mode conditions and transmission properties in SOI waveguides. This subsection will first introduce the modes of light in two-dimensional waveguides. This will be followed by a description of the types of near-infrared silicon-based waveguides and their single-mode conditions. Finally, the loss of light in waveguides will be briefly described.

2.3.1 Propagation modes in 2D optical waveguides

As an electromagnetic wave, the transmission of light in an optical waveguide necessarily satisfies Maxwell's equations. The material and structural dimensions of the optical waveguide become the boundary conditions for solving Maxwell's equations. Solving Maxwell's equations in an optical waveguide will result in several different sets of eigenvalues and their corresponding eigenfunctions. The eigenvalues are the propagation constants β of the mode in the optical waveguide, and the eigenfunctions are the field distribution of the corresponding electromagnetic field components in the waveguide cross section, which is called the mode in the optical waveguide.

We have derived the analysis of the reduction of Maxwell's equations in Chapter 1. It will

not be repeated here. We directly list the reduced electromagnetic field equations obtained after simplification:

$$\nabla \times \mathbf{E}(\mathbf{r}) = i\omega\mu_0\mathbf{H}(\mathbf{r}) \tag{2.1}$$

$$\nabla \times \mathbf{H}(\mathbf{r}) = -i\omega\varepsilon_0\varepsilon(\mathbf{r})\mathbf{E}(\mathbf{r}) \tag{2.2}$$

In the above equation, ε_0 and μ_0 are the vacuum permittivity and vacuum permeability, respectively; for non-magnetic media, $\mu = \mu_0$. n is the refractive index of the medium and $\varepsilon = \varepsilon_0 n^2$.

In the following, we proceed to solve Maxwell's equations in a two-dimensional planar dielectric waveguide and then analyze the modes of the electromagnetic field in it. The structure of the planar dielectric optical waveguide is shown in Figure 2.8. It consists of a core layer, a substrate and a cladding layer with refractive indices n_1, n_2 and n_3 respectively, and $n_1 > n_2 \geq n_3$. where the thickness of the core layer is d. In a planar waveguide, it can be considered that the width of the layer is much larger than its thickness, so we have

$$\frac{\partial \mathbf{E}}{\partial y} = \frac{\partial \mathbf{H}}{\partial y} = 0. \tag{2.3}$$

For electromagnetic waves propagating along the z-axis direction, they are all independent of y. Assuming that the direction of the electric field is in the y-direction, we can therefore deduce that

$$E_y(x, z, t) = E(x)exp[i(\beta z - \omega t)] \tag{2.4}$$

$$H_x(x, z, t) = H(x)exp[i(\beta z - \omega t)]. \tag{2.5}$$

By substituting equations 2.4 and 2.5 into equation 2.1 and 2.2, we get

$$\begin{cases} \beta E_y = -\omega\mu H_x \\ \dfrac{\partial E_y}{\partial x} = i\omega\mu H_z \\ \dfrac{\partial H_z}{\partial x} = i\beta H_x + i\omega\varepsilon E_y \end{cases} \tag{2.6}$$

$$\begin{cases} \beta H_y = \omega\varepsilon E_x \\ \dfrac{\partial H_y}{\partial x} = -i\omega\varepsilon E_z \\ \dfrac{\partial E_z}{\partial x} = i\beta E_x - i\omega\mu H_y. \end{cases} \tag{2.7}$$

Observing the two systems of equations, one can derive the electromagnetic component E_y, H_x, H_z contained in equation 2.6, where the electric field exists only in the transverse direction. The electric field component does not exist in the direction of wave propagation and is called TE wave (transverse electric field wave); the other group contains electromagnetic

separation H_y, E_x, E_z, where the magnetic field component does not exist in the direction of wave propagation and is called TM wave (transverse magnetic field wave). The electric field of the TE mode of electromagnetic wave only exists in the transverse direction and the electric field component does not exist in the direction of wave propagation; the magnetic field of TM wave exists only in the transverse direction and does not exist in the direction of wave propagation. For TE and TM waves, we have: $E_z = 0$ and $H_z = 0$, respectively.

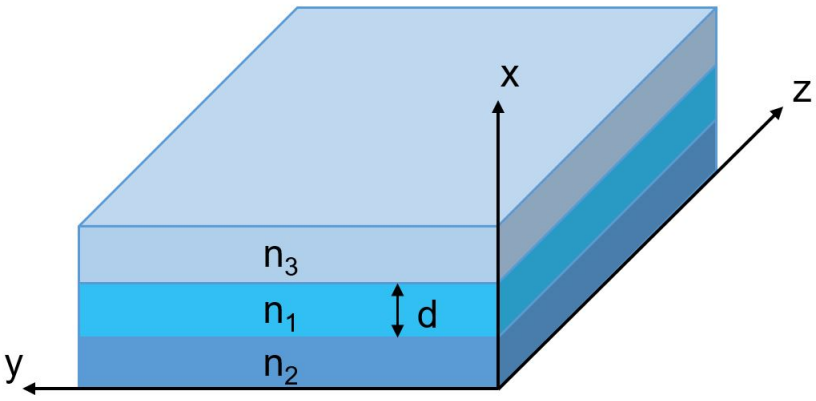

Figure 2.8: 1D planar waveguide.

By substituting them into equation 2.6 and 2.7 for simplification, we can get the fluctuation equations of TE and TM waves as

$$\frac{\partial^2 E_y}{\partial x^2} + (k_0^2 n_j^2 - \beta^2) E_y = 0 \tag{2.8}$$

$$\frac{\partial^2 H_y}{\partial x^2} + (k_0^2 n_j^2 - \beta^2) H_y = 0 \tag{2.9}$$

In the above equation, $k_0 = \omega\sqrt{\varepsilon_0 \mu_0} = 2\pi/\lambda$.

Solving the fluctuation equations under the boundary conditions, we can distinguish the modes of the flat waveguide as i) guided mode ($k_0 n_2 < \beta < k_0 n_1$), ii) substrate mode ($k_0 n_3 < \beta \leq k_0 n_2$) and iii) diffraction mode ($0 \leq \beta \leq k_0 n_3$) depending on the propagation constants β of the obtained solutions.

Only in the guided mode condition, the electromagnetic wave can propagate in the waveguide layer; while in the substrate mode case, the light wave will diffract through the substrate and out of the waveguide layer; and in the diffraction mode case, the light wave will diffract through the substrate and the cladding layer respectively and out of the waveguide layer. Usually, we think that the cladding layer and substrate layer have absorption and scattering effects, which make the loss of light waves significant. Therefore, we want to avoid the substrate and diffraction modes.

According to the form of the solution of the fluctuation equation in the guided mode, we

assume that the electric field inside the layer satisfies the following equations

$$E_y(x) = \begin{cases} A_3 \exp(-\delta x), & 0 \le x < +\infty \\ A\cos(\kappa x) + B\sin(\kappa x), & -d \le x \le 0 \\ A_2 \exp(\gamma x), & -\infty < x \le -d \end{cases} \tag{2.10}$$

The parameter dependence in the above equation is

$$\begin{cases} \kappa = (k_0^2 n_1^2 - \beta^2)^{1/2} \\ \gamma = (\beta^2 - k_0^2 n_2^2)^{1/2} \\ \delta = (\beta^2 - k_0^2 n_2^2)^{1/2} \end{cases} \tag{2.11}$$

Then from the relational equation 2.6 of $H_z(x)$ and $E_y(x)$ and the boundary conditions it is derived that

$$\begin{cases} E_y(0^-) = E_y(0^+) \\ E_y(-d^-) = E_y(-d^+) \\ H_z(0^-) = H_z(0^+) \\ H_z(-d^-) = H_z(-d^+) \end{cases} \tag{2.12}$$

Here we can derive the mode instantiation equation for the flat waveguide TE mode as

$$\tan(\kappa d) = \frac{\kappa(\gamma + \delta)}{\kappa^2 - \gamma\delta} \tag{2.13}$$

In the above equation, κd is a independent variable, and multiple groups of eigenvalue propagation constants and their corresponding field distributions can be obtained by the numerical plotting method. Each set of solutions corresponds to one propagation mode of the waveguide. Similarly, we can obtain the mode eigenvalue equation of TM mode as

$$\tan(\kappa d) = \frac{n_1^2 \kappa(n_2^2\delta + n_3^2\gamma)}{n_2^2 n_3^2 \kappa^2 - n_1^4 \gamma\delta} \tag{2.14}$$

Above we have described the basic approach to waveguide mode analysis. For the analysis of multilayer flat waveguides, wire waveguides, and ridge waveguides, the basic difference with the method of analyzing 2D planar waveguide modes is only the difference in boundary conditions.

2.3.2 Guided light in silicon waveguide

There are various types of waveguides used in silicon-based photonics as illustrated in Figure 2.9. Some of the most frequently used ones are the wire waveguide, the rib waveguide and the slot waveguide. Among these, wire waveguide was used for the optical waveguide in the samples of this thesis. This subsection describes the electromagnetic field modes in these

types of silicon-based waveguides [134] and their single-mode conditions.

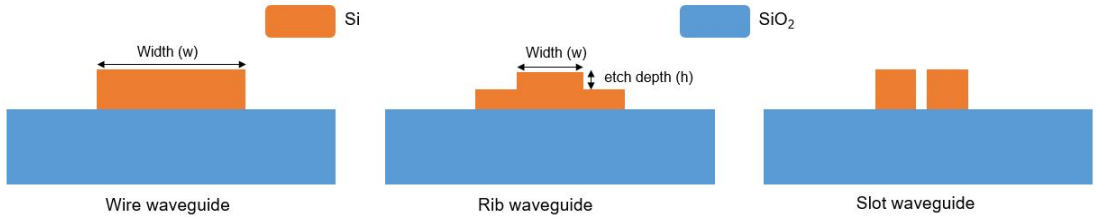

Figure 2.9: Schematic representation of three basic types of silicon waveguides.

a) Wire waveguide Wire waveguide is the most common silicon-based waveguide and it was chosen in this thesis as a medium for optical mode transmission. It is commonly used for routing because of its ease of fabrication and the tight bend radius it may provide. The wire waveguide consists mainly of an upper layer of Si waveguide set on a lower layer of SiO_2 substrate. Sometimes the upper layer of the Si waveguide can be covered with a cladding layer. Modes with an effective refractive index higher than that of the lower SiO_2 substrate will not be radiated into the substrate or the cladding. Such modes will be guided in the silicon waveguide. The profile of the TE fundamental mode at wavelength of 1.55 µm in a 220 nm thick, 500 nm wide waveguide is given in Figure 2.10 (b). Each guided mode propagates

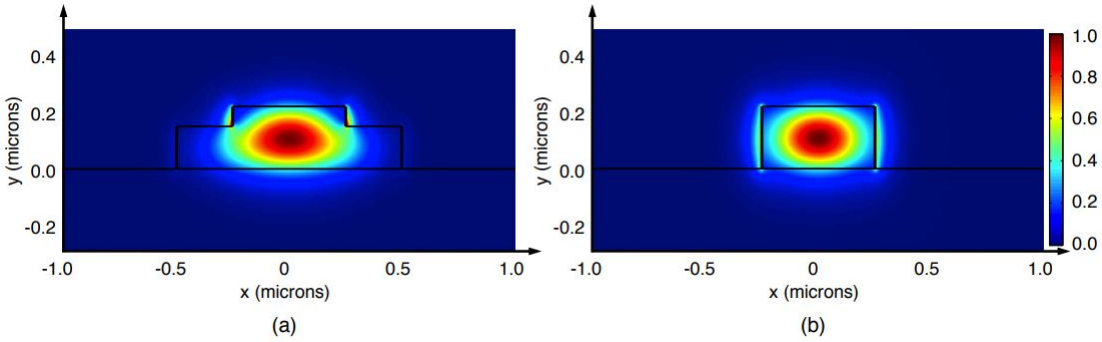

Figure 2.10: Simulated fundamental TE mode profile [135]. (a) Rib waveguide. (b) Wire waveguide.

through the waveguide at a group velocity of $v_g = c/n_{eff}$, where c represents the speed of light in vacuum and n_{eff} is the effective refractive index of the corresponding mode. This group velocity v_g indicates the intensity at which the optical power is confined in the top silicon waveguide.

For wire waveguide, the main parameters are the height and width of the waveguide. For the height, since we choose a silicon layer thickness of 220 nm in the SOI, the height of the silicon waveguide here is also 220 nm. This is also the height chosen for most of the wire waveguides [136–138]. Figure 2.11 gives the variation of effective refractive index with waveguide width w for TE and TM modes of silicon-based waveguide at 1.55µm

wavelength. From the figure, we can see that for 1.55µm wavelengths only the modes above the thick dotted line are guided. And for a 220nm thick wire waveguide, to get a single TE mode at 1.55µm wavelength, the width of the waveguide needs to be around 440nm [139]. Thus, the single-mode filter waveguide in this thesis is chosen to have a width of 450 nm. Subsequently, as the width of the waveguide increases, the number of modes it supports also increases. In applications, wire waveguides can usually be found in integrated optical cir-

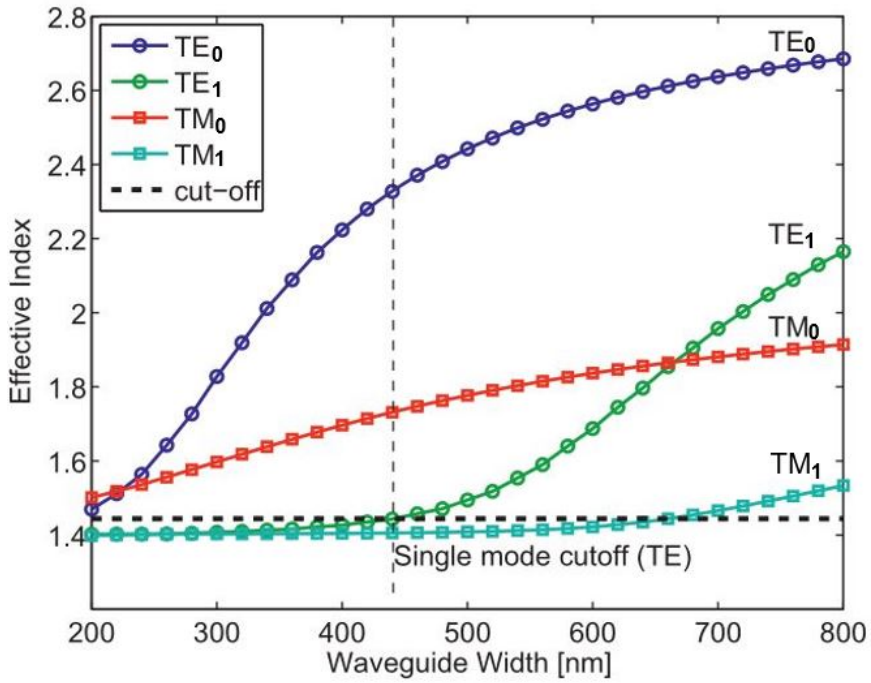

Figure 2.11: Simulation of the effective index n_{eff} of the waveguide modes versus the width *w* of a wire waveguide, for a silicon thickness of 220 nm at 1.55µm [127].

cuits [140, 141] and photodiodes [142]. Also wire waveguides can also be found in on-chip polarization diversity circuits [143]. In addition to applications in passive devices, silicon wire waveguides are also effective application platforms for various nonlinear optical effects [144, 145]. Generally speaking, bulk silicon has weak nonlinear effects. In wire waveguides, however, stronger optical power density is generated due to the tight confinement of light in its core. Therefore the corresponding nonlinear effects can be greatly enhanced. Using this principle, silicon wire waveguides can be used to design phase shifters in Mach-Zehndar interferometers (MZIs) [146].

b) Rib waveguide The rib waveguide has more parameters than the wire waveguide. For a rib waveguide with a width of 500 nm above and 1 µm below and a slab of 70 nm, its TE fundamental mode is shown in Figure 2.10 (a). Since there are two slabs and the connection is at a right angle of 90 degrees, the modes in the rib waveguide will inevitably radiate into the cladding or the air. And for the same degree of bending, the rib waveguide has a greater loss than the wire waveguide [147–149]. The effective refractive index of the mode

with wavelength 1.55µm in the rib waveguide with respect to the top slab width is shown in Figure 2.12, where the thickness of the upper slab is 90 nm and the width of the lower slab is 1µm. It can be seen from the figure that this waveguide does not support the propagation of any TM modes. This type of rib waveguide is generally used in optoelectronic devices such as electo-optic modulators.

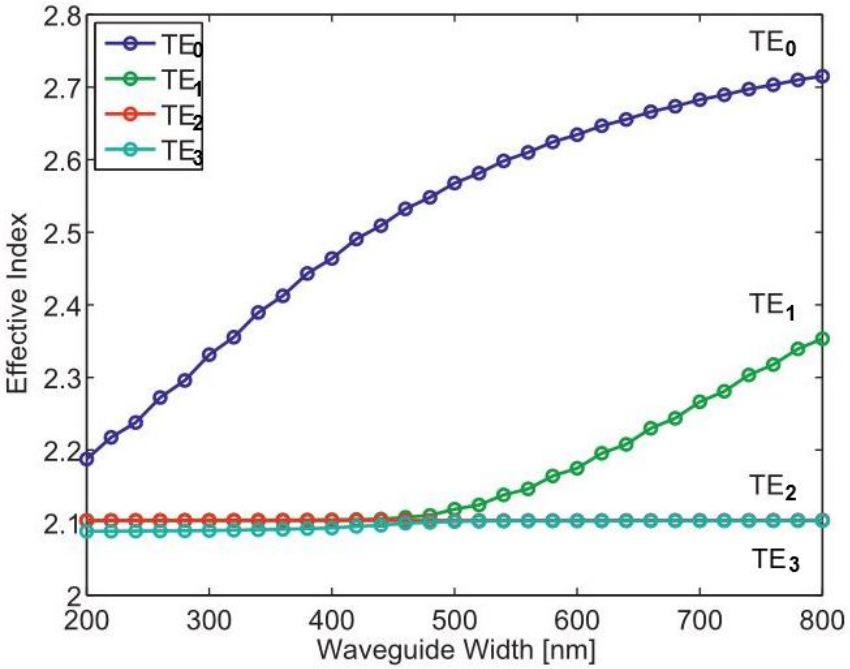

Figure 2.12: Simulation of the effective index n_{eff} of the waveguide modes versus the width *w* of a rib waveguide, for a silicon thickness of 220nm and etch depth *h* of 90 nm at 1.55µm [127].

As described above, the design parameters of the rib waveguide are much more flexible. Through reasonable design and continuous improvement, rib waveguides can be widely used in the infrared domain [150, 151]. In addition, the special structure of rib waveguide makes it more advantageous for particle confinement. The lower sidewall also makes the rib waveguide have a smaller transmission loss. This can be used to propel particles over longer distances and is more favorable for light trapping [152].

c) Slot waveguide The electromagnetic wave modes in both wire and rib waveguides are confined into a silicon medium with a high refractive index. In contrast, for slot waveguide, the guided modes will propagate in cladding or air with a low refractive index. On both sides of the low refractive index medium are silicon-based barriers. A kind of slot waveguide on SOI with 220nm silicon layer is shown in Figure 2.13.

The advantage of slot waveguides can be attributed to the fact that most of the conducted light is confined to the low refractive index region, i.e., between two silicon media. This special structure allows more light to come into contact with the surrounding medium directly.

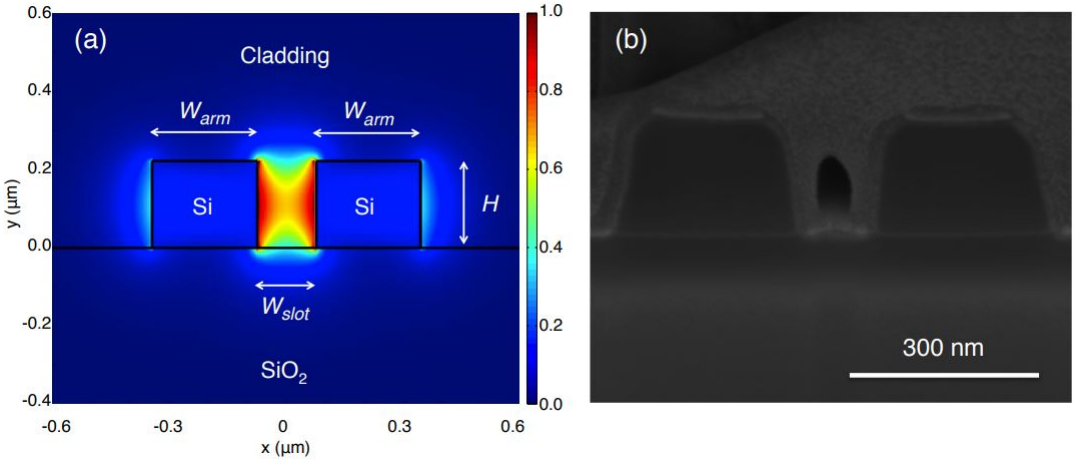

Figure 2.13: Cross section of a slot waveguide. (a) Schematic diagram and the simulated mode profile for the fundamental quasi-TE mode. W_{arm} = 270 nm, W_{slot} = 150 nm, H = 220 nm, and the upper cladding material is silicon oxide. (b) SEM image of the focused ion beam (FIB) milled cross section of a fabricated device [153].

This strong contact will greatly increase the sensitivity of the waveguide so that slot waveguide can be used in optical sensors [154–157]. Besides, slot waveguides can also be used for optical switching [158] and optical amplification [159] in integrated electronics because they can generate high intensity electromagnetic fields in low refractive index media.

2.3.3 Waveguide loss

When light propagates in a waveguide, it undergoes loss due to absorption by the medium, scattering at the interface or radiation of energy outward during propagation. The sources of loss can be divided into three categories: absorption loss, scattering loss and radiation loss. Scattering loss and radiation loss both originate from photons leaving the waveguide and entering free space. These two types of losses play a major role in dielectric waveguides. Absorption losses correspond to photons being absorbed, usually transferring energy to atoms or electrons. This loss plays a major role in waveguides of semiconductor materials.

For several silicon-based waveguides on the SOI platform introduced above, a comparison of their propagation losses can be seen in Table 2.1.

a) Absorption loss

The absorption loss is more significant in semiconductor waveguides. Due to the existence of interband absorption and intraband absorption in semiconductor materials, the optical wave modes are absorbed by interacting with semiconductor materials as they propagate through the waveguide.

When the energy of the photon is greater than the band gap energy, the photon excites the

Table 2.1: Comparison SOI waveguide platforms along with their propagation losses.

Waveguide	Range	Configuration	Propagation Loss
Silicon on silica	Near-IR	Silicon-on-silica wire waveguide	∼0.6 dB/cm [160] (∼1550 and 2000 nm)
	Near-IR	Silicon-on-silica rib (70-nm etch depth) waveguide	∼0.1 − 0.2 dB/cm [160] (∼ 1550 and 2000 nm)
	Mid-IR	Silicon-on-silica rib (70-nm etch depth) waveguide	∼1.5 dB/cm [161] (∼3800 nm)
	Near-IR	Silicon-on-silica slot waveguide	∼2.28 ± 0.03 dB/cm [162] (∼1064 nm)
	Near-IR	Silicon-on-Silica slot waveguide	∼3.7 dB/cm [163] (∼1550 nm)

electrons in the valence band to the conduction band and is thus absorbed by the material. This is called interband absorption [164]. In direct bandgap semiconductors, interband absorption can lead to large absorption coefficients. To avoid the attenuation of waveguide modes due to this loss, optical waveguide modes with photon energies smaller than the semiconductor bandgap can be selected for the application.

The photons in the waveguide can also transfer energy to electrons in the conduction band or holes in the valence band. At this point, the energy of the electron or hole will be excited to a high energy state. This is free carrier absorption, sometimes called intraband absorption [165, 166]. Free carrier absorption also includes absorption losses from the excitation of electrons in the shallow host state near the conduction band, or from the excitation of holes in the shallow acceptor state near the valence band.

b) Scattering loss The scattering loss can be further divided into bulk scattering loss and surface scattering loss. The bulk scattering loss is caused by material defects inside the waveguide. The loss of optical modes per unit length due to this loss depends on the number of scattering centers per unit length and the size of the scattering centers relative to the wavelength [167]. The surface scattering loss is the scattering loss caused by the roughness of the waveguide interface. From the perspective of the ray of light model, the waveguide modes are continuously reflected by the waveguide interface as they propagate through the waveguide [168]. And higher order modes experience more interface reflections for the same propagation length compared to lower order modes. Therefore, the higher-order modes are scattered by the interface with more energy than the lower-order modes and the interface scattering loss is greater.

c) Radiation loss

The energy of the waveguide mode can also be lost from the waveguide by means of

radiation, also known as radiation loss [169]. For wire waveguides, the radiation loss of the lower order modes away from the cutoff condition can generally be neglected. However, for higher-order modes beyond the cutoff condition, the energy of the waveguide mode is coupled to the radiation mode outside the waveguide. For regular waveguides, the waveguide modes are orthogonal to each other with no energy coupling. But for waveguides with irregular shapes or inhomogeneous materials, the energy of the lower order modes can be lost by coupling to the higher order modes and then coupling from the higher order modes to the radiation modes.

In addition, for curved waveguides, the radiation loss of the waveguide mode increases dramatically [170]. As the radius of curvature of the waveguide gradually increases, the radiation loss of the waveguide gradually decreases. When the radius of curvature of the waveguide tends to infinity, the waveguide becomes a straight waveguide. At this point, the radiation loss of the waveguide tends to zero. The phase velocity at each point of the straight waveguide is the same constant, so it can develop into a stable wavefront.

2.4 Conclusion

In this chapter, we first introduced the fabrication platform applied in this thesis, i.e., SOI. Subsequent subsections were shown for the preparation method and specific parameters of SOI. The SOI with 220 nm thick silicon layer from SOITEC is used in our experiments, and then I introduced different optical coupling methods for silicon photonics. The final method chosen in this thesis is the edge coupling method. The second subsection of this chapter describes specifically the effective refractive index method used in the thesis. This is a computational method that uses two-dimensional calculations to approach three-dimensional structures. This method was chosen for this thesis to calculate the band diagram of a slab photonic crystal. And the effective refractive index of the single TE mode in the Si slab is $n_{eff,TE} = 2.845$ for 1.55µm. The results of the calculations will be shown later in Chapter 4. The third subsection of this chapter described in detail the different kinds of waveguides in silicon photonics. Starting from the principles of propagation modes in two-dimensional optical waveguides, I showed the optical modes in different kinds of optical waveguides and their corresponding single-mode conditions. The wire waveguide were used in this thesis as a medium for optical mode transmission. And the single mode condition of the width w of wire waveguide for TE mode at 1.55µm is around 440nm. This value will also be taken into consideration in the single mode filter in the final fabricated device. Finally, I briefly introduced the optical loss in different kinds of waveguides and their principles.

Chapter 3

Design and simulation of GPC lens for infrared domain

Contents

Gradient index lens have attracted a lot of attention, and there is a great deal of research being applied to this field, from invisibility cloaks and illusion devices to planar lenses [171, 172]. Again, refraction at the interface between air and glass, for example, can be designed to produce high quality lenses by designing the shape of the interface. Alternatively, the refractive index of a medium can be varied spatially to control the length of the optical path in a region, resulting in a gradient index (GRIN) optical element.

GRIN optical elements are well known, but less common than refractive optical elements because of the difficulty of producing large, controlled index variations in conventional materials. However, GRIN optics is notable because some GRIN lens designs exist that correspond to perfect imaging instruments, usually based on a spherical or cylindrical symmetric inhomogeneous refractive index distribution [173]. At the same time, integrated silicon photonics is promising in a variety of fields, including optical communications [174], sensors [175], and quantum photonics [176], due to the unique advantages of high integration density, low cost, and compatibility with semiconductor (CMOS) manufacturing processes [177].

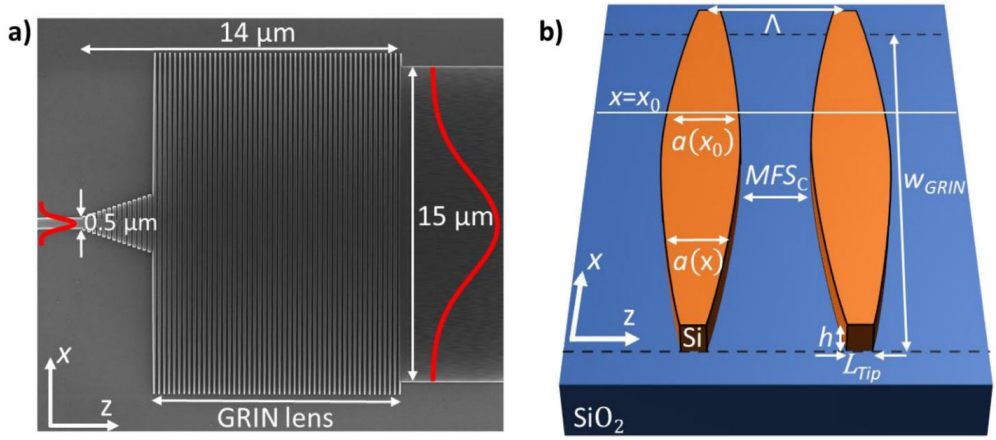

Figure 3.1: (a) Scanning electron microscopy (SEM) image of the proposed spot size converter. (b) Schematic of the subwavelength structure. Its effective structure is fabricated on the SOI platform done by J.M.Luque-González et al [88].

Also, it is well known that gradient refractive index optics in the near-infrared band are mainly limited by the processing means. The emergence of EBL technology is a good solution to this need. At the same time, the SOI platform naturally becomes a perfect carrier for gradient refractive index optics in the near-infrared band because of its high fit with semiconductor processing technology. J.M.Luque-González et al. designed and processed a SOI-based gradient refractive index lens (See Figure 3.1) [88]. In their work, they demonstrated the use of anisotropic subwavelength gratings SWG-based GRIN materials to achieve ultracompact, robust, and efficient spot size converters. The whole structure was fabricated in a 220nm thick SOI platform. The buried oxide (BOX) and the upper SiO2 cladding are

2 µm and 2.2 µm thick, respectively. Similarly, L.H.Gabrielli proposed and implemented an on-chip Luneburg lens by varying the thickness of the silicon layer in the SOI and thus its effective refractive index (See Figure 3.2) [178]. In their work, the device was fabricated on a Silicon-On-Insulator (SOI) wafer with 250nm top Si layer and 3µm buried SiO_2. Focused ion beam (FIB), inductively coupled plasma reactive ion etching (ICP-RIE) and plasma-enhanced, chemical vapor deposition (PECVD) were used in the fabrication process.

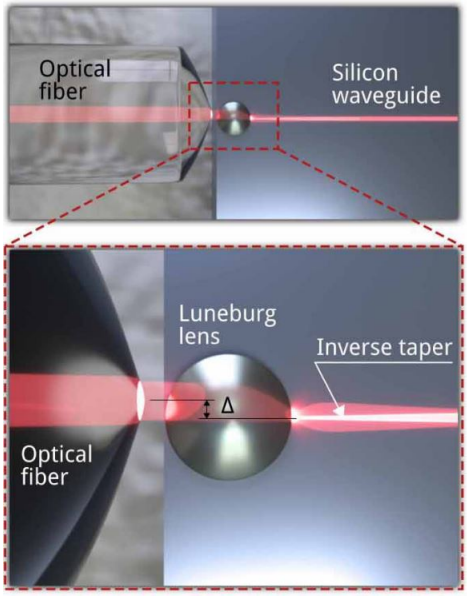

Figure 3.2: Up: A lensed fiber is used to couple light into the silicon waveguide. Down: Zoomed-in illustration ofthe coupling region. The device had the ability to provide improved tolerance in fiber-to-chip optical links for future communication networks [178].

Due to the limitations of the implementation technology, most gradient refractive index lenses at optical frequency can only focus light in the plane, and have no effect on the light from the third dimension. However, Y.-Y. Zhao et al. designed and experimentally implemented a three-dimensional Luneburg lens operating in the near-infrared wavelength band [179]. They reported the experimental implementation of a 3D Luneburg lens in the infrared band fabricated by a Femtosecond laser direct writing (FsLDW) technique (See Figure 3.3). Based on their proposal, the 3D Luneburg lens was designed and fabricated with multilayered GRIN 3D simple cubic metamaterial structures working at optical frequencies.

In this chapter, we will first introduce the design guidelines for flat lens in SOI platforms. And then we will introduce the design and simulation of square lattice and hexagonal lattice photonic crystal lens respectively according to the lattice shape. Among them, the flat lens designed in the second band of the hexagonal lattice are fabricated and characterized. Finally, we will present the design and simulation of a Half Maxwell fisheye lens in the near-infrared band.

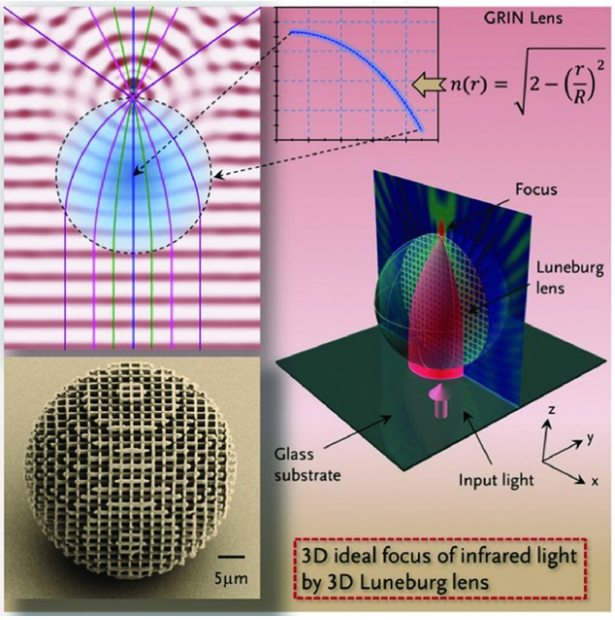

Figure 3.3: Right: Schematic representation of an ideal focus for 3D Luneburg lens. Left: Ray tracing of an ideal Luneburg lens and scanning electron microscope images of the 3D Luneburg lens. Simulated and experimental results simultaneously exhibit interesting 3D ideal focusing performance of the 3D Luneburg lens for the infrared light at the wavelength of 6.25μm [179].

3.1 Principles of flat GPC lens on SOI

Research on photonic crystal lens has been going on for a long time [38, 122, 180]. And the research on gradient refractive index lens is even earlier [181–183]. The combination of these two concepts gave rise to the concept of gradient photonic crystal lens [56]. The design of the gradient refractive index photonic crystal lens in this thesis is based on the design elements of the previous O.Pinchuk's article [184]. They proposed a design method for metamaterial-based gradient effective index lens. Through their research, they showed that there is an equation that evolves the effective index of the medium as a function of the properties of the flat lens to be designed (see Equation 3.1).

$$n(R) = n(0) - \frac{\sqrt{f^2 + R^2} - f}{d} \tag{3.1}$$

This is a simplified model of the gradient index lens, the advantage of which is that the designed lens is bidirectional. It can both focus and collimate light. In the equation above, $n(0)$ is the index in the center of lens. And f is the focus length, d is the thickness of lens, R is the distance to the center of lens. From this equation we can see that for a converging lens (regardless of positive or negative refractive index), the absolute value of its refractive index decreases from the center to the edge (see Figure 3.4).

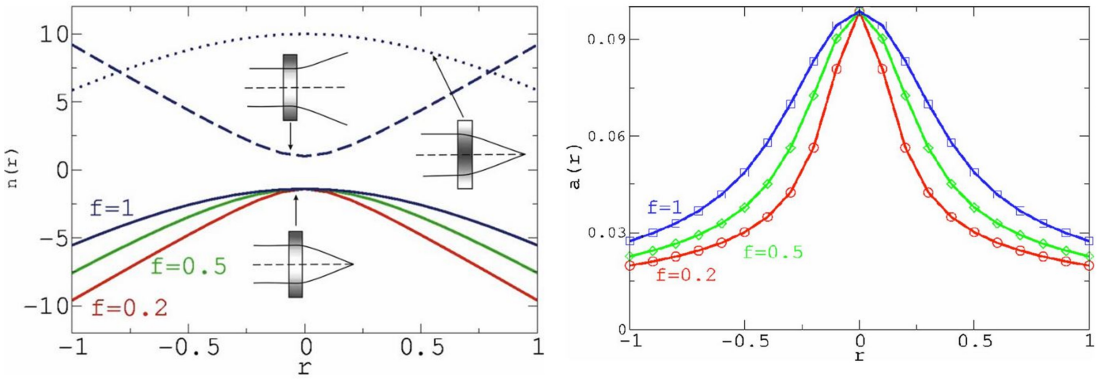

Figure 3.4: Right: Effective index profile of a gradient index lens. Left: Profile of the diameters of the holes as a function of the distance from the optical axis. [184]

Also, the work of F. Gaufillet, a previous PhD student within this group [185], has provided much useful information for this thesis. The operating frequencies of the flat lens he designed are mainly focused on the microwave band [71] (See Figure 3.5). The two-dimensional FDTD simulations demonstrated the effectiveness of the designed lens. For the experimental demonstration, printed circuit board material and metallic wires were used as the dielectric medium [72].

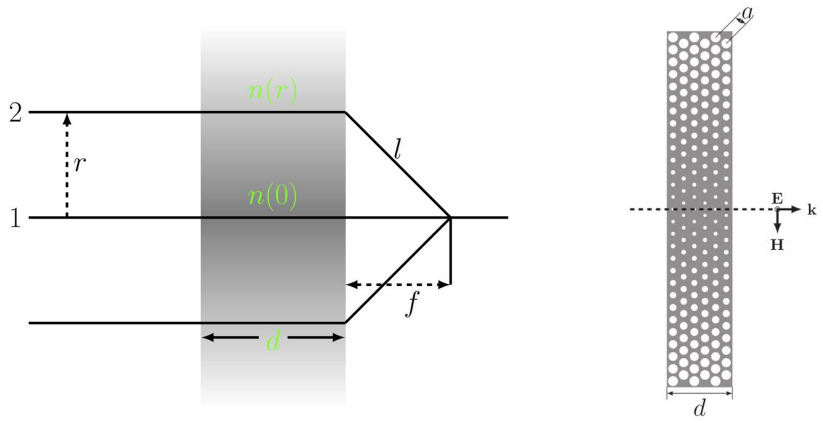

Figure 3.5: Right: Gradient-index lens which behaves as a phase compensator, that is, all the incident parallel rays converge towards the focal point with the same optical path. Left: Sketches of the two 2D graded photonic crystal lens which consists of six layers of air holes in dielectric medium. [71]

In this thesis, the lens operated in the near-infrared band at 1.55µm. At this wavelength, perfect plane waves were not readily available. We use the TE fundamental mode in a 10µm wide waveguide as the incident light. It can be approximated as a plane wave. TE is chosen instead of TM because the effective refractive index of the silicon-based waveguide for TE mode is greater than that of TM mode in the near-infrared band. This allows a better confine-

ment of light in silicon waveguides. The lattice constant a of the photonic crystal also needs to be carefully chosen when designing the size of air holes to accommodate a larger range of effective refractive index variations.

Due to the limitation of fabrication means in the NIR band, etching air holes in the silicon layer will be used as the main means in this thesis. This is because the processing difficulty of etching air holes is significantly lower than that of etching Si columns. Another reason is that the NIR light has to be confined to the silicon-based waveguide structure as much as possible. If silicon pillars were chosen, then a significant portion of the light would be scattered into the air.

In this thesis there are two main lattice structures, the square lattice and the hexagonal lattice. The filling factors of the air holes of both lattices can be found in

$$\eta_{\text{square}} = \frac{\pi \times D^2}{4 \times a^2} \tag{3.2}$$

$$\eta_{\text{hexagonal}} = \frac{2}{\sqrt{3}} \times \frac{\pi \times D^2}{4 \times a^2}, \tag{3.3}$$

where D is the diameter of the corresponding air holes and a is the period of square or hexagonal lattice. Combining Equation 3.1-3.3 with the curve, we finally derived for the variation of the refractive index with the radius of the air hole, we can obtain the size of the air hole at different locations.

3.2 Flat GPC lens with square lattice

This section will focus on the design and simulation of a flat lens of a square lattice photonic crystal. For the calculation of the energy band and EFC of the photonic crystal, we use the MPB open package [1] from MIT mentioned in Chapter 1. For the subsequent simulation part, we used the FDTD method (using the software and solver package Lumerical) to perform 3D simulations of the device.

3.2.1 Normalized frequency chosen in the 1st band of square lattice

In square lattice photonic crystals, the case where the normalized frequency is chosen to be in the first band is the most common. It is well known that the equi-frequency curves in the first band are generally circular. This meets our expectations very well. It is relatively easy to start this thesis with it. Therefore, we will first introduce this case in this subsection. For subwavelength devices, the relationship between structure size and operating wavelength is very important. Here we take the normalized frequency. It is defined as follows, where a is

the lattice period of photonic crystal.

$$\varpi = a/\lambda \tag{3.4}$$

Design method and modeling

At a given r/a, the first band does not overlap with the other bands. Therefore, we only plotted the first band to make it clearer. From Figure 3.7 we can conclude that the first band curve gradually shifts upward as the filling factor of the air holes increases.

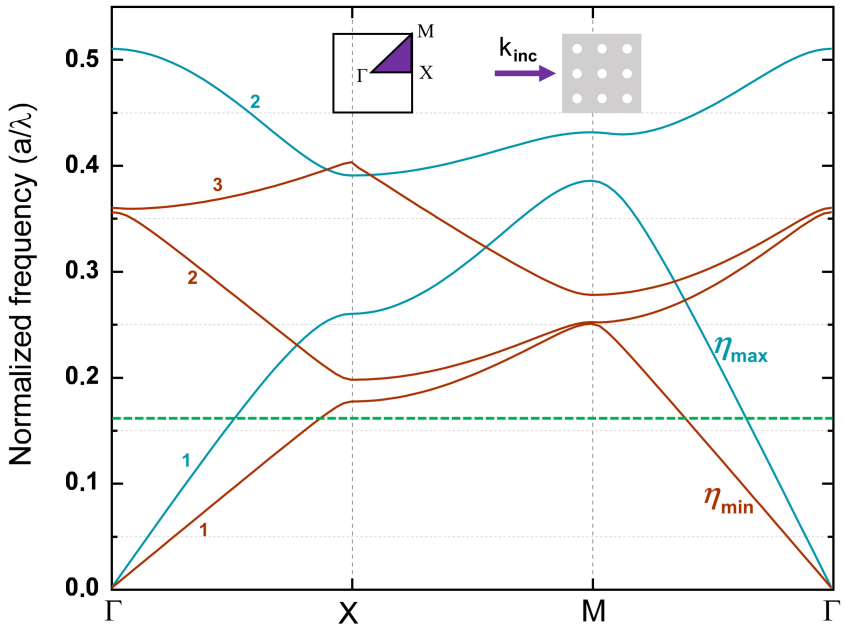

Figure 3.6: The band structure of square lattice photonic crystal with two selected filling factor $\eta_{min} = r/a = 0.16$ and $\eta_{max} = r/a = 0.45$. The green dashed line is the chosen normalized frequency $\varpi = a/\lambda = 0.168$.

From the band diagram, we can basically determine the value of the lattice constant to be selected. On the one hand, the selected lattice constant should not be too small and should not put pressure on the fabrication latter. On the other hand, the selected lattice constant should not be too large to make the corresponding r/a selectable range too small. Here we choose a lattice constant of 260nm, which means that the normalized frequency is ϖ=0.168. As can be seen from the Figure 3.7, this normalized frequency is close to satisfy the maximum of EFC with circular shape. The corresponding effective refractive index at this point can be selected from the maximum range. The band structure of two final selected filling factors is plotted in Figure 3.6. Next, we calculated the equi-frequency curve at this normalized frequency. The equi-frequency curves allow us to determine whether the photonic crystal can be considered as an isotropic homogeneous medium.

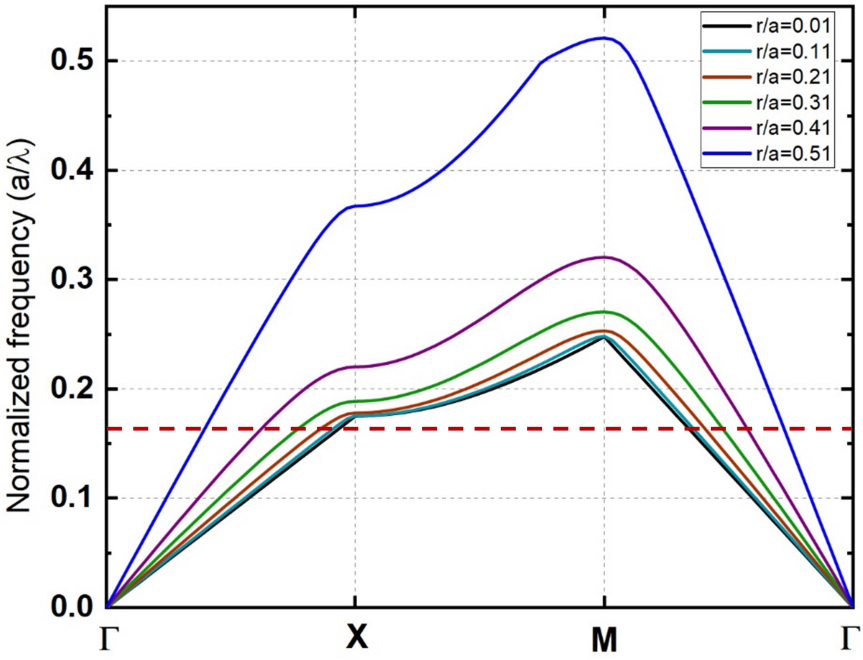

Figure 3.7: The 1st band structure of square lattice photonic crystal with different ratio r/a for TE mode, where r is radius of air holes and a is lattice constant. The red dashed line is the chosen normalized frequency $\varpi = 0.168$.

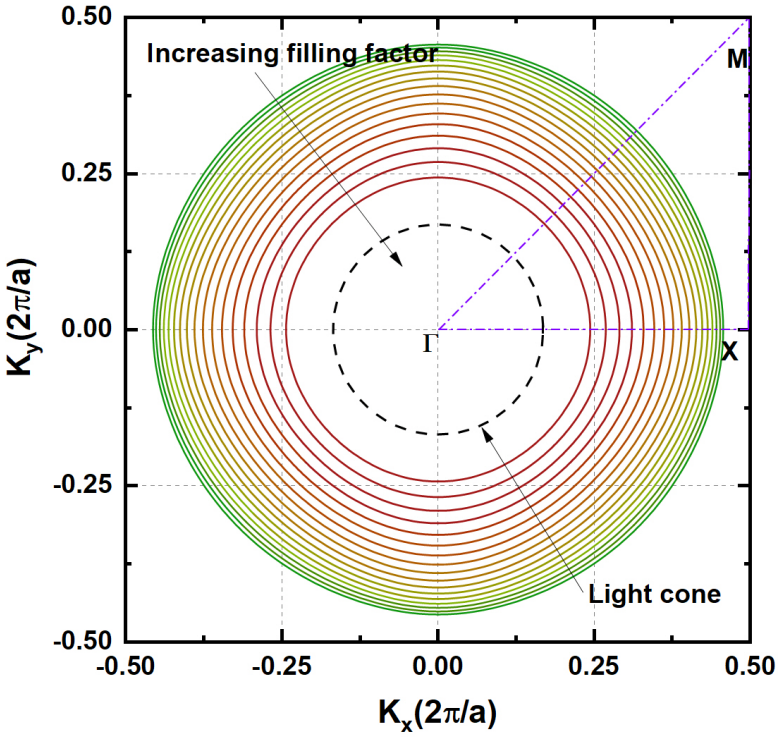

Figure 3.8: The EFC diagrams for normalized frequency $\varpi = 0.168$ in the 1st band of square lattice photonic crystal. The radius of EFC is decreasing with increasing of air filling factor.

As we expected, the equi-frequency curves of the first band obtained from the calculation are circular (See Figure 3.8). And the radius of the equi-frequency curve decreases with the increase of the air hole radius. For such homogeneous medium, we derived a curve (See Figure 3.9) of its effective refractive index as a function of the air hole radius and air filling factor η using Curve Fitting in Matlab

$$n_{\text{eff}} = -7.255\left(\frac{r}{a}\right)^3 - 2.29\left(\frac{r}{a}\right)^2 - 0.0776\left(\frac{r}{a}\right) + 2.823 \tag{3.5}$$

$$= -7.255\eta^3 - 2.29\eta^2 - 0.0776\eta + 2.823. \tag{3.6}$$

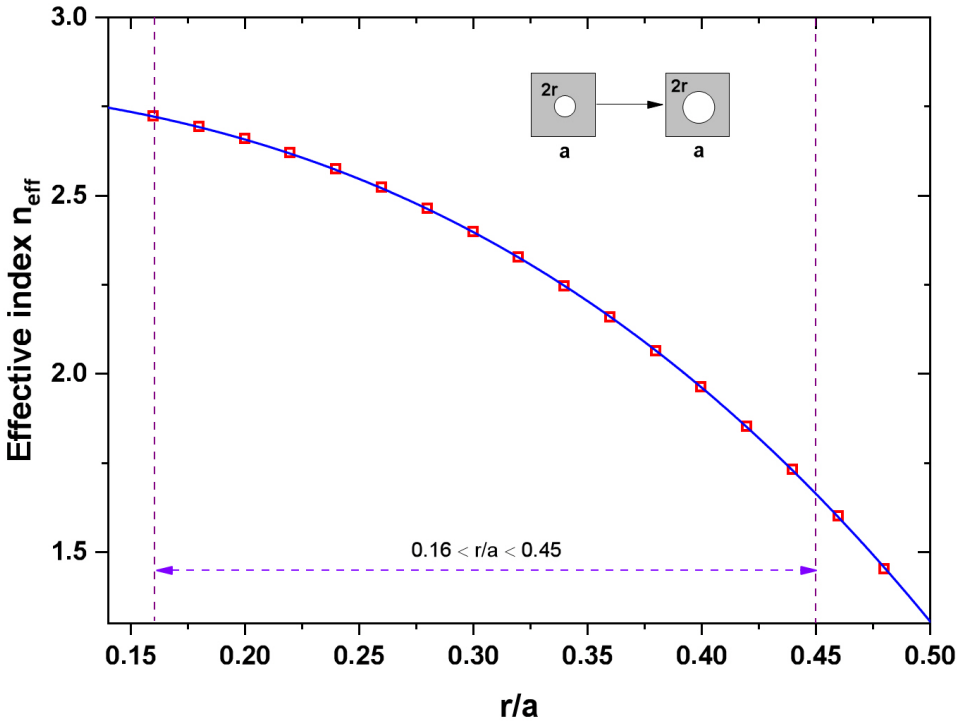

Figure 3.9: The deduced curve of the fist band of square lattice, which is the relationship of the effective index with the filling ratio r/a.

Combining with the previous design Equation 3.1 for focusing lens, we obtained the radius distribution of the air holes. In this case of the first band of the square lattice, we designed the lens with a width of 1.8µm and a length of 6µm. It consisted of 7 vertical rows of etched air holes. The smallest air hole in the lens was located in the middle of the lens, and its radius was approximately 41nm. The largest air holes were located at the top and bottom edges of the lens, and its radius was approximately 117nm.

The thickness and length of the lens here were smaller compared to the lens we designed later. This is due to the relatively low position of the first band of the square photonic crystal for TE mode. And the normalized frequency is smaller than in the case of the second band. Thus, we have chosen a smaller lattice constant. This in turn affected the size of the subsequent lens design.

Numerical simulation results

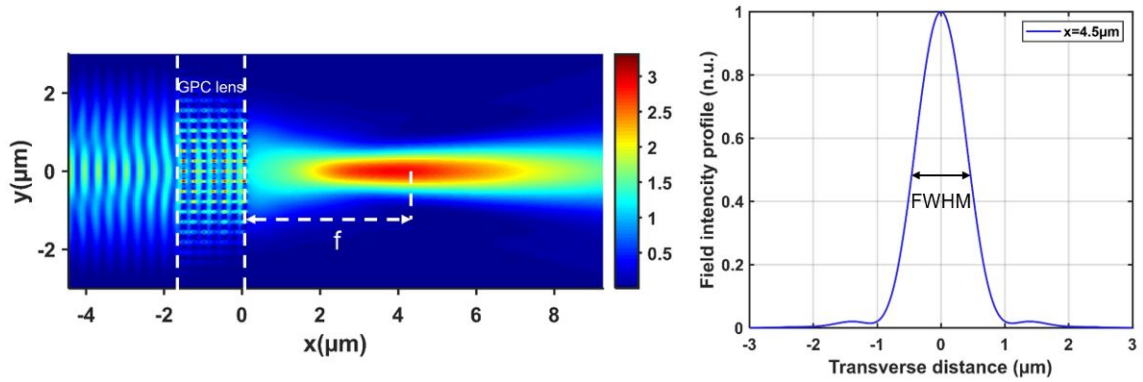

Figure 3.10: Left: $|E_y|^2$ distribution of the TE fundamental mode at 1.55μm in the 1st band of designed flat GPC lens with square lattice. The focus length is $f = 4.2m$. Right: The $|E_y|^2$ field intensity distribution along y direction at the focus point. FWHM = 0.895μm.

The 3D simulation results using Lumerical FDTD show that the designed lens is able to focus the incident light (See Figure 3.10). In silicon-based photonics in the near-infrared band, the used modes are confined in a silicon waveguide. The mode in the waveguide is actually an approximate Gaussian spot rather than a plane wave. In the first band of a square photonic crystal, we have designed a lens with a length of 6μm, so that the width of the incident waveguide is approximately 6μm. In this case the whole lens is more like a mode-size converter. Meanwhile, the FWHM at the focal point is $FWHM = 0.895\mu m = 0.577\lambda$, here $\lambda = 1.55\mu m$. This is a smaller value because the mode width of our incident light is only 6μm. Therefore, the converging focal point naturally has a narrower point.

In our 3D FDTD simulation, the modes of the yz-plane are also taken into account. From Figure 3.11 we can see that the modes in the yz-plane at the input interface are also focused after passing through the lens.

Other simulations of the point source were used to verify the collimation function of the lens. For this purpose, a TE-mode point source was placed at the focal point of the lens. The simulation results in Figure 3.12 demonstrate that the lens can collimate the point source to an approximate plane wave.

It is important to note here that the point source used in the simulation is a perfect point source. In fact, it is difficult to obtain a perfect point source on a silicon wave guide in the NIR band. Therefore, in the later fabrication we have used the method that appeared before [186] to approximate an on-chip point source.

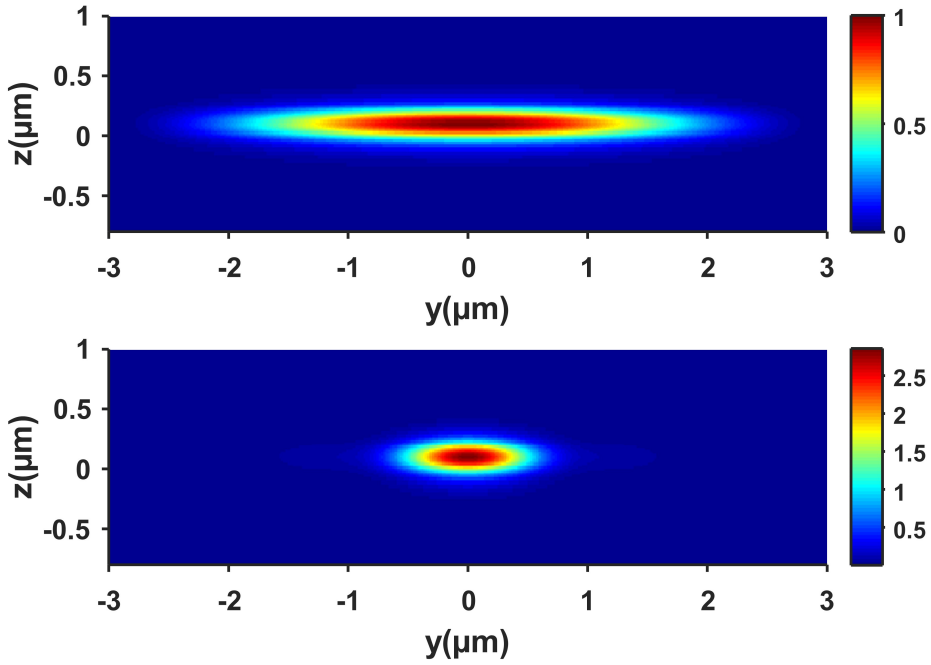

Figure 3.11: The $|E_y|^2$ field intensity distribution in yz plane at λ=1.55μm in the 1st band of square lattice. (a) The field intensity distribution at the input interface. (b) The field intensity distribution at the focus point.

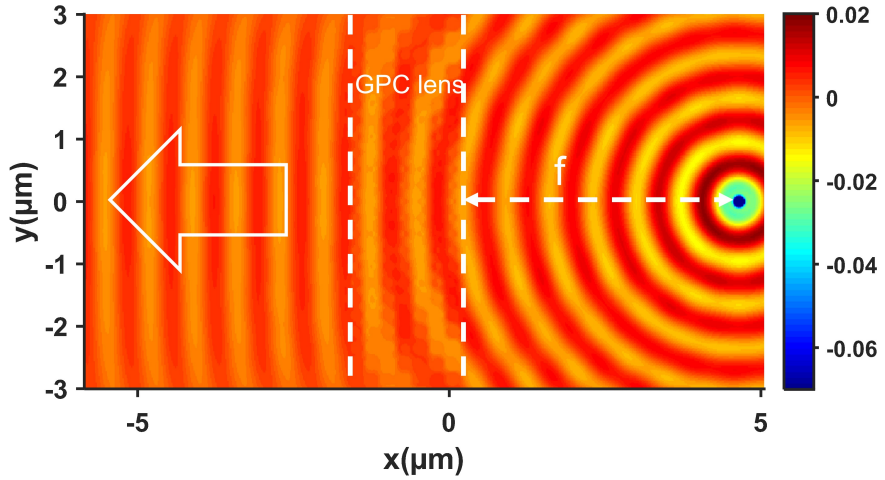

Figure 3.12: The diagram of H_z field distribution when the incident wavelength is λ=1.55μm for TE point source. The normalized frequency ϖ is in the 1st band of square lattice.

3.2.2 Normalized frequency chosen in the 2nd band of square lattice

This part will focus on the case where the normalized frequency is in the second band. As in the previous case, the desired operating wavelength is 1.55μm, so that we need to modify the periodic lattice constant to change the normalized frequency to be in the second band.

Design method and modeling

The first thing to do is to look at the band diagram of a square lattice photonic crystal (see Figure 3.13). In the band diagram, we can derive a reasonable range of normalized frequencies.

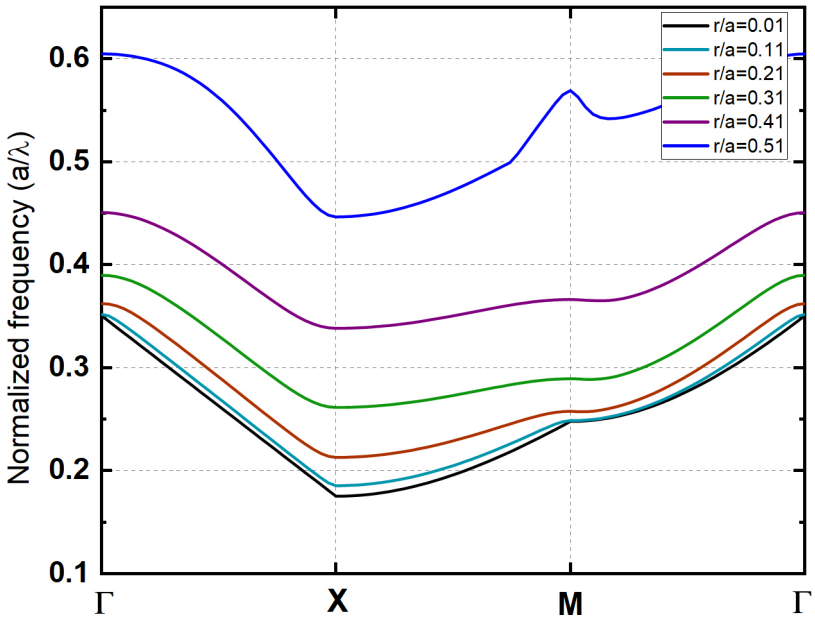

Figure 3.13: The 2nd band structure of square lattice photonic crystal with different ratio r/a for TE mode, where r is radius of air holes and a is lattice constant.

From the second band, we can see that in order to select the largest possible range of air hole radius, the range of normalized frequencies ϖ is roughly 0.25-0.35. In this range, we have chosen several normalized frequencies, i.e. different lattice constants a. In the next step we calculate the EFC diagram (see Figure 3.14) and proceed with the analysis.

The EFCs of square lattice photonic crystal are illustrated in Figure 3.14 for four different normalized frequency at the second band. Their shapes are more like square than circle. Thus, for other normalized frequencies in the second band of the square lattice, the EFC would also resemble a square shape, which means it is not a homogeneous medium. We could clearly see that with different lattice periods, that is to say different normalized frequencies ϖ, we got different shapes of EFC in second band. Back to the band structure, we could find that at the point Γ, the corresponding normalized frequency is not the same. This is unlike the first band in which case the frequency is all zero at Gamma point.

More importantly for a non-homogeneous medium, we cannot find a global effective refractive index to model it. Therefore the normalized frequency in the second band of the square lattice is not suitable for our design requirements.

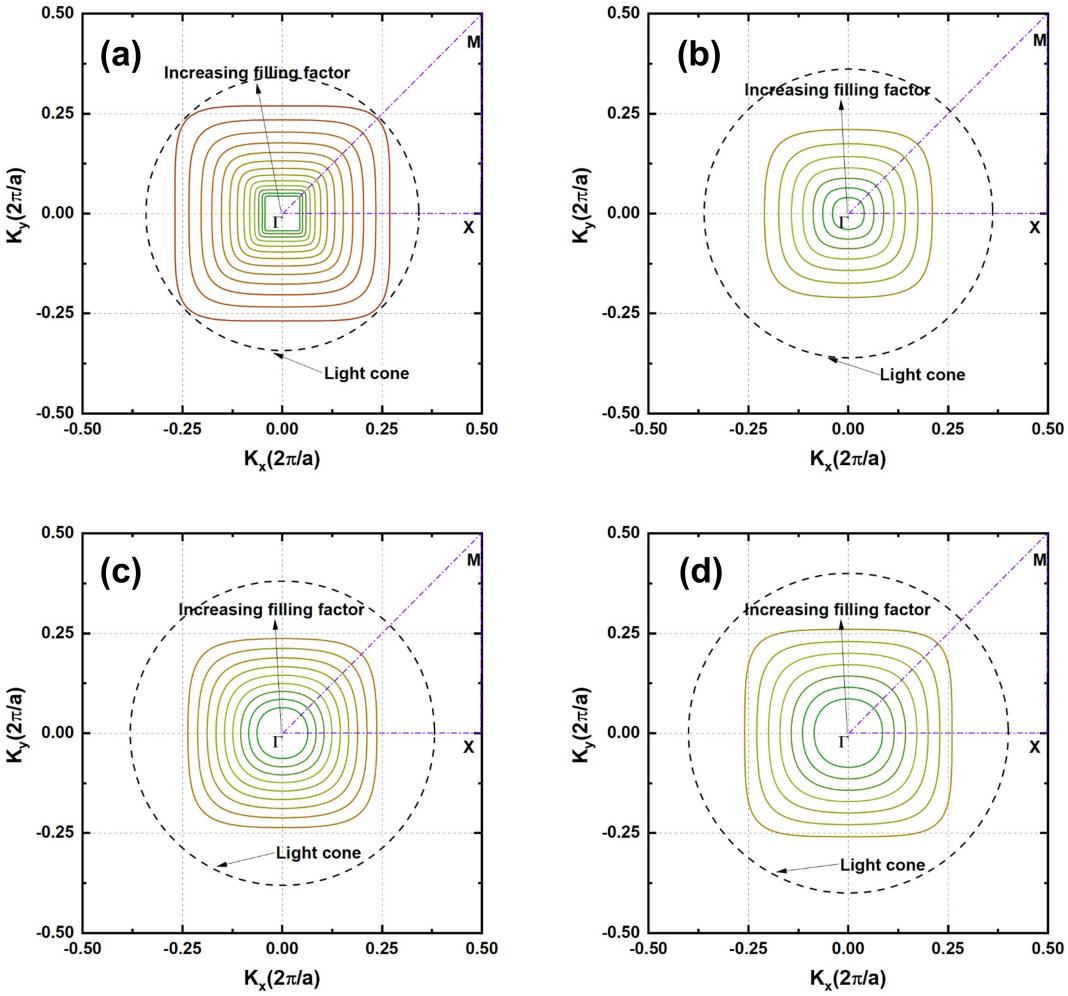

Figure 3.14: EFC diagram for different normalized frequency ϖ in the 2nd band of square lattice. (a) a=530nm, ϖ=0.342, r/a from 0.1 to 0.36. (b) a=560nm, ϖ=0.361, r/a from 0.22 to 0.34. (c) a=590nm, ϖ=0.381, r/a from 0.30 to 0.38. (d) a=620nm, ϖ=0.4, r/a from 0.35 to 0.41. It is clear that these EFCs are not circular.

3.2.3 Conclusion of square lattice GPC

This subsection focuses on the design and simulation of square lattice graded photonic crystals. For a graded refractive index photonic crystal lens with normalized frequency in the first band, it had a circular equi-frequency curve. Therefore, it can be used as a homogeneous medium and obtain an effective refractive index. And then, we derived the effective refractive index from the EFC as a function of the air hole radius. For the designed flat lens, the simulation results of the FDTD algorithm showed that it can focus and collimate the light well. Therefore, it is a 'real' lens that can work in the near-infrared band. For the case where the normalized frequency was in the second band, the EFC obtained from our calculation was square rather than circular. Therefore, the PCs lens in this case was not a homogeneous medium and thus was not considered in our design.

In the design simulation of the square lattice lens, we can get two important hints:

- Since our target working band is near-infrared band, it is difficult to obtain plane waves. We need to carefully choose the width of the incident waveguide so that the mode of the incident light is an approximate plane wave. This indirectly determines the length of the lens that we can design.

- Similarly, for the collimation function, the design and selection of the on-chip point source must be taken seriously.

These two points are also to be anticipated when designing the lens later. At the same time, these two issues are well addressed in the design and final processing of the hexagonal lattice lens.

3.3 Flat GPC lens with hexagonal lattice

This section will focus on the design and simulation of hexagonal lattice flat gradient photonic crystal lens. Like the previous case of the square lattice, here again we used the MPB package [1] for the band diagram and EFC calculations. Subsequently, we used the 3D FDTD of the Lumerical software for the simulation.

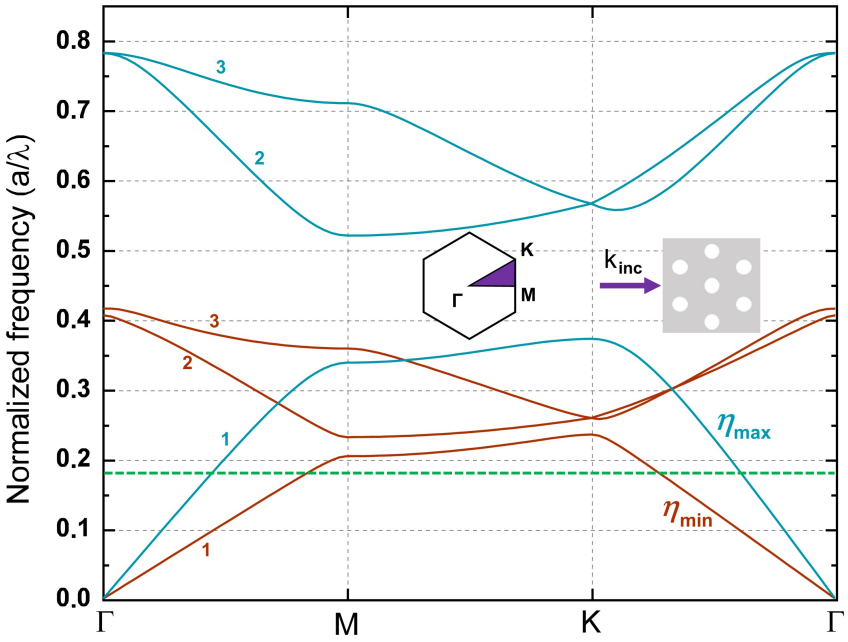

Figure 3.15: First three band structures ($\eta_{max} = 0.46$ and $\eta_{min} = 0.16$) of hexagonal lattice photonic crystal. The green dashed line indicates the normalized frequency ϖ=0.187 in the 1st band.

3.3.1 Normalized frequency chosen in the 1st band of hexagonal lattice

This subsection will focus on the case when the normalized frequency is in the first band of the hexagonal lattice photonic crystal. We will see that, like the first band of the square lattice mentioned earlier, the EFC is also circular in the first band of the hexagonal lattice. Afterwards, we have used the 3D FDTD simulation in Lumerical. The TE fundamental mode in the 10μm waveguide is used as a source for near plane waves.

3.3.1.1 Design method and modeling

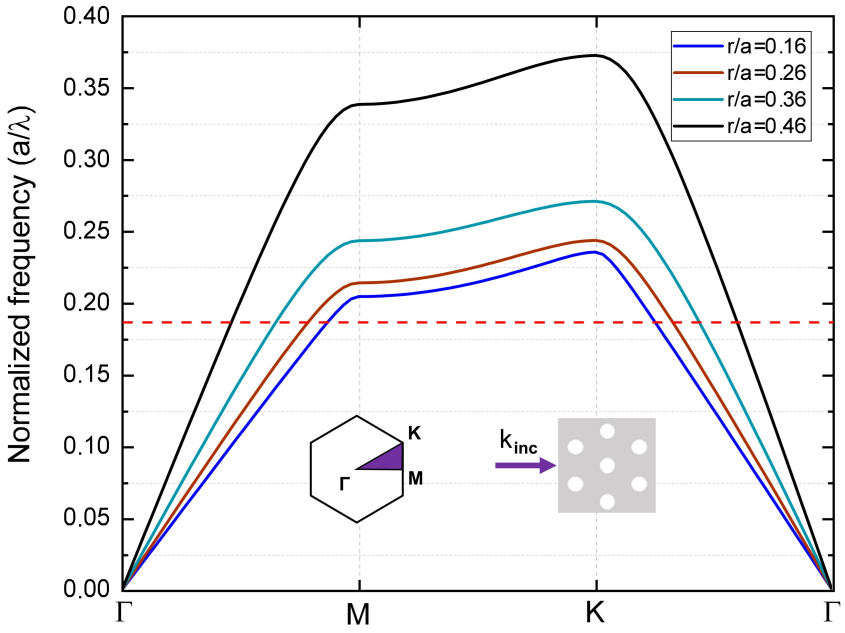

Figure 3.16: The 1st band structure of hexagonal lattice photonic crystal with different ratio r/a from 0.16 to 0.46, which r is the radius of air holes and a is the lattice constant. The red dashed line indicates the normalized frequency ϖ=0.187.

We first calculated the band diagram of a hexagonal lattice photonic crystal. Here we show only the first band part for the sake of clarity (See figure 3.16). It is known that the first band exists independently without overlapping with the other bands.

The normalized frequency of 0.187 is chosen from the energy band diagram. And the fabrication constraints are also taken into account, so the range of r/a=0.16 to 0.46 is chosen in the band diagram. The normalized frequency of 0.187 implies a lattice constant of 290nm. We then calculated the EFC at this normalized frequency. As can be seen in Figure 3.17, the EFC in the first band is approximately circular. From this, we can deduce a curve of the

effective refractive index as a function of the air hole radius (See Figure 3.18)

$$n_{\text{eff}} = -2.213\left(\frac{r}{a}\right)^3 - 6.117\left(\frac{r}{a}\right)^2 + 0.269\left(\frac{r}{a}\right) + 2.814 \tag{3.7}$$

$$= -2.213\eta^3 - 6.117\eta^2 + 0.269\eta + 2.814. \tag{3.8}$$

Combined with the previous principles of planar lens design, we derived the diameter of the air hole from the center to the edge of the lens. The smallest air hole in the lens was located in the middle of the lens, and its radius was approximately 52nm. The largest air holes were located at the top and bottom edges of the lens, and its radius was approximately 132nm.

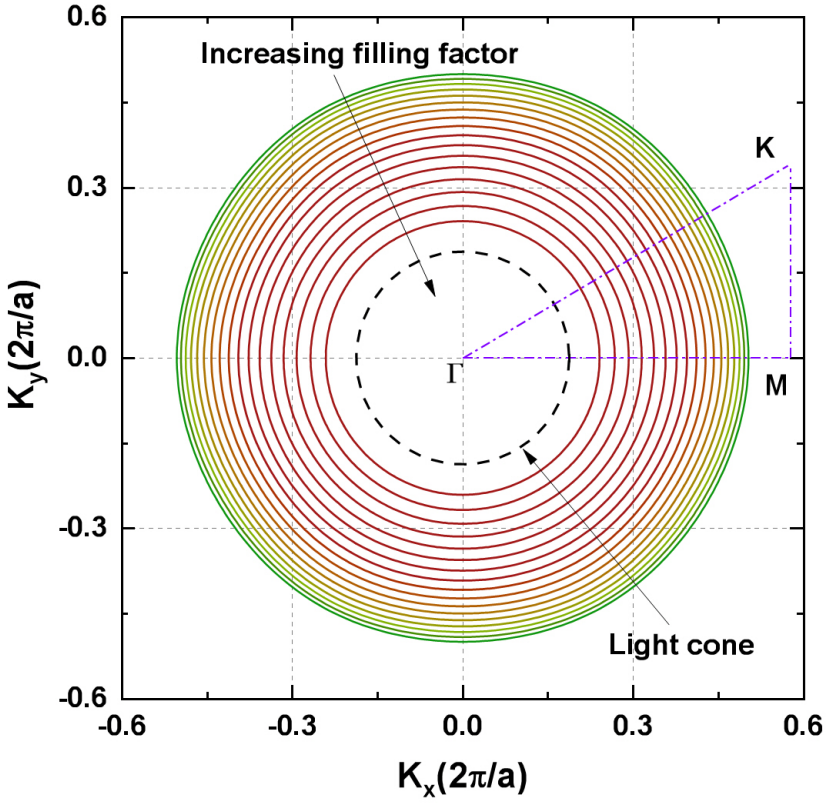

Figure 3.17: The EFC diagrams for normalized frequency $\varpi = 0.187$ in the 1st band of hexagonal lattice photonic crystal. The radius of EFC is decreasing with increasing of filling factor η.

3.3.1.2 Numerical simulation results

From Figure 3.19, we can see that the designed lens has a focusing effect on plane waves with a wavelength of 1.55μm. The focal point is located at approximately $x = 9\mu m$. The thickness of the lens is $d = 3.3\mu m$. So the focal length is approximately $f = 7.5\mu m$. The full width at half maximum at focal point is $FWHM = 1.35\mu m = 0.87\lambda$, here $\lambda = 1.55\mu m$.

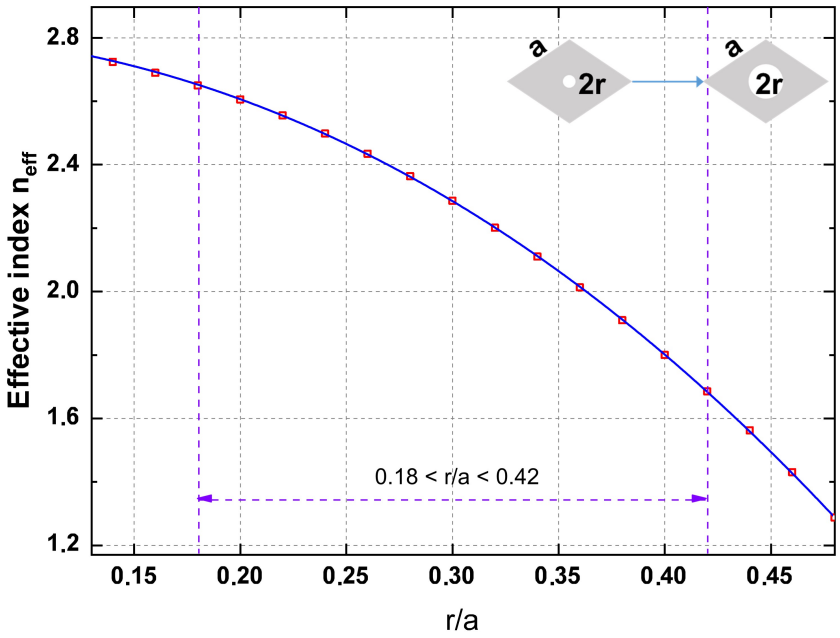

Figure 3.18: Calibration curve deduced from the EFCs at normalized frequency ϖ=0.187 in the 1st band of a hexagonal lattice. The useful part is η = r/a $\in$ [0.18, 0.42].

We also studied the electric field intensity distribution in the yz-plane. From Figure 3.21 we can conclude more intuitively that the lens focuses plane waves. Also, from Fig. 3.21 (a) we can see that the incident approximate plane wave is actually a mode with intensity into a Gaussian distribution. It has the maximum intensity at the center and the minimum intensity at the edges.

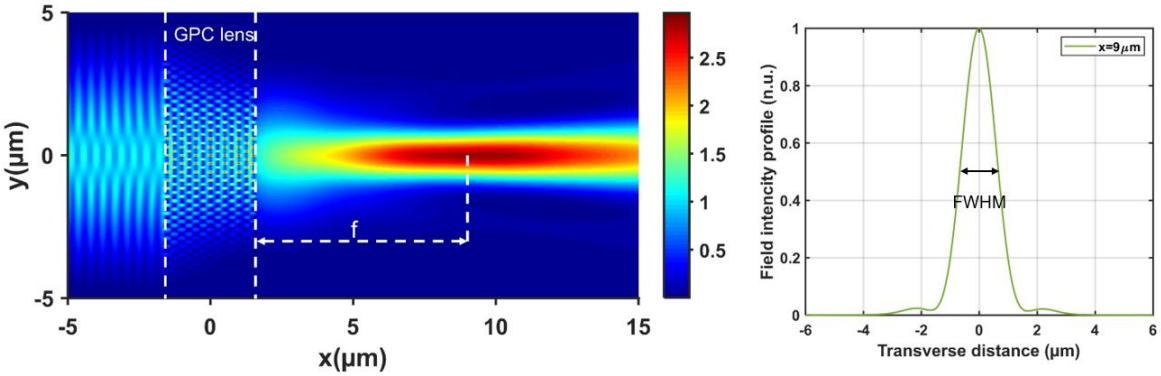

Figure 3.19: Left: $|E_y|^2$ distribution of the TE fundamental mode at 1.55µm (1st band) in the designed flat GPC lens with hexagonal lattice. The focus length is $f = 7.6m$. Right: The $|E_y|^2$ field intensity distribution along y direction at the focus point for incident $\lambda = 1.55\mu m$. FWHM = 1.35µm = 0.87λ.

The simulation of point light sources was also taken into account (See Figure 3.20). A point light source of TE mode was placed at the focal point of the lens. Through the simu-

lation, we found that an approximate plane wave was emitted at the exit surface of the lens. This demonstrated that our flat lens is capable of collimating the light from the point source into a plane wave.

Although the lens operating in the first band of the hexagonal lattice photonic crystal were not finally chosen for fabrication, much of the Half Maxwell-fisheye lens we covered later comes from here. Because the half Maxwell-fisheye lens discussed later is also normalized to the frequency in the first band of the photonic crystal, and it is also a hexagonal lattice.

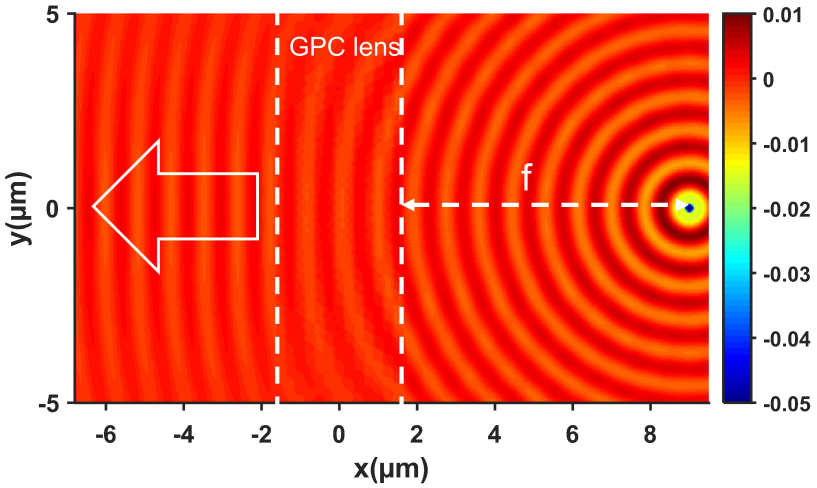

Figure 3.20: The H_z field distribution of designed hexagonal lattice GPCs lens when the incident wavelength is λ=1.55μm (1st band) for TE point source.

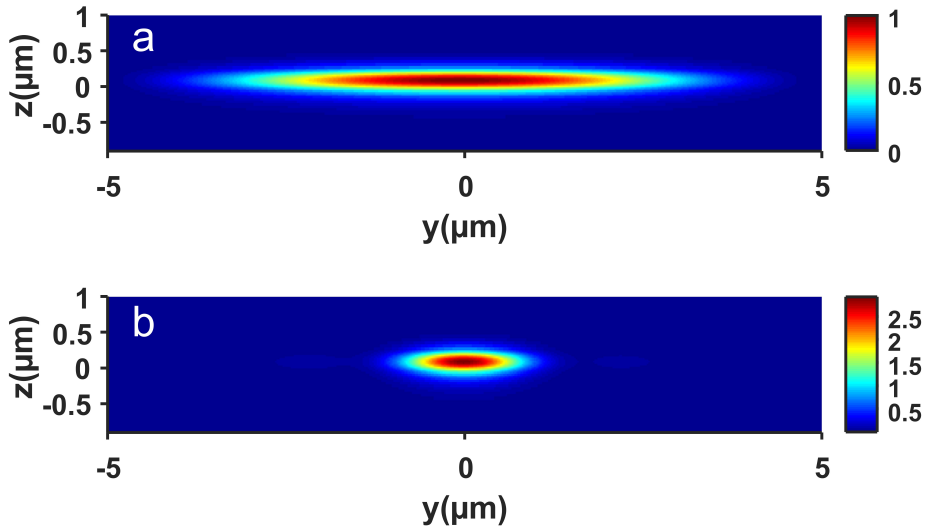

Figure 3.21: The $|E_y|^2$ field intensity distribution in yz plane at λ=1.55μm (1st band) of designed hexagonal lattice GPCs lens. (a) The field intensity distribution before incidence. (b) The field intensity distribution at the focus point.

3.3.2 Normalized frequency chosen in the 2nd band of hexagonal lattice

This subsection will focus on the design and simulation of hexagonal photonic crystals when the normalized frequency is in the second band of hexagonal lattice. The designed GPCs lens has a negative effective index at this point. This is also the case where the final choice of fabrication and characterization is made in this thesis.

3.3.2.1 Design method and modeling

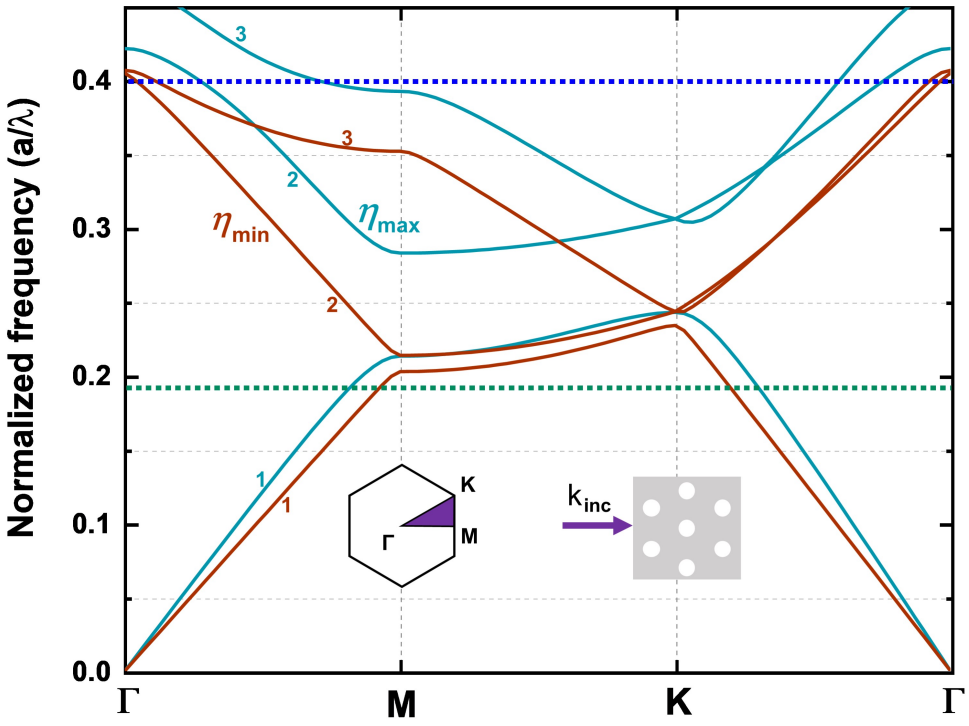

Figure 3.22: First three bands ($\eta_{max} = 0.26$ and $\eta_{min} = 0.1$) of hexagonal lattice photonic crystal. The blue dashed line is the normalized frequency 0.4 in the 2nd band and the green dashed line is the normalized frequency 0.194 in the 1st band.

First three bands of hexagonal lattice photonic crystal with extremal value of filling factor $\eta_{max} = 0.26$ and $\eta_{min} = 0.1$ are shown in Figure 3.22. The blue dashed line indicates the target normalized frequency $\varpi = 0.4$, which is in the second band. The green dashed line indicates another operating frequency $\varpi = 0.194$, which is in the first band. The incident wave vector k_{inc} is along the $\Gamma - M$ direction. Figure 3.23 is the second band extracted separately with different filling factor $\eta = r/a$. It shows that the larger it is for the same value of the r/a interval, the larger the gap between the different band lines. Therefore, we need to find a circular EFC region, but with a large range of r/a. It is difficult to find such a shared region if the band line with the same interval value of r/a rises very quickly. That is, the variation of the derived effective indices will be small.

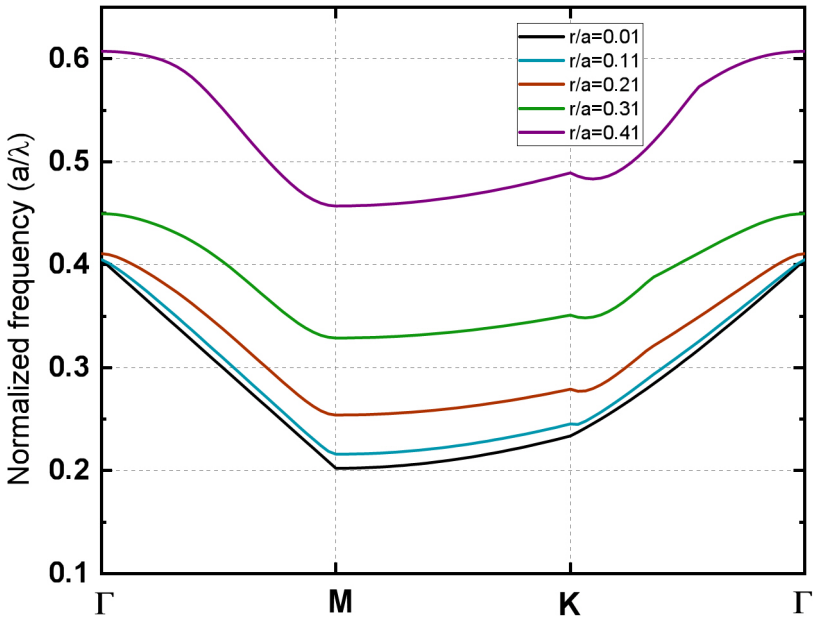

Figure 3.23: The 2nd band structure of hexagonal lattice photonic crystal with different filling factor $\eta = r/a$ from 0.01 to 0.41, where r is the radius of air holes and a is the lattice constant.

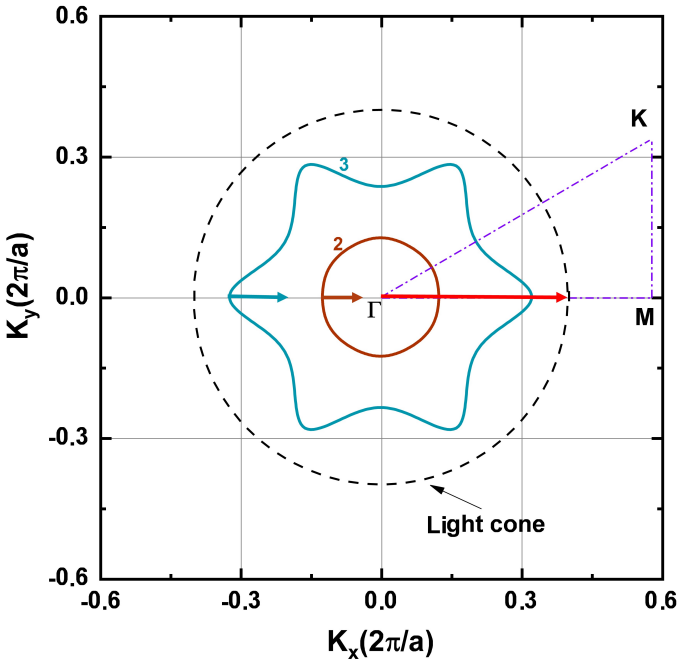

Figure 3.24: The EFC for the 2nd and 3rd band when the filling ratio $r/a = 0.24$ at normalized frequency $\varpi = 0.4$. The red arrows represent the wave vectors for incident wave and the brown and blue arrow represent the refractive waves for 2nd and 3rd band.

This is critical to the design of the graded index lens. We choosed different lattice periods

on the basis of the band diagram which were: a=500nm, 550nm, 600nm, 620nm, 635nm, 650nm. The corresponding normalized frequencies were:ϖ=0.323, 0.355, 0.387, 0.4, 0.41, 0.419. The EFCs corresponding to these normalized frequencies helped us to choose the appropriate case, that is, $\varpi = a/\lambda = 0.4$ (See Figure 3.26).

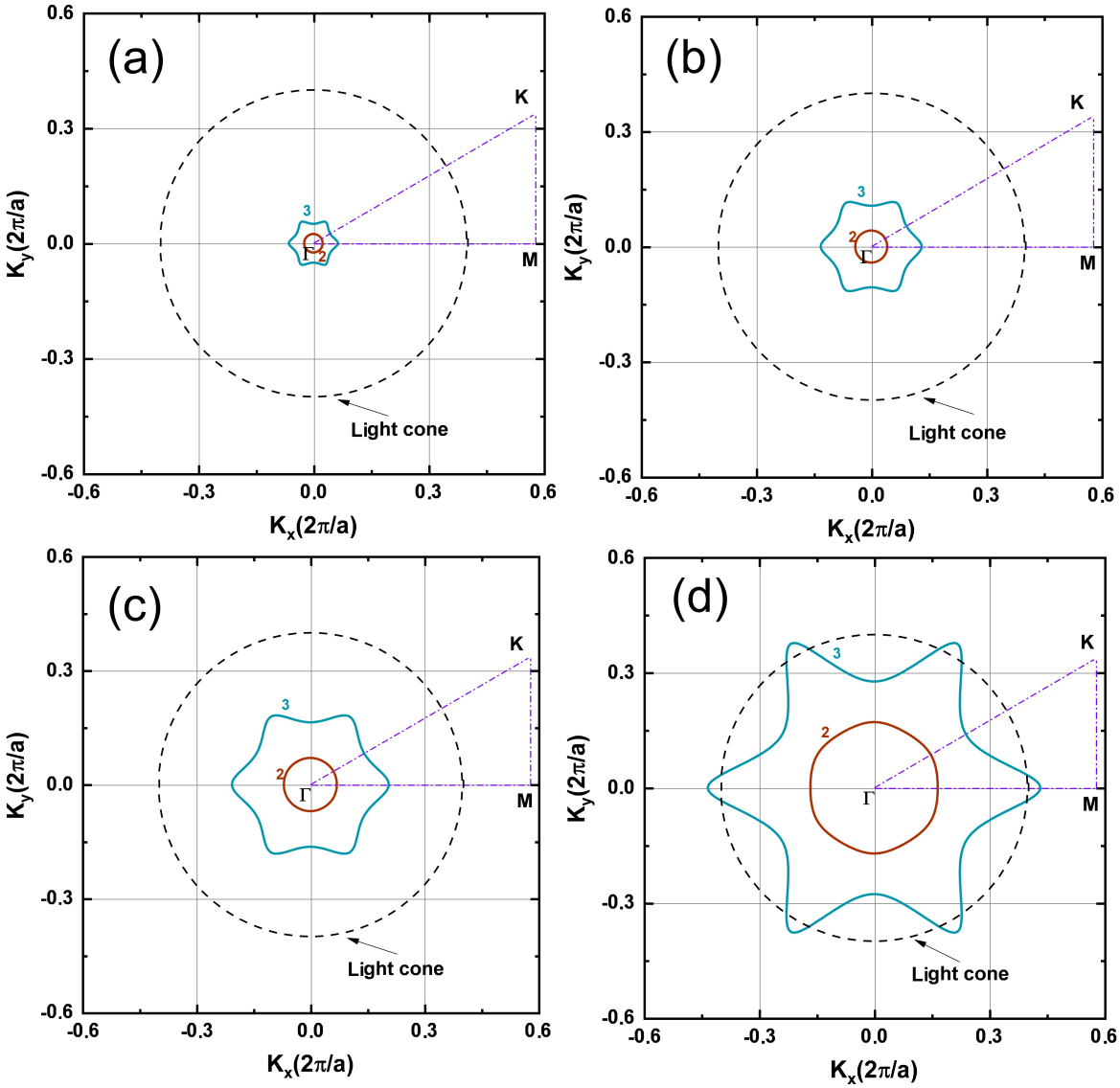

Figure 3.25: The EFC of the 2nd and 3rd band at normalized frequency $\varpi = 0.4$ for different filling ratio r/a. (a) $r/a = 0.1$. (b) $r/a = 0.16$. (c) $r/a = 0.2$. (d) $r/a = 0.26$.

From the band diagram we also can see that there are two bands at the normalized frequency 0.4. We therefore plotted the EFC diagram for different filling factors separately (see Figure 3.24 and 3.25). From the EFC diagram we can draw:

- In Fig. 3.24, when the incident direction is Γ-M, the intersection of the third band is at a cusp position. In other words, this mode is highly divergent [187]. In gradient

photonic crystal lens, the propagation vector of light changes direction gradually due to the gradient of index. When the wave vector changes gradually, the mode of the second band also changes gradually. But the mode of the third band will suddenly change the direction of propagation and will diverge.

- The second band is approximately circular. So for this mode, the photonic crystal is equivalent to a homogeneous isotropic medium. The third band is star-shaped, so photonic crystals cannot be regarded as homogeneous isotropic media for this mode, and thus do not have an equivalent effective refractive index. Therefore, it does not contribute to the lensing effect [188].

Figure 3.26 gives us lots of information of the impact of normalized frequency to the shape of EFC in the second band. It turns out that the shape of the EFC becomes relatively square or hexagonal depending on the shape of the lattice. For a certain value of r/a, the area within the EFC decreases as the normalized frequency increases. This is because it is closer to the Γ point in this case. For certain values of the normalized frequency, increasing the filling factor of the air holes is expected to increase the area inside the EFC. In this case, EFCs with larger fill factors are more like circular shape compared to EFCs with smaller fill factors.

Another important information we noticed was: as the normalized frequency ϖ increases, the range of scales r/a available will be narrowed. This will have a negative impact on our lens design, because we need a wide enough range of filling factor to meet sufficient size variance between different air holes in the lens. Too small range of filling factor would be extremely challenging to later fabrication.

Therefore, we need to compromise between keeping the EFC approximately circular and having the largest possible filling factor range. In this thesis, I have chosen lattice period a=620nm. Because at this normalized frequency, the shape of the EFC is relatively circular. At the same time we can have a relatively large filling factor range to make subsequent fabrication process easier.

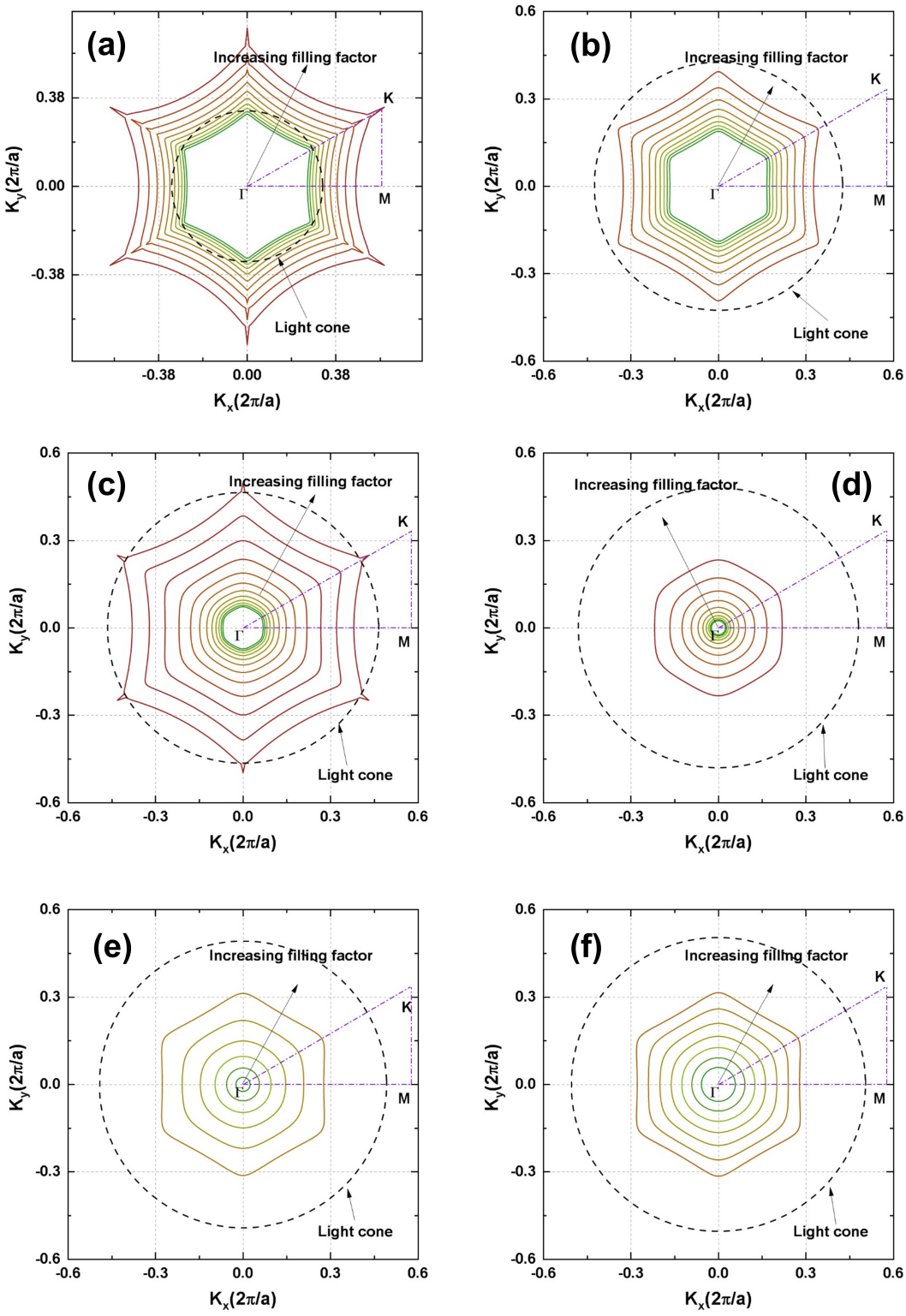

Figure 3.26: EFC diagrams for different normalized frequency ϖ in the 2nd band of hexagonal structure. (a) a = 500nm, ϖ = 0.323, r/a from 0.1 to 0.28. (b) a = 550nm, ϖ = 0.355, r/a from 0.1 to 0.26. (c) a = 600nm, ϖ = 0.387, r/a from 0.1 to 0.22. (d) a = 620nm, ϖ = 0.4, r/a from 0.1 to 0.28. (e) a = 635nm, ϖ = 0.41, r/a from 0.21 to 0.31. (f) a = 650nm, ϖ = 0.419, r/a from 0.26 to 0.32.

The deduced curve

The EFC allows us to derive the relationship curve between the effective refractive index and the air hole radius (See Figure 3.27). The derived equation is:

$$n_{\text{eff}} = -77\left(\frac{r}{a}\right)^3 + 25\left(\frac{r}{a}\right)^2 - 3.3\left(\frac{r}{a}\right) + 0.095 \tag{3.9}$$

$$= -77\eta^3 + 25\eta^2 - 3.3\eta + 0.095 \tag{3.10}$$

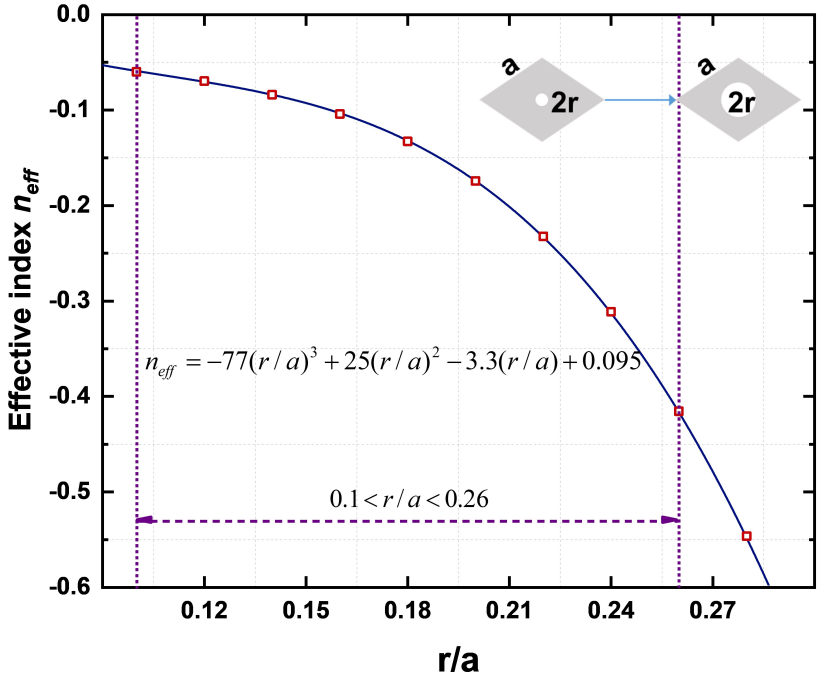

Figure 3.27: The deduced curve is the relationship of the effective index with the filling ratio r/a. (2nd band)

From the derived curve, we can see that the absolute value of the effective refractive index of the lens increases as the radius of the air hole increases. However, since the normalized frequency is in the second band, its effective refractive index is negative. Based on the relationship between the effective refractive index and the radius of the air holes, combined with the previous equation 3.1 for the graded index lens, we can then calculate the size of the air hole at any position of the lens.

3.3.2.2 Numerical simulation results

The subsequent simulations were computed in Lumerical using 3D FDTD. Suitable meshes were selected in the simulations for better resolution. The boundary condition is PML (Perfect Match Layer) and the light source is selected as a TE fundamental mode light source in a 10µm wide waveguide. SOI platform with a top 220nm silicon layer on a 3µm silica

substrate has been taken into consideration. For the point source, the TE mode point source of Lumerical FDTD is used.

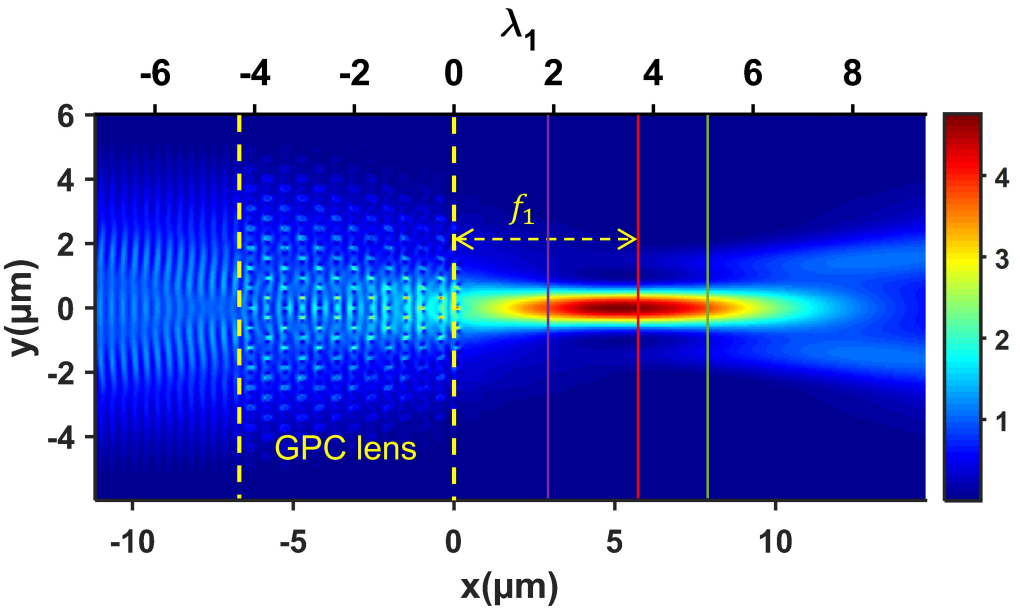

Figure 3.28: The $|E_y|^2$ field intensity distribution when the incident wavelength is λ_1=1.55μm (2nd band of hexagonal lattice) for TE fundamental mode light source. The focal point is located approximately at f_1=5.9μm from the lens' exit plane.

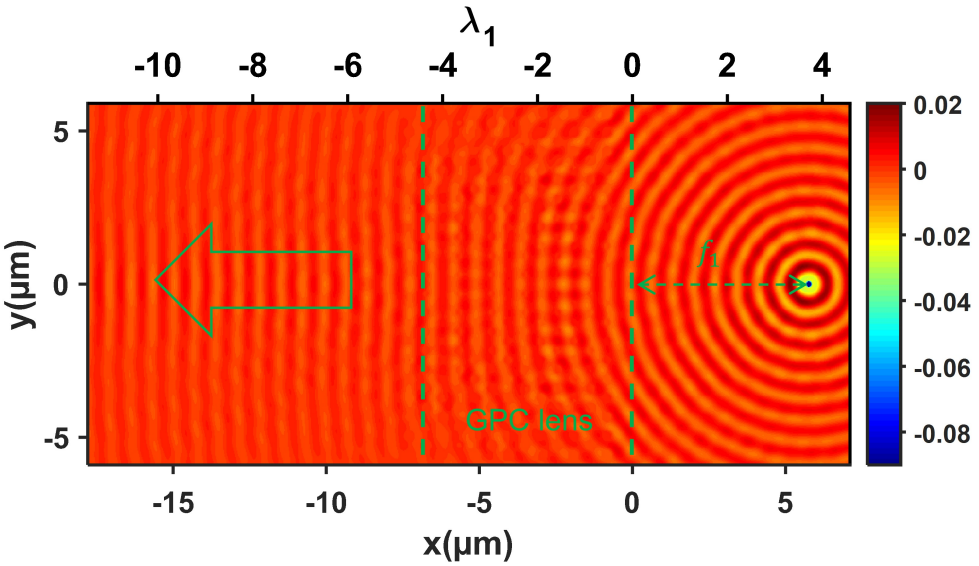

Figure 3.29: The H_z field distribution when the incident wavelength is λ_1=1.55μm for TE point source (2nd band of hexagonal lattice). The light source is located approximately at f_1=6μm from the lens' incident surface.

Through the simulation results of the incident plane light wave (see Figure 3.28), we

found that the lens can focus the plane wave to the focal point very well. Also, we found that the focal length of the flat lens is about $f_1 = 3.9\lambda_1$, λ_1= 1.55μm. This focal length is in the order of magnitude of the thickness of the lens. Therefore, this lens cannot be considered as a thin lens. Figure 3.29 show that the flat lens can not only focus plane waves to the point source, but also can collimate the light from the point source into plane waves.

Also, by analyzing the field intensity in the y-direction of the cross-section we can obtain a more intuitive focusing effect (see Figure 3.30). It can be seen that the field intensity distribution in the y-axis direction exhibits an approximately Bessel Gaussian distribution at several different locations from the plane of emission. The maximum field strength is found at y=0, which is the mid-axis position of the lens. The FWHM at the focal point is $0.56\lambda_1$, λ_1=1.55μm.

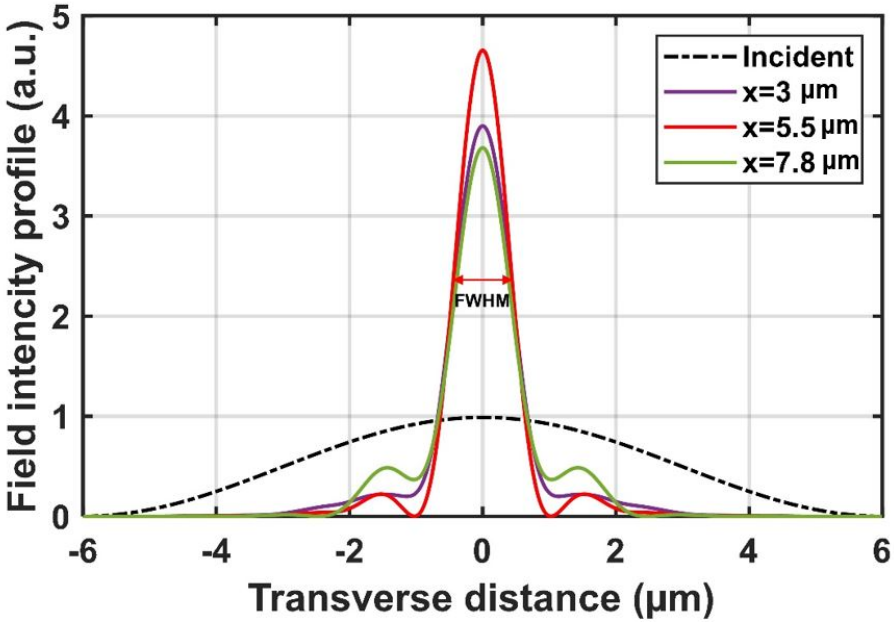

Figure 3.30: The $|E_y|^2$ field intensity distribution along y direction at the different positions from the lens' exit plane (2nd band). The color is the same as used in Figure 3.28. For the field intensity at the focus point, the FWHM is $0.56\lambda_1$, where λ_1=1.55μm.

As the FDTD simulation were done in 3D, we can also get the profile of the field in yz-plane. Our effective structure is in the topmost 220nm thick silicon layer of the SOI platform. In the Figure 3.31, we can see the focusing effect of the lens in the yz-plane. Before incidence, the light was a TE fundamental mode in a 10μm wide 220nm thick waveguide, and after passing through the lens, we found that it focuses into a smaller and lighter spot at the focal point.

So far, we have demonstrated through simulations that the designed flat lens is capable of focusing and collimating light at 1.55μm which is in the 2nd band of hexagonal lattice PCs. This is in line with our original design intention. By appropriately extending the wavelength

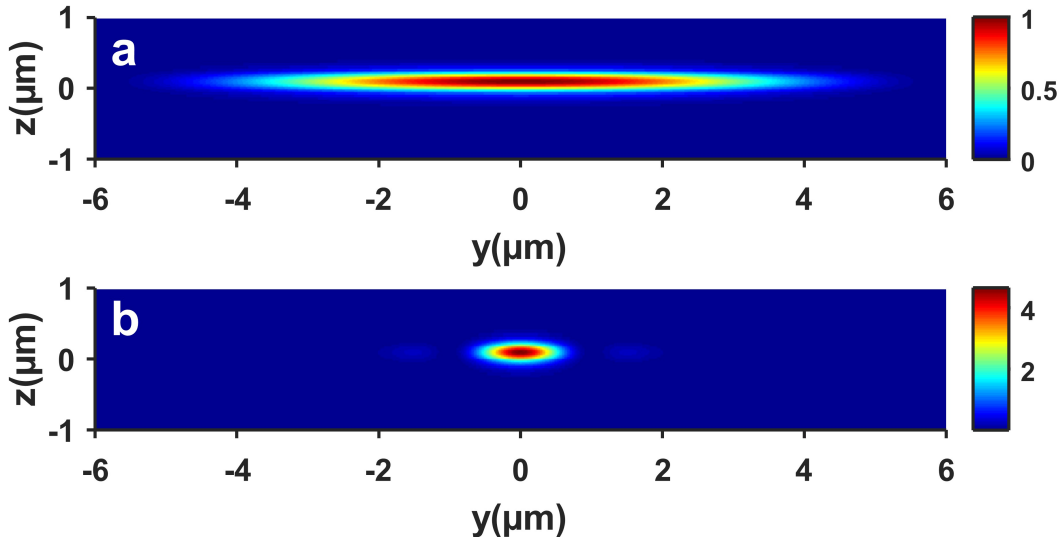

Figure 3.31: The $|E_y|^2$ field intensity distribution at yz plane λ_1=1.55μm (2nd band of hexagonal lattice). (a) The incident field intensity distribution. (b) The field intensity distribution at the focus point.

range of the simulation, we have found that the focusing and collimation functions of the lens are still effective at 3.2μm wavelength which is in the 1st band of hexagonal lattice PCs. This phenomenon means a dual-band flat lens. A possible explanation is that when the wavelength increases to λ_2=3.2μm, the corresponding normalized frequency is ϖ=0.194, which corresponding to the green line in Figure 3.22. So this normalized frequency is right in the first band. And as far as we know, the EFCs of the first band are always circular for different r/a. Therefore, at this normalized frequency, the PCs is also equivalent to a homogeneous medium. Its refractive index distribution is also in accordance with the general convex lens law, i.e., the refractive index is small at the edges and large at the center. Therefore, the lens is able to focus light at this instance (See Figure 3.32). Comparing the field intensity at the focal point in Figure 3.30 ($FWHM_1 = 0.56\lambda_1$) and Figure 3.34 ($FWHM_2 = 0.71\lambda_2$), we can see that we obtain a higher resolution (close to the diffraction limit) when the refractive index is negative (2nd band). This is due to the amplified transmission of evanescent waves linked to photon bound states [32].

Through more simulation studies, we found that the lens can also collimate light at a wavelength of 3.2 μm (See Figure 3.33). This simulation result shows that for light with a wavelength of 3.2 μm, the lens we have designed can focus plane waves and collimated point sources. For this wavelength, it also behaves as a real lens. Similarly, for a wavelength of 3.2μm, we obtained the FWHM at the focal point and the field intensity distribution in the yz plane, as in Figure 3.35. We have summarized and published the above design and simulation results in *Dual band flat lens with negative index for silicon photonics* [188].

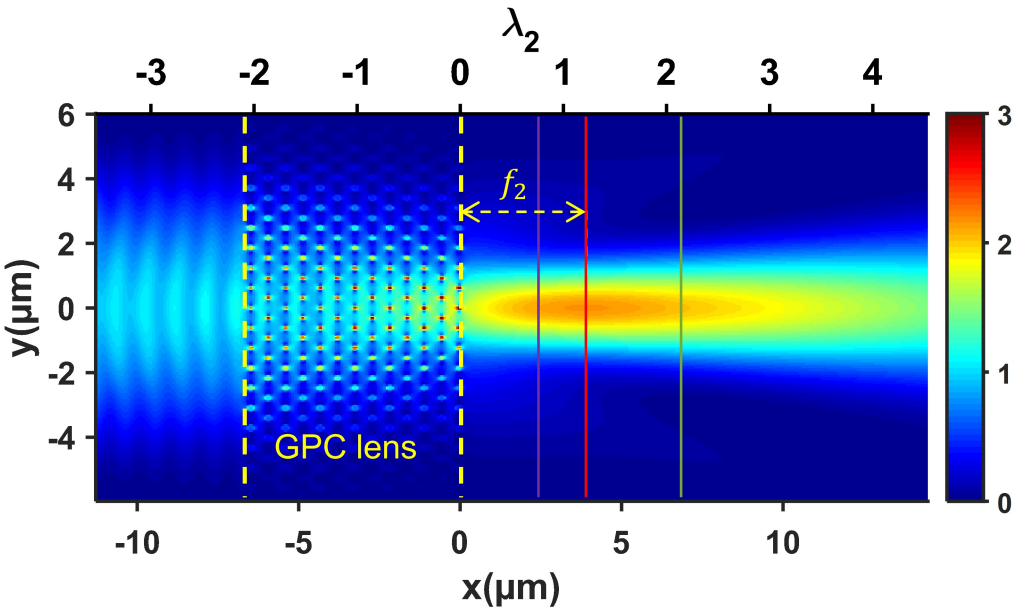

Figure 3.32: The $|E_y|^2$ field intensity distribution when the incident wavelength is λ_2=3.2μm (1st band of hexagonal lattice) for TE fundamental mode light source. The focal point is located approximately at f_2= $1.15\lambda_2$ from the lens' exit plane, $\lambda_2 = 3.2$μm.

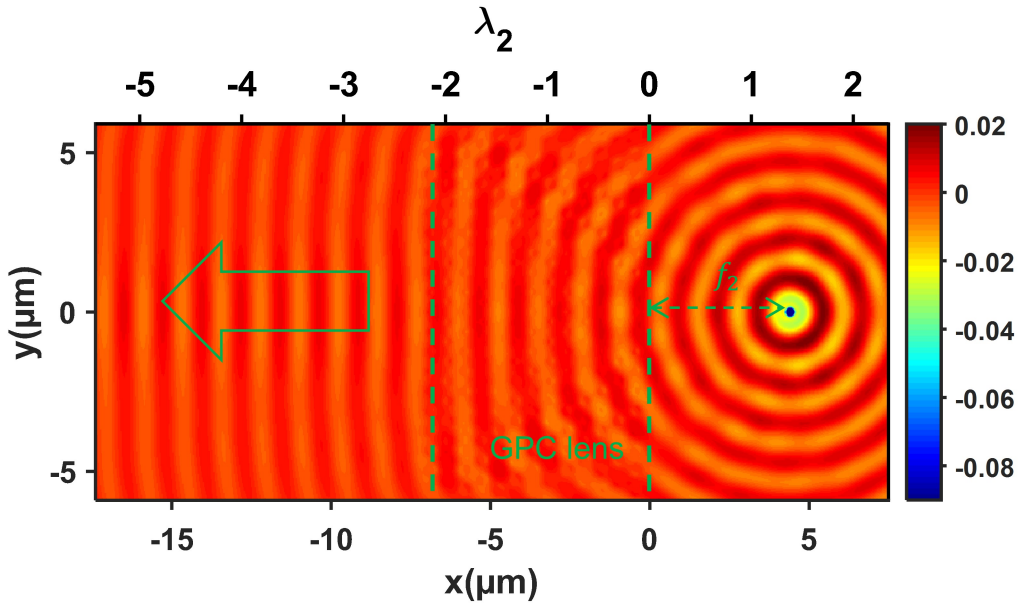

Figure 3.33: The E_y field distribution when the incident wavelength is λ_2=3.2μm for TE point source (1st band of hexagonal lattice). The light source is located approximately at f_2=3.68μm from the lens' incident surface.

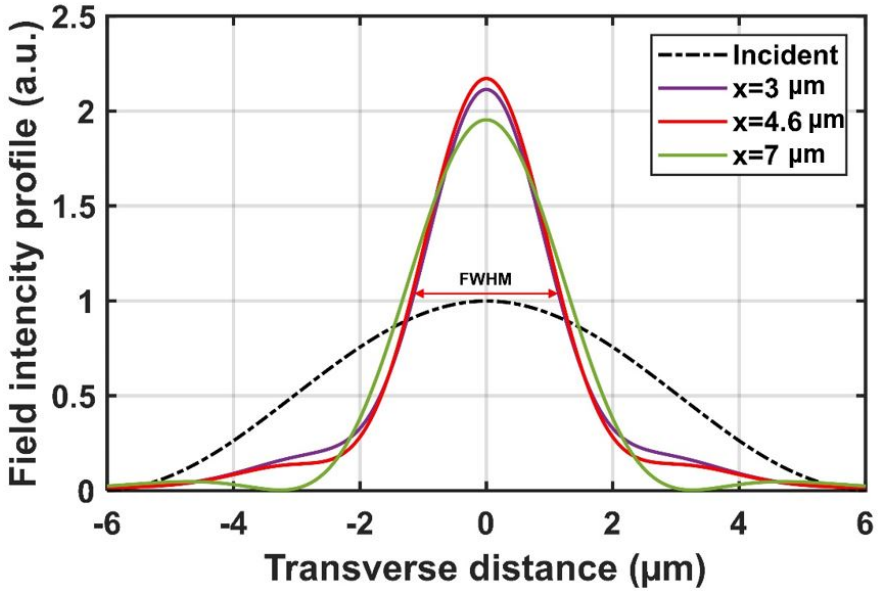

Figure 3.34: The $|E_y|^2$ field intensity distribution along y direction at the different positions from the lens' exit plane (1st band of hexagonal lattice). The color is the same as used in Figure 3.32. For the field intensity at the focus point, the FWHM is $0.71\lambda_2$, which λ_2=3.2μm.

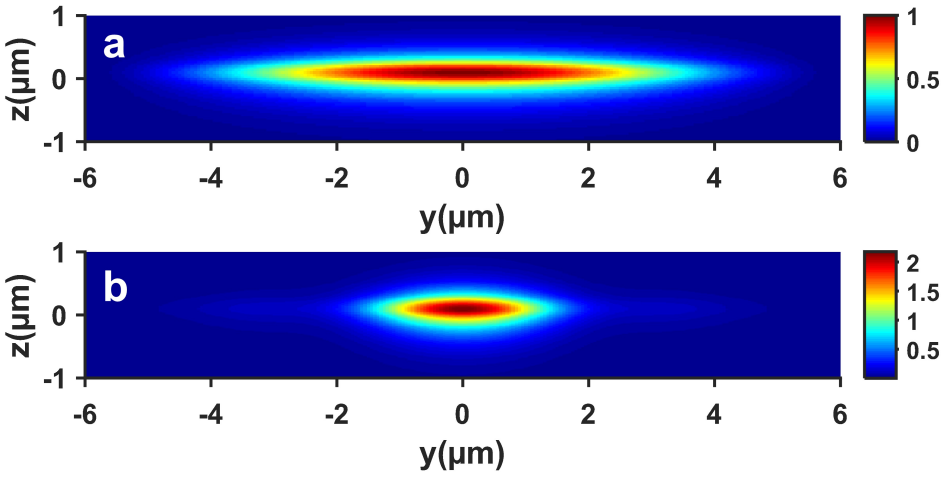

Figure 3.35: The $|E_y|^2$ field intensity distribution at yz plane for λ_2=3.2μm (1st band of hexagonal lattice). (a) The field intensity distribution before incidence. (b) The field intensity distribution at the focus point.

3.4 Mimic a point source on SOI

Our design aims to be a true flat lens. This means that the lens is bi-directional. As mentioned earlier, the approximation of a plane wave on the SOI is achieved by using a waveguide with a width of 10μm. The TE fundamental mode in the waveguide can be approximated as a plane

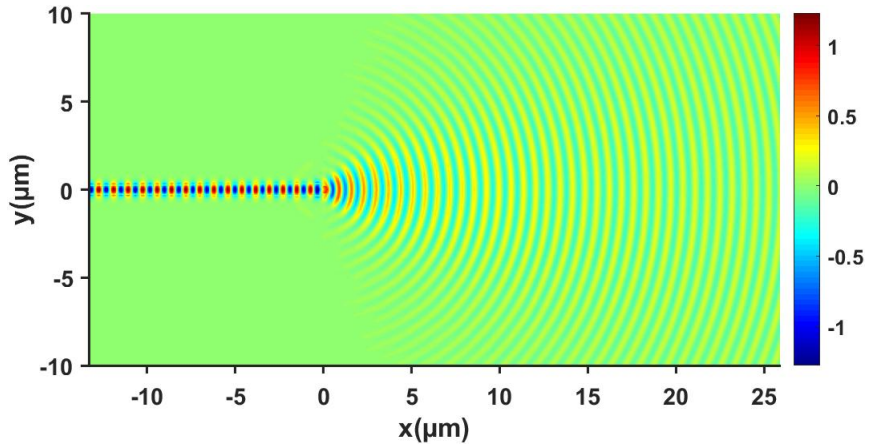

Figure 3.36: The simulation result of E_y field distribution of the designed on chip point source at 1.55μm.

wave. For point sources it is relatively more complicated. The point light source in this thesis is inspired by a related article by Didier Lippens et al. [186, 189–192]. Specifically, we use a gradual reduction of the waveguide width to approximate a point source. An air hole with a radius of 240 nm is placed at the end of the sharp waveguide (width 800nm) as a resonant cavity. Such a structure was successfully implemented in the simulation to approximate a point source (See Figure 3.36).

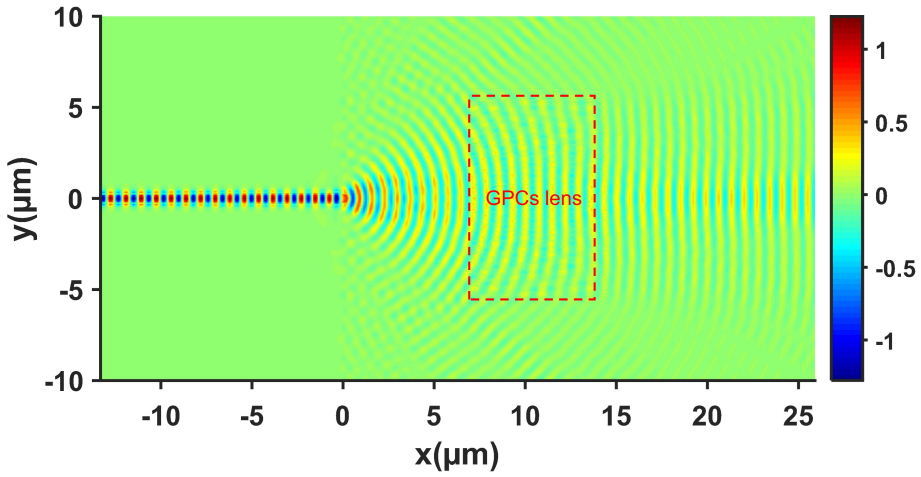

Figure 3.37: The E_y field distribution of the designed on chip point source with GPCs lens placed after. The circular wavefront of the point source becomes a parallel forward wavefront after passing through the GPCs lens.

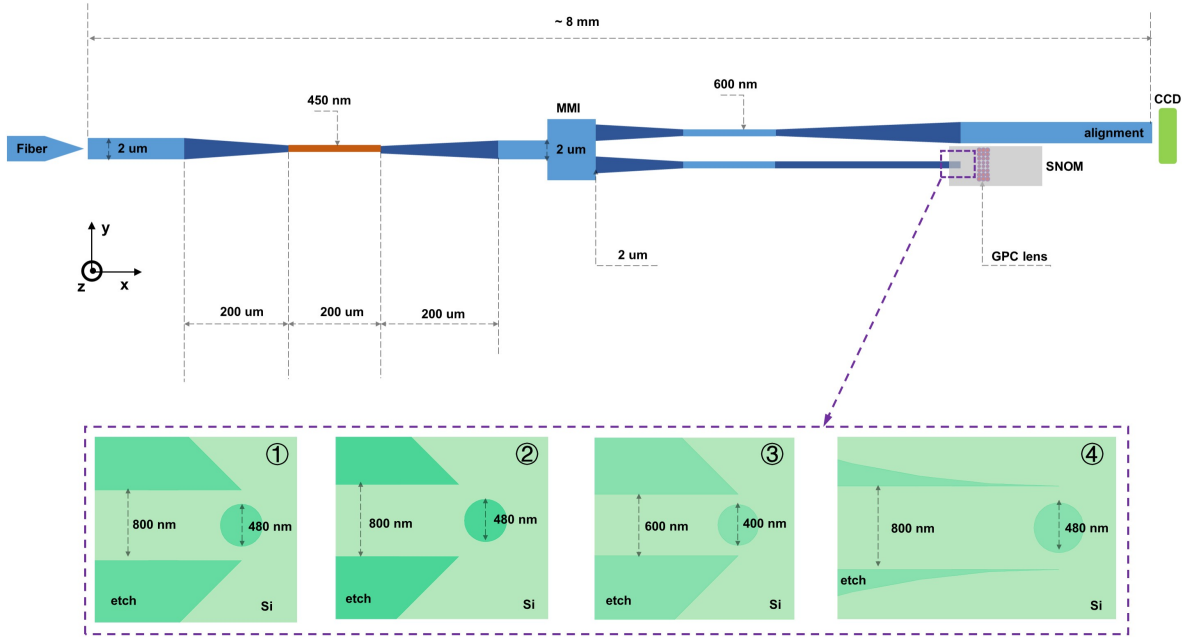

Figure 3.38: Sketch of the experimental setup designed to verify the lens collimation function. Four different structures were finally fabricated to mimic a point source on SOI. They were placed behind one of the output arms of the MMI (multimode interferometer). The other output arm of the MMI is the optical alignment reference when using the SNOM [193]. The gray area corresponds to the zone of SNOM.

Four different point light possibilities are applied to the SOI during the actual fabrication process because of sufficient space. By changing the size of the air holes at the end of the waveguide and by changing the etched shape on both sides of the tip waveguide, we try to simulate the on-chip point light source as well as possible. Also, the characterization of the point source and its field after passing through the lens is considered only using the SNOM technique. A schematic diagram of the experimental characterization using the SNOM technique is given in Figure 3.38. Unlike the design used for the focusing function, one of the arms derived by the MMI no longer expands to a width of 10µm but keeps its narrow width value. We have modified the size and structure at the end of the narrow waveguide to give it four possibilities.

This method of a mimic on-chip point source can only be as close to a perfect point source as possible. However, as can be seen from the simulation results in Figure 3.37, the intensity of the incident waves is not the same everywhere in a wavefront. The intensity at the position near the center is higher than the intensity of the light at the top and bottom sides. Behind the lens, the wavefront are plane. And the intensity of the wave near the central axis of the lens is higher than the intensity at the top and bottom.

3.5 Half-Maxwell fish-eyes for infrared application

A Maxwell fisheye lens is a spherical non-uniform symmetric lens that converges point light sources at the edge of the lens to the edge of the symmetric sphere. For such a non-uniform medium, the refractive index at the center of the lens is maximum and the refractive index at the edges is minimum. The refractive index n_{eff} distribution in the lens satisfies Equation 3.11 [194], which r stands for radial position inside the lens body, and n_{max} is the maximum refractive index, r_{max} is the lens' radius.

$$n(r) = \frac{n_{\max}}{\left(\frac{r}{r_{\max}}\right)^2 + 1} \tag{3.11}$$

A half-Maxwell fisheye lens retains most of the characteristics of a Maxwell fisheye lens, except that it is half spherical as the name implies. It is characterized by its ability to focus incident plane waves into a focal point. Similarly, it is able to collimate the point source at the edge of the lens into a plane wave. Its refractive index distribution is identical to that of a fisheye lens, i.e., it satisfies the Equation 3.11.

Extensive research has been devoted to Maxwell fisheye lenses and Half Maxwell fisheye lenses [60, 195, 196]. Gaufillet et al. have designed 2D Maxwell fisheye lenses and Half Maxwell fisheye lenses [74]. Heahland et al. have realized the design and processing of silicon-based Half Maxwell fisheye lenses for terahertz applications [194, 197]. In this thesis, we designed a Half Maxwell fisheye lens based on the SOI platform, and the simulation results proved that it is effective in the near-infrared domain.

3.5.1 Design method

From equation 3.11 we can draw several conclusions:

1. The maximum refractive index is at the center of the lens while the minimum refractive index is at the edge of the lens.
2. The refractive index at the center is twice as high as at the edges.
3. The maximum refractive index at the center can be chosen as desired.

Considering that we are implementing in the SOI platform, the maximum diameter of the lens should be chosen $r_{max} = 10\mu m$. Cause in the 10µm waveguide we can obtain a TE fundamental mode that approximates a plane wave. The effective refractive index of a 220nm thick silicon layer for 1.55µm TE mode is approximately 2.85, so we should not exceed this value when choosing n_{max}.

For the Half Maxwell-fisheye lens, we chose the case when the normalized frequency ϖ is set in the first band of the hexagonal lattice photonic crystal. The specific design process and method we have described in the previous subsection 3.3.1, so we will not repeat them here. The lattice constant a=290nm, the normalized frequency is ϖ=0.187. The relationship between the effective refractive index and the radius of the air hole can be expressed by the equation

$$n_{\text{eff}} = -2.213\left(\frac{r}{a}\right)^3 - 6.117\left(\frac{r}{a}\right)^2 + 0.269\left(\frac{r}{a}\right) + 2.814. \tag{3.12}$$

Notice that in equation 3.12, the r is the radius of air hole which is different from in equation 3.11. With this equation, we derived that the maximum effective index is in the center of lens which is $n_{eff_{max}} = 2.78$. And the minimum effective index is at the edge of lens which is $n_{eff_{min}} = 1.39$. Thus, the corresponding minimum air holes radius in the center of lens which is 28∼29nm and $r/a = 0.1$. The corresponding maximum air holes radius is at the edge of lens which is 135∼136nm and $r/a = 0.466$. This achieves a maximum effective refractive index that is twice as large as the minimum effective refractive index. Again, fabrication tolerance is taken into account.

3.5.2 Numerical simulation results

The 3D FDTD in Lumerical is used for the simulation of the structure. The whole structure is realized on a 220 nm SOI. TE fundamental mode light source in a 10 µm wide waveguide incident along the x-axis into the designed Half Maxwell fisheye lens. In the collimation simulation, a point source is placed at the edge of the lens.

As the Figure 3.39 illustrates, the focus point of the lens is in fact not exactly at the edge of the lens. This is because what is incident is an approximate plane wave. In a 10µm wide waveguide, the field intensity distribution of the TE fundamental mode is in fact a Gaussian distribution. The focus point is located at $x = 6\mu m$. And the FWHM at focus point is $FWHM = 0.924\mu m = 0.6\lambda$, here $\lambda = 1.55\mu m$ (See Figure 3.40). When a point source is located at the surface of designed Half Maxwell Fisheye, it also can collimate to a plane wave (See Figure 3.41).

Further studies were used on more frequencies. We performed simulations for 1450nm (See Figure 3.42) and 1650nm (See Figure 3.43), respectively. It is found that the designed lens converged the incident near-plane waves for both frequencies. However, their focal positions change. At 1450nm, the focal point is at approximately 5.9µm, while at 1650nm, the focal point is at approximately 6.15µm. Also, the field intensity distribution at the focal point is slightly different. At 1450nm, the full width at half maximum is $FWHM = 0.804\mu m = 0.55\lambda$, here $\lambda = 1.45\mu m$. While at 1650nm, the full width at half maximum is $FWHM = 1.14\mu m = 0.7\lambda$, here $\lambda = 1.65\mu m$.

In the near-infrared domain, the Half Maxwell-fisheye lens we designed can be used as a

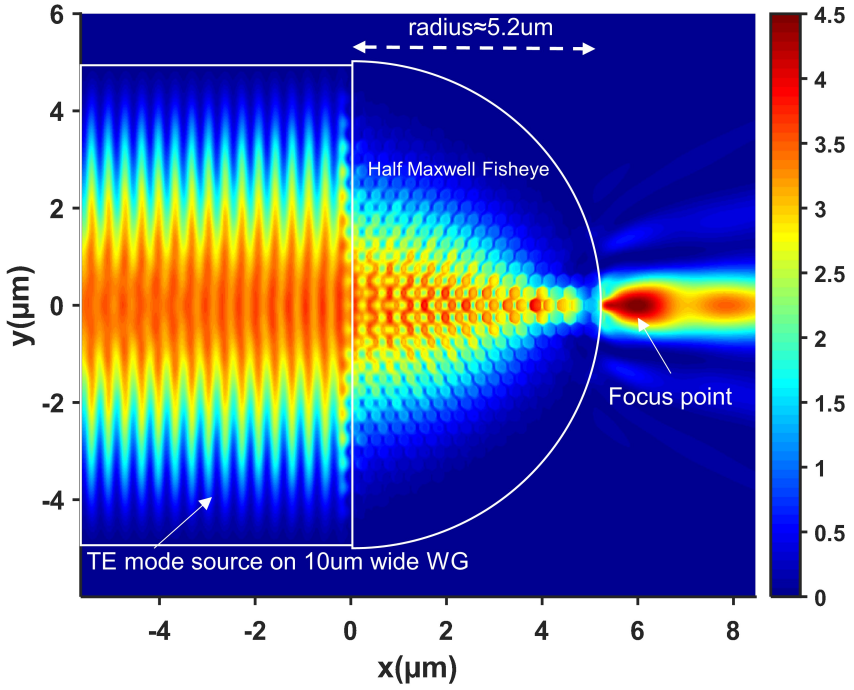

Figure 3.39: $|E_y|^2$ distribution of the TE fundamental mode at 1.55μm in the designed Half Maxwell fisheye. The incident waveguide is 10μm wide and the focus point is about 0.7μm away from the lens' surface.

mode size converter. Similar Luneburg lens applications can be found in the article of Zhang et al. [172].

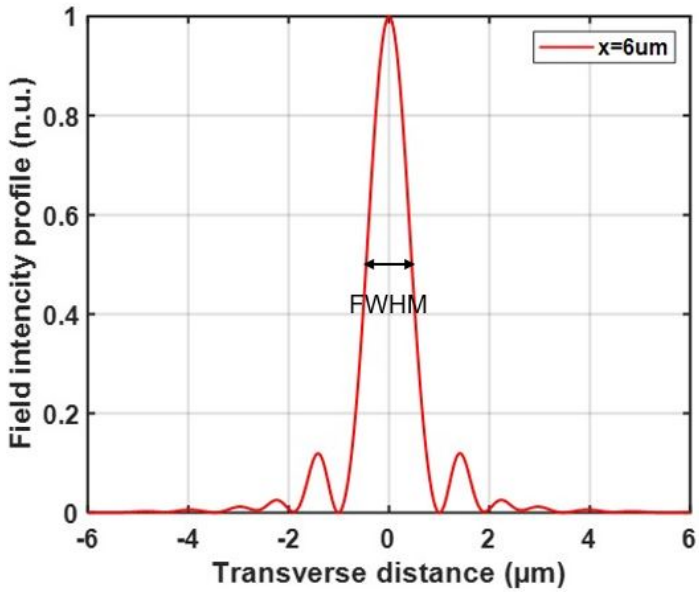

Figure 3.40: The $|E_y|^2$ field intensity distribution along y direction at the focus point for incident $\lambda = 1.55\mu m$. $FWHM = 0.924\mu m = 0.6\lambda$, here $\lambda = 1.55\mu m$.

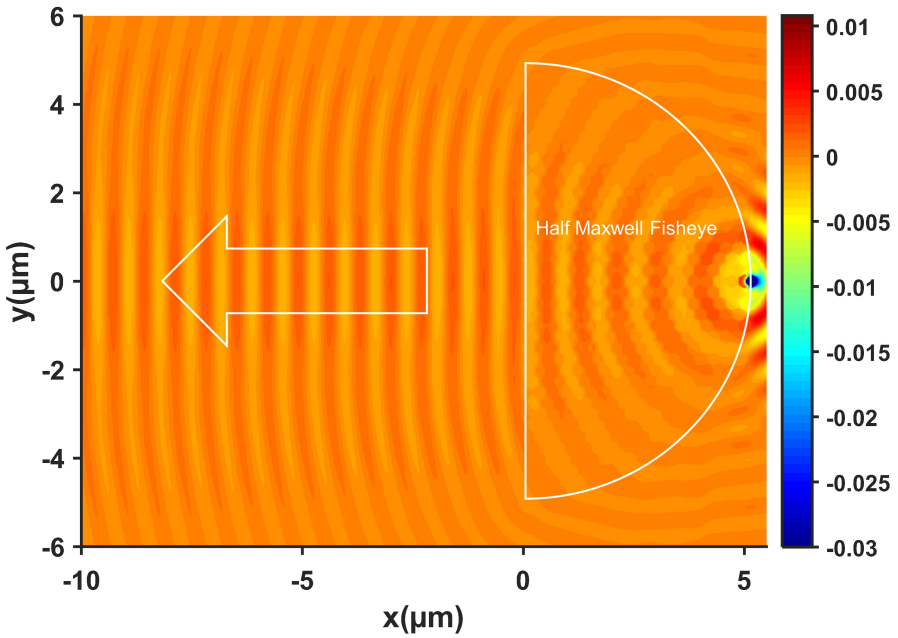

Figure 3.41: The H_z field distribution when a point source at 1.55μm is placed at the edge of designed Half Maxwell fisheye. The transmitted wave is a plane wave.

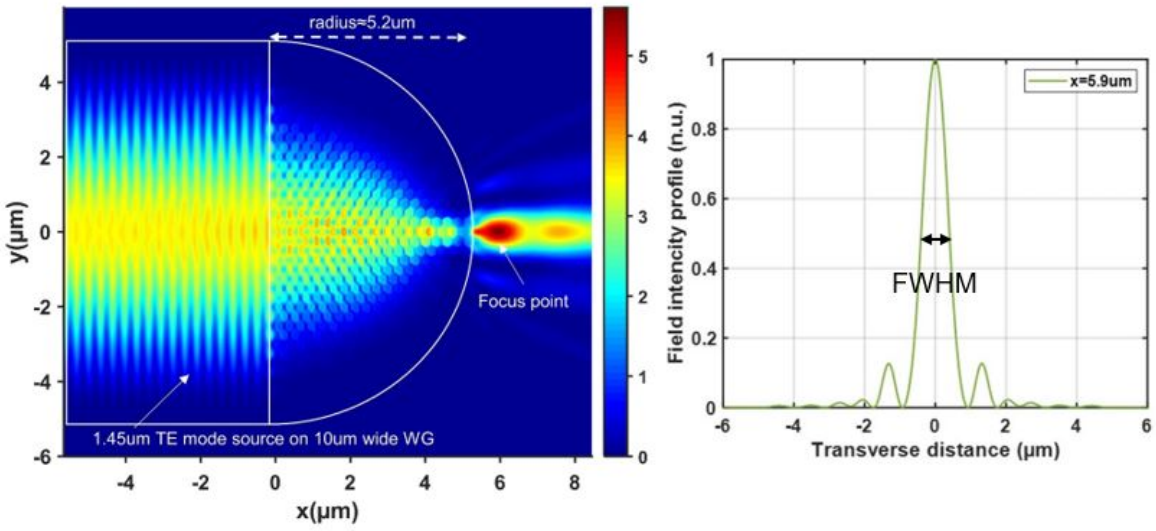

Figure 3.42: Left: $|E_y|^2$ distribution of the TE fundamental mode at 1.45μm in the designed Half Maxwell fisheye. Right: The $|H_z|^2$ field intensity distribution along y direction at the focus point for incident $\lambda = 1.45\mu m$. $FWHM = 0.804\mu m = 0.55\lambda$, here $\lambda = 1.45\mu m$.

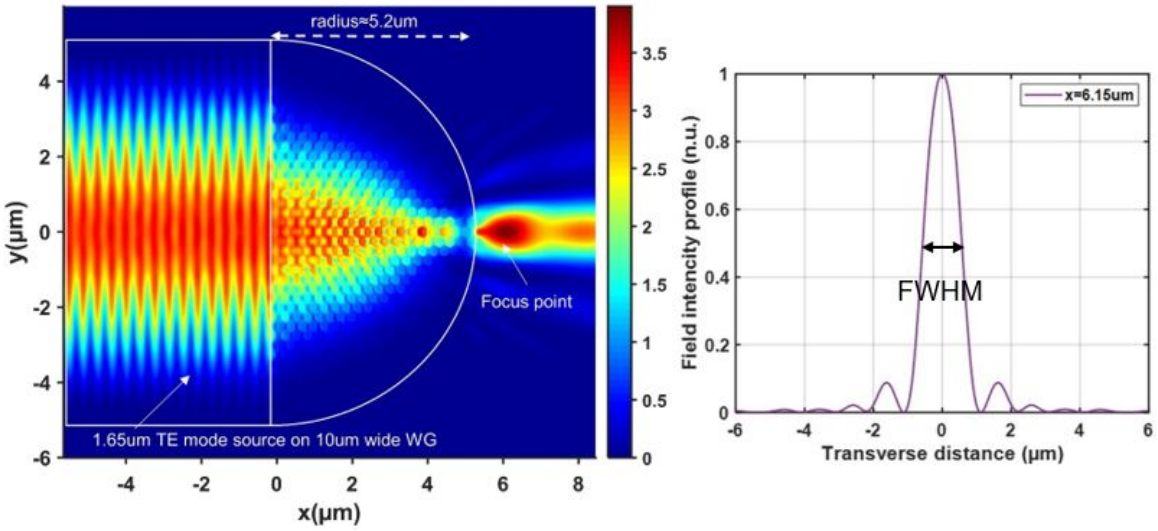

Figure 3.43: Left: $|E_y|^2$ distribution of the TE fundamental mode at 1.65µm in the designed Half Maxwell fisheye. Right: The $|H_z|^2$ field intensity distribution along y direction at the focus point for incident $\lambda = 1.65\mu m$. $FWHM = 1.14\mu m = 0.7\lambda$, here $\lambda = 1.65\mu m$.

3.6 Conclusion

This section presents the design and simulation of gradient photonic crystal lens on the SOI platform in the near-infrared band. For flat lens, depending on the normalized frequency and photonic crystal lattice shape, we first present the lens design and simulation when the normalized frequency is in the first band and in the second band of a square lattice photonic crystal. Then, we present the lens design and simulation for the first band and the second band of a hexagonal lattice photonic crystal. For the first band, the EFCs are always circular and the PCs could be considered as a homogeneous medium. For the second band, the EFCs of the square lattice are square shape. In comparison, the EFCs of the hexagonal lattice are closer to circular and the effective index is negative in this case. Thus, we have chosen the case when the normalized frequency is in the second band of hexagonal lattice. Further, we design and simulate four different on-chip point source structures for the collimation function of the flat lens. Finally, we present the design and simulation results of a Half Maxwell-fisheye lens on a SOI platform in the near-infrared band.

Chapter 4

Nano-fabrication technologies and characterization methods

Contents

The main manufacturing goal of this thesis is to realize the gradient photonic crystal lens working in the near-infrared domain (mainly wave length 1.55µm). Therefore, for this purpose, the corresponding fabrication technology must be at the nanometer scale. Cause the interaction between electromagnetic waves and matter depends not only on the electromagnetic properties of the matter, but also directly on the spatial size of the material structure.

In addition, the gradient photonic crystal is extremely sensitive to the change of the size of holes or columns in the device, so the nanofabrication in this thesis is challenging. In order to meet the nano-fabrication tolerance, the minimum air hole diameter in the flat lens in this thesis should satisfy the requirements $\phi_{min} \geq 120nm$. And silicon photonics is considered to be the key technology for modern optical applications in the near-infrared domain. On the one side, the silicon microelectronics processing technology is quite mature. On the other side, the emergence of electron beam lithography has brought silicon-based processing technology to the higher level. Thus, the samples in this thesis are fabricated and characterized on the SOI (Silicon on Insulator) platform. Figure 4.1 shows the scope of subwavelength electromagnetism and the SOI structure used in this thesis.

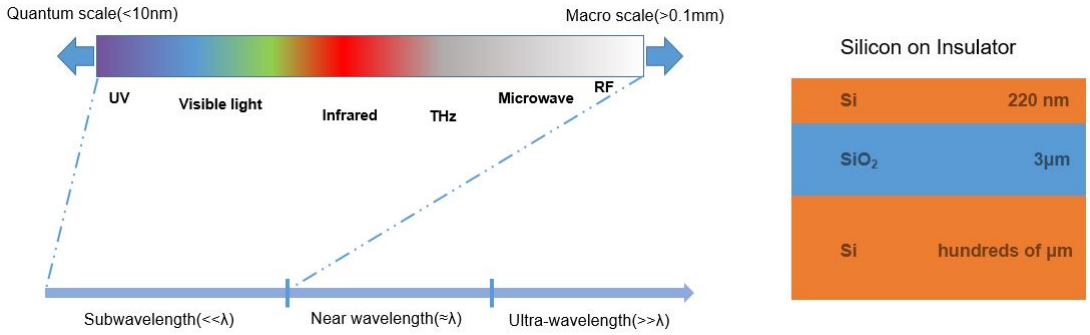

Figure 4.1: Left: The research scale of electromagnetics. Right: SOI platform parameters.

This chapter will mainly present the fabrication and experimental characterization of gradient photonic crystals on the SOI platform. First, we will gradually present different steps of the nano-fabrication technology involved in this thesis in details. Then we will present the sample characterization techniques, that is, electron microscopy and SNOM (Scanned near-field optical microscopy) technology. The entire fabrication was performed in the clean room of laboratory C2N. Part of the characterization work benefited from the optical characterization platform of the CRIME group. The SNOM characterization was performed in the ICB laboratory in Dijon.

4.1 Fabrication of graded photonic crystal on SOI platform

The sample processing is carried out in the ultra-clean room of laboratory C2N. Gradient photonic crystals are applied to SOI platform with no cladding at the end of fabrication process.

The uppermost layer of SOI used in this thesis is a 220nm thick silicon layer. The second is a 3um thick silicon dioxide layer. The bottom is a hundred of μm thick silicon substrate . The main techniques used are electron beam lithography (EBL) and inductively coupled plasma (ICP) dry etching. The test sample was first fabricated to test the dose of EBL and the difference of processed air holes. The whole fabrication process can refer to the following steps (see Figure 4.2).

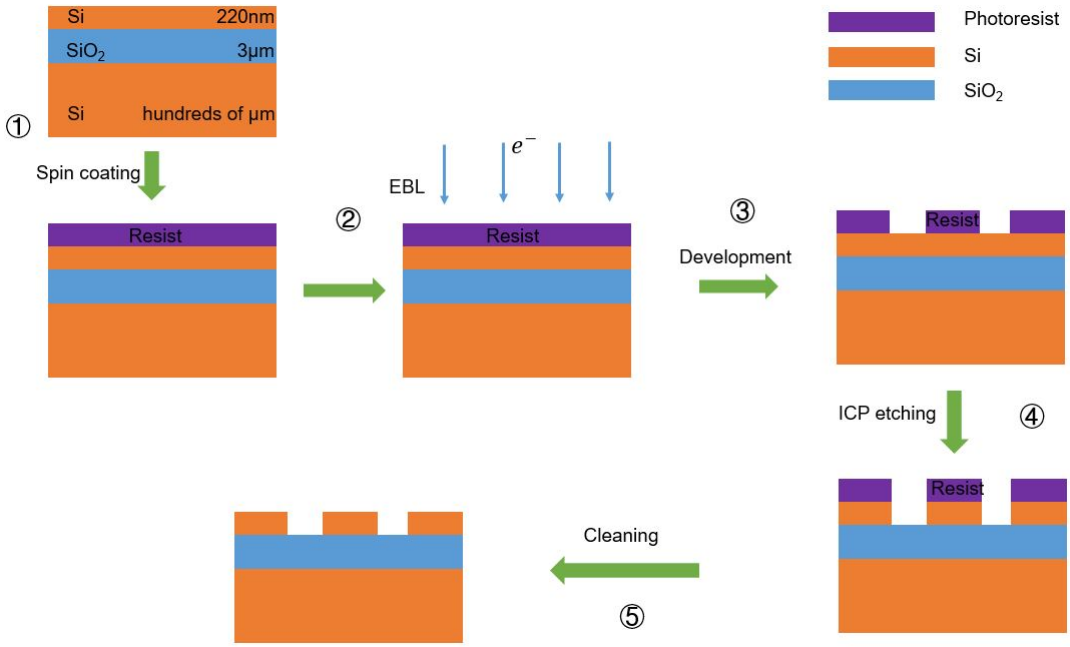

Figure 4.2: Nano-fabrication process used in this thesis. The nanofabrication steps used in this thesis can be divided into: 1) SOI preparation and resist spin coating. 2) EBL process. 3) Development process. 4) ICP etching. 5) Final cleaning.

1) The surface of the SOI platform bought from the manufacturer is cleaned and electron resist is spin-coated. The pattern is then printed on the resist layer by electron beam lithography. By development, we remove the resist part injected by the electron to obtain the pattern. 2) The dry etching technology etches the pattern to the uppermost silicon layer. 3) The sample needs to be thoroughly cleaned to remove the resist and organic impurities. The following sections will introduce each of these steps in detail.

4.1.1 Substrate surface cleaning

Pre-cleaning of the surface is necessary. If there are organic substances and other compounds remaining on the surface, the subsequent resist spin surface will be uneven. And this would affect the EBL process. Usually, acetone solution and isopropanol solution are used for substrate cleaning. Nitrogen guns are used to dry the substrate surface and remove dust on the

surface. Before spin-coating the resist, pre-baking is also necessary. The baking temperature and time will affect the spin coating quality of the resist.

4.1.2 Resist spin coating

The resist used in EBL is of two kinds, positive and negative. The development process later will remove the part of the positive resist that has been injected with electrons during EBL. Conversely, the development process will maintain the negative resist parts that have been injected with electrons during EBL. The ZEP520A resist used in this project is a positive resist like PMMA. The relationship between spin coating thickness and spin coating speed for different dilution of ZEP520A can be seen in Figure 4.3.

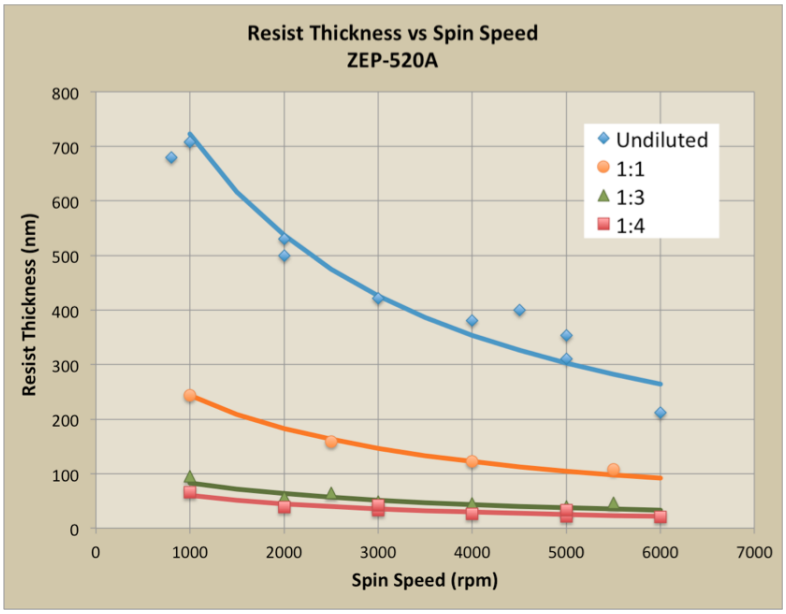

Figure 4.3: The relationship between the spin coating thickness with the spin rate and the dilution ratio of ZEP520A [198].

The spin coating process of resist can be carried out according to the following steps. To begin with, drop the resist solution onto the center of the sample surface and cover one-third to one-half of the sample surface. Then rotate the stage so that the resist covers the entire surface. The thickness of the spin coating layer depends on the concentration of the resist solution, the rotation rate and the rotation time. The resist can be diluted with anisole to meet different concentration requirements. The faster the rotation speed and the longer the rotation time, the thinner the thickness of the resist layer. After spin coating, the resist needs to be baked to stabilize it for electron writing.

4.1.3 EBL process

EBL is the key step in fabrication procedure. The aim of EBL is to define precisely different patterns that will be further etched on the top Si layer. And the reason for choosing EBL as a fabrication tool is that it can realize a high resolution with a high accuracy. The process is somehow the same as back-end design in integrated circuit. The working principle of most electron beam etching systems can be seen in Figure 4.5. But the difference is that EBL is mainly used in different labs and has not been used in industrial product because its high time cost and unstable stat. Its advantage is nano-scale processing rather than mass production.

4.1.3.1 Principle of EBL

In our case, the lattice period is around 600nm and the average radius of air holes is around 100nm. For this, it is important to choose a proper and stable nano-fabrication facility. There are mainly four EBL machines in our lab. The Nanobeam4 system has been used in my thesis. It could be operated at 80kV voltage and has a resolution up to 2nm, which is also the case in this thesis. This means that the diameter of the air holes must be an integer multiple of 2 in the following mask design. Figure 4.4 Left illustrates the NB4 electron beam etching system at C2N lab.

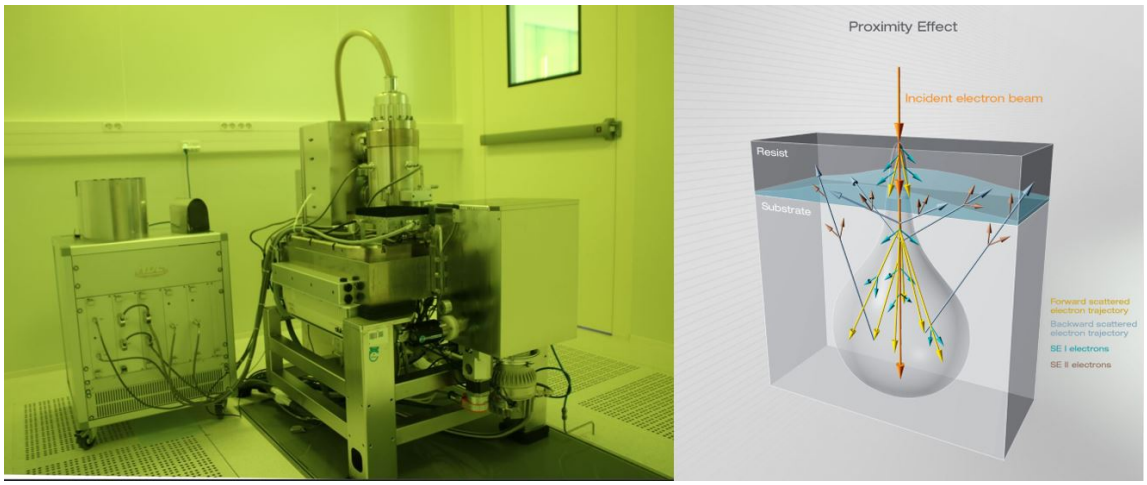

Figure 4.4: Left: The nanobeam4 EBL system installed in laboratory C2N's clean room. Right: Schematic diagram of proximity effect [199] in EBL process.

The EBL direct writing system is mainly divided into electron optical system, vacuum system, high-speed graphics generation system. The electron optical system generates an electron beam and focuses the electron beam to a spot of a few nanometers in diameter (about 5nm in our case). At the same time, by controlling the switch and deflection of the beam spot, the three basic parts including the electron gun, the electron lens and the electronic deflection system are controlled. The vacuum system ($< 1.9 \times 10^{-6}$mbar) is used to reduce the energy

dispersion and electron scattering of electrons. Because there is a high voltage in the electron beam generation process, the ionized molecules gas that bombard the cathode will cause severe electron beam energy dispersion, which introduces aberrations. At the same time, the electron beam is easily scattered by gas molecules during propagation. So high vacuum components are also an essential part of the electron beam system.

The workbench usually uses a laser interferometer as feedback to achieve precise positioning of the exposure point. The high-speed graphics generation system converts the computer language GDSII into the machine language that controls the electron beam brake, deflector and sample stage. For large-area graphic exposure, the high-speed graphic generation system can decompose the entire graphic area into multiple small areas for scanning separately through graphic decomposition. The proximity effect and the stitching error are the main factors that affect the quality of EBL.

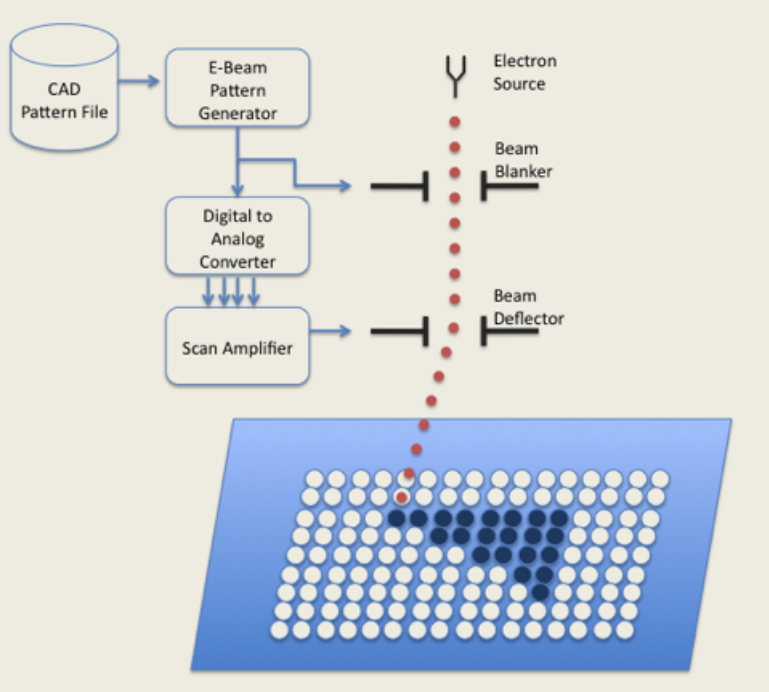

Figure 4.5: Principle of EBL system [198]. The electrons are emitted by the high-voltage gun and deflected by the deflector into the working cavity. The pattern is converted from the CAD file to the file recognized by the EBL system and finally written on the sample.

One important thing we should be aware when using EBL is the proximity effect. Indeed, the back-scattering electrons has a significant effect on the homogeneity of the patterns. After entering the resist layer, there are parts of electrons which interact with both the resist and top Si layer becoming secondary scattered electrons. This will cause the region outside the spot to be a non-zero dose region, which will end up with a wider exposure region. The proximity effect has been corrected by using Raith software. And in order to value the influence of proximity effect and suitable dose factor, one test sample has been fabricated at the beginning.

We found that with certain dose factor, the radius of air holes is enlarge for 4-6nm on average. In consequence, we pre-reduce the radius of air holes in mask design to against this effect.

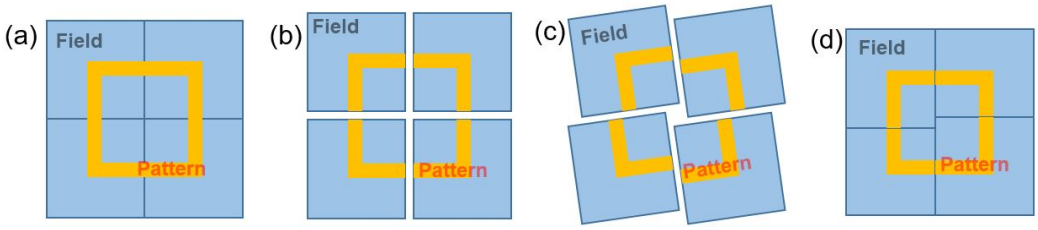

Figure 4.6: (a) Perfect writing state. (b)(c)(d) Different types of stitching error.

Another thing to try to avoid when using EBL is the stitching error. In the basic working principle of EBL, the writing of electrons mainly depends on the deflection of the electron beam. But under normal circumstances, our samples are larger than the deflection range of the electron beam. At this time, the control motor will move the platform to the next position for electron beam writing. In this way, our style is 'stitched' by different fragments (See Figure 4.6). Inevitably, there will be overlap or gap between different segments, which is called stitching error [200]. The large area that requires a mobile platform moving to write electrons is Main-field. There are numbers of Sub-field areas in a Main-field, where electronic writing can rely on the deflection of the electron beam. Due to the presence of stitching error, it is important to avoid key structures such as waveguides and air holes appearing on the boundary of Main-field. Therefore, for each pattern, Main-field and Sub-field need to be specially defined.

The whole EBL process could be divided into two steps: 1) numerical mask design before entering clean room and 2) applying EBL on SOI inside clean room. They will be discussed in the following sections.

4.1.3.2 Numerical mask design

The first step of operating an EBL writing is to design numerical pattern files which are known as masks (See Figure 4.7). Then the lithography system transits these pattern files on the photo-resist which is like primitive camera obscura. Unlike photography technology, EBL system uses numerical mask instead of a real one and it needs time (dozens of hours in our case) to write the pattern on resist instead of a single flash. There are numerous softwares for doing this, including some powerful ones from Synopsys and Cadence. The software L-edit from Tanner EDA has been used in my thesis to define the necessary pattern files. The file format of mask in my case is GDSII which stand for Graphic Design System. Normally, the EBL system can't read GDSII format directly. Therefore, we then transfer GDS files to pattern files which could be understood by EBL system. In our case, the software *nbpat* that comes with our EBL system NB4 was used for this file type conversion.

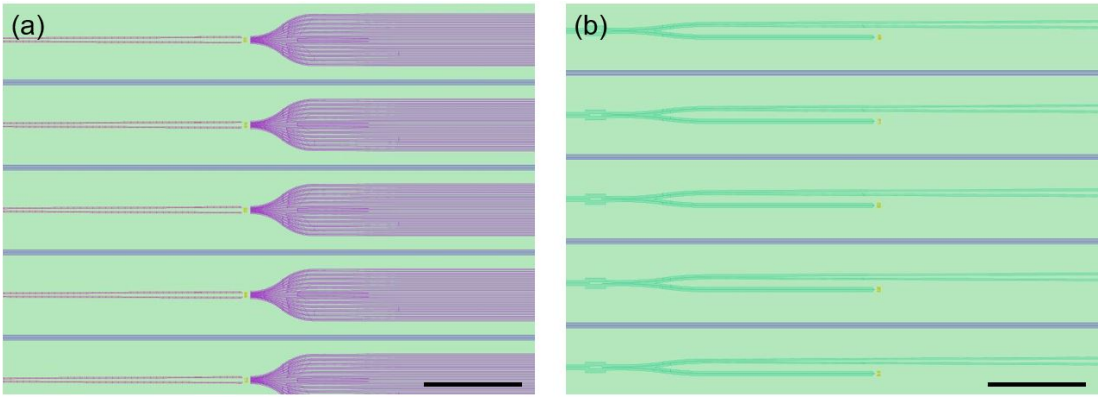

Figure 4.7: (a) Design mask for the focus part. A single structure consists of input waveguide, lens and output waveguide. Multiple sets of output waveguides are used to detect the output electric field. (b) Design mask for collimation part of SNOM characterization. Straight waveguides are used to ensure that each structure remains independent without interference from adjacent structures. Scale bar 200µm.

After definition of pattern files, we also need the code file which acts as the instruction order for EBL. We call this kind of instruction order the *job* file. Many fabrication parameters like the beam current and positions of different patterns could be defined in job file. In this thesis, the beam writing step size has been chosen to be 2nm. The operating current for EBL system is 0.5nA. The dose factor is 2.1, which takes control of the number of electrons entering the silicon layer. In fact, The density of the electron beam (number of electron per second) is constant. Therefore, the dose factor is actually the residence time of the electron gun in a specific position. The longer it stays, the more electrons are emitted at this location. The beam current mainly takes control of the beam spot size which in our case is 5nm for a 0.48nA or 0.5nA beam current. With high current, the spot size increases which will reduce the EBL's writing time.

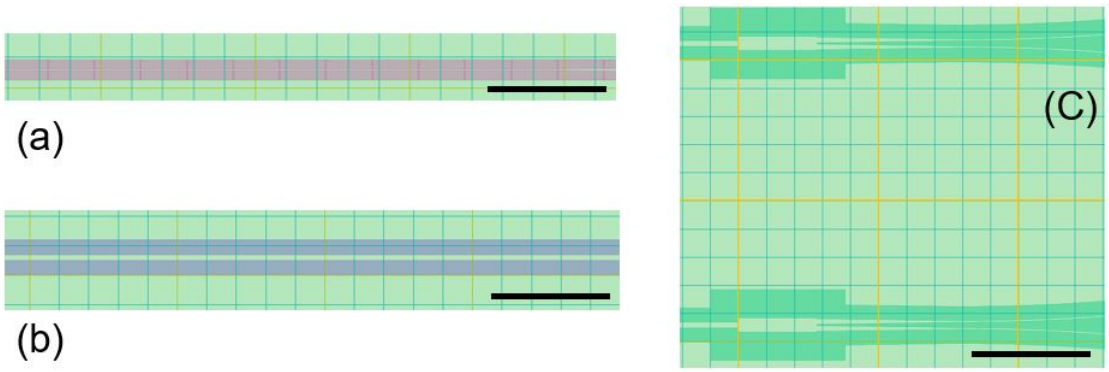

Figure 4.8: (a) Mono mode filter wave guide. (b) Long straight wave guide to isolate different part. (c) MMI splitter. Yellow blocks represent the Main-field and green blocks represent the Sub-field. Scale bar 40µm.

One example of sub-field and main-field can be seen in Figure 4.8. In a main-field, EBL uses electron gun deflection to write patterns without moving the platform. Scanning writing is performed by dividing a main field into many sub-fields. The yellow line in the figure is the boundary line of the main-field and the green line is the boundary line of the sub-field. The important structure should be avoided as far as possible at the boundary of the main-field.

4.1.3.3 Operating procedure of EBL system NB4

Before using the operating system of EBL, the corresponding beam current should be calibrated by our clean room engineers. When the calibration of beam current is finished, we can then book a time to launch our batch. Usually, the system is in a vacuum status. Therefore, the first thing to do is to check the system status and open the vacuum airlock. Then we take the chuck out of system to sample room where we load our sample on the suitable chuck position.

After putting the chuck back to the tray, we pump the system to a vacuum stat ($< 1.9 \times 10^{-6}$mbar). Normally it takes 15mins to 20mins to get a standard vacuum environment. Once the vacuum is ready in the chamber, the beam current is set and the auto conjugate can be operated. Also, a well manually focusing is recommended to get a good focusing result. Then the pre-defined job file is loaded into the EBL system. The system will run a grammar check on the job file. But it will not check the patterns' position or other parameters. In my thesis, one 2cm x 2cm sample will take 30 hours to finish the whole pattern's writing. It is a long writing time because of the 2nm resolution and because there are more than 60 structures on it.

4.1.4 Development before etching

Just as in photography, development can make the structure visible. The purpose of the development is to remove the positive resist which has been written by the electrons. Thus, we can get the pattern on the resist layer. The bigger the concentration of the developer solution, the faster the development speed and the shorter the development time required. The smaller the concentration of the developer solution, the longer it takes, but the reaction is milder, which facilitates the control of the development process. The basic environment of the development operation is shown in Figure 4.9 (a). After development, we can make preliminary observations of the sample using a high magnification optical microscope, see Figure 4.9 (b). This allows to detect possible problems at an early stage. In this way, timely intervention can be made and damage caused by subsequent manipulation of the sample can be avoided.

The development method is shown in the Figure 4.10. The sample is clamped by tweezers and placed horizontally in the developer solution. Then the tweezers are moved vertically

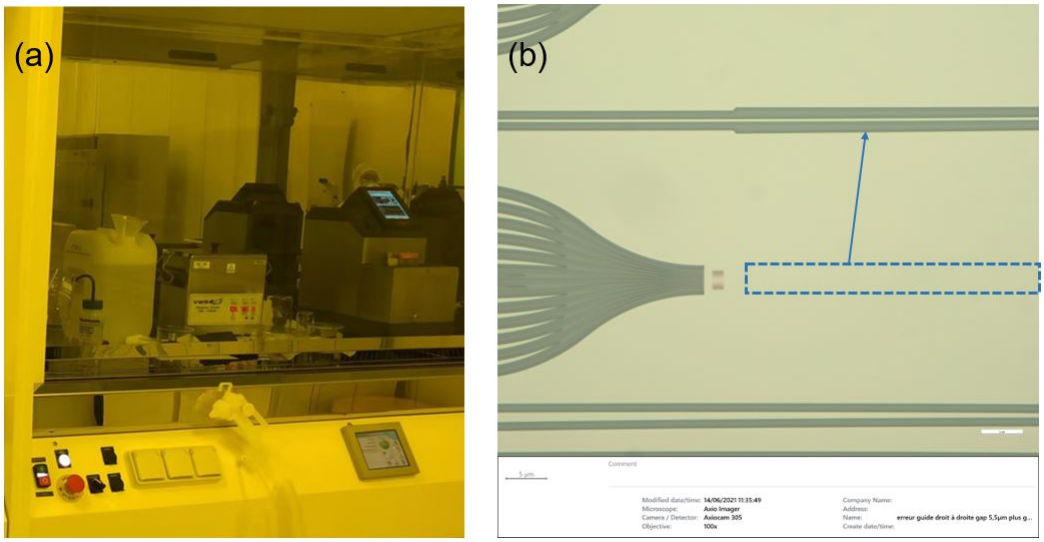

Figure 4.9: (a) Wetbench area in EBL room for development. (b) The optical microscope inspection after development is more convenient than the electron microscope. The pattern is still in the resist layer. The misalignment of the input waveguide can be seen in the figure.

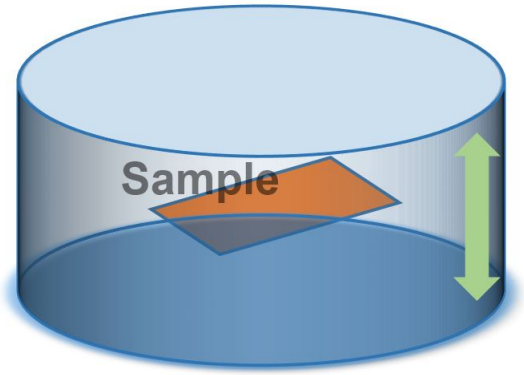

Figure 4.10: Schematic of development process.

to make the developer impact the surface of the sample. Moving too fast will cause the sample to fall off. If the speed is too slow, the development will be insufficient. Also if the tweezers are moved horizontally, the sample surface cannot be impacted and the development is weakened.

The developing temperature also has an effect on the developing speed. In our case, first, the sample is placed in developer ZED-N50 or AR600-546 for 40 seconds and then 30 seconds in isopropyl alcohol (IPA) to stop the development. Then the sample is placed under the blow gun of N_2 for drying the surface. The whole development process has been done under the clean room temperature (21°C). Then the optical microscopy is applied on the sample to get a preliminary lithography result.

4.1.5 ICP etching on silicon layer

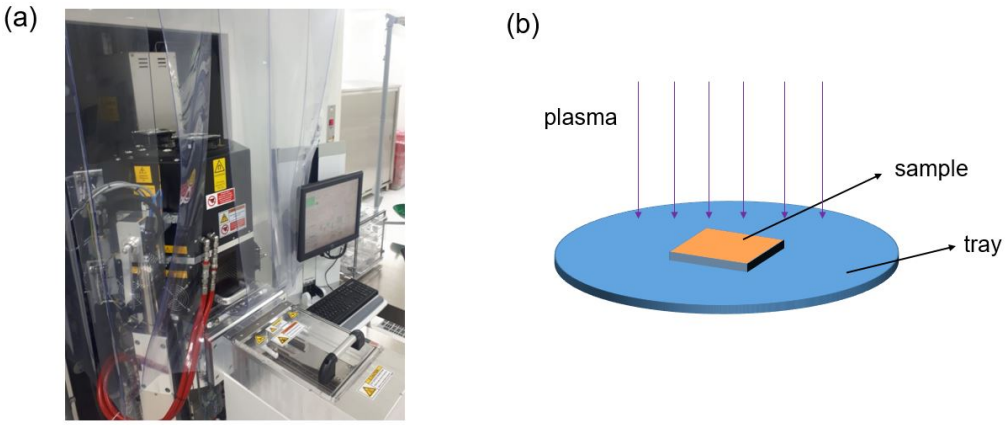

Figure 4.11: (a) ICP-DRIE system in the clean room of laboratory C2N used in this thesis. (b) Schematic of etching principle. The small sample is placed on the tray into the etching chamber. The dry etching gas hits the surface of the sample from above to achieve the purpose of etching.

The etching process has been applied using Inductively Coupled Plasma Deep Reactive Ion Etching (ICP-DRIE) system from STS company as shown in Figure 4.11 (a). The whole set of equipment has two independent emission sources. One set makes the etching gas glow discharge through inductive coupling to generate high-density plasma. The other set acts on the plasma, causing it to direct physical bombardment of the sample. The working etching gas mainly includes SF_6 and C_4F_8. The former is mainly used to etch the silicon layer. The latter acts as a passivation to protect the sidewalls.

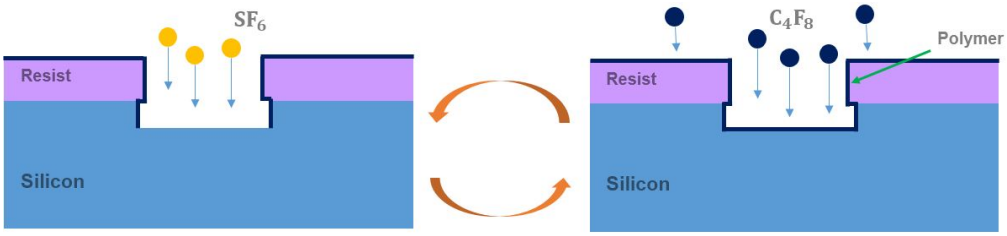

Figure 4.12: Schematic of Bosch DRIE method used to silicon etching. SF_6 is used to form fluorine-based reactive species to act silicon isotropic etching. Then SF_6 pulse is turn off and C_4F_8 pulse is turn on. C_4F_8 can create a resistant passivation polymer layer on the sidewalls and whole surface. The cycle continues until the etching is completed.

One advantage of DRIE is that it uses a Bosch process as shown in Figure 4.12 in which etching and passivation are alternately performed so that the sidewalls can be etched in a controlled manner. Each time SF_6 plasma etches down as much as possible. This is because the passivation polymers on the sidewalls are not directly bombarded by the SF_6 plasma, so

these polymers will last longer. This protects the sidewalls from being etched to achieve the purpose of anisotropic etching.

The sample is then placed on top of the tray (See Figure 4.11 (b)) with inorganic oil acting as adhesive. After entering the chamber of ICP system, a standard 220nm zero degree silicon etching is then performed. This etching process takes relative short time (about 20 seconds). After this, the pattern will be etched into the silicon layer in our case. Then the sample will be transfer to final cleaning step.

4.1.6 Final cleaning

The final cleaning procedure is aim at remove all unnecessary resist, organic or impurity substance on the surface of sample. Two main methods are used in this thesis. The first one is O_2 plasma cleaning which is operated on DIENER Nano machine as shown in Figure 4.13. After placing our sample in the chamber, the timer is set to 3 minutes for O_2 plasma cleansing the resist. For other organic impurities, we then use the Piranha solution which is a mixture of H_2SO_4 and H_2O_2. The mixture has strong oxidizing properties and can completely remove almost all organic matter on the substrate. Pure water with 17°C must be prepared before the process. The sample is placed in Piranha solution for 10 seconds and then in pure water for 5 seconds on average. Repeat the above operation several times. Also shaking the tweezers with samples in pure water is needed to accelerate heat dissipation. Special gloves and face mask should be on to protect the skin and eyes. Then N_2 is used to dry the samples as former steps.

Figure 4.13: The O_2 plasma cleaner system by DIENER Nano is used in this thesis. The sample is placed on a large carrier into the box. Active oxygen plasma then fill the box and clean the surface of the sample.

4.1.7 Sample cleavage

The cutting process has been done using the back-end facilities outside clean room. For a specific diagram of the cleavage operation, refer to Figure 4.14. The mark for cutting is pre-made when designing the mask and now it is used for alignment of cutting. First, a diamond knife is used to create a scratch on the marked position of the sample. Then apply pressure on both ends of the scratch on the sample to split the sample. When a special knife is used to produce scratches on the sample surface, the pressure applied should not be so great as to break the sample. And too little pressure is not enough to produce deep enough scratches. Therefore several attempts are necessary. If a slanted sample boundary is produced in the end, this will have an impact on subsequent sample characterization.

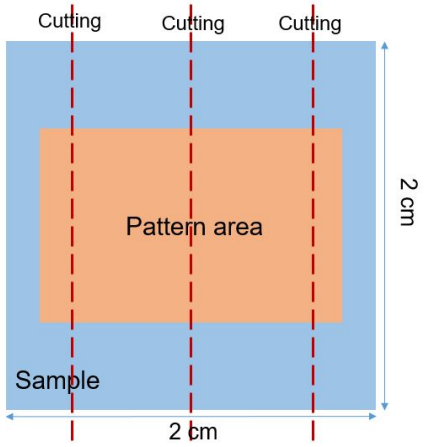

Figure 4.14: Schematic diagram of cutting sample. Three splits are used for square samples. Apply pressure to the left and right of the cutting line to complete the cut. The two middle blocks contain designed valid structures.

After the sample is cut, the dust on the surface should be blown off with a nitrogen gun and placed in the sample box. Due to our choice of edge coupling, in the subsequent characterization process, we should avoid touching the two sides of the rectangle with tweezers to avoid damaging the input and output waveguide. During the movement of the sample, use tweezers to clamp the underneath part that has no effective structure. Also, since the samples need to be transported long distances to another laboratory for SNOM characterization, the tape in the clean room is placed in a box. Then the sample wa met on the tape to fix it to avoid collision and overturning during transportation.

4.2 Results and observation with SEM

In this section, some images of Scanning Electron Microscopy are presented to show the result of fabrication and give some ideas of characterizations. Due to the limited resolution

of optical microscopes, it is difficult to observe clear structures below 0.5um. Therefore, the electron microscope characterization of the sample is very necessary.

Scanning electron microscope is a new type of microscope for observing nano-level structures. It uses the secondary scattered electrons that are emitted by the electron beam onto the sample and scanned by the sensor to image. Two structures processed in this thesis are shown in Figure 4.15 as an example. The electron microscope can photograph with a certain angle tilt. The electrons under the action of high accelerating voltage are incident on the surface of the sample, and produce elastic or inelastic scattering with the nucleus and the electrons outside the nucleus of the sample material, and then stimulate physical signals such as secondary electrons.

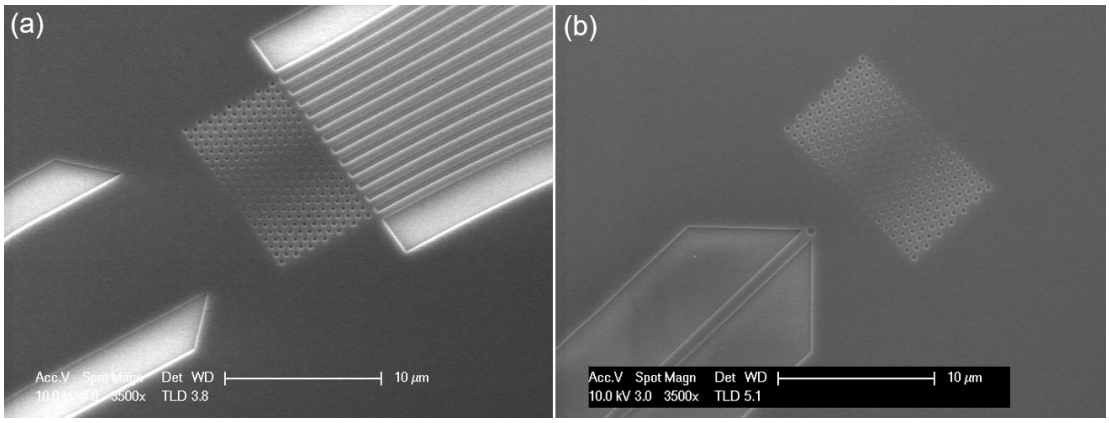

Figure 4.15: (a) The focus structure under the electron microscope. Light enters the lens from the waveguide on the left. The emitted light is derived from the emission waveguide for measurement. (b) The processed collimation structure is composed of on-chip approximate point light sources and lens. SNOM technology instead of the exit waveguide will be used to detect the exit electric field.

The intensity of these physical signals will vary with the characteristics of the sample surface. Subsequently, these signals are collected by the corresponding detectors, amplified proportionally in turn, and transmitted to the display. In the end, we will get a scanned image that reflects the surface characteristics of the sample. Its working principle is somewhat similar to electron beam lithography. Or we can say that electron beam lithography is a more advanced scanning electron microscope system, which has a mobile platform that can be accurate to the sub-nanometer level. The scanning electron microscope photos in this thesis mainly use the models Philips XL30SFEG and Raith150, among which Raith150 is mainly used for size measurement. The electron microscopy images of the sample containing the waveguide and air hole side sections are shown in Figure 4.16.

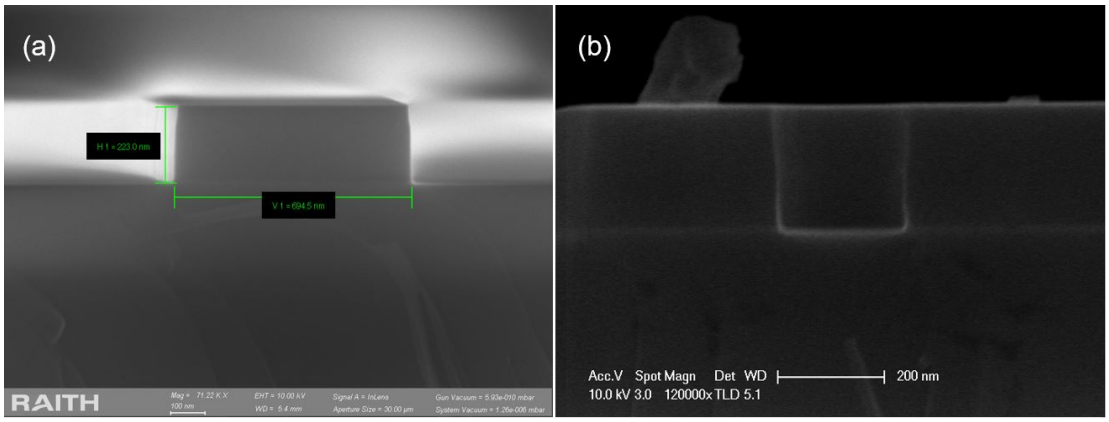

Figure 4.16: (a) Cross-sectional view of the output waveguide on the SOI. The design size is 700nm. The width can be reduced to increase the resolution. (b) Cross-sectional view of the etched air hole. The side walls are approximately vertical.

4.3 Experimental characterization of samples

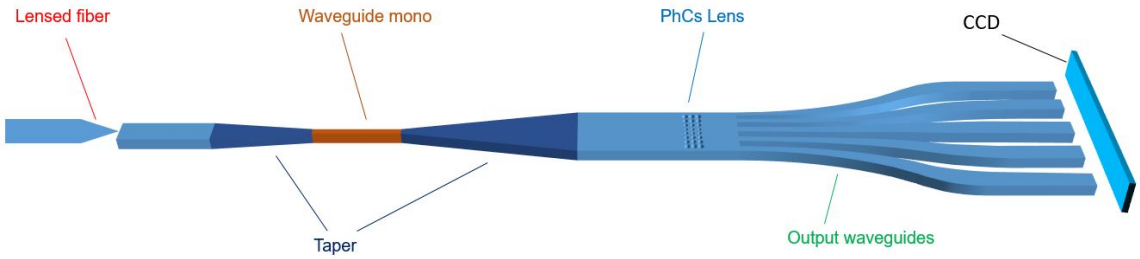

Figure 4.17: Schematic diagram of the overall structure designed for characterization. The light is guided into the multimode waveguide by the lensed fiber. The subsequent single-mode waveguide ensures that the wave is in the fundamental mode. 13 output waveguides are used to direct the light from the output field into the charge-coupled device (CCD) camera.

Two main characterization methods are used in this thesis. First, several sets of waveguides [38] are used to detect the intensity of the emitted electric field as shown in Figure 4.17. By changing the distance from the exit waveguide to the exit surface, we can get a rough overview of the output electric field (See Figure 4.18 (a)). Then, more precise and advanced SNOM technology was used for sample characterization. Through SNOM, we can directly obtain the electric field information at the output end of the lens (See Figure 4.18 (b)). This section will introduce two different characterization methods.

At the same time, we cannot obtain a perfect plane wave in a silicon-based waveguide. In this thesis, a 10µm wide waveguide is used for the input end of the lens. Also single-mode waves are critical. Therefore, the single-mode waveguide is placed behind the edge coupler. The tapered area is to used to smooth the transition of different waveguides, which requires

it to have enough length. A more specific description of the parameters will be shown in the next chapter.

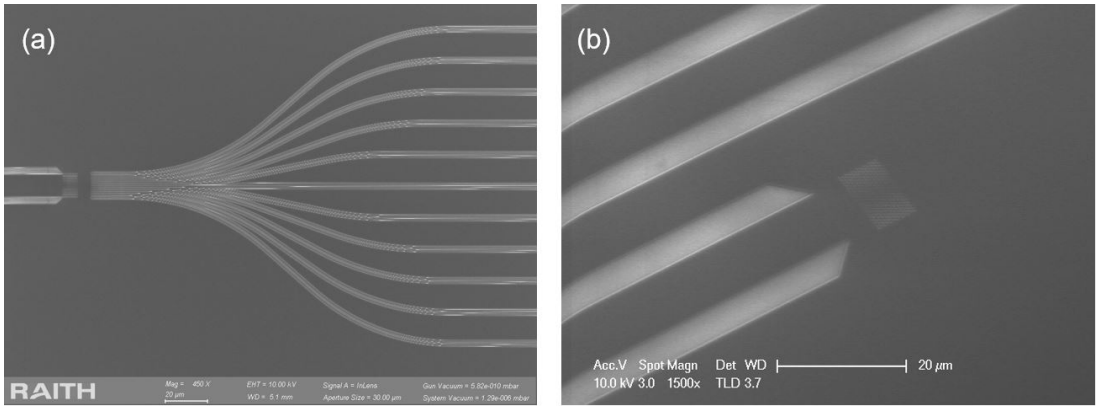

Figure 4.18: Structure used for characterization under an electron microscope. (a) The sets of output waveguide is used as a preliminary characterization tool. (b) The characterization structure designed for SNOM does not have output waveguides.

Edge coupling and grating coupling are two commonly used coupling methods to guide the light into chip. In this thesis, edge coupling is chosen. The light is guided through the lensed fiber into the on-chip waveguide. Edge coupling has high requirements for alignment accuracy. Therefore, it is necessary to adjust the horizontal and vertical directions of the lensed fiber and the waveguide to achieve the highest coupling efficiency.

4.3.1 Preliminary measurement using sets of wave-guides

In order to first verify whether the sample meets the design requirements, multiple sets of output wave-guides are placed on the exit surface of the lens to detect the electric field strength. The wave-guide is 700nm wide each, and there are 13 wave-guides to cover the entire exit surface. Changing the distance between them and the exit surface can obtain an arbitrary range of electric field strength. It should be noted that this multi-group waveguide method can only be used to detect focal points and for plane wave detection we must use the SNOM method. The entire characterization setup must be built on a precision optical platform as shown in Figure 4.19. Vibration should be avoided as much as possible during the characterization process. The light generated by the laser reaches the sample after passing through the polarizer. The sample is placed on the stage. The Elliot-Martock system can precisely regulate the movement of the stage in the x-y-z direction. With the microscope placed above the sample, we align the incident waveguide and the lensed fiber in the x-y plane. At the same time, we observe the image of the infrared camera to complete the alignment in the z-axis direction. Then we remove the beam splitter so that the output signal enters the linear CCD camera which is used to collect the light derived from the set of waveguides. Subse-

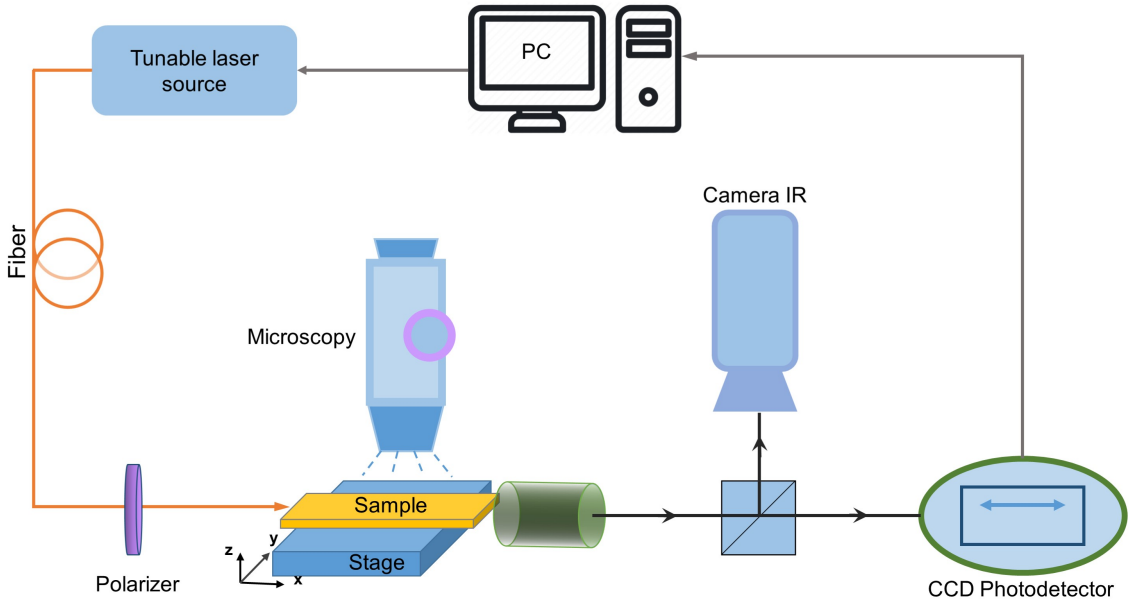

Figure 4.19: Diagram of characterization setup using sets of waveguides.

quently, the optical information is imported into the Labview software on the computer for signal processing. The results will be further discussed in Chapter 5.

4.3.2 Measurement with SNOM

SNOM stands for Scanning Near Field Optical Microscope. As the name implies, it involves a scanning probe microscope. This microscope uses a special probe to collect the evanescent waves generated from the surface of the sample. Using this method, we can break the resolution limit. Thus, information such as the intensity of the field to be observed can be obtained more accurately and directly. The SNOM technique used in this thesis was done in the Laboratoire Interdisciplinaire Carnot de Bourgogne (ICB) in Dijon. The experimental setup was built as shown in Figure 4.20. First, as in the previous output waveguide test method, a tunable laser in TE mode is used to inject the light source into the input waveguide. The edge coupling method is the same as before. Similarly, a single-mode filter with a length of 200µm and a width of 450nm is used to obtain a pure fundamental TE mode. A special dual-arm structure was used for the SNOM test. One arm of this structure goes straight through our effective structure and is used for probe detection. The other auxiliary arm is a straight waveguide and does not contain the effective structure. The function of this auxiliary arm is to facilitate the alignment of the input lensed fiber with the input waveguide. By collecting the light intensity at the end of the auxiliary arm, we can get a clear idea of the alignment efficiency [193]. The SNOM is set to run in collection mode to collect the field intensity at the sample surface. By adjusting the distance z_{scan} between the probe and the sample surface, we can obtain the information of the evanescent field for subsequent analysis. The

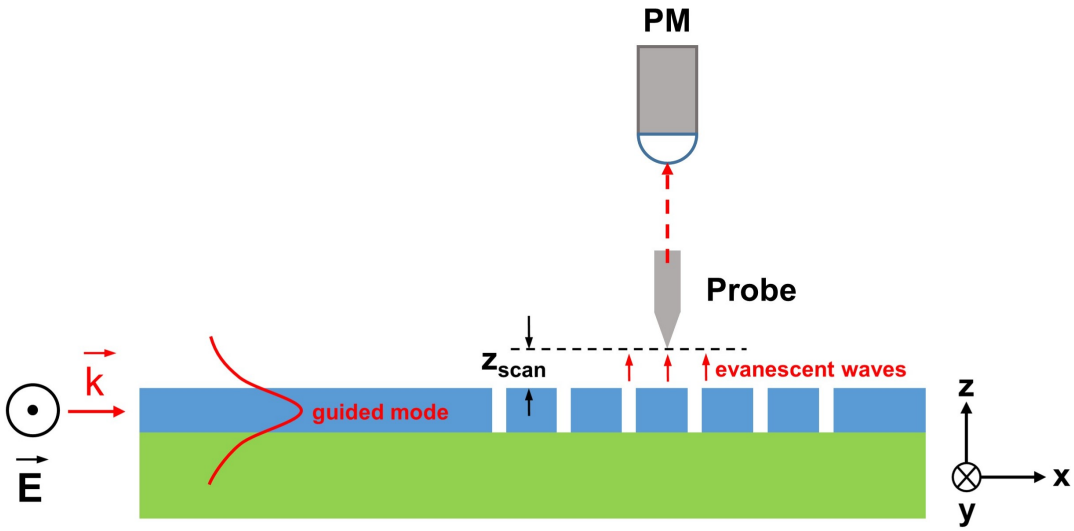

Figure 4.20: Diagram of characterization setup using SNOM. The PM is a photomultiplier which converts the light signal into an electrical signal.

whole characterization process requires a very flat sample surface and a high stability of the experimental platform. Any unnecessary vibration would affect the characterization results. Therefore, several repetitions of the characterization are necessary.

What can be expected is that the SNOM obtains the distribution of the evanescent field emitting from the sample surface [201, 202]. With this comes the fact that we cannot pick the content of the evanescent field. Specifically, the field emitting from the sample surface will inevitably contain some light scattered upward by the etched air hole. The out-of-plane diffraction fields generated by these air holes on the guided mode light have a high intensity and can affect the SNOM characterization results [203]. Therefore, we cannot ignore the CCD camera characterization results obtained from sets of output waveguides. Because the set of output waveguides gives us the in-plane intensity of the optical field without the diffracted field from the air hole. This characterization method with sets of output waveguide has a greater signal-to-noise ratio [204], although the resolution is limited. Combining the results from these two characterization methods allows us to perform a more accurate analysis. Again, specific SNOM characterization results will be discussed further in Chapter 5.

4.4 Conclusion

In this chapter, we present the main processes of nano-fabrication technology used in this thesis. In presenting each specific step, I highlight the relevant instrumentation and materials used. Each laboratory's clean room has its own working guidelines. General safety training and chemical supply training are mandatory before entering the clean room at C2N. After-

wards in the clean room we have two main techniques to use, namely EBL and ICP-etching. Other related electronic templates and job files preparation, samples preparation and their surfaces cleaning are all around these two main techniques.

In general it takes more than 30 hours to expose a 2cm x 2cm sample in this work using EBL with a resolution of 2nm. Therefore, we usually start the machine on Friday night and collect the sample on the following Monday. The ICP etching and cleaning that follows takes a relatively short time. We then need to make a preliminary observation of the sample using a scanning electron microscope. If it does not meet the basic requirements then it needs to be re-fabricated. Of these, obtaining the ideal size of the air holes and ensuring that their sidewalls are vertical is the most challenging. The two characterization methods involved in this work are described later in this chapter. In the absence of the SNOM technique, the distribution of the output electric field intensity can be obtained approximately using the set of output waveguides. The SNOM technique, on the other hand, can provide higher resolution and more intuitive results. The sample structure which corresponds to SNOM measurement is also more compact and takes up less space. Last but not least is the cutting sample process. We need to cut the sample twice and divide it into four pieces. The vertical cut should be parallel to the boundary and not tilted because an tilted cut would destroy the effective structure. On the other hand, the sidewalls of the cut marks at the edges should also be smooth and strictly perpendicular. This ensures a smooth optical coupling afterwards. If the cut is not good, we will also lose time and have to rework it. Therefore, strict manufacturing guidelines and advance planning must be followed so as to increase the possibility of a successful sample.

Chapter 5

Realization and characterization of GPC lens

Contents

5.1 Realization of GPC flat lens on SOI

Like we described in Chapter 4, the processing and manufacturing of the samples is implemented on the SOI platform. In our case, the top silicon layer is 220nm thick, the following is a 3µm thick SiO_2 layer, and the bottom layer is the silicon substrate. The SOI we used is fabricated by SOITEC.

A typical structure designed for characterization with output waveguide sets is given in Figure 5.1. Light is directed onto the chip via optical fiber and edge coupling. Firstly, the light passed through a single mode filter 450nm wide and 200µm long to obtain a single mode. A sufficiently long transition taper waveguide was used to connect the waveguides of different widths. The input waveguide before our lens was a 10µm wide waveguide to obtain a near plane wave. We designed the lens to be placed at a position 5µm behind the waveguide. At the outgoing end of the lens, 13 waveguides of 700 nm width were used to collect the output field intensity.

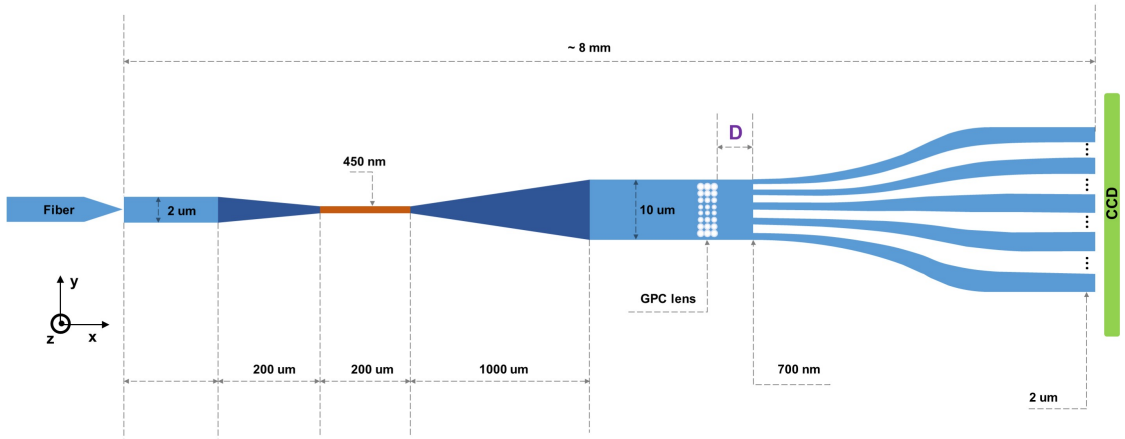

Figure 5.1: Sketch of the experimental structure designed for characterization using sets of output waveguide. The TE fundamental mode passing through the single-mode filter is guided through a 10µm width waveguide into the lens. Behind the output interface of the lens, there are multiple output waveguides to detect and collect the intensity of the output field after the lens. A CCD camera is placed behind the set of output waveguides to collect light.

By varying the distance D between the output waveguides and the lens' outgoing surface, we placed multiple sets of output waveguides. Different resolutions can be obtained by varying the step size of the placed set of output waveguides [205]. In our sample, the step size of the emitting waveguides is 0.5 µm. Their distance to the lens output surface ranges from 0.5 µm to 30 µm. A total of 60 sets of such output waveguides are used to obtain the intensity of the emitted electric field. Multimode interferometers (MMI) splitters are used to split light into two parts of equal intensity. This is to facilitate sample characterization using

SNOM later (see Figure 5.2).

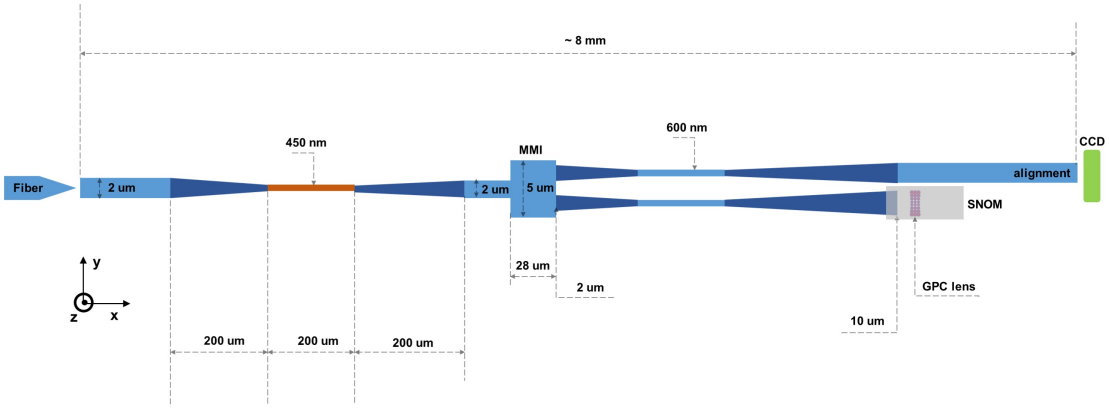

Figure 5.2: Sketch of the experimental setup designed for characterization using SNOM. The TE fundamental mode passing through the single-mode filter is guided into the MMI and thus split into two parts. One auxiliary arm with a CCD camera at the end is used to facilitate the alignment between the lensed fiber and the input waveguide during SNOM characterization. The other arm directs the light into the lens to perform the scanning of SNOM.

After determining and proving that the convergence function of the lens was effective, we fabricated new samples to characterize the collimation function. An approximate on-chip point source was placed at different distances from the lens' incident plane. The distance from the point source to the lens' output surface ranges from 3.5µm to 9.5µm in steps of 0.5µm. Four different point sources are designed and fabricated. The field through the lens is planned to be collected and characterized by means of SNOM. The design of the simulated point light source here is referenced from articles before [189–191].

A test sample was first processed to test and adjust the parameters of the electron beam lithography, such as the dose factor. With the test sample, we found that the diameter of the resulting hole was about 14-15nm larger than the design hole diameter at the specific dose factor. Therefore, the dose factor was increased and the diameter was reduced by 12nm on the left side and 8nm on the right side when performing new fabrication. The left and right sides have the same structure and mirror distribution except for the different size of the air holes in the lens. This allows us to save processing space to obtain greater efficiency.

SEM images of the different samples are shown in Figure 5.3 and Figure 5.4.

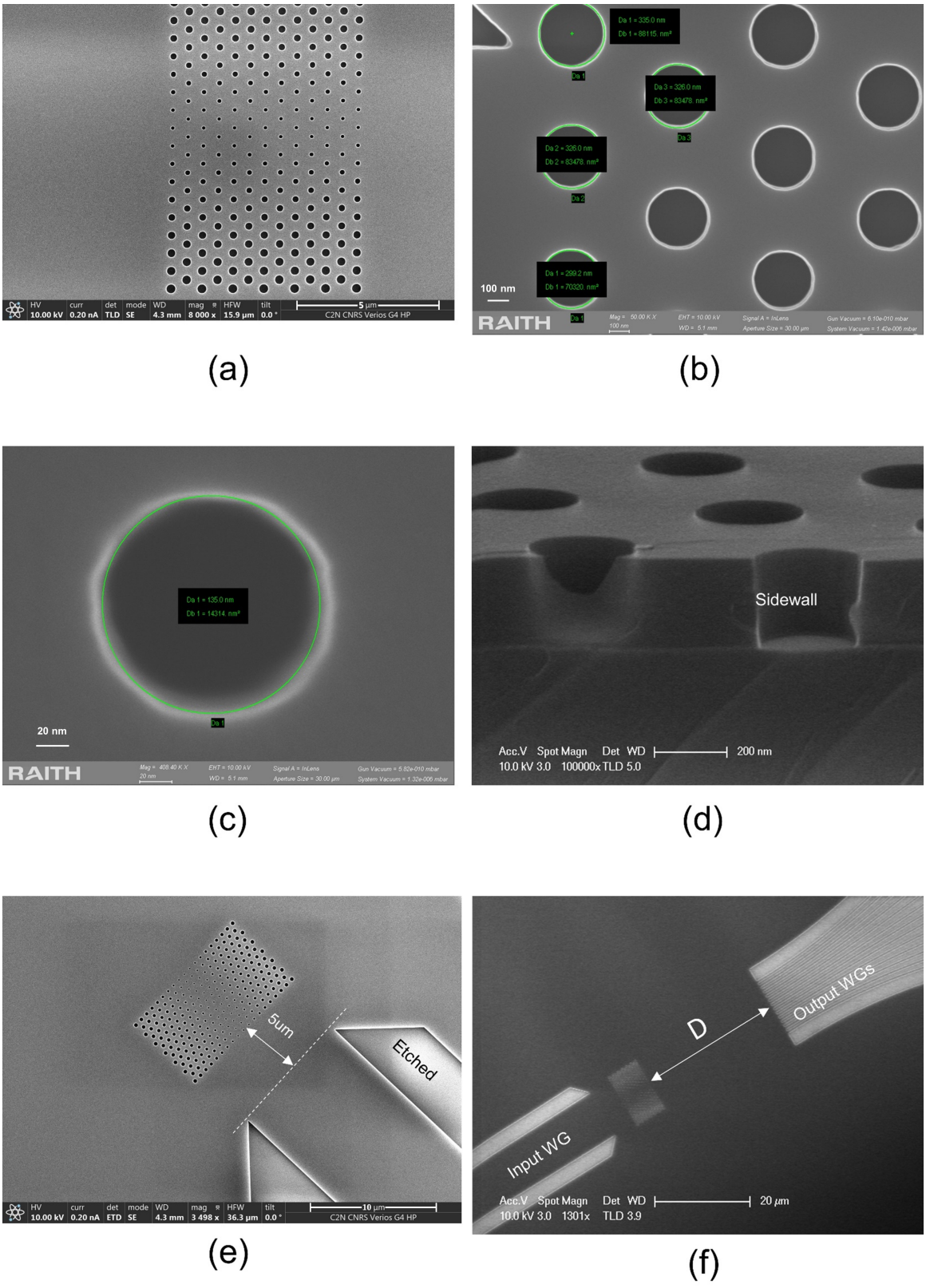

Figure 5.3: SEM images of fabricated flat lens. (a) General top view of lens. (b) Size measurement of air holes in the test sample. (c) The minimum diameter size of air holes in the test sample is around 135nm. (d) Side shot of the etched air hole. (e) The lens was placed at approximately 5µm from the input waveguide. (f) Changing the distance D in the figure to obtain the focus length.

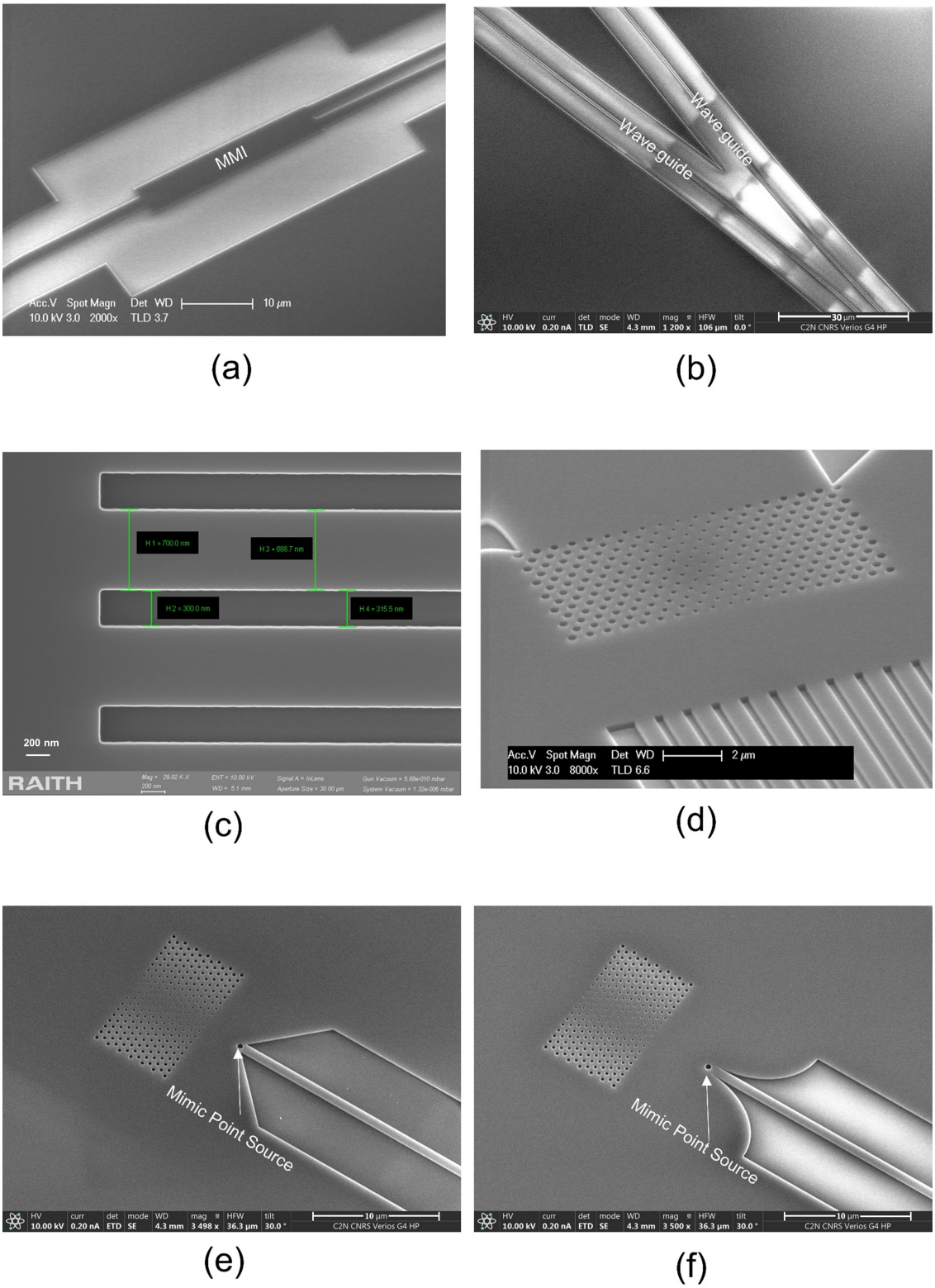

Figure 5.4: SEM images of fabricated flat lens. (a) MMI fabricated for SNOM measurement after. (b) The two identical waveguides were separated after the MMI. (c) The output waveguide was 700nm wide and the distance between each is 300nm. (d) Tilted view of lens and output waveguides. (e) One possibility of designed on-chip point source. (f) Another possibility of designed on-chip point source.

5.2 Realization of Half Maxwell-Fisheye on SOI

For the characterization structure designed for Half Maxwell-Fisheye, we took the same structure as the flat lens before (see Figure 5.5). The diameter of the Half Maxwell-Fisheye lens was also designed to have a length of about 10.4 µm to accommodate a 10 µm wide input waveguide. The structures using the set of output waveguides and the structures using using SNOM were processed on the same 2cm x 2cm SOI platform. For the structure using the set of output waveguides, we chose 30 different distances D, ranging from 0µm to 14.5µm with spaced 0.5µm intervals. For the structures characterized using SNOM, four identical ones were designed to ensure fabrication tolerance. The specific characterization methods and procedures are identical to those of the previous flat lens and will not be repeated here.

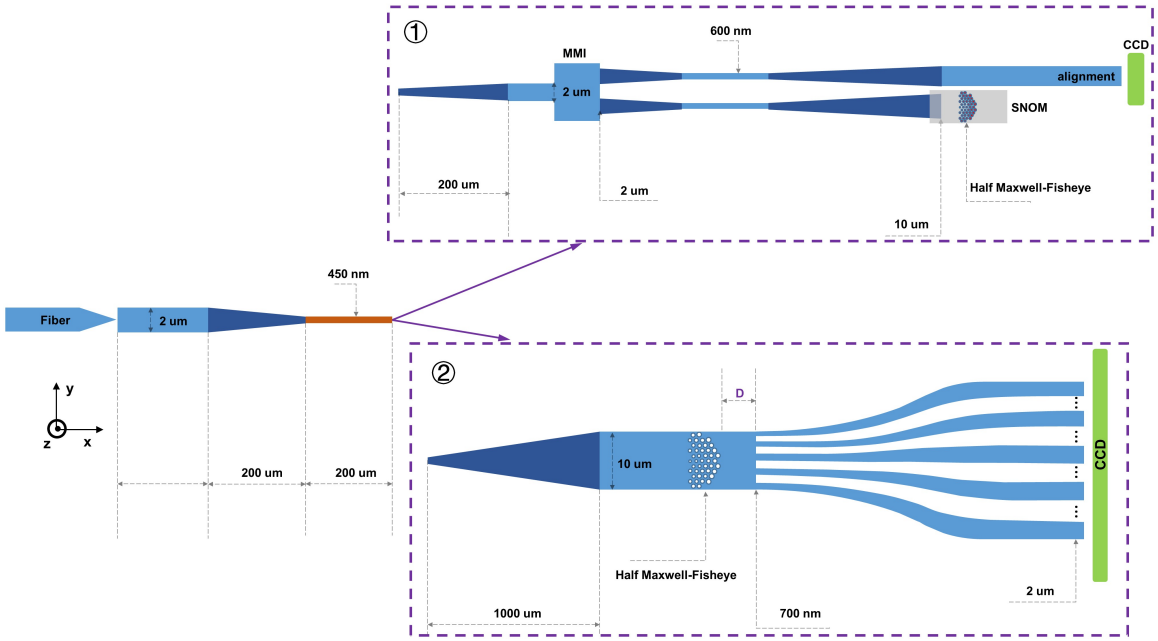

Figure 5.5: Sketch of the experimental setup designed for Half Maxwell-Fisheye characterization. The structure is basically the same except that Half Maxwell-Fisheye is used to replace the previous flat lens. Two characterization methods, the set of output waveguides (Down) and SNOM (Up), were designed for the measurement.

The samples obtained from the first processing were not ideal. After the EBL process, some resist remained due to insufficient development. This further affected the dry etching afterwards. In Figure 5.6, we can see that some small air holes in the center of Half Maxwell-Fisheye lens were not etched. And for the large air holes after etching, their edges are also non-regular. We had planned the subsequent fabrication, but it was interrupted by the suddenly pass away of our engineer and the lack of time. For these reasons, the Half Maxwell-Fisheye lens was not characterized in the end.

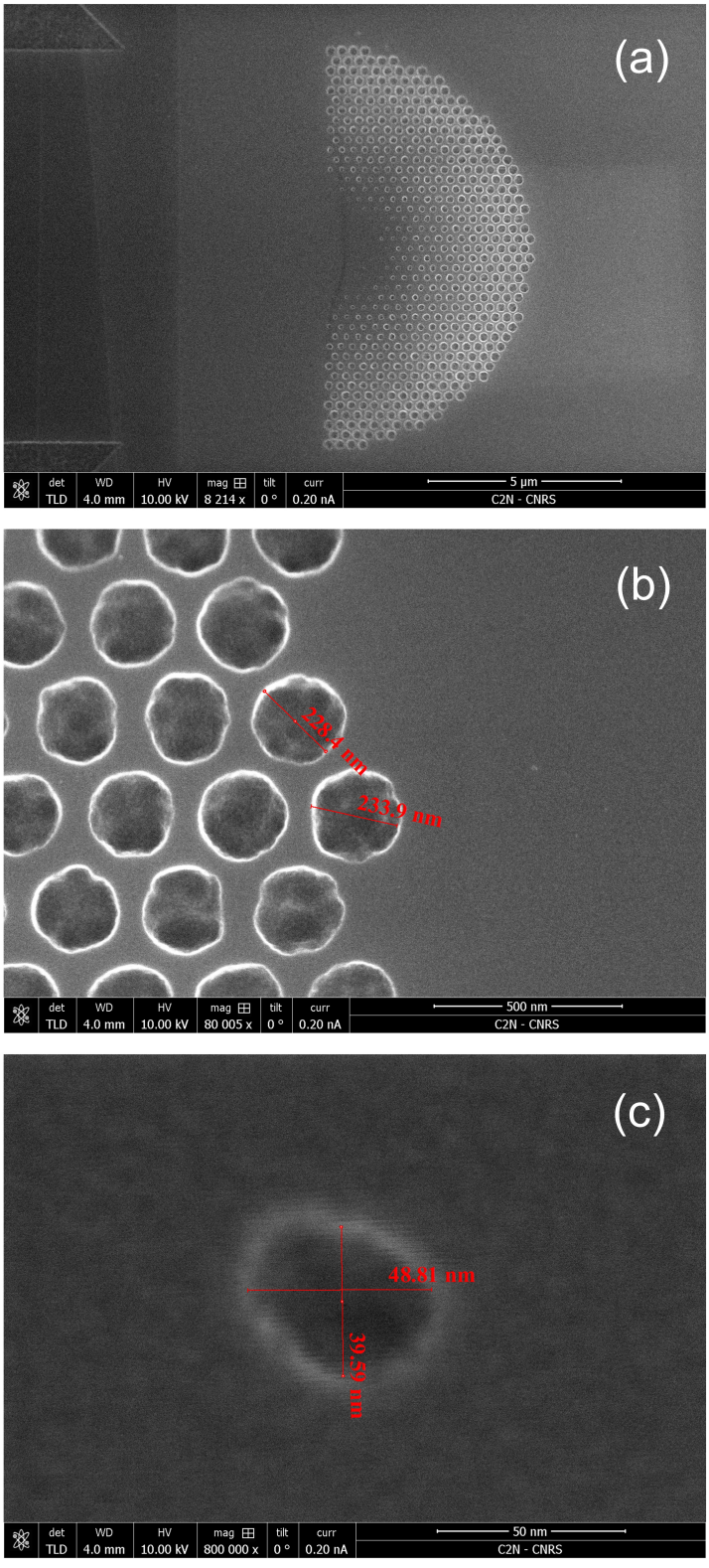

Figure 5.6: SEM images of the first fabricated Half Maxwell-Fisheye lens. (a) A general view of the Half Maxwell-Fisheye. (b) Large air holes region at the edge of the lens. Their boundaries are not regular and not fully etched. (c) The smallest air hole that was etched, which is obviously not circular. Generally, the size of the air holes is smaller than designed because of insufficient development and followed etching.

5.3 Characterization by the set of output waveguides

The principles of characterization platform construction and usage details have been introduced in Chapter 4. In this section, the results obtained from the characterization of the sample using the set of output waveguides will be described in detail.

As shown in the previous section, the set of output waveguides is composed of 13 output waveguides 700 nm wide and 300 nm apart in the beginning. This allows the set of output waveguides to be 13 µm wide, which is slightly larger than the length of the lens at 11.6 µm. Thus, the set of output waveguides can completely cover the lens and thus collect all the light emitted from the output of the lens. At the same time, each of the output waveguide width gradually increases from 700 nm to 2 µm at the end. The distance between different waveguides also gradually increases. This is to facilitate the measurement by CCD camera. We then processed dozens of such set of waveguides by varying the distance D. The interval between the different sets is 0.5 µm, and the closest distance to the lens output surface is 0.5 µm. With such different set of waveguides, we can obtain the field intensity distribution behind the lens output. In the actual characterization, we have obtained the field intensity distribution at the distance of 0.5µm, 1µm, 2µm....26µm. We use a linear CCD camera to obtain the field intensity in the waveguide. Since these are preliminary measurements, a resolution of 1µm is not very high. The final more accurate experimental measurements will be given using the SNOM technique. The lasers used in the experiments range from 1.5 µm to 1.64 µm with a resolution of 1 nm. We have scanned the entire available wavelength range. Due to the limitation of the spectral range of the laser machine, we were unable to obtain results above 1.64 µm wavelength. Since the distance between the set of output waveguides is 1µm (resolution 1µm), I used interpolation to process the data.

The output field intensity distribution at some wavelengths is shown in Figure 5.7-5.9.

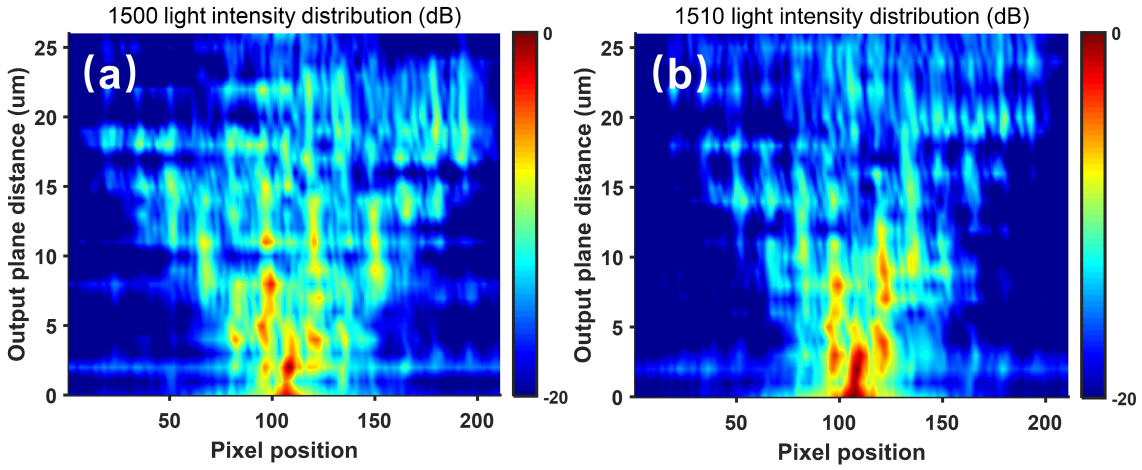

Figure 5.7: Colormap of normalized light intensity distribution collected by CCD camera as a function of output plane distance D for single wave length. (a) λ= 1.5µm. (b) λ= 1.51µm.

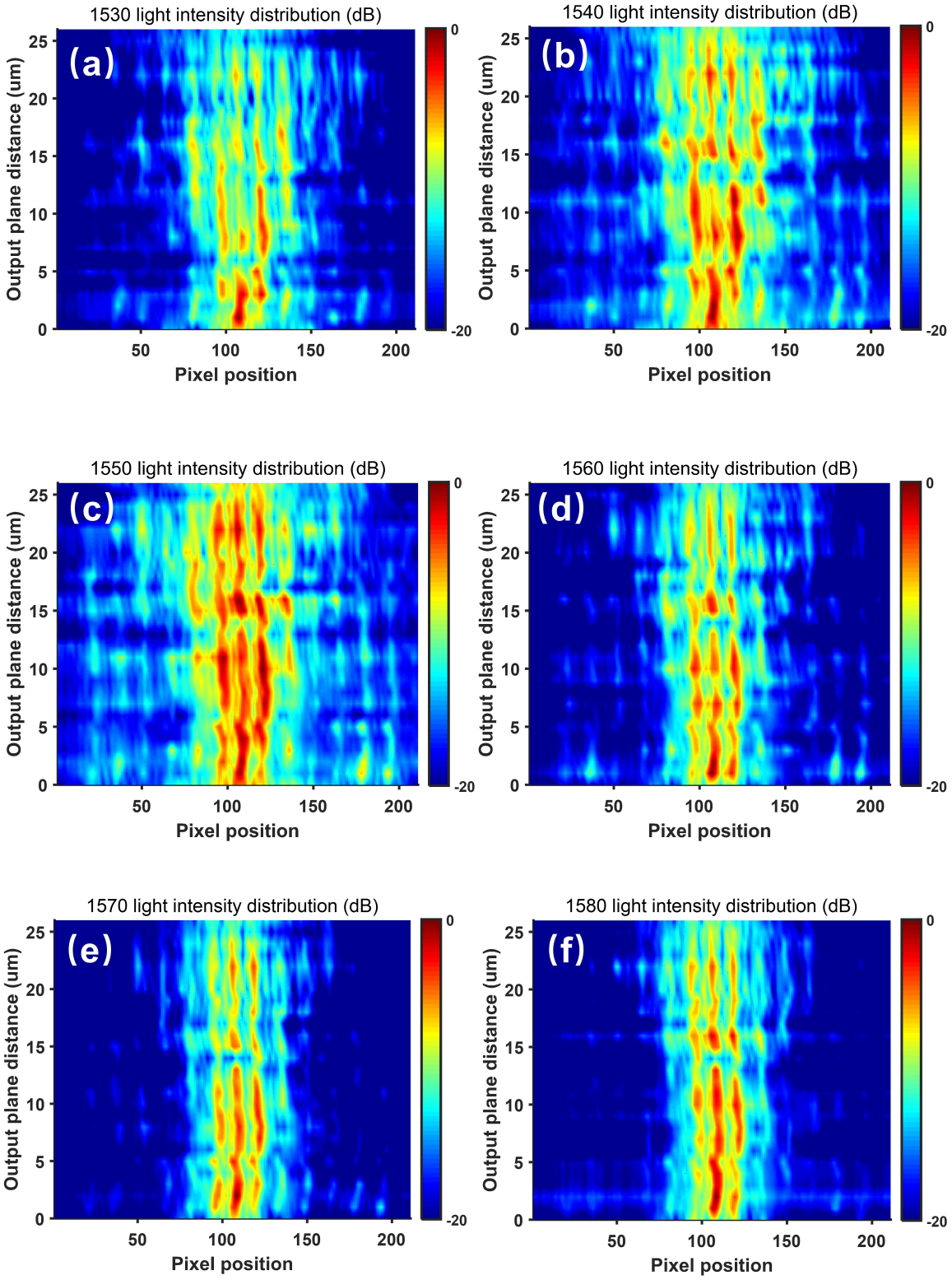

Figure 5.8: Colormap of normalized light intensity distribution collected by CCD camera as a function of output plane distance D for single wave length. (a) λ= 1.53µm. (b) λ= 1.54µm. (c) λ= 1.55µm. (d) λ= 1.56µm. (e) λ= 1.57µm. (f) λ= 1.58µm.

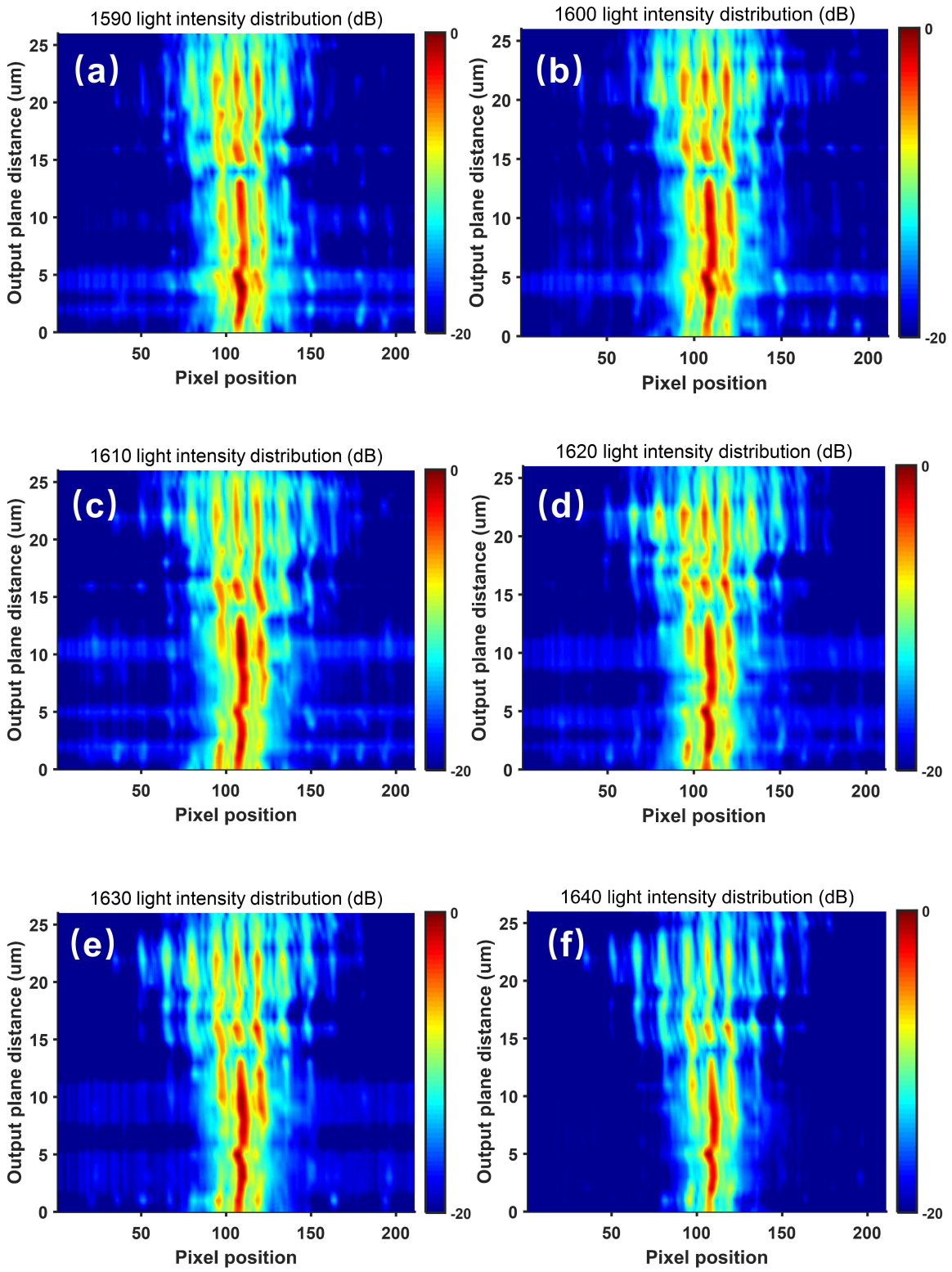

Figure 5.9: Colormap of normalized light intensity distribution collected by CCD camera as a function of output plane distance D for single wave length. (a) λ= 1.59µm. (b) λ= 1.6µm. (c) λ= 1.61µm. (d) λ= 1.62µm. (e) λ= 1.63µm. (f) λ= 1.64µm.

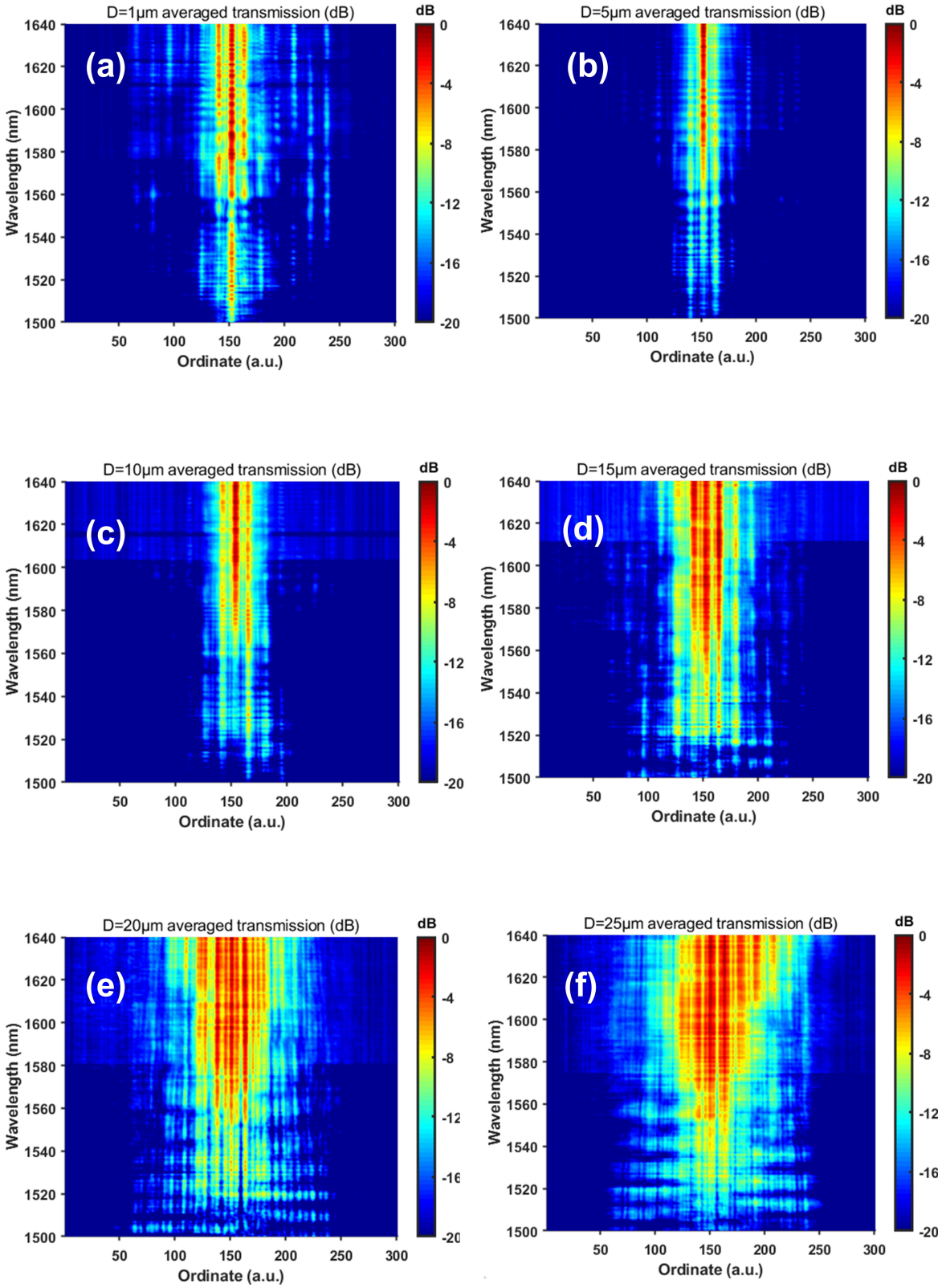

Figure 5.10: Colormap of normalized light intensity distribution as a function of frequency for the GPCs lens with output plane distance D. (a) D=1μm. (b) D=5μm. (c) D=10μm. (d) D=15μm. (e) D=20μm. (f) D=25μm. D is the distance from the output waveguide plane to the lens.

By analyzing the field intensity distribution at the output corresponding to different wavelength, when the focusing effect does not occur, we can clearly see that the field strength exists in all 13 output waveguides. As the wavelength gradually increases, the intensity of the field in several waveguides away from the central axis gradually decreases. The field intensity in the waveguides near the central axis of the lens, especially at the central axis, gradually increases. Starting from 1.6 μm, we can already observe the focusing effect more clearly. Since our output waveguides cover the distance from 0.5μm to 26μm from the lens, we can observe a sufficient range of field intensity distribution. At 1.64 μm, the intensity of the output field is almost entirely concentrated at the middle waveguide and reaches the highest value (see Figure 5.9 (f)). And we can see from the distribution of the output field intensity that the focal point position is about 5μm away from the lens output surface, which is consistent with the previous simulation results. The field intensity at locations too close to and far from the lens output surface are weaker than those at the focal point.

Also we must note that the results shown in Figures 5.7-5.9 are after normalization of the field intensity at each wavelength. And for different wavelengths, the field intensity in the same output plane is different. In other words, the transmission efficiency of the lens is different for different wavelengths. This part of the result we show in Figure 5.10. We have chosen the case when the distance between the set of output waveguides and the lens is D=1μm, 5μm, 10μm, 15μm, 20μm, 25μm. It can be seen that the field strength always increases with wavelength for different positions of the output plane. The field intensity at a wavelength of 1.64 μm is much higher than the field intensity at a wavelength of 1.5 μm for all values of distance D. In other words, the transmission efficiency of the lens for 1.64 μm is much higher than that for 1.5 μm. Therefore, when we analyze the Figure 5.7-5.9, we should also consider that the field intensities are different at different wavelengths.

To show the relative intensity of the field at different wavelengths, we can use a more intuitive diagram. In Figure 5.11 the field intensity distribution at the output is shown for wavelength of 1.5μm, 1.55μm, 1.6μm and 1.64μm without normalization for each frequency. As we can see, the intensity of the peak at wavelength 1.64μm is about four times higher than the peak intensity at wavelength 1.5μm. Also, the lens output field intensity is increasing with wavelength. Therefore, although the output light has a peak at about D= 3μm at wavelength 1.5μm, it is not a true focusing effect at this point.

Analysis of wavelength shift

For the available wavelength range 1.5μm to 1.64μm, the intensity of the output field at 1.64μm is almost concentrated at the middle waveguide of the 13 output waveguides. The field strength at the middle waveguide is also significantly greater than that at other wavelengths at this time (see Figure 5.11). For the target wavelength of 1.55μm used in the simulation, the output field strength is concentrated at the middle three waveguides only (see Figure 5.8 (c)). The intensity of field is also not as strong as at 1.64μm. There are two

possible explanations for this shift.

1) Errors caused by fabrication. Though we have taken many measures to reduce the unwanted effects of fabrication errors in the actual process. Such measures include the use of left and right mirror structures, fabricating test samples and repeated fabrication, and correction of the proximity effect of EBL. However, when we are using SEM for observation and measurement of structures, there is a measurement error of $\pm$ 5 nm. Therefore, it is unlikely that the actual air hole size obtained in the end will be exactly the same as the size in the simulation. There is also the fact that the calibration current of the EBL is different every time, basically between 0.48 nA and 0.51 nA. This results in different sample feature sizes for each fabrication process. And it is well known that photonic crystals are very sensitive to the size of their unit structures. Thus, the final shift in wavelength could occur.

2) The error caused by using EIM when modeling. As introduced in Chapter 2, the effective index method is an approximate method that uses 2D calculations to approach the 3D structure. As an approximation method, errors are inevitable. Especially when the corresponding structure has a high refractive index contrast like in our case (n_{Si}=3.47, n_{SiO_2}=1.44), the accuracy of the effective index method is decreased [116, 123, 125]. Therefore, the uncertainty introduced when we apply EIM to calculate the band diagram of 3D structured photonic crystals will have an impact on the subsequent design. In summary, the above two factors could be the main reasons for the wavelength shift.

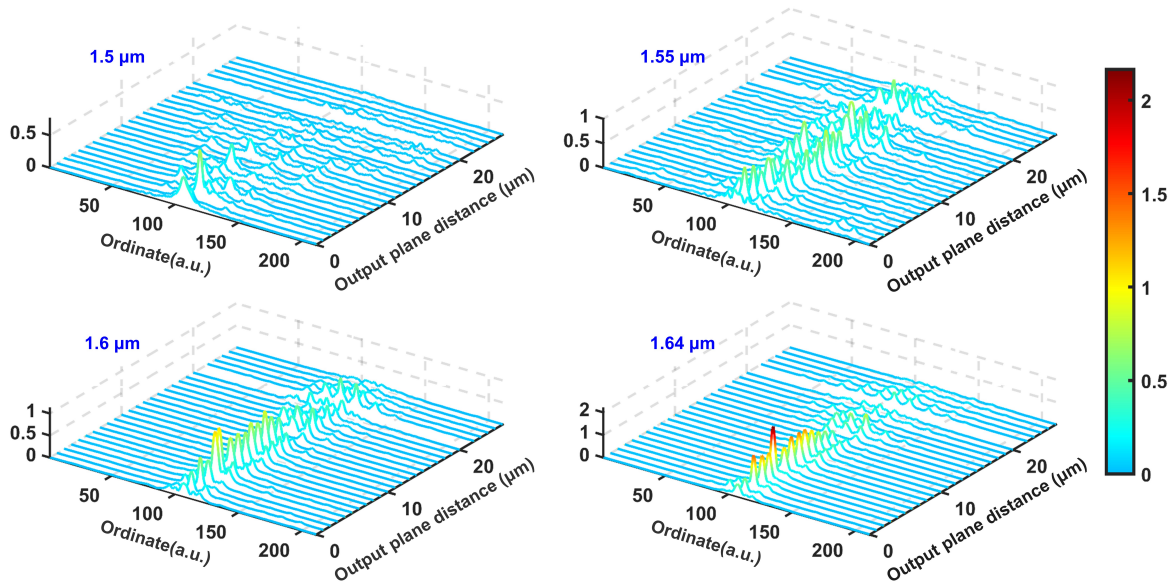

Figure 5.11: Evolution of the distribution of absolute light intensity with the variation of output plane distance D at different operation frequencies. D is the distance from the output waveguide plane to the lens.

5.4 Characterization by SNOM

After the initial test results were obtained using the output waveguide set, we used the SNOM technique to further characterize the sample in order to obtain a higher resolution. I have described the SNOM technique and the initial setup earlier in this manuscript in Chapter 4, so I will not repeat it here. During the SNOM characterization, the vibration of the laboratory construction caused some impact on the characterization platform. In order to minimize this negative effect and to improve the characterization accuracy, the samples were repeatedly tested and the SNOM probe was replaced and adjusted.

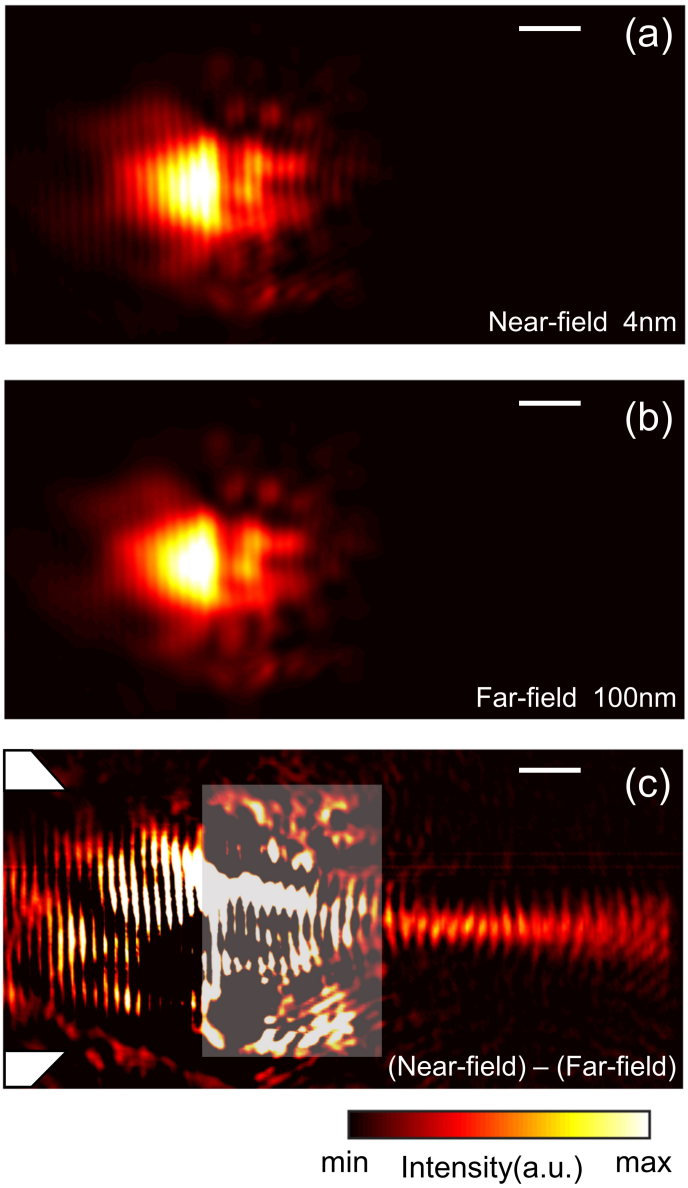

Figure 5.12: SNOM images recorded at (a) 4nm near-field and (b) 100nm far-field above the sample surface. (c) SNOM image of the lens after subtracting the near-field image by the far-field one. The gray color area corresponds to the lens. Scale bar 2 μm.

For the processing of SNOM characterization data I used WSXM software [206]. This is a free, specially developed software for processing scanning probe microscopy data. By using this software, I loaded and visualized the data obtained from the characterization and performed preliminary data processing. The software also contains a variety of ways to process raw data. For further data processing I also used the MATLAB software. In the following, I will show and analyze the obtained SNOM characterization results.

Figure 5.12 shows the images obtained when the microscope probes are at 4 nm (near-field) and 100 nm (far-field) on the sample surface, respectively. We can see that the directly obtained image mainly consists of the intense maximum of the detected light and high frequency oscillation waves. The intensity maxima, also known as the bright spot, is caused by the scattering of the guided light by the air holes. The lens produces an out-of-plane radiation leakage to the guided light. The high-frequency oscillation wave (see Figure 5.12 (a)), on the other hand, originates from the evanescent tail of the in-plane guided waves inside the top Si layer. Comparing (a) and (b) in Figure 5.12, the intensity of the saturated bright spot decreases and the intensity of the oscillation wave diminishes as the probe is moved away from the sample surface. This phenomenon reveals the evanescent behavior of the collected light. At the same time, the microscope probe is more efficient in collecting diffraction waves caused by air holes than in-plane guided waves. This analysis is based on the fact that when the probe reaches a distance of 100 nm from the sample surface (see Figure 5.12 (b)), the oscillation waves greatly weakened while the bright spots remain visible and strong. This characterization result is also consistent with the simulation results which we will present below.

In addition, the intensity of the out-of-plane diffraction field is so high that we cannot observe the distribution of the field behind the lens, regardless of the location of the probe. To reduce the effect of this scattered field, we subtracted the near-field image by the far-field image [193]. By this subtractive extraction, we minimize the influence of the bright spots generated by the scattered field on the results. Thus, we could obtain a more specific visualization of the field distribution of the oscillating wave, i.e., the guided wave in the silicon layer. In Figure 5.12 (c), it is clearly observed from the corrected SNOM results that the wave front advances in parallel before entering the lens. After, the wave front bends and converges when passing through the lens region. While after the lens, the guided light focuses to the lens center axis. This is consistent with the results of our previous simulations.

a) Field distribution at different locations from the sample surface

The simulation results shown previously in Chapter 3 are all about the distribution of the field at the middle of the 220 nm thick silicon layer. Since the light is confined in the silicon layer, we get the distribution of the guided light in the silicon slab. And after that we adopt two different characterization methods, respectively, the sets of output waveguide and the SNOM technique to obtain the field distribution. For the set output waveguides, it is this intensity

distribution of the guided light that we will obtain. Therefore, we can and will compare the results obtained from the set of output waveguides characterization with the previous simulation results. As for the SNOM technique, its probe is at a certain distance from the sample surface. Therefore, it detects not only the evanescent field generated by the guide light but also the out-of-plane diffraction field caused by the air holes in the lens [203]. Thus, the distribution of the field at this position may be different from the previous simulation results. So what we will show below is the distribution of the field at different locations from the surface of the silicon layer.

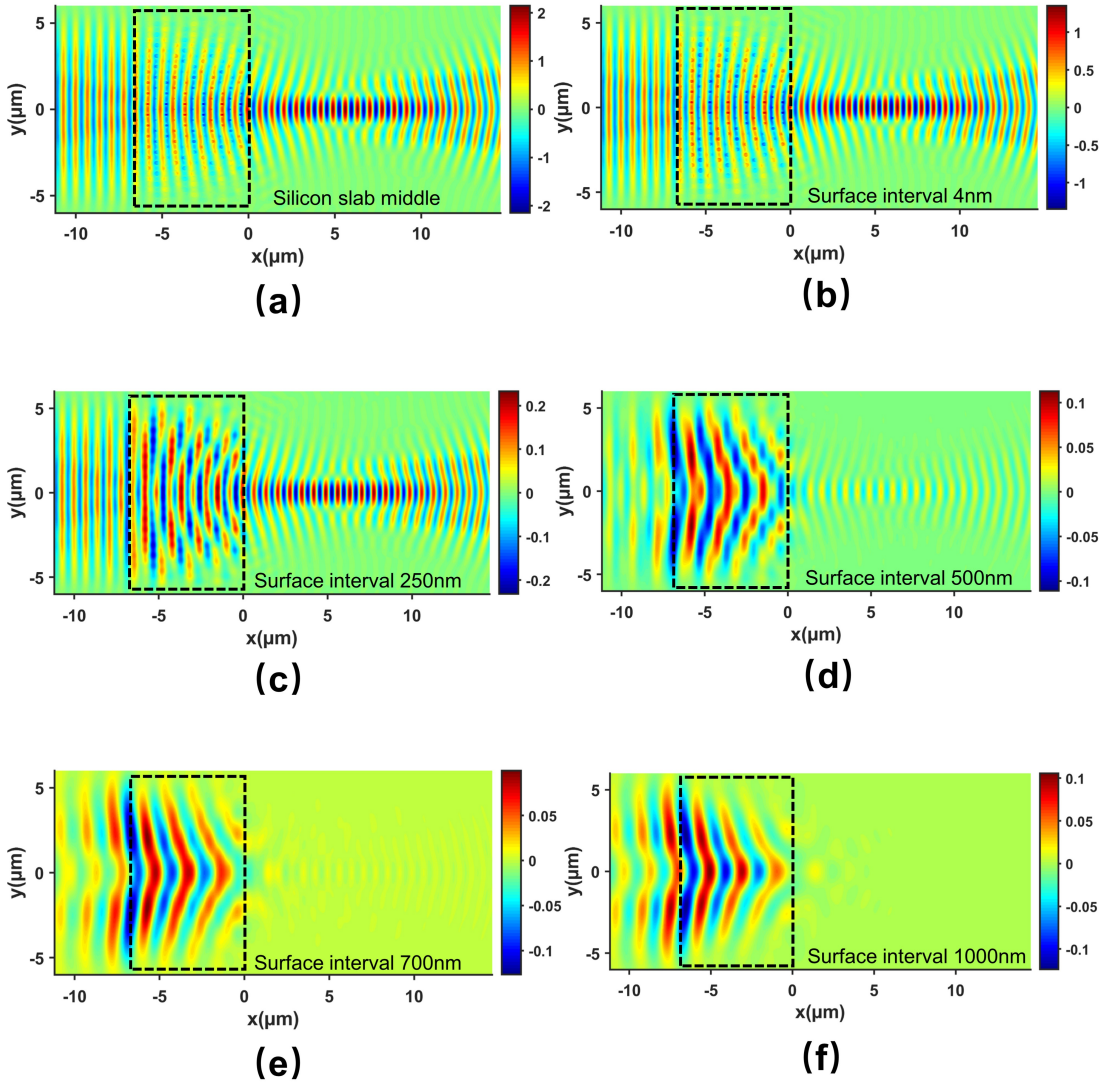

Figure 5.13: Distribution of the E_y field at different distances from the top Si layer surface. (a) Middle of the 220nm silicon layer. (b) z_{sim}=4nm from the surface. (c) z_{sim}=250nm from the surface. (d) z_{sim}=500nm from the surface. (e) z_{sim}=700nm from the surface. (f) z_{sim}=1000nm from the surface. Inside the black dashed box is the lens.

From Figure 5.13 we can observe that the oscillating wave after the lens' output side

dominates when the position is in the middle of the top silicon layer. And as the position gradually moves away from the surface of the top silicon layer, the intensity of the diffraction field caused by the air holes in the lens will gradually be greater than the intensity of the evanescent field generated by the guided light in the silicon layer. When the distance from the Si layer surface is 700 nm, only a weak oscillation wave exists after the lens' output side. And when the distance continues to increase to 1000 nm (see Figure 5.13 (f)), almost no oscillation wave is observed after the lens. Also, the intensity of the observed field is mainly concentrated in the diffraction field region directly above the lens. And the intensity of the diffraction field is only slightly weaker at this time compared to the case when the distance is 500 nm (see Figure 5.13 (d)). This phenomenon can be understood as the diffraction field above the lens is caused by the multiple scattering of light by the air holes in the lens. The diffraction field can propagate further and decay weaker than the evanescent field (i.e., the oscillation wave in the figure) generated by the guided light, which exists only near the surface of the silicon layer. The simulations and analysis in this subsection will help us to understand the results obtained by the SNOM measurement.

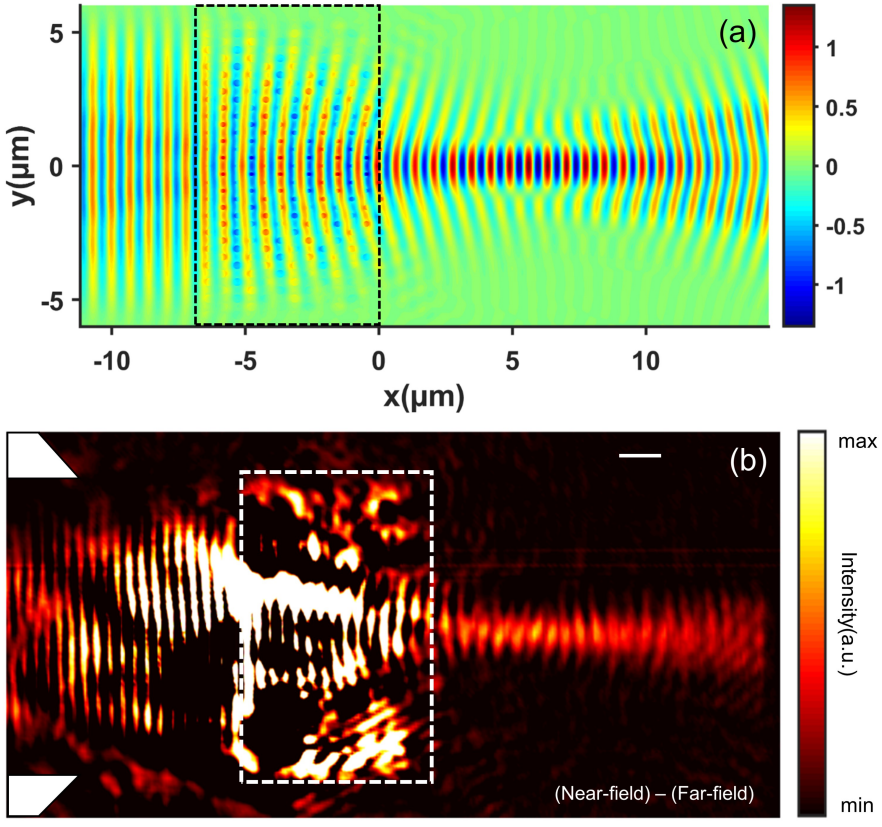

Figure 5.14: Comparison of simulation results with SNOM characterization results. (a) Field E_y distribution at z_{sim}=4nm from the top Si surface. (b) SNOM image of the lens after subtracting the near-field (z_{scan}=4nm) image by the far-field (z_{scan}=100nm) one. Scale bar 2 μm.

After analyzing the field distribution at different distances from the top Si surface, we

compare the simulation results with the previously obtained SNOM extraction results (see Figure 5.14). We can see that the lens focuses the plane wave. And the previous operation of using the near-field minus the far-field makes the field after lens much clearer. We can conclude that the experimental results match with the simulation results.

b) Quantitative analysis

To further quantitative analysis of the SNOM results and to provide a better visualization of the field distribution of the guided light, I used the DERIVATIVE filter in the WSXM software. This filter makes the boundaries in the image clearer and the contrast more pronounced, while the regions of a constant slope are shown with the same color. In other words, this filter allows us to minimize the negative impact of bright spots caused by diffracted waves and to focus more on the analysis of the oscillation waves generated by the guided light.

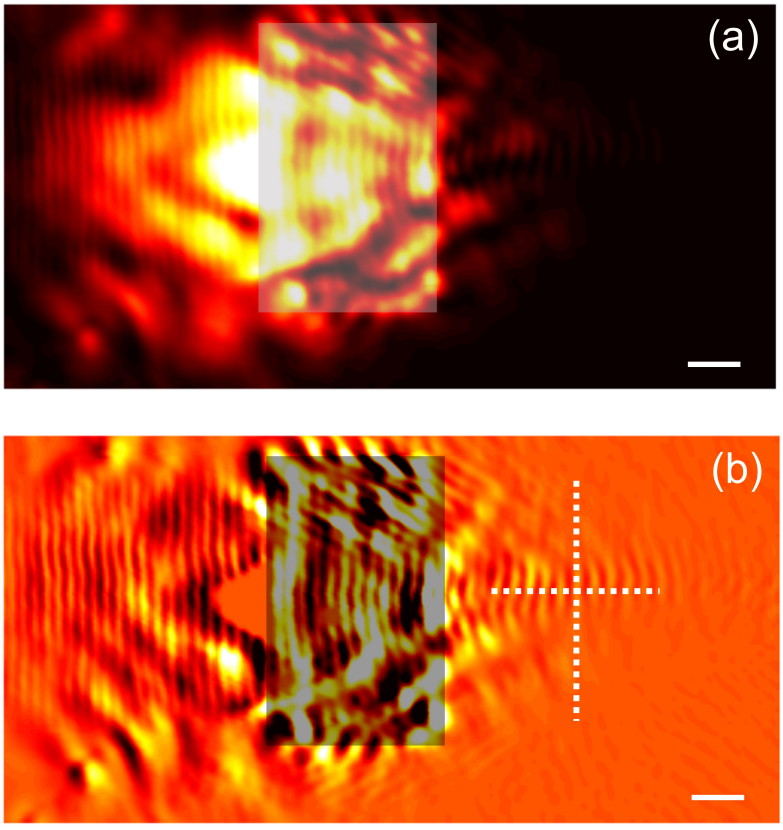

Figure 5.15: (a) The original SNOM image of the lens. (b) Image after Derivative filter. Scale bar 2 µm.

The unfiltered SNOM image is given in Figure 5.15 (a) while the Derivative filtered image is shown in (b). We can see that the oscillation waves are shown more clearly in (b) while the bright spots are filtered. The shaded area in both images is the location of the lens. With the filtered image, we can clearly observe the bending and focusing effect of the lens on the guided light. We then extracted the experimental data from the field behind the lens in (b) and

compared it with the previous simulation results. At the focal point of about 5.7µm behind the lens, we compared the experimental and simulated results in both vertical and horizontal sections (see Figure 5.16 (a) and (b)). As can be seen from the figures, quantitative agreement is achieved in both directions. The experimental results are in agreement with the predictions of the previous numerical simulations. The FWHM of the horizontal direction at the focal point is 0.87µm = 0.53 λ, here $\lambda = 1.63$µm.

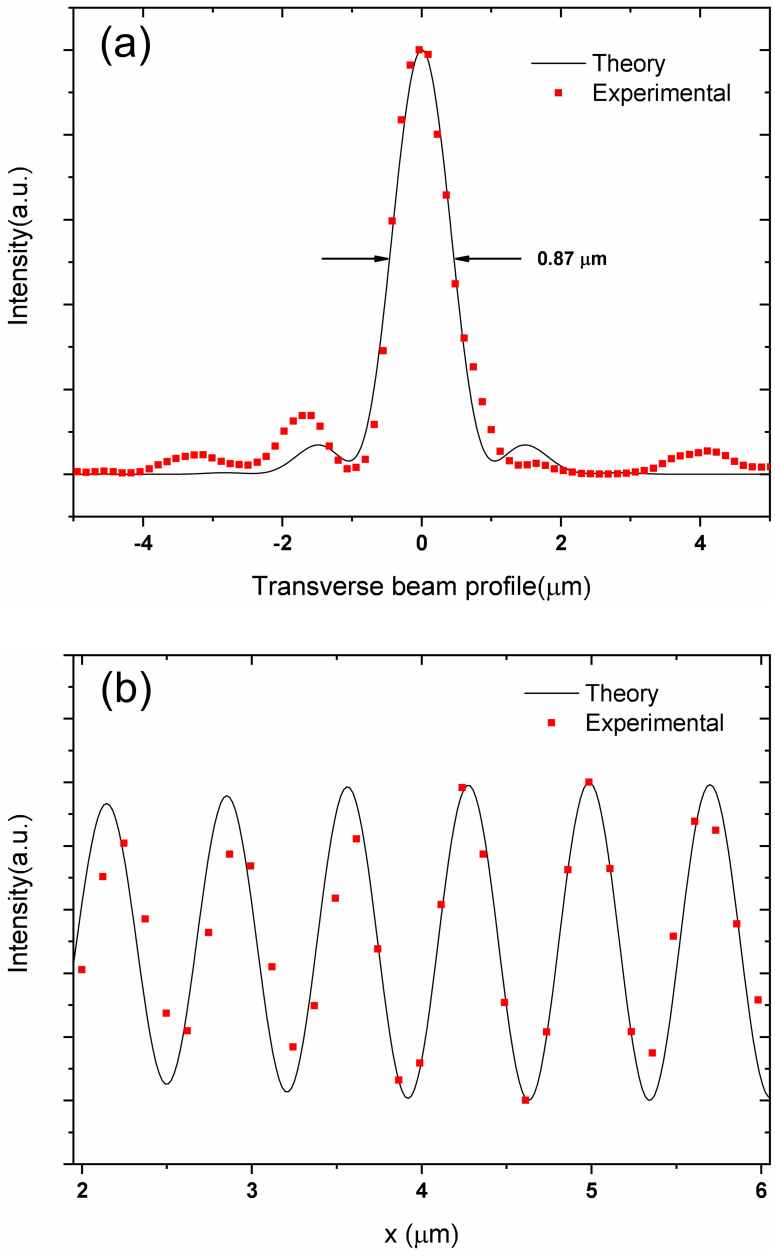

Figure 5.16: (a) Comparison of experimental and theoretical data at the vertical white dotted line (focal plane) shown in Figure 5.15 (b). FWHM = 0.87µm = 0.53 λ, here $\lambda = 1.63$µm. (b) Comparison of experimental and theoretical data at the horizontal white dotted line shown in Figure 5.15 (b).

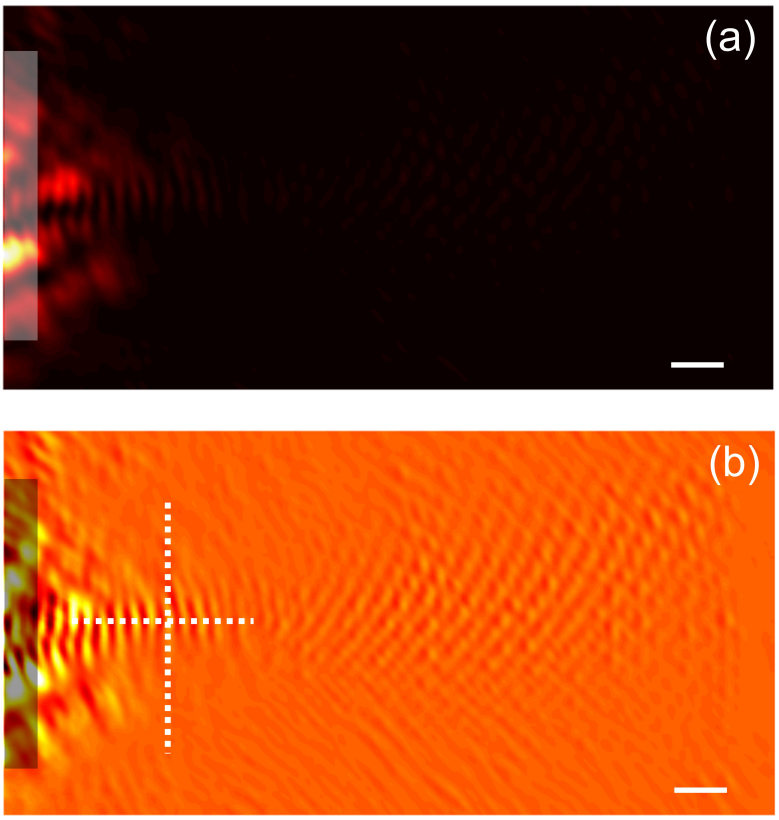

Figure 5.17: (a) The original SNOM image of the lens with resetting the scan start point at the back half of the lens. (b) Image after Derivative filter. Scale bar 2 µm.

Similar characterization results are also obtained when we set the starting point of the probe in the back half of the lens to avoid as much as possible the influence of out-of-plane scattering fields to focus on the field behind the lens. From Figure 5.17 (a) we can see that almost no bright spots appear in the plot. Then I used the Derivative filter for the processing and the results are shown in Figure 5.17 (b). As before, from the figure we can obtain the conclusion of the bending and focusing effect of the lens on the guided light. We then quantitatively analyzed and compared the experimental data with the previously obtained simulation data (see Figure 5.18 (a) and (b)). The experimental results agree well with the simulation results in both horizontal and vertical directions. Also the FWHM in the longitudinal direction at the focal point of about 5.8 µm behind the lens is 0.87µm = 0.53 λ, here $\lambda = 1.63$µm.

So far, we have shown the results of SNOM characterization of the focusing functional structure on the sample. Yet we did not obtain the SNOM characterization results for the collimation structure in the sample due to the construction works in the ICB lab in Dijon. The large amount of vibration generated by the construction can adversely affect the SNOM characterization.

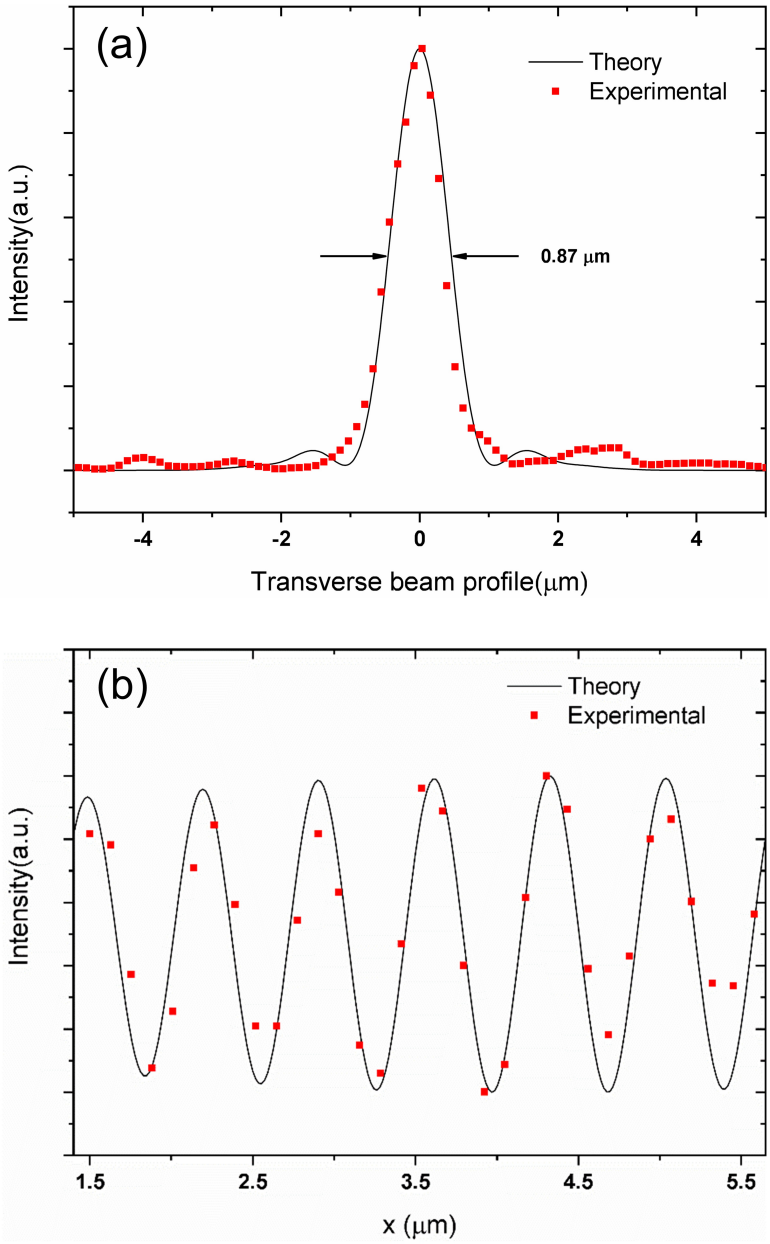

Figure 5.18: (a) Comparison of experimental and theoretical data at the vertical white dotted line (focal plane) shown in Figure 5.17 (a). FWHM = 0.87μm = 0.53 λ, here $\lambda = 1.63\mu$m. (b) Comparison of experimental and theoretical data at the horizontal white dotted line shown in Figure 5.17 (b).

For the filter function, we can also use the FFT filter in software WSXM to filter out the diffraction fields [203]. Figure 5.19 gives a comparison of the two filters. It can be seen from the Figure 5.19 (c) that the FFT filter can also remove the diffraction field generated by the air holes to obtain the oscillation wave generated by the guided light. By comparison, the DERIVATIVE filter (see Figure 5.19 (b)) is more effective. Also its output is stable with less subjective factors. So in this thesis, I choose to use the DERIVATIVE filter.

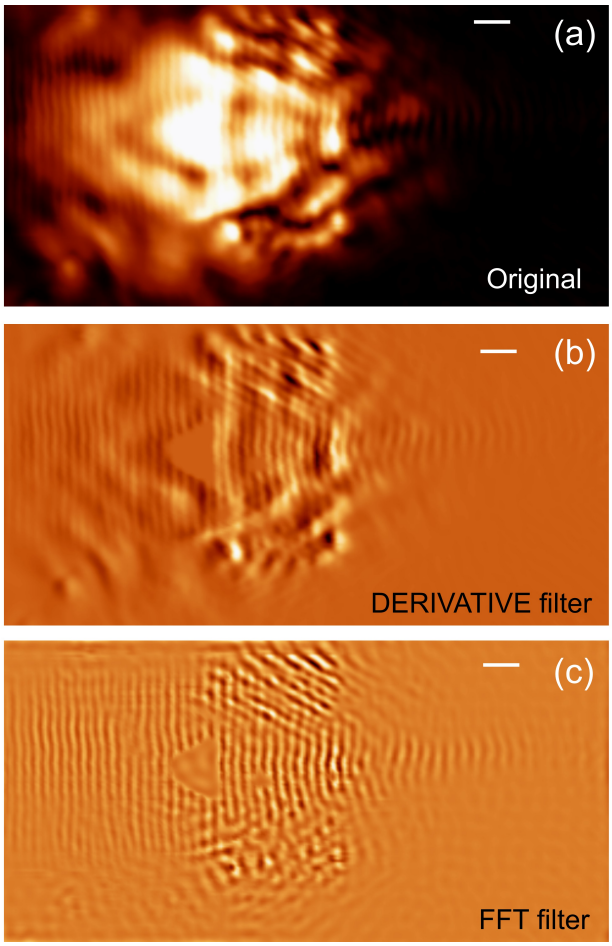

Figure 5.19: Comparison of two different filter in WSXM software. (a) The original SNOM image of the lens. (b) Image after the DERIVATIVE filter. (c) Image after the FFT filter. Scale bar 2 µm.

5.5 Conclusion

This chapter first presents in detail the processing and fabrication of the samples in this thesis, including the flat lens and the Half Maxwell-Fisheye lens. The SEM images allow us to clearly observe all the features of the resulting sample after nanofabrication. Subsequently for the flat lens, we used two different methods for the characterization, the set of output waveguides and the SNOM, respectively. This chapter then presents the results obtained by the two different characterization methods. For the set of output waveguides, we obtain the field intensity distribution of the guided light inside the Si waveguide. For the single cell structure on the sample, we scanned between 1.5µm to 1.64µm with 1nm intervals. I then used MATLAB to process the obtained data to obtain the intensity distribution of the output field at a specific wavelength. The results show that the designed lens is capable of focusing plane waves from 1.6µm to 1.64µm. The transmittance of the lens is maximized at 1.64µm. The wavelength shift compared to the previous simulation results is due to fabrica-

tion errors and approximations in the EIM modeling. For the SNOM technique, we obtain the distribution of the field at a specific distance from the top Si layer surface. In order to obtain accurate results, multiple repeat scans are necessary. By the operation of subtracting the near-field and far-field images, we minimize the effect of the diffraction field generated by the air holes. This allows us to see more clearly the distribution of the field behind the lens. Simulation results of the field distribution at different distances from the silicon surface are also added for better understanding of the SNOM images. The results obtained by SNOM are then quantitatively analyzed and compare with the previous simulation results. Finally, we confirm that the experimental results are consistent with the previous simulation results.

General conclusion

In this thesis, we have realized the full process from theoretical simulation to experimental characterization of graded photonic crystal devices on the SOI platform for near-infrared applications. Nanofabrication as well as two characterization methods (sets of output waveguide and SNOM) are highlighted.

The photonic crystal structure is set in a 220 nm thick silicon layer. For this 3D photonic crystal slab, we used the effective index method (EIM) to calculate its band diagram. By using MIT's MPB open software package, we obtained the desired band diagram of the photonic crystal as well as the equi-frequency curve (EFC). Photonic crystals with square lattice and hexagonal lattice were considered separately. For the specific lattice, we calculated the equi-frequency curve when the normalized frequency is in the first and second band, respectively. Subsequently, we picked the case when the equi-frequency curve is circular. This is because at this point, the photonic crystal can be considered as a uniform homogeneous medium and has an equivalent effective index. When the normalized frequency is in the first band, the effective index of the photonic crystal is positive. When the normalized frequency is in the second band, the effective index of the photonic crystal is considered to be negative. By analytically calculating the relationship between the filling factor η and the effective index of the photonic crystal, we then obtained the deduced curve. In turn, we obtained the filling factor (i.e., air hole diameter) at different locations in the lens.

The simulation of the photonic crystal device was performed in Lumerical FDTD software. 3D simulation environment was used in this thesis. For the flat lens, we found that the designed lens can focus the incident plane wave to the focal point. Also, it can collimate the point source into a plane wave. In all cases, the focal point has a higher resolution when the normalized frequency is in the second band of the photonic crystal. For the Half Maxwell-fisheye lens, the theoretical simulation results proved that it can focus the incident plane wave to the edge of the lens. Similarly, it can collimate a point source at the edge into a plane wave. All simulations were performed in the near-infrared domain, mainly at 1.55 μm. We also designed and simulated an on-chip point source in the NIR domain. This is a gradually narrowing waveguide structure. A circular air-hole resonant cavity at the end of the waveguide is used to simulate the point source. Theoretical simulations proved that this structure can produce an effect in the silicon layer that approximates that of a point source. We then chose the case when the normalized frequency is in the second band of the hexagonal

lattice photonic crystal for the next fabrication step.

SOI wafer (220nm Si / 3 μm SiO_2) from SOITEC was selected for the experimental processing platform. Two main nanofabrication techniques involved in this thesis were nanolithography and dry etching. The nanolithography machine used in this thesis is the Nanobeam 4. Its calibration current was set at 0.5nA to obtain a step size of 2 nm. The voltage was set to 80 kV to obtain an electron beam size of 5 nm. For dry etching, we used the ICP-DRIE from *SPTS technologies*. A standard silicon etching process at 220nm depth was applied to the top Si layer. The fabrication was done in the C2N's clean room. The work outside the cleanroom focused on the mask and file preparation for NB4 machine. The final samples were processed on 2cm x 2cm SOI platform. After cutting, a perfect testable sample is a long rectangular piece of about 2cm x 0.8cm. Also, two main characterization methods were used in this thesis. One is to collect the field intensity at the emitting end of the lens in the form of sets of output waveguides. In this way, the light guide intensity was collected in the top silicon layer of the SOI. This characterization method was performed in C2N. The other is to use the more advanced SNOM technique. The SNOM characterization method was performed in ICB laboratory in Dijon.

For the cell structure of either characterization method, a 200 μm long and 450 nm wide single mode filter is present at the input end to ensure that the TE fundamental mode is obtained. Tapered waveguides connect the filter to the straight waveguide. For cell structures using output waveguides, the input side of the lens is a 10 μm wide waveguide to simulate an approximate plane wave. At the output side of the lens are 13 waveguides 700nm wide and spaced 300nm apart. The distance between them is progressively increased in a fan shape to avoid coupling between the waveguides. By varying the distance between this group of waveguides and the output side of the lens, we obtained information about the intensity of output field. A total of 60 different distances D, from 0.5 μm to 30 μm, were processed on a single SOI platform. And for the cell structure using SNOM technique, we used the multimode interferometer (MMI) structure. One auxiliary arm of MMI is used for the alignment of the input fiber for SNOM characterization. The other arm is connected to the designed lens. The SNOM probe scanned above the lens and in the adjacent area. For this cell structure, we process several on one SOI platform to ensure processing tolerance. Finally, we fabricated the on-chip point source with 4 possible structures. Again, by varying the distance between the point source and the lens, we tried to find the right situation where it could be collimated.

Afterwards, we used SEM to present the fabricated samples, which included the flat lens with negative effective index and the Half Maxwell fisheye. Then we used the two methods to characterize the sample. When using the set of output waveguides, we performed the scan measurement using different wavelengths of light (1.5 μm to 1.64 μm, 1 nm apart) for each distance D. As a result, we obtained spectral intensity distributions at different D positions. We then extracted the data analytically to obtain the field intensity distribution at different distances from the lens exit at specific wavelengths. Through our analysis, we found that

the lens can focus light at wavelengths from 1.6μm to 1.64μm. In this case, the output field intensity was almost concentrated in the central waveguide. The focal point was located at 5μm from the exit surface of the lens. Another non-normalized analysis shows that the lens has the highest transmission at 1.64 μm. The field strength at the focal point at 1.64 μm is greater than at other wavelengths. After analysis, the wavelength shift is caused by the variation of the air hole diameter due to fabrication and the approximation by using the EIM method.

After obtaining preliminary measurement results of the sample using the set of output waveguide, we used SNOM to characterize the sample to realize a better resolution. When scanning with SNOM, different probes were placed and repeated to get the best results. At the same time, the distance between the probe and the surface of the silicon layer was adjusted (in near-field mode was 4 nm, in far-field mode was 100nm or 250nm). Based on the results already obtained by using the set of output waveguide, the wavelengths used in SNOM measurement were mainly concentrated at 1.63 μm. The area scanned by the probe was a rectangular area of 30μm x 15μm including the lens. After obtaining the raw data, the data were analyzed and processed using the open source software WSXM. At the same time, we used the near-field minus far-field method to minimize the effect of the scattered field generated by the air holes. The results proved that the designed lens can focus the high frequency oscillation waves generated by the guided light in the waveguide, which is consistent with previous simulation results. We then performed a quantitative analysis of the SNOM results. By adjusting the position of field monitor, we obtained the distribution of the output field in the horizontal and vertical directions. In both directions, the experimentally obtained results are consistent with the theoretical results of previous simulations.

The SNOM characterization of the point source was not completed due to vibration interference caused by the laboratory construction. And the Half Maxwell-fisheye lens was not finally fabricated successfully due to the sudden passing away of our engineer and lack of time.

Overall, this thesis focuses on the development and application of graded photonic crystal devices in the near-infrared band applied on SOI platform. We have analyzed the feasibility of lens design for different graded photonic crystals with different bands and have designed, fabricated and characterized the flat lens with negative effective index. The work in this thesis provides insights and opportunities for the development of silicon photonic including photonic integrated circuit, on-chip optical communication and nano optical devices.

List of Figures

List of Tables

Bibliography

[1] Steven G Johnson and J D Joannopoulos. Block-iterative frequency-domain methods. *Optics Express*, 8(3):173–190, 2001.

[2] Sajeev John. Strong localization of photons in certain disordered dielectric superlattices. *Physical Review Letters*, 58(23):2486–2489, 1987.

[3] Eli Yablonovitch. Inhibited Spontaneous Emission in Solid-State Physics and Electronics. *Physical Review Letters*, 58(20), 1987.

[4] Bodo D. Wilts, Kristel Michielsen, Hans De Raedt, and Doekele G. Stavenga. Iridescence and spectral filtering of the gyroid-type photonic crystals in parides sesostris wing scales. *Interface Focus*, 2(5):681–687, 2012.

[5] Jiyu Sun, Bharat Bhushan, and Jin Tong. Structural coloration in nature. *RSC Advances*, 3(35):14862–14889, 2013.

[6] Eileen Armstrong and Colm O'Dwyer. Artificial opal photonic crystals and inverse opal structures-fundamentals and applications from optics to energy storage. *Journal of Materials Chemistry C*, 3(24):6109–6143, 2015.

[7] Farzaneh Fathi, Mohammad Reza Rashidi, Parvin Samadi Pakchin, Sohrab Ahmadi-Kandjani, and Arash Nikniazi. Photonic crystal based biosensors: Emerging inverse opals for biomarker detection. *Talanta*, 221(September 2020):121615, 2021.

[8] Yuanjin Zhao, Luoran Shang, Yao Cheng, and Zhongze Gu. Spherical colloidal photonic crystals. *Accounts of Chemical Research*, 47(12):3632–3642, 2014.

[9] Wanlin Wang, Guo Ping Wang, Wang Zhang, and Di Zhang. Reversible thermochromic response based on photonic crystal structure in butterfly wing. *Nanophotonics*, 7(1):217–227, 2018.

[10] Daniel J. Brink, Nic G. Van der Berg, and Andre J. Botha. Iridescent colors on seashells: An optical and structural investigation of Helcion pruinosus. *Applied Optics*, 41(4):717–722, 2002.

[11] Mengxi Zhou, Djilali Kourtiche, Julien Claudel, Francois Deschamps, Isabelle Magne, Patrice Roth, Pierre Schmitt, Martine Souques, and Mustapha Nadi. Interference thresholds for active implantable cardiovascular devices in occupational low-frequency electric and magnetic fields: a numerical and in vitro study. *Medical Engineering & Physics*, 104:103799, 2022.

[12] Pete Vukusic and J Roy Sambles. Photonic structures in aquatic systems. *Nature*, 424(August):850–855, 2003.

[13] Vukusic P, Sambles J R, and Lawrence C R. Colour mixing in wing scales of a butterfly. *Nature*, 404(March):457, 2000.

[14] David W. Lee. Iridescent blue plants. *American Scientist*, 85:56–63, 1997.

[15] J D Joannopoulos, S G Johnson, J N Winn, and R D Meade. *Photonic Crystals: Molding the Flow of Light - Second Edition*. Princeton University Press, 2011.

[16] E. Yablonovitch, T. J. Gmitter, and K. M. Leung. Photonic band structure: The face-centered-cubic case employing nonspherical atoms. *Physical Review Letters*, 67(17):2295–2298, 1991.

[17] A. K. Zvezdin and V. I. Belotelov. Magnetooptical properties of two dimensional photonic crystals. *European Physical Journal B*, 37(4):479–487, 2004.

[18] Jose M. Escalante and Sergey E. Skipetrov. Level spacing statistics for light in two-dimensional disordered photonic crystals. *Scientific Reports*, 8(1):11569, 2018.

[19] M. Notomi. Theory of light propagation in strongly modulated photonic crystals: Refractionlike behavior in the vicinity of the photonic band gap. *Physical Review B - Condensed Matter and Materials Physics*, 62(16):10696–10705, 2000.

[20] M. E. Zoorob, M. D.B. Charlton, G. J. Parker, J. J. Baumberg, and M. C. Netti. Complete photonic bandgaps in 12-fold symmetric quasicrystals. *Nature*, 404(6779):740–743, 2000.

[21] J. G. Fleming, S. Y. Lin, I. El-Kady, R. Biswas, and K. M. Ho. All-metallic three-dimensional photonic crytal with a large infrared bandgap. *Nature*, 417(6884):52–55, 2002.

[22] Alongkarn Chutinan and Susumu Noda. Waveguides and waveguide bends in two-dimensional photonic crystal slabs. *Phys. Rev. B*, 62:4488–4492, Aug 2000.

[23] Marin Soljačić, Steven G. Johnson, Shanhui Fan, Mihai Ibanescu, Erich Ippen, and J. D. Joannopoulos. Photonic-crystal slow-light enhancement of nonlinear phase sensitivity. *Journal of the Optical Society of America B*, 19(9):2052, 2002.

[24] Yoshihiro Akahane, Takashi Asano, Bong Shik Song, and Susumu Noda. High-Q photonic nanocavity in a two-dimensional photonic crystal. *Nature*, 425(6961):944–947, 2003.

[25] Charles Kittel. Introduction to Solid State Physics, 8th edition, 2004.

[26] A. Einstein. Über einen die erzeugung und verwandlung des lichtes betreffenden heuristischen gesichtspunkt. *Annalen der Physik*, 322(6):132–148, 1905.

[27] Chapter 1 Elements of basic theory of anisotropic wave propagation. In Ilya Tsvankin, editor, *Handbook of Geophysical Exploration: Seismic Exploration*, volume 29 of *Handbook of Geophysical Exploration: Seismic Exploration*, pages 1–59. Pergamon, 2001.

[28] V. G Veselago. The Electrodynamic of Substances with Simultaneous Negative Values of e and μ. *Soviet Physics Uspekhi*, 10(4):509–514, 1968.

[29] J. B. Pendry. Negative refraction makes a perfect lens. *Physical Review Letters*, 85(18):3966–3969, 2000.

[30] David R. Smith and Norman Kroll. Negative refractive index in left-handed materials. *Physical Review Letters*, 85(14):2933–2936, 2000.

[31] Nanfang Yu, Patrice Genevet, Mikhail A. Kats, Francesco Aieta, Jean Philippe Tetienne, Federico Capasso, and Zeno Gaburro. Light propagation with phase discontinuities: Generalized laws of reflection and refraction. *Science*, 334(6054):333–337, 2011.

[32] Chiyan Luo, Steven Johnson, D. Joannopoulos, and B. Pendry. Subwavelength imaging in photonic crystals. *Physical Review B - Condensed Matter and Materials Physics*, 68(4):1–15, 2003.

[33] S. Foteinopoulou and C. M. Soukoulis. Electromagnetic wave propagation in two-dimensional photonic crystals: A study of anomalous refractive effects. *Physical Review B - Condensed Matter and Materials Physics*, 72(16):1–20, 2005.

[34] T. Decoopman, G. Tayeb, S. Enoch, D. Maystre, and B. Gralak. Photonic crystal lens: From negative refraction and negative index to negative permittivity and permeability. *Physical Review Letters*, 97(7):1–4, 2006.

[35] Takashi Matsumoto, Kun-Sun Eom, and Toshihiko Baba. Focusing of light by negative refraction in a photonic crystal slab superlens on silicon-on-insulator substrate. *Optics Letters*, 31(18):2786, 2006.

[36] Ting Xu, Amit Agrawal, Maxim Abashin, Kenneth J. Chau, and Henri J. Lezec. All-angle negative refraction and active flat lensing of ultraviolet light. *Nature*, 497(7450):470–474, 2013.

[37] Hideo Kosaka and Takayuki Kawashima. Superprism phenomena in photonic crystals. *Physical Review B - Condensed Matter and Materials Physics*, 58(16):R10096–R10099, 1998.

[38] A. Lupu, E. Cassan, S. Laval, L. El Melhaoui, P. Lyan, and J. M. Fedeli. Experimental evidence for superprism phenomena in SOI photonic crystals. *Optics Express*, 12(23):5690, 2004.

[39] Chiyan Luo, Marin Soljačić, and J. D. Joannopoulos. Superprism effect based on phase velocities. *Optics Letters*, 29(7):745, 2004.

[40] Jean Dellinger, Damien Bernier, Benoit Cluzel, Xavier Le Roux, Anatole Lupu, Frédérique de Fornel, and Eric Cassan. Near-field observation of beam steering in a photonic crystal superprism. *Optics Letters*, 36(7):1074, 2011.

[41] Hideo Kosaka, Takayuki Kawashima, Akihisa Tomita, Masaya Notomi, Toshiaki Tamamura, Takashi Sato, and Shojiro Kawakami. Self-collimating phenomena in photonic crystals. *Applied Physics Letters*, 74(9):1212–1214, 1999.

[42] Lijun Wu, Michael Mazilu, and Thomas F. Krauss. Beam steering in planar-photonic crystals: From superprism to supercollimator. *Journal of Lightwave Technology*, 21(2):561–566, 2003.

[43] Jonghwa Shin and Shanhui Fan. Conditions for self-collimation in three-dimensional photonic crystals. *Optics Letters*, 30(18):2397, 2005.

[44] Rafif E. Hamam, Mihai Ibanescu, Steven G. Johnson, J. D. Joannopoulos, and Marin Soljacic. Broadband super-collimation in a hybrid photonic crystal structure. *Optics Express*, 17(10):8109, 2009.

[45] Peter T. Rakich, Marcus S. Dahlem, Sheila Tandon, Mihaii Banescu, Marin Soljačić, Gale S. Petrich, John D. Joannopoulos, Leslie A. Kolodziejski, and Erich P. Ippen. Achieving centimetre-scale supercollimation in a large-area two-dimensional photonic crystal. *Nature Materials*, 5(2):93–96, 2006.

[46] V. Purlys, L. Maigyte, D. Gailevičius, M. Peckus, R. Gadonas, and K. Staliunas. Supercollimation by axisymmetric photonic crystals. *Applied Physics Letters*, 104(22), 2014.

[47] Emmanuel Centeno and David Cassagne. Graded photonic crystals. *Optics Letters*, 30(17):2278, 2005.

[48] Sz Chin Steven Lin, Tony Jun Huang, Jia Hong Sun, and Tsung Tsong Wu. Gradient-index phononic crystals. *Physical Review B - Condensed Matter and Materials Physics*, 79(9):1–6, 2009.

[49] David Cassagne Emmanuel Centeno and Jean-Paul Albert. Mirage and superbending effect in two-dimensional graded photonic crystals. *Physical Review B - Condensed Matter and Materials Physics*, 73(23), 2006.

[50] E. Centeno and D. Felbacq. Rigorous vector diffraction of electromagnetic waves by bidimensional photonic crystals. *Journal of the Optical Society of America A*, 17(2):320, 2000.

[51] D. Felbacq, G. Tayeb, and D. Maystre. Scattering by a random set of parallel cylinders. *J. Opt. Soc. Am. A*, 11(9):2526–2538, Sep 1994.

[52] Emmanuel Centeno, David Cassagne, and Jean Paul Albert. Optical mirage in graded photonic crystals. *Photonic Crystal Materials and Devices III*, 6182:61821H, 2006.

[53] Olivier Vanbésien and Emmanuel Centeno. *Dispersion Engineering for Integrated Nanophotonics*, volume 9781848215641 of *FOCUS Series*. Wiley, 2014.

[54] Eric Akmansoy, Emmanuel Centeno, Kevin Vynck, David Cassagne, and Jean Michel Lourtioz. Graded photonic crystals curve the flow of light: An experimental demonstration by the mirage effect. *Applied Physics Letters*, 92(13):28–31, 2008.

[55] Emmanuel Centeno, Eric Akmansoy, Kevin Vynck, David Cassagne, and Jean Michel Lourtioz. Light bending and quasi-transparency in metallic graded photonic crystals. *Photonics and Nanostructures - Fundamentals and Applications*, 8(2):120–124, 2010.

[56] Hamza Kurt and David S. Citrin. Graded index photonic crystals. *Optics Express*, 15(3):1240, 2007.

[57] H. Kurt, E. Colak, O. Cakmak, H. Caglayan, and E. Ozbay. The focusing effect of graded index photonic crystals. *Applied Physics Letters*, 93(17):13–16, 2008.

[58] M. Turduev, I. H. Giden, and H. Kurt. Design of flat lens-like graded index medium by photonic crystals: Exploring both low and high frequency regimes. *Optics Communications*, 339:22–33, 2015.

[59] Borislav Vasic, Goran Isic, Rados Gajic, and Kurt Hingerl. Controlling electromagnetic fields with graded photonic crystals in metamaterial regime. *Optics Express*, 18(19):20321, 2010.

[60] S. Hadi Badri, H. Rasooli Saghai, and Hadi Soofi. Multimode waveguide crossing based on a square Maxwell's fisheye lens. *Applied Optics*, 58(17):4647, 2019.

[61] S. Hadi Badri and M. M. Gilarlue. Silicon nitride waveguide devices based on gradient-index lenses implemented by subwavelength silicon grating metamaterials. *Applied Optics*, 59(17):5269, 2020.

[62] S. Hadi Badri, M. M. Gilarlue, and S. G. Gavgani. Ultra-thin silicon-on-insulator waveguide bend based on truncated Eaton lens implemented by varying the guiding layer thickness. *Photonics and Nanostructures - Fundamentals and Applications*, 39(September 2019):100766, 2020.

[63] S. Hadi Badri, H. Rasooli Saghai, and Hadi Soofi. Polymer multimode waveguide bend based on a multilayered Eaton lens. *Applied Optics*, 58(19):5219, 2019.

[64] S. Hadi Badri and M. M. Gilarlue. Low-index-contrast waveguide bend based on truncated Eaton lens implemented by graded photonic crystals. *Journal of the Optical Society of America B*, 36(5):1288, 2019.

[65] Khanh-Van Do, Xavier Le Roux, Delphine Marris-Morini, Laurent Vivien, and Eric Cassan. Experimental demonstration of light bending at optical frequencies using a non-homogenizable graded photonic crystal. *Optics Express*, 20(4):4776, 2012.

[66] Eric Cassan, Khanh Van Do, Jean Dellinger, Xavier Le Roux, Frédérique de Fornel, and Benoit Cluzel. Polarization beam splitting using a birefringent graded photonic crystal. *Optics Letters*, 38(4):459, 2013.

[67] Eric Cassan, Khanh Van Do, Charles Caer, Delphine Marris-Morini, and Laurent Vivien. Short-wavelength light propagation in graded photonic crystals. *Journal of Lightwave Technology*, 29(13):1937–1943, 2011.

[68] Khanh Van Do, Xavier Le Roux, Charles Caer, Delphine Marris-morini, Nicolas Izard, and Laurent Vivien. Wavelength Demultiplexer Based on a Two-Dimensional Graded Photonic Crystal. *IEEE Photonics Technology Letters*, 23(15):1094–1096, 2011.

[69] Jean Dellinger, K. Van Do, Xavier Le Roux, Frédérique De Fornel, Eric Cassan, and Benoît Cluzel. Hyperspectral optical near-field imaging: Looking graded photonic crystals and photonic metamaterials in color. *Applied Physics Letters*, 101(14), 2012.

[70] F. Gaufillet and E. Akmansoy. Design and experimental evidence of a flat graded-index photonic crystal lens. *Journal of Applied Physics*, 114(8):10–15, 2013.

[71] F. Gaufillet and E. Akmansoy. Design of flat graded index lenses using dielectric Graded Photonic Crystals. *Optical Materials*, 47:555–560, 2015.

[72] Fabian Gaufillet and Éric Akmansoy. Metallic graded photonic crystals for graded index lens. *Applied Physics A: Materials Science and Processing*, 109(4):1071–1074, 2012.

[73] F. Gaufillet and E. Akmansoy. Graded photonic crystals for luneburg lens. *IEEE Photonics Journal*, 8(1), 2016.

[74] Fabian Gaufillet and Eric Akmansoy. Maxwell Fish-Eye and Half-Maxwell Fish-Eye Based on Graded Photonic Crystals. *IEEE Photonics Journal*, 10(3):1–12, 2018.

[75] Duncan T. Moore. Gradient-index optics: a review. *Appl. Opt.*, 19(7):1035–1038, Apr 1980.

[76] Wikipedia contributors. Gradient-index optics — Wikipedia, the free encyclopedia, 2022. [Online; accessed 4-October-2022].

[77] Albertas Žukauskas, Ieva Matulaitienė, Domas Paipulas, Gediminas Niaura, Mangirdas Malinauskas, and Roaldas Gadonas. Tuning the refractive index in 3d direct laser writing lithography: towards grin microoptics. *Laser & Photonics Reviews*, 9(6):706–712, 2015.

[78] Henrik Melkonyan, Kenaish Al Qubaisi, Karen Sloyan, Anatol Khilo, and Marcus S. Dahlem. Gradient-index optical fiber lens for efficient fiber-to-chip coupling. *Opt. Express*, 25(12):13035–13045, Jun 2017.

[79] Christian R. Ocier, Corey A. Richards, Daniel A. Bacon-Brown, Qing Ding, Raman Kumar, Tanner J. Garcia, Jorik van de Groep, Jung Hwan Song, Austin J. Cyphersmith, Andrew Rhode, Andrea N. Perry, Alexander J. Littlefield, Jinlong Zhu, Dajie Xie, Haibo Gao, Jonah F. Messinger, Mark L. Brongersma, Kimani C. Toussaint, Lynford L. Goddard, and Paul V. Braun. Direct laser writing of volumetric gradient index lenses and waveguides. *Light: Science and Applications*, 9(1), 2020.

[80] M. Plihal and A. A. Maradudin. Photonic band structure of two-dimensional systems: The triangular lattice. *Physical Review B*, 44(16):8565–8571, 1991.

[81] K. M. Ho, C. T. Chan, and C. M. Soukoulis. Existence of a photonic gap in periodic dielectric structures. *Physical Review Letters*, 65(25):3152–3155, 1990.

[82] P. Silvester. A General High-Order Finite-Element Waveguide Analysis Program. *IEEE Transactions on Microwave Theory and Techniques*, 17(4):204–210, 1969.

[83] J. B. Pendry and A. MacKinnon. Calculation of photon dispersion relations. *Physical Review Letters*, 69(19):2772–2775, 1992.

[84] Karlheinz Bierwirth, Norbert Schulz, and Eritz Arndt. Finite-Difference Analysis of Rectangular Dielectric Waveguide Structures. *IEEE Transactions on Microwave Theory and Techniques*, 34(11):1104–1114, 1986.

[85] Ardavan F. Oskooi, David Roundy, Mihai Ibanescu, Peter Bermel, J.D. Joannopoulos, and Steven G. Johnson. Meep: A flexible free-software package for electromagnetic simulations by the fdtd method. *Computer Physics Communications*, 181(3):687–702, 2010.

[86] Hsing-Yi Chen and I-Young Tarn. Analysis of electromagnetic radiation from a video output amplifier inside a monitor by using fdtd method. *IEEE Transactions on Electromagnetic Compatibility*, 39(4):394–397, 1997.

[87] Ardavan F. Oskooi, David Roundy, Mihai Ibanescu, Peter Bermel, J. D. Joannopoulos, and Steven G. Johnson. Meep: A flexible free-software package for electromagnetic simulations by the FDTD method. *Computer Physics Communications*, 181(3):687–702, 2010.

[88] José Manuel Luque-González, Robert Halir, Juan Gonzalo Wangüemert-Pérez, José De-Oliva-Rubio, Jens H. Schmid, Pavel Cheben, Íñigo Molina-Fernández, and Alejandro Ortega-Moñux. An Ultracompact GRIN-Lens-Based Spot Size Converter using Subwavelength Grating Metamaterials. *Laser and Photonics Reviews*, 13(11):1–7, 2019.

[89] Taku Itoh and Soichiro Ikuno. Efficient simulation of electromagnetic wave propagation in complex shaped domain by hybrid method of fdtd and mtdm based on interpolating moving least squares method. *IEEE Transactions on Magnetics*, 53(6):1–4, 2017.

[90] Ahmad Rifqi Md Zain and Richard M. De La Rue. Modelling of Photonic Crystal (PhC) Cavities: Theory and Applications. *Photonic Crystals - A Glimpse of the Current Research Trends*, pages 1–19, 2019.

[91] Hirotsugu Fusayasu, Seiji Hamada, Hiroto Inoue, Nobuyuki Kadonishi, Shinkuro Fujino, Koji Fujiwara, and Yoshiyuki Ishihara. A novel technique combining cip method with fdtd method for implementing efficient absorbing boundary condition in 3-d high frequency electromagnetic field analysis. *IEEE Transactions on Magnetics*, 44(6):1470–1473, 2008.

[92] Bo Zhang, Yun Yi, Yan-Tao Duan, Zheng Chen, and Bin Chen. Efficient 3-d laguerre-based fdtd method using a new temporal basis. *IEEE Transactions on Antennas and Propagation*, 64(5):2027–2032, 2016.

[93] Majid Ahmadlou, Mahmoud Kamarei, and Mohammad Hossein Sheikhi. Negative refraction and focusing analysis in a left-handed material slab and realization with a 3D photonic crystal structure. *Journal of Optics A: Pure and Applied Optics*, 8(2):199–204, 2006.

[94] Kane Yee. Numerical solution of initial boundary value problems involving maxwell's equations in isotropic media. *IEEE Transactions on Antennas and Propagation*, 14(3):302–307, 1966.

[95] Allen Taflove and Morris E. Brodwin. Numerical solution of steady-state electromagnetic scattering problems using the time-dependent maxwell's equations. *IRE Transactions on Microwave Theory and Techniques*, 23(8):623–630, August 1975.

[96] Allen Taflove. Application of the finite-difference time-domain method to sinusoidal steady-state electromagnetic-penetration problems. *IEEE Transactions on Electromagnetic Compatibility*, EMC-22(3):191–202, 1980.

[97] Wikipedia contributors. Finite-difference time-domain method — Wikipedia, the free encyclopedia, 2022. [Online; accessed 26-August-2022].

[98] J.S. Juntunen and T.D. Tsiboukis. Reduction of numerical dispersion in FDTD method through artificial anisotropy. *IEEE Transactions on Microwave Theory and Techniques*, 48(4):582–588, 2000.

[99] Jean-Pierre Berenger. A perfectly matched layer for the absorption of electromagnetic waves. *Journal of Computational Physics*, 114(2):185–200, 1994.

[100] Chao Xiang, Joel Guo, Warren Jin, Lue Wu, Jonathan Peters, Weiqiang Xie, Lin Chang, Boqiang Shen, Heming Wang, Qi Fan Yang, David Kinghorn, Mario Paniccia, Kerry J. Vahala, Paul A. Morton, and John E. Bowers. High-performance lasers for fully integrated silicon nitride photonics. *Nature Communications*, 12(1):6650, 2021.

[101] Yoav Hazan, Ahiad Levi, Michael Nagli, and Amir Rosenthal. Silicon-photonics acoustic detector for optoacoustic micro-tomography. *Nature Communications*, 13(1):1488, 2022.

[102] Andres D. Neira, Gregory A. Wurtz, and Anatoly V. Zayats. All-optical switching in silicon photonic waveguides with an epsilon-near-zero resonant cavity [Invited]. *Photonics Research*, 6(5):B1, 2018.

[103] G. T. Reed, G. Mashanovich, F. Y. Gardes, and D. J. Thomson. Silicon optical modulators. *Nature Photonics*, 4(8):518–526, 2010.

[104] Lawrence R. Chen. Silicon photonics for optical communications and microwave photonics. In *Optics InfoBase Conference Papers*, volume Part F138-ACPC 2019, page S4H.2. Optica Publishing Group, 2019.

[105] Enxiao Luan, Hossam Shoman, Daniel M. Ratner, Karen C. Cheung, and Lukas Chrostowski. Silicon photonic biosensors using label-free detection. *Sensors (Switzerland)*, 18(10), 2018.

[106] Xiaosheng Zhang, Kyungmok Kwon, Johannes Henriksson, Jianheng Luo, and Ming C. Wu. A large-scale microelectromechanical-systems-based silicon photonics LiDAR. *Nature*, 603(7900):253–258, 2022.

[107] Xuejun Xu, Shaowu Chen, Jinzhong Yu, and Xiaoguang Tu. Realization of SOI submicrometer optical waveguide components. *Optoelectronic Devices and Integration II*, 6838:68380L, 2007.

[108] Thomas Ferreira De Lima, Alexander N. Tait, Armin Mehrabian, Mitchell A. Nahmias, Chaoran Huang, Hsuan Tung Peng, Bicky A. Marquez, Mario Miscuglio, Tarek El-Ghazawi, Volker J. Sorger, Bhavin J. Shastri, and Paul R. Prucnal. Primer on silicon neuromorphic photonic processors: Architecture and compiler. *Nanophotonics*, 9(13):4055–4073, 2020.

[109] Bhavin J. Shastri, Alexander N. Tait, T. Ferreira de Lima, Wolfram H.P. Pernice, Harish Bhaskaran, C. D. Wright, and Paul R. Prucnal. Photonics for artificial intelligence and neuromorphic computing. *Nature Photonics*, 15(2):102–114, 2021.

[110] Ting Hu, Bowei Dong, Xianshu Luo, Tsung-Yang Liow, Junfeng Song, Chengkuo Lee, and Guo-Qiang Lo. Silicon photonic platforms for mid-infrared applications [Invited]. *Photonics Research*, 5(5):417, 2017.

[111] M. Bruel, B. Aspar, B. Charlet, C. Maleville, T. Poumeyrol, A. Soubie, A.J. Auberton-Herve, J.M. Lamure, T. Barge, F. Metral, and S. Trucchi. "smart cut": a promising new soi material technology. In *1995 IEEE International SOI Conference Proceedings*, pages 178–179, 1995.

[112] B. Aspar, M. Bruel, H. Moriceau, C. Maleville, T. Poumeyrol, A. M. Papon, A. Claverie, G. Benassayag, A. J. Auberton-Hervé, and T. Barge. Basic mechanisms involved in the Smart-Cut® process. *Microelectronic Engineering*, 36(1-4):233–240, 1997.

[113] Michel Bruel, Bernard Aspar, and Andre Jacques Auberton-Hervé. Smart-cut: A new silicon on insulator material technology based on hydrogen implantation and wafer bonding. *Japanese Journal of Applied Physics, Part 1: Regular Papers and Short Notes and Review Papers*, 36(3 SUPPL. B):1636–1641, 1997.

[114] Riccardo Marchetti, Cosimo Lacava, Lee Carroll, Kamil Gradkowski, and Paolo Minzioni. Coupling strategies for silicon photonics integrated chips [Invited]. *Photonics Research*, 7(2):201, 2019.

[115] T. Shoji, Tai Tsuchizawa, Toshifumi Watanabe, K. Yamada, and Hirofumi Morita. Low loss mode size converter from 0.3 /spl mu/m square si wire waveguides to singlemode fibres. *Electronics Letters*, 38:1669–1670, 2002.

[116] Min Qiu. Effective index method for heterostructure-slab-waveguide-based two-dimensional photonic crystals. *Applied Physics Letters*, 81(7):1163–1165, 2002.

[117] T. F. Krauss, R. M. De La Rue, and S. Brand. Two-dimensional photonic-bandgap structures operating at near-infrared wavelengths. *Nature*, 383(6602):699–702, 1996.

[118] A. Karlsson, B. Jaskorzynska, M. Qiu, K. Azizi, and M. Swillo. Numerical studies of mode gaps and coupling efficiency for line-defect waveguides in two-dimensional photonic crystals. *Physical Review B - Condensed Matter and Materials Physics*, 64(15):1–5, 2001.

[119] S. Olivier, H. Benisty, M. Rattier, C. Weisbuch, M. Qiu, A. Karlsson, C. J.M. Smith, R. Houdré, and U. Oesterle. Resonant and nonresonant transmission through waveguide bends in a planar photonic crystal. *Applied Physics Letters*, 79(16):2514–2516, 2001.

[120] Jens Buus. The effective index method and its application to semiconductor lasers. *IEEE Journal of Quantum Electronics*, 18:1083–1089, 1982.

[121] Min Qiu, Bozena Jaskorzynska, Marcin Swillo, and Henri Benisty. Time-domain 2D modeling of slab-waveguide-based photonic-crystal devices in the presence of radiation losses. *Microwave and Optical Technology Letters*, 34(5):387–393, 2002.

[122] A. Berrier, M. Mulot, M. Swillo, M. Qiu, L. Thylén, A. Talneau, and S. Anand. Negative refraction at infrared wavelengths in a two-dimensional photonic crystal. *Physical Review Letters*, 93(7):1–4, 2004.

[123] Sebastian A. Schulz, Anthony H.K. Park, Israel De Leon, Jeremy Upham, and Robert W. Boyd. Beyond the effective index method: Improved accuracy for 2D simulations of photonic crystal waveguides. *Journal of Optics (United Kingdom)*, 17(7), 2015.

[124] Shouyuan Shi, Caihua Chen, and Dennis W. Prather. Revised plane wave method for dispersive material and its application to band structure calculations of photonic crystal slabs. *Applied Physics Letters*, 86(4):10–13, 2005.

[125] Manfred Hammer and Olena V. Ivanova. Effective index approximations of photonic crystal slabs: A 2-to-1-D assessment. *Optical and Quantum Electronics*, 41(4):267–283, 2009.

[126] Hanhong Gao, Baile Zhang, Steven G. Johnson, and George Barbastathis. Design of thin–film photonic metamaterial Lüneburg lens using analytical approach. *Optics Express*, 20(2):1617, 2012.

[127] Lukas Chrostowski and Michael Hochberg. *Silicon Photonics Design: From Devices to Systems*. Cambridge University Press, 2015.

[128] Damien Bernier. Propriétés de superprisme des cristaux photoniques sur substrats SOI pour le démultiplexage en longueur d'onde. *Thèse de doctorat Université de Paris-Sud*, 2008.

[129] Daniel Benedikovic, Mathias Berciano, Carlos Alonso-Ramos, Xavier Le Roux, Eric Cassan, Delphine Marris-Morini, and Laurent Vivien. Dispersion control of silicon nanophotonic waveguides using sub-wavelength grating metamaterials in near- and mid-IR wavelengths. *Optics Express*, 25(16):19468, 2017.

[130] M. Alipour-Beyraghi, T. Fathollahi Khalkhali, A. Bananej, and J. Mostafavi-Amjad. Polarization-independent and tunable flat lenses based on graded index two-dimensional photonic crystals. *Optics Communications*, 420(January):133–140, 2018.

[131] Qi Wu, John M. Gibbons, and Wounjhang Park. Graded negative index lens by photonic crystals. *Opt. Express*, 16(21):16941–16949, Oct 2008.

[132] T. Aalto, K. Solehmainen, M. Harjanne, M. Kapulainen, and P. Heimala. Low-loss converters between optical silicon waveguides of different sizes and types. *IEEE Photonics Technology Letters*, 18(5):709–711, 2006.

[133] Sailong Wu, Xin Mu, Lirong Cheng, Simei Mao, and H. Y. Fu. State-of-the-art and perspectives on silicon waveguide crossings: A review. *Micromachines*, 11(3):326, mar 2020.

[134] R. Palmer, L. Alloatti, D. Korn, W. Heni, P. C. Schindler, J. Bolten, M. Karl, M. Waldow, T. Wahlbrink, W. Freude, C. Koos, and J. Leuthold. Low-loss silicon strip-to-slot mode converters. *IEEE Photonics Journal*, 5(1):2200409–2200409, 2013.

[135] Xu Wang, Wei Shi, Han Yun, Samantha Grist, Nicolas A. F. Jaeger, and Lukas Chrostowski. Narrow-band waveguide Bragg gratings on SOI wafers with CMOS-compatible fabrication process. *Optics Express*, 20(14):15547, 2012.

[136] Galina Georgieva, Karsten Voigt, Anna Peczek, Christian Mai, and Lars Zimmermann. Design and performance analysis of integrated focusing grating couplers for the transverse-magnetic TM00 mode in a photonic BiCMOS technology. *Journal of the European Optical Society*, 16(1):7, 2020.

[137] Qianfan Xu, Vilson R. Almeida, Roberto R. Panepucci, and Michal Lipson. Experimental demonstration of guiding and confining light in nanometer-size low-refractive-index material. *Optics Letters*, 29(14):1626, 2004.

[138] Daoxin Dai, Yongbo Tang, and John E Bowers. Mode conversion in tapered submicron silicon ridge optical waveguides. *Optics Express*, 20(12):13425, 2012.

[139] Soon T. Lim, Ching E. Png, Eng A. Ong, and Yong L. Ang. Single mode, polarization-independent submicron silicon waveguides based on geometrical adjustments. *Optics Express*, 15(18):11061, 2007.

[140] Sharee McNab, Nikolaj Moll, and Yurii Vlasov. Ultra-low loss photonic integrated circuit with membrane-type photonic crystal waveguides. *Optics Express*, 11(22):2927, 2003.

[141] Yuan Meng, Yizhen Chen, Longhui Lu, Yimin Ding, Andrea Cusano, Jonathan A. Fan, Qiaomu Hu, Kaiyuan Wang, Zhenwei Xie, Zhoutian Liu, Yuanmu Yang, Qiang Liu, Mali Gong, Qirong Xiao, Shulin Sun, Minming Zhang, Xiaocong Yuan, and Xingjie Ni. Optical meta-waveguides for integrated photonics and beyond. *Light: Science and Applications*, 10(1):235, 2021.

[142] Ryan Going, Tae Joon Seok, Jodi Loo, Kyle Hsu, and Ming C. Wu. Germanium wrap-around photodetectors on Silicon photonics. *Optics Express*, 23(9):11975, 2015.

[143] Hiroshi Fukuda, Koji Yamada, Tai Tsuchizawa, Toshifumi Watanabe, Hiroyuki Shinojima, and Sei-ichi Itabashi. Silicon photonic circuit with polarization diversity. *Optics Express*, 16(7):4872, 2008.

[144] Mark A. Foster, Amy C. Turner, Jay E. Sharping, Bradley S. Schmidt, Michal Lipson, and Alexander L. Gaeta. Broad-band optical parametric gain on a silicon photonic chip. *Nature*, 441(7096):960–963, 2006.

[145] Hiroki Takesue, Hiroshi Fukuda, Tai Tsuchizawa, Toshifumi Watanabe, Koji Yamada, Yasuhiro Tokura, and Sei-ichi Itabashi. Generation of polarization entangled photon pairs using silicon wire waveguide. *Optics Express*, 16(8):5721, 2008.

[146] Ryoichi Kasahara, Kei Watanabe, Mikitaka Itoh, Yasuyuki Inoue, and Akimasa Kaneko. Extremely low power consumption thermooptic switch (0.6 mw) with suspended ridge and silicon-silica hybrid waveguide structures. In *2008 34th European Conference on Optical Communication*, pages 1–2, 2008.

[147] A.G. Rickman, G.T. Reed, and F. Namavar. Silicon-on-insulator optical rib waveguide loss and mode characteristics. *Journal of Lightwave Technology*, 12(10):1771–1776, 1994.

[148] Antoine Brimont, Xuan Hu, Sébastien Cueff, Pedro Rojo Romeo, Guillaume Saint Girons, Amadeu Griol, Andrea Zanzi, Pablo Sanchis, and Régis Orobtchouk. Low-loss and compact silicon rib waveguide bends. *IEEE Photonics Technology Letters*, 28(3):299–302, 2016.

[149] L. Vivien, F. Grillot, E. Cassan, D. Pascal, S. Lardenois, A. Lupu, S. Laval, M. Heitzmann, and J. M. Fédéli. Comparison between strip and rib SOI microwaveguides for intra-chip light distribution. *Optical Materials*, 27(5):756–762, 2005.

[150] Milan M. Milošević, Petar S. Matavulj, Pengyuan Y. Yang, Alvise Bagolini, and Goran Z. Mashanovich. Rib waveguides for mid-infrared silicon photonics. *Journal of the Optical Society of America B*, 26(9):1760, 2009.

[151] Yusheng Qian, Seunghyun Kim, Jiguo Song, Gregory P. Nordin, and Jianhua Jiang. Compact and low loss silicon-on-insulator rib waveguide 90° bend. *Optics Express*, 14(13):6020, 2006.

[152] Balpreet Singh Ahluwalia, Øystein Ivar Helle, and Olav Gaute Hellesø. Rib waveguides for trapping and transport of particles. *Optics Express*, 24(5):4477, 2016.

[153] Xu Wang, Samantha Grist, Jonas Flueckiger, Nicolas A. F. Jaeger, and Lukas Chrostowski. Silicon photonic slot waveguide Bragg gratings and resonators. *Optics Express*, 21(16):19029, 2013.

[154] Vittorio M.N. Passaro and Mario la Notte. Optimizing SOI slot waveguide fabrication tolerances and strip-slot coupling for very efficient optical sensing. *Sensors*, 12(3):2436–2455, 2012.

[155] Carlos Angulo Barrios. Ultrasensitive nanomechanical photonic sensor based on horizontal slot-waveguide resonator. *IEEE Photonics Technology Letters*, 18(22):2419–2421, 2006.

[156] Carlos A. Barrios, Kristinn B. Gylfason, Benito Sánchez, Amadeu Griol, H. Sohlström, M. Holgado, and R. Casquel. Slot-waveguide biochemical sensor. *Optics Letters*, 32(21):3080, 2007.

[157] Francesco Dell'Olio and Vittorio M. Passaro. Optical sensing by optimized silicon slot waveguides. *Optics Express*, 15(8):4977, 2007.

[158] Alejandro Martínez, Javier Blasco, Pablo Sanchis, José V. Galán, Jaime García-Rupérez, Emmanuel Jordana, Pauline Gautier, Youcef Lebour, Sergi Hernández, Romain Guider, Nicola Daldosso, Blas Garrido, Jean Marc Fedeli, Lorenzo Pavesi, and Javier Martí. Ultrafast all-optical switching in a silicon-nanocrystal-based silicon slot waveguide at telecom wavelengths. *Nano Letters*, 10(4):1506–1511, 2010.

[159] Carlos Angulo Barrios and Michal Lipson. Electrically driven silicon resonant light emitting device based on slot-waveguide. *Optics Express*, 13(25):10092, 2005.

[160] Günther Roelkens. Photonic integration: beyond telecom and datacom. In *European Conference Interventional Oncology*, 2014.

[161] M Nedeljkovic, AZ Khokhar, Y Hu, Xia Chen, J Soler Penades, S Stankovic, HMH Chong, DJ Thomson, FY Gardes, GT Reed, et al. Silicon photonic devices and platforms for the mid-infrared. *Optical Materials Express*, 3(9):1205–1214, 2013.

[162] Xiangdong Li, Xue Feng, Xian Xiao, Kaiyu Cui, Fang Liu, and Yidong Huang. Experimental demonstration of silicon slot waveguide with low transmission loss at 1064 nm. *Optics Communications*, 329:168–172, 2014.

[163] Kapil Debnath, Ali Z Khokhar, Stuart A Boden, Hideo Arimoto, Swe Zin Oo, Harold MH Chong, Graham T Reed, and Shinichi Saito. Low-loss slot waveguides with silicon (111) surfaces realized using anisotropic wet etching. *Frontiers in Materials*, 3:51, 2016.

[164] Jun Tan, Richard A. Soref, and Wei Jiang. Interband scattering in a slow light photonic crystal waveguide under electro-optic tuning. *Optics Express*, 21(6):6756, 2013.

[165] L. Monteagudo-Lerma, S. Valdueza-Felip, F. B. Naranjo, P. Corredera, L. Rapenne, E. Sarigiannidou, G. Strasser, E. Monroy, and M. González-Herráez. Waveguide saturable absorbers at 155 μm based on intraband transitions in GaN/AlN QDs. *Optics Express*, 21(23):27578, 2013.

[166] Mahmoud A. Gaafar, Dirk Jalas, Liam O'Faolain, Juntao Li, Thomas F. Krauss, Alexander Yu Petrov, and Manfred Eich. Reflection from a free carrier front via an intraband indirect photonic transition. *Nature Communications*, 9(1):1447, 2018.

[167] Richard Wolf, Ingo Breunig, Hans Zappe, and Karsten Buse. Scattering-loss reduction of ridge waveguides by sidewall polishing. *Optics Express*, 26(16):19815, 2018.

[168] Matthew W. Puckett, Kaikai Liu, Nitesh Chauhan, Qiancheng Zhao, Naijun Jin, Haotian Cheng, Jianfeng Wu, Ryan O. Behunin, Peter T. Rakich, Karl D. Nelson, and Daniel J. Blumenthal. 422 Million intrinsic quality factor planar integrated all-waveguide resonator with sub-MHz linewidth. *Nature Communications*, 12(1):934, feb 2021.

[169] Rana Poushimin and Tahmineh Jalali. Radiation losses in photonic crystal slab waveguide to enhance LEDs efficiency. *Superlattices and Microstructures*, 122:426–433, 2018.

[170] Xinya Wang, Xiaoming Yu, Matthew J. Berg, Pingping Chen, Brice Lacroix, Sasan Fathpour, and Shuting Lei. Curved waveguides in silicon written by a shaped laser beam. *Optics Express*, 29(10):14201, 2021.

[171] Qi Wu, Jeremiah P. Turpin, and Douglas H. Werner. Integrated photonic systems based on transformation optics enabled gradient index devices. *Light: Science and Applications*, 1(NOVEMBER):1–6, 2012.

[172] Yong Zhang, Yu He, Hongwei Wang, Lu Sun, and Yikai Su. Ultra-Broadband Mode Size Converter Using On-Chip Metamaterial-Based Luneburg Lens. *ACS Photonics*, 2020.

[173] John Hunt, Talmage Tyler, Sulochana Dhar, Yu-Ju Tsai, Patrick Bowen, Stéphane Larouche, Nan M. Jokerst, and David R. Smith. Planar, flattened Luneburg lens at infrared wavelengths. *Optics Express*, 20(2):1706, 2012.

[174] Xuetao Gan, Ren Jye Shiue, Yuanda Gao, Inanc Meric, Tony F. Heinz, Kenneth Shepard, James Hone, Solomon Assefa, and Dirk Englund. Chip-integrated ultrafast graphene photodetector with high responsivity. *Nature Photonics*, 7(11):883–887, 2013.

[175] M. Carmen Estevez, Mar Alvarez, and Laura M. Lechuga. Integrated optical devices for lab-on-a-chip biosensing applications. *Laser and Photonics Reviews*, 6(4):463–487, 2012.

[176] Yichen Shen, Nicholas C. Harris, Scott Skirlo, Mihika Prabhu, Tom Baehr-Jones, Michael Hochberg, Xin Sun, Shijie Zhao, Hugo Larochelle, Dirk Englund, and Marin Soljacic. Deep learning with coherent nanophotonic circuits. *Nature Photonics*, 11(7):441–446, 2017.

[177] Daoxin Dai, Jared Bauters, and John E. Bowers. Passive technologies for future large-scale photonic integrated circuits on silicon: Polarization handling, light nonreciprocity and loss reduction. *Light: Science and Applications*, 1(MARCH):1–12, 2012.

[178] Lucas H. Gabrielli and Michal Lipson. Integrated Luneburg lens via ultra-strong index gradient on silicon. *Optics Express*, 19(21):20122, 2011.

[179] Yuan Yuan Zhao, Yong Liang Zhang, Mei Ling Zheng, Xian Zi Dong, Xuan Ming Duan, and Zhen Sheng Zhao. Three-dimensional Luneburg lens at optical frequencies. *Laser and Photonics Reviews*, 10(4):665–672, 2016.

[180] Damien Bernier. Efficient band-edge light injection in two-dimensional planar photonic crystals using a gradual interface. *Optical Engineering*, 48(7):070501, 2009.

[181] Jeffrey M. Gordon. Spherical gradient-index lenses as perfect imaging and maximum power transfer devices. *Applied Optics*, 39(22):3825, 2000.

[182] S. Doric and E. Munro. General Solution of the Non-Full-Aperture Luneburg Lens Problem. *Journal of the Optical Society of America*, 73(8):1083–1086, 1983.

[183] R. H.H. Kroger, M. C.W. Campbell, R. D. Fernald, and H. J. Wagner. Multifocal lenses compensate for chromatic defocus in vertebrate eyes. *Journal of Comparative Physiology A: Sensory, Neural, and Behavioral Physiology*, 184(4):361–369, 1999.

[184] Anatoliy O. Pinchuk and George C. Schatz. Metamaterials with gradient negative index of refraction. *Journal of the Optical Society of America A*, 24(10):A39, 2007.

[185] Fabian Gaufillet. *Cristaux photoniques à gradient : dispositifs et applications*. Thèse de doctorat, Université Paris Sud 11, November 2014.

[186] Nathalie Fabre, Loïc Lalouat, Benoit Cluzel, Xavier Mélique, Didier Lippens, Frédérique De Fornel, and Olivier Vanbésien. Optical near-field microscopy of light focusing through a photonic crystal flat lens. *Physical Review Letters*, 101(7):1–4, 2008.

[187] Hideo Kosaka, Takayuki Kawashima, Akihisa Tomita, Masaya Notomi, Toshiaki Tamamura, Takashi Sato, and Shojiro Kawakami. Superprism phenomena in photonic crystals: Toward microscale lightwave circuits. *J. Lightwave Technol.*, 17(11):2032, Nov 1999.

[188] Quan Yue and Éric Akmansoy. Dual-band flat lens with negative index for silicon photonics. *Applied Physics A*, 128(7):627, 2022.

[189] Maxence Hofman, Didier Lippens, and Olivier Vanbésien. Image reconstruction using a photonic crystal based flat lens operating at 1 55 μm. *Applied Optics*, 49(30):5806–5813, 2010.

[190] Geoffroy Scherrer, Maxence Hofman, Wojciech Migaj, Boris Gralak, Xavier Ḿlique, Olivier Vanb́sien, Didier Lippens, Colette Dumas, Benoit Cluzel, and Fŕdrique De Fornel. Interface engineering for improved light transmittance through photonic crystal flat lenses. *Applied Physics Letters*, 97(7):3–6, 2010.

[191] N. Fabre, L. Lalouat, B. Cluzel, X. Mélique, D. Lippens, F. De Fornel, and O. Vanbésien. Measurement of a flat lens focusing in a 2D photonic crystal at optical wavelength. *2008 Conference on Quantum Electronics and Laser Science Conference on Lasers and Electro-Optics, CLEO/QELS*, 2:6–7, 2008.

[192] N. Fabre, S. Fasquel, C. Legrand, X. Mélique, M. Muller, M. François, O. Vanbésien, and D. Lippens. Towards focusing using photonic crystal flat lens. *Opto-electronics Review*, 14(3):225–232, 2006.

[193] Yulong Fan, Benoît Cluzel, Marlène Petit, Xavier Le Roux, Anatole Lupu, and Andre De Lustrac. 2D Waveguided Bessel Beam Generated Using Integrated Metasurface-Based Plasmonic Axicon. *ACS Applied Materials and Interfaces*, 12(18):21114–21119, 2020.

[194] Daniel Headland, Masayuki Fujita, and Tadao Nagatsuma. Half-Maxwell fisheye lens with photonic crystal waveguide for the integration of terahertz optics. *Optics Express*, 28(2):2366, 2020.

[195] Benjamin Fuchs, Olivier Lafond, Sébastien Rondineau, and Mohamed Himdi. Design and Characterization of Half Maxwell Fish-Eye Lens Antennas in Millimeter Waves. *IEEE Transactions on Microwave Theory and Techniques*, 54(6):2292–2300, 2006.

[196] Hongnan Xu and Yaocheng Shi. Metamaterial-Based Maxwell's Fisheye Lens for Multimode Waveguide Crossing. *Laser and Photonics Reviews*, 12(10):1–8, 2018.

[197] Daniel Headland, Andreas Kurt Klein, Masayuki Fujita, and Tadao Nagatsuma. Dielectric slot-coupled half-Maxwell fisheye lens as octave-bandwidth beam expander for terahertz-range applications. *APL Photonics*, 6(9), 2021.

[198] Washington Nanofabrication Facility. *Working principal*, 2012. `https://ebeam.wnf.uw.edu/ebeamweb/index.html`.

[199] Raith Technology. *Proximity effect correction*, 2020. `https://www.raith.com/technology/nanofabrication-software/proximity-effect-correction/`.

[200] Alexei L. Bogdanov, Jean Lapointe, and Jens H. Schmid. Electron-beam lithography for photonic waveguide fabrication: Measurement of the effect of field stitching errors on optical performance and evaluation of a new compensation method. *Journal of Vacuum Science & Technology B, Nanotechnology and Microelectronics: Materials, Processing, Measurement, and Phenomena*, 30(3):031606, 2012.

[201] Rémi Briche, Aziz Benamrouche, Pierre Cremillieu, Philippe Regreny, Jean-Louis Leclercq, Xavier Letartre, Alexandre Danescu, and Ségolène Callard. Tubular optical microcavities based on rolled-up photonic crystals. *APL Photonics*, 5(10):106106, 2020.

[202] Remi Briche. *Semiconducting origamis : photonic resonators and topological applications*. Theses, Université de Lyon, July 2021.

[203] Joś Marqús-Hueso, Lorenzo Sanchis, Benoit Cluzel, Fŕdrique De Fornel, and Juan P. Martínez-Pastor. Genetic algorithm designed silicon integrated photonic lens operating at 1550 nm. *Applied Physics Letters*, 97(7):10–13, 2010.

[204] Zhuoran Fang, Rui Chen, Albert Ryou, and Arka Majumdar. 1D Self-Healing Beams in Integrated Silicon Photonics. *ACS Photonics*, 8(7):2139–2147, 2021.

[205] Yulong Fan, Xavier Le Roux, Alexander Korovin, Anatole Lupu, and Andre De Lustrac. Integrated 2D-Graded Index Plasmonic Lens on a Silicon Waveguide for Operation in the Near Infrared Domain. *ACS Nano*, 11(5):4599–4605, 2017.

[206] I. Horcas, R. Fernández, J. M. Gómez-Rodríguez, J. Colchero, J. Gómez-Herrero, and A. M. Baro. WSXM: A software for scanning probe microscopy and a tool for nanotechnology. *Review of Scientific Instruments*, 78(1):13705, 2007.

Publication list

Journal

1. Quan YUE and Éric AKMANSOY. Dual-band flat lens with negative index for silicon photonics. Applied Physics A, 128(7):627, 2022.

2. Graded flat lens with negative index for silicon photonics, on going redaction.

Conference

1. Quan YUE, Éric AKMANSOY. Graded Index Flat Lens With Negative Index Operating at 1.55 μm. Congrès OPTIQUE of SFO, Dijon (France), 5-9 July 2021 (Poster).